Site surveys for the deployment of infrasound mobile stations in the Azores Islands

Dissertação de Mestrado

Maria do Céu Neto de Jesus

Mestrado em

VULCANOLOGIA E RISCOS GEOLÓGICOS

SICUT AURORA SCIENTIA LUCET
UNIVERSIDADE DOS AÇORES

Ponta Delgada
2022

Site surveys for the deployment of infrasound mobile stations in the Azores Islands

Dissertação de Mestrado

Maria do Céu Neto de Jesus

Orientadores

Doutor Nicolau Maria Berquó de Aguiar Wallenstein
PhD em Geologia (especialidade de Vulcanologia),
Professor Associado, Universidade dos Açores

Doutora Paola Campus
PhD in Geophysics of the Lithosphere and Geodynamics,
Consultant Researcher, UniFI - Università degli Studi di Firenze

Dissertação de Mestrado submetida como requisito parcial para obtenção do grau de
Mestre em Vulcanologia e Riscos Geológicos

In loving memory of my sacred triplet,

Eduardo, Maria, and Francisco

TABLE OF CONTENTS

TABLE OF CONTENTS ... I

LIST OF FIGURES ... VII

LIST OF TABLES ... XII

LIST OF PHOTOS ... XIII

ACKNOWLEDGEMENTS ... XIV

ABSTRACT ... XV

RESUMO ... XVI

CHAPTER 1. INTRODUCTION TO INFRASOUND ... 1

1.1. Framework and objective of the work ... 1
  1.1.1. Motivation ... 1
  1.1.2. Study relevance ... 1
  1.1.3. Research objectives ... 2
  1.1.4. Dissertation structure and organization ... 2
1.2. Infrasound concept and definition ... 3
1.3. Infrasound waves: propagation and characteristics ... 4
  1.3.1. Temperature ... 5
  1.3.2. Wind ... 6
  1.3.3. Ruling parameters for infrasound propagation ... 7
    1.3.3.1. Infrasound attenuation: absorption and dispersion ... 7
    1.3.3.2. Infrasound waveguides ... 8
    1.3.3.3. Infrasound phases/arrivals ... 9
    1.3.3.4. Topography influence ... 11
1.4. Infrasound sources ... 11
  1.4.1. Volcanic eruptions ... 14
1.5. Infrasound Monitoring and its applications ... 15
  1.5.1. The IMS infrasound network ... 15
  1.5.2. Scientific and civil applications ... 16
  1.5.3. Volcano infrasound monitoring strategies ... 17
  1.5.4. Monitoring strategies in oceanic islands ... 18
1.6. Infrasound background noise ... 19
  1.6.1. Wind-generated infrasound noise ... 20
  1.6.2. Power Spectral Density (PSD) ... 22

1.6.3. Probability Density Function (PDF) 25
1.7. Infrasound permanent Stations 26
1.7.1. Infrasound arrays 26
1.7.1.1. Array elements 26
1.7.1.2. Central Facility (CF) 33
1.7.1.3. Global Communications Interface (GCI) 33
1.7.2. Array Design 33
1.7.2.1. Small apertures 35
1.7.3. Signal detection and processing 35
1.7.3.1. Signal-to-Noise Ratio (SNR) and detection capability 36
1.8. Infrasound mobile stations 37
1.8.1. Application in volcano monitoring 38
1.8.2. Examples of temporary infrasound arrays 38
1.8.2.1. CTBTO portable array 38
1.8.2.2. Temporary infrasound UniFI arrays 39
1.8.2.3. Temporary infrasound arrays at Volcán de Fuego, Guatemala 40

CHAPTER 2. THE AZORES ISLANDS 41
2.1. General settings of the Azores Islands 41
2.1.1. Geological framework 41
2.1.1.1. Seismicity 42
2.1.1.2. Volcanism 43
2.1.2. Wind patterns 44
2.2. Active central volcanoes 45
2.2.1. São Miguel Island 45
2.2.1.1. Sete Cidades volcano 46
2.2.1.1.1. Tectonics 47
2.2.1.1.2. Eruptive history 47
2.2.1.2. Fogo volcano 48
2.2.1.2.1. Tectonics 48
2.2.1.2.2. Eruptive history 49
2.2.1.3. Furnas volcano 50
2.2.1.3.1. Tectonics 50
2.2.1.3.2. Eruptive history 51
2.2.2. Terceira Island 52

2.2.2.1. Pico Alto volcano ... 53
2.2.2.1.1. Tectonics ... 54
2.2.2.1.2. Eruptive history ... 54
2.2.2.2. Santa Bárbara volcano ... 54
2.2.2.2.1. Tectonics ... 55
2.2.2.2.2. Eruptive history ... 55
2.2.3. Faial Island ... 55
2.2.3.1. Caldeira volcano ... 56
2.2.3.1.1. Tectonics ... 57
2.2.3.1.2. Eruptive history ... 57
2.2.4. Pico Island ... 58
2.2.4.1. Montanha do Pico volcano ... 59
2.2.4.1.1. Tectonics ... 60
2.2.4.1.2. Eruptive history ... 60

CHAPTER 3. SITE SURVEY METODOLOGY ... 62
3.1. Introduction to site surveys ... 62
3.2. Monitoring volcanic eruptions in the Azores Islands ... 62
3.2.1. Eruptive scenarios ... 63
3.2.1.1. Sete Cidades volcano (São Miguel Island) ... 64
3.2.1.2. Fogo volcano (São Miguel Island) ... 65
3.2.1.3. Furnas volcano (São Miguel Island) ... 66
3.2.1.4. Pico Alto volcano (Terceira Island) ... 67
3.2.1.5. Santa Bárbara volcano (Terceira Island) ... 68
3.2.1.6. Caldeira volcano (Faial Island) ... 69
3.2.1.7. Montanha do Pico volcano (Pico Island) ... 70
3.2.2. Preliminary selection ... 71
3.2.2.1. Constraints and their requirements ... 72
3.2.2.1.1. Infrasound background noise ... 72
3.2.2.1.2. Topography, area, and land cover ... 73
3.2.2.1.3. Logistics, security, and environmental conditions ... 74
3.2.2.2. Pre-selected sites in the Azores Islands ... 74
3.2.3. Assessment in situ of the pre-selected sites - São Miguel Island ... 81
3.2.4. Field survey and final selection ... 82
3.2.4.1. Final definition in situ of the array configuration ... 82

3.2.4.2. Gathering and calibration and of all necessary equipment 82
3.2.4.2.3. Deployment of an infrasound array 83
3.2.4.2.4. Signal testing and recording 85
3.2.4.2.5. Data analysis and final selection of the sites 85
3.3 Discussion of the results 85

CHAPTER 4. 2022 SÃO JORGE ISLAND SEISMOVOLCANIC CRISIS - STUDY CASE 89
4.1. Background of the seismovolcanic crises 89
4.1.1. São Jorge Island - geological framework 89
4.1.1.1. Manadas fissure volcanic system 90
4.1.2. 2022 Seismovolcanic crisis - current situation 91
4.2. Site survey and deployment of a mobile infrasound array 93
4.2.1. Preliminary selection of sites on São Jorge Island 94
4.2.1.1. Constraints and requirements 94
4.2.1.1.1. Infrasound background noise 94
4.2.1.1.2. Topography, size, and land cover 95
4.2.1.1.3. Logistics, security, and environmental conditions 95
4.2.1.2. Pre-selected sites on São Jorge Island 96
4.2.2. Gathering and calibration of all necessary equipment 98
4.2.3. Assessment in *situ* of the pre-selected sites 99
4.2.4. Field survey - deployment of SJ1 array 100
4.2.4.1. Deployment of SJ1 array 101
4.2.4.3. Signal testing and recording 104
4.3. Data processing and analysis from SJ1 104
4.3.1. Meteorological conditions on São Jorge Island 104
4.3.2. Power Spectral Density (PSD) 106
4.4. Discussion of the results 108

FINAL CONSIDERATIONS 112

REFERENCES 115
Bibliography 115
Webography 128
Data 129

ANNEXES

A. Preliminary selection of sites in the Azores Islands A-1
A.1. Sete Cidades volcano (São Miguel Island) A-1
  A.1.1. Eruptive scenarios SC1 and SC2 (Map) A-1
  A.1.2. LC and IS arrays (Map) A-3
  A.1.3. Features of the LC and IS arrays (Table) A-5
A.2. Fogo volcano (São Miguel Island) A-7
  A.2.1. Eruptive scenarios FO1 and FO2 (Map) A-7
  A.2.2. LC and IS arrays (Map) A-9
  A.2.3. Features of the LC and IS arrays (Table) A-11
A.3. Furnas volcano (São Miguel Island) A-13
  A.3.1. Eruptive scenario FU1 (Map) A-13
  A.3.2. LC and IS arrays (Map) A-15
  A.3.3. Features of the LC and IS arrays (Table) A-17
A.4. Pico Alto volcano (Terceira Island) A-19
  A.4.1. Eruptive scenario PA1 (Map) A-19
  A.4.2. LC and IS arrays (Map) A-21
  A.4.3. Features of the LC and IS arrays (Table) A-23
A.5. Santa Bárbara volcano (Terceira Island) A-25
  A.5.1. Eruptive scenario SB1 (Map) A-25
  A.5.2. LC and IS arrays (Map) A-27
  A.5.3. Features of the LC and IS arrays (Table) A-29
A.6. Caldeira volcano (Faial Island) A-31
  A.6.1. Eruptive scenario CA1 (Map) A-31
  A.6.2. LC and IS arrays (Map) A-33
  A.6.3. Features of the LC and IS arrays (Table) A-35
A.7. Montanha do Pico volcano (Pico Island) A-37
  A.7.1. Eruptive scenario MP1 (Map) A-37
  A.7.2. LC and IS arrays (Map) A-39
  A.7.3. Features of the LC and IS arrays (Table) A-41

B. Assessment in *situ* of the pre-selected sites - São Miguel Island B-1
B.1. Sites to assess in *situ* (Map) B-1
B.2. Characterization of the assessed sites (Tables and Photos) B-3
B.3. Sites selected for signal testing (Map) B-48

C. 2022 São Jorge Island seismovolcanic crisis - study case C-1
C.1. Geological framework of São Jorge Island (Map) C-1
C.2. Seismic activity on São Jorge Island: 19-03-2022 to 02-11-2022 (Map) C-3
C.3. Pre-selected sites for survey at São Jorge Island (Map) C-5
C.4. Array configurations (Maps) C-7
C.5. Deployment of SJ1 (Photos from the 1st and 2nd visit). C-9

D. Field equipment D-1
D.1. IS array equipment (SEISMOWAVE's SISTEM and MB3d datasheets) D-1
D.2. LC array equipment (Table) D-7

E. Meteorological data E-1

LIST OF FIGURES

CHAPTER 1. INTRODUCTION TO INFRASOUND

Figure 1.1 – Acoustic waveform spectrum (in Maceira *et al.*, 2017). 3

Figure 1.2 - Effective sound speed vertical gradient (Design World Staff, 2010). 5

Figure 1.3 - Vertical gradient in average global atmospheric temperature. These variations are due to changes in the chemical and physical characteristics of the atmosphere with altitude, according to the USSA 1976 (adapted; in Evers and Haak, 2010). 6

Figure 1.4 - Simulation of infrasound wave propagation for the meteor explosion observed offshore Portugal (40.5N, 18.0W) on March 9th, 2017. The red, blue, and green paths represent the tropospheric (*Iw*), stratospheric (*Is*), and thermospheric (*It*) arrivals, respectively. Correspondingly, the effective sound velocity models toward the West and the East are displayed in black on the left and right side of the figure, with the effective velocity at the ground represented by a gray-dashed line (in Marty, 2019). 10

Figure 1.5 - Natural and man-made sources of infrasound (CTBTO, 2022). 12

Figure 1.6 - Example waveforms of four naturals infrasound sources (in Soloman *et al.*, 2018). 12

Figure 1.7 - IMS infrasound network, as of June 2017, with certified stations (green), installed stations (turquoise), stations under construction (orange), planned stations (red), and the IDC (purple) (in Marty, 2019). 16

Figure 1.8 - Infrasound noise at 1 Hz as a function of average wind speed during 2004 for the IMS infrasound station I31KZ, Kazakhstan. The different coloured symbols represent the average values for each month of the year. Dashed lines, with slopes of 2, 3, and 4, are for reference (in Bass *et al.*, 2006). 22

Figure 1.9 - Infrasound network noise models for all times and seasons for low-noise (heavy red line), median-noise (green) and high-noise (heavy blue line) conditions. The 5th (red) and 95th percentiles (blue) comprise a full year's data of tens stations (in Bowman *et al.*, 2005). 23

Figure 1.10 - Noise power density at Chã das Mulas, in São Miguel Island, Azores. In black is shown a single power density estimate taken from the filtered pressure data. The yellowish curves are the 10th, 50th and 90th percentile noise levels from the entire experiment. The 5 second microbarom is not observed at times of high noise (Hedlin *et al.*, 2000). 24

Figure 1.11 - PDFs in February 2017 for IMS infrasound stations a) I06AU (H6), b) I49GB (H2), c) I16CN (H3), and d) I37NO (H7). The Power Spectral Densities (PSDs) are computed over 1-h time-period using Welch's method and are corrected from the system response including WNRS, sensor, and data acquisition system. The grey-dashed lines represent a high- and low-noise model according to Bowman *et al*. (2005) infrasound noise models (in Marty, 2019). 25

Figure 1.12 - Schematic illustration of an IMS infrasound station (in Marty, 2019). 26

Figure 1.13 - Schematic overview of the absolute infrasound sensor MB2005 (in Ponceau and Bosca, 2010). 27

Figure 1.14 - Inlet port scheme (CTBTO, 2022) 29

Figure 1.15 - Configuration of array element with pipe structures to reduce wind noise (CTBTO, 2022). 30

Figure 1.16 - Four most common types of pipe array configurations installed at IMS infrasound stations: a) rosette; b) star; c) hexagonal closed pack; and d) radial (in Marty, 2019). 30

Figure 1.17 - Infrasound array element general design (ARISE, 2013). 32

Figure 1.18 - Possible configurations of infrasound arrays (CTBTO, 2022). 34

Figure 1.19 - Infrasound arrays operated by UniFI around the world (in Campus *et al*., 2017) 39

Figure 1.20 - Temporary and permanent infrasound monitoring networks at Volcán de Fuego. Red (May 2018) and blue circles (November-December 2018) are temporary deployments; orange circles indicate the permanent seismo-acoustic network. The grey-filled area illustrates, qualitatively, the footprint of the 3rd, June 2018 Pyroclastic Density Current (PDC) (in Diaz-Moreno *et al*., 2020) 40

CHAPTER 2. THE AZORES ISLAND

Figure 2.1 – Geological framework of the Azores Islands. MAR – Mid-Atlantic Ridge; TR – Terceira Rift; EAFZ – East Azores Fracture Zone; GF – Gloria Fault (modified by Pimentel (2015) from Lourenço *et al*. (1998), Vogt and Jung (2004), Beier *et al*. (2008)), and Georgen and Sankar (2010)) 42

Figure 2.2 - Epicentral locations of destructive earthquakes during historical times (in Gaspar *et al*., 2015b). 43

Figure 2.3 - Location of historical subaerial and submarine eruptions (in Gaspar *et al.,* 2015b). 44

Figure 2.4 - Location of volcanic systems on São Miguel Island, identified by red colour. SCV - Sete Cidades volcano; PFVS - Picos fissural volcanic system; FGV - Fogo volcano; CFVS - Congro fissural

volcanic system; FRV - Furnas volcano; PV - Povoação volcano; NVS - Nordeste volcanic system (in Madeira *et al.,* 2015).. 46

Figure 2.5 - Location of the 4 central volcanoes on Terceira Island, identified by red colour. SBC - Santa Bárbara caldera; PAC - Pico Alto caldera; GM - Guilherme Moniz caldera; SCC - Serra do Cume caldera, i.e., Cinco Picos caldera (in Madeira *et al*., 2015). 52

Figure 2.6. - Location of the only active central volcano on Faial Island, identified by red colour. FC - Faial caldera, i.e., Caldeira volcano (in Madeira *et al*., 2015). 56

Figure 2.7 - Location of Pico Mountain volcano on Pico Island, identified by red colour. PV - Pico volcano (in Madeira *et al*., 2015). 59

CHAPTER 3. SITE SURVEY METODOLOGY

Figure 3.1 - Eruptive scenarios SC1 and SC2, Sete Cidades volcano. Volcanic and tectonic structures are from Carmo (2013), modified by CIVISA... 64

Figure 3.2 - Eruptive scenarios FO1 and FO2, Fogo volcano. Volcanic and tectonic structures are from Carmo (2013), modified by CIVISA.. 66

Figure 3.3 - Eruptive scenario FU1, Furnas volcano. Volcanic and tectonic structures are from Carmo (2013), modified by CIVISA. 67

Figure 3.4 - Eruptive scenario PA1, Pico Alto volcano. Volcanic and tectonic structures are from Madeira (2005), modified by CIVISA.. 68

Figure 3.5 - Eruptive scenario SB1, Santa Bárbara volcano. Volcanic and tectonic structures are from Madeira (2005), modified by CIVISA.. 69

Figure 3.6- Eruptive scenario CA1, Caldeira volcano. Volcanic and tectonic structures are from Madeira (1998), modified by CIVISA. 70

Figure 3.7- Eruptive scenario M1, Montanha do Pico volcano. Volcanic and tectonic structures are from Madeira (1998), modified by CIVISA. 71

Figure 3.8 - Options of Google Earth Pro® that were selected to visualise the area in study............. 76

Figure 3.9 - Step 1 and 2 for FU1 (Furnas volcano), showing the source location, the IS42 back azimuth (blue) and the buffers of 5 km (red), 7.5 km (white) and 15 km (purple). 78

Figure 3.10 - Step 1 and 2 for contemporaneous eruptive scenarios of SC1 and SC2 (Sete Cidades volcano), showing the two sources' location, the two IS42 back azimuths (blue) and the two buffers of 5 km (red), 7.5 km (white) and 15 km (purple).. 78

Figure 3.11 - Step 3 for one IS array to monitor the eruptive scenario SB1 of Santa Bárbara volcano, in Terceira Island. The yellow stretch represents the azimuth from the source (NNW); the yellow points illustrate each sensor, and the 4 sensors form a centred triangular configuration marked in red colour. The 4 colourful arcs of circles show the same spherical acoustic wavefront propagating through time and space. In ascending order of time, this wavefront arrives to IS-SB-01_3 (green), IS-SB-01_2 (white), IS-SB-01_4 (blue), and at last to IS-SB-01_1 (orange)... 80

CHAPTER 4. 2022 SÃO JORGE ISLAND SEISMOVOLCANIC CRISIS - STUDY CASE

Figure 4.1 - Geological framework of São Jorge Island, illustrating its (1) volcanic complexes, (2) tectonics, as well (3) the vents of both historical eruptions at Manadas fissure volcanic system (modified by CIVISA from: (1) Madeira and Brum da Silveira, 2003, (2) Madeira, 1998, and (3) Zanon and Viveiros, 2019). 90

Figure 4.2 - Seismic activity on São Jorge Island since 19 March 2022 until 2 November 2022 (data from CIVISA, 2022).. 92

Figure 4.3 - Daily frequency of recorded earthquakes during the current seismovolcanic crises (in CIVISA, 2022d).. 93

Figure 4.4 - Pre-selected sites for survey at São Jorge Island, with the back azimuths from the eruptive fissure considered to IS42 station. Historical vent's locations are from Zanon and Viveiros (2019) and probable eruptive fissure is from Madeira (1998), all data modified by CIVISA. 97

Figure 4.5 - Configuration of SJ1 from the 1st visit. 102

Figure 4.6 - Configuration of SJ1 after the 2nd visit. 103

Figure 4.7 – SJ1 arrays deployments compared geometries. 103

Figure 4.8 – Meteorological data (IPMA, 2022) of the periods selected to analyse PSDs: 19/04/2022 12 AM - 20/04/2022 12 AM for the 1st array (left) and 23/05/2022 12 AM - 24/05/2022 12 AM for the 2nd array (right) (see complete plot in Annex E). 105

Figure 4.9 – Raw (left) and filtered (right) data of the period between 19/04/2022 12 AM to 20/04/2022 12 AM (1st array). 107

Figure 4.10 – PSD plot (left) and spectrogram of sensor 1 (right) from the data of the period between 19/04/2022 12 AM to 20/04/2022 12 AM (1st array) (blue transparency represents the interval of frequencies between 1 and 8 Hz). 107

Figure 4.11 – Raw (left) and filtered (right) data of the period between 23/05/2022 12 AM to 24/05/2022 12 AM (2nd array). 108

Figure 4.12 – PSD plot (left) and spectrogram of sensor 1 (right) from the data of the period between 23/05/2022 12 AM to 24/05/2022 12 AM (2nd array) (blue transparency represents the interval of frequencies between 1 and 8 Hz). 108

Figure 4.13 – PSD plots for the 1st array (left) 2nd array (right) from the data of the periods between 19/04/2022 12 AM to 20/04/2022 12 AM, and 23/05/2022 12 AM to 24/05/2022 12 AM, respectively (blue transparency represents the interval of frequencies between 1 and 8 Hz). 109

Figure 4.14 - Comparison of the NLNM (New Low Noise Model) and NHNM (New High Low Noise Model) with previously proposed models between 0.01 and 8 Hz (Marty *et al.*,2021). A blue transparency was added to represent the interval of frequencies between 1 and 8 Hz. 110

LIST OF TABLES

CHAPTER 3. SITE SURVEY METODOLOGY

Table 3.1 - Classification of the eruptive scenarios in the Azores Islands and respective back azimuths from IS42 station.. 77

CHAPTER 4. 2022 SÃO JORGE ISLAND SEISMOVOLCANIC CRISIS - STUDY CASE

Table 4.1 - Back azimuths from the pre-selected sites to the probable eruptive fissure. 97

Table 4.2 - Site characterization of SJ1. 100

LIST OF PHOTOS

CHAPTER 1. INTRODUCTION TO INFRASOUND

Photo 1.1 - MB2005 aneroide microbarometer, IS42 Graciosa, Portugal. 28

Photo 1.2 - Inlet port of noise reducing pipe array, IS42 Graciosa, Portugal 29

Photo 1.3 - Element H1 from IS42 Graciosa, Azores, Portugal. 32

Photo 1.4 - CF from IS42 Graciosa, Azores, Portugal. 33

Photo 1.5 - Installation of CTBTO portable array in Tsukuba, Japan, in March 2010 (in Mialle *et al*., 2010). 38

Photo 1.6 - Portable site equipment ready for deployment in Bermuda, 2019 (in Robertson *et al*., 2021). 39

CHAPTER 2. THE AZORES ISLANDS

Photo 2.1 - Caldera of Sete Cidades volcano (photo courtesy of Nicolau Wallenstein). 47

Photo 2.2 - Caldera of Fogo volcano (photo courtesy of Nicolau Wallenstein). 48

Photo 2.3 - Caldera of Furnas volcano: parish of Furnas (left) and Lagoa das Furnas (right) (photo courtesy of Nicolau Wallenstein). 50

Photo 2.4 - Pico Alto volcano (photo courtesy of Adriano Pimentel). 53

Photo 2.5 - Santa Bárbara volcano (photo courtesy of Adriano Pimentel). 54

Photo 2.6 - Caldeira volcano (left) (photo courtesy of Adriano Pimentel) and its caldera (right) (photo courtesy of Nicolau Wallenstein). 57

Photo 2.7 - Montanha do Pico volcano (photo courtesy of Nicolau Wallenstein). 59

CHAPTER 4. 2022 SÃO JORGE ISLAND SEISMOVOLCANIC CRISIS - STUDY CASE

Photo 4.1 - Partial view of the eastern section of the Manadas fissure volcanic system, from west to east (photo courtesy of Nicolau Wallenstein). 91

ACKNOWLEDGMENTS

If this research study could have infinite co-authors, this page would never end. It is not an easy task do orderly express in a text my huge gratitude for everybody that has contributed to the current reading of this document. Every word, every blank space, every dot carries, in the same amount, all of them concerns, happiness, generosity, pride, and sometimes a little despair.

I am very grateful to Prof. Nicolau Wallenstein, the supervisor behind this work, who wait two years, patiently almost the time, to finally see it accomplished. It was two long years of hard work and discussion on the subject that would be even harder without his confidence on my work.

I am very grateful to Dra. Paola Campus, for her availability in clarifying all the doubts regarding infrasound site surveys as well as data processing of the results.

I am very grateful to my co-workers, Sandro Matos and Arturo Montalvo, for all the support given as wiser people on the subject, which was a new knowledge field for myself.

I am very grateful to my Italian colleagues from UniFI, Duccio Gheri, Giacomo Belli, also Prof. Emanuele Marchetti, whose mobile infrasound array (SJ1) was deployed in São Jorge through a collaboration between UniFI and IVAR/CIVISA. Again, to Duccio and Giacomo for always being available to helping me on MATLAB® issues.

I am very grateful to IVAR an CIVISA researchers for providing all data used on the presented maps.

I am very grateful to Dr Carlos Ramalho from IPMA by providing the meteorological data of São Jorge Island.

I am very grateful to Jéssica Uchoa for teaching me quickly how to manage QGIS® software.

I am very grateful for my 'best friends' for all emotional and motivational "couching" on the outsides, every time a break to breath was essential.

I am very grateful for my amazing big family, in the Azores, in mainland, in the rest of the world, even in the stars. They always saw the better version of myself, and I am very happy to be part of their lives.

ABSTRACT

Low-frequency sound waves (< 20 Hz), known as infrasound, are generated by natural and man-made sources, such as volcanic eruptions, seismic activity, quarry activities, nuclear explosions, among others, which induce micro pressure variations in the atmosphere. Thus, travelling through waveguides in atmosphere, infrasound can propagate over long distance with low attenuation. Therefore, since the beginning of the XXI century, infrasound techniques have been employed to monitor and analyse a myriad of acoustic events, from military to civil and scientific applications.

The geological history of the Azores Islands has been recording important seismic and volcanic activity, which lead to expect future eruptive events from their active volcanoes. Therefore, located in the middle of the North Atlantic, the archipelago is an excellent platform to develop a regional infrasound monitoring network. The deployment of infrasound arrays in case of any emergency, as the 2022 volcanic unrest of Manadas fissure volcanic system on São Jorge Island, would be a valuable input to the existing monitoring networks of CIVISA/IVAR, particularly to identify precursor signals of volcanic activity through the detection of seismoacoustic events, and an indispensable tool for monitoring possible eruptive activity. Additionally, IVAR is responsible for the operation and maintenance of the IMS infrasound station IS42, located on Graciosa Island, which has a major contribution for the Azorean region in the detection of all type of infrasound sources from all the world, and would display a significant role in association with other infrasound arrays, as the situation in São Jorge Island with SJ1 array.

Nevertheless, before the deployment of any infrasound array, site surveys must be conducted to select the sites with the best overall conditions, particularly with a good signal-to-noise ratio. Thus, this research work has adapted known methodologies for site surveys to deploy infrasound arrays in the Azores Islands, considering its central volcanoes as the infrasound source reference, through hypothetically eruptive scenarios. All steps of the survey were herein detailed, namely (1) the preliminary selection, (2) the assessment in situ of the pre-selected sites, which was only possible on São Miguel Island, and (3) field survey and final selection. This last step was conducted in São Jorge Island, given the opportunity that came up with the seismovolcanic crisis. Therefore, the same site survey methodology was applied for a volcanic fissure system and an infrasound array (SJ1) was deployed to support the other monitoring networks, specially the seismic one, in the detection of seismoacoustic events. Hence, SJ1 was set up to detect volcanic infrasound in case of an eruption start on Manadas fissure volcanic system.

Keywords: Infrasound; Volcano monitoring; Site surveys; Array; São Jorge Island; Noise analysis.

RESUMO

Ondas sonoras de baixa frequência (< 20 Hz), conhecidas como infrassons, são geradas por fontes naturais e artificiais que induzem pequenas variações na pressão atmosférica, tais como erupções vulcânicas, sismos, explosões em pedreiras, explosões nucleares, entre outras. Através de canais na atmosfera, os infrassons podem propagar-se por longas distâncias sofrendo pouca atenuação. Desde o início do século XXI, os infrassons têm vindo a ser aplicados na monitorização de diversos tipos de eventos acústicos, tanto para aplicações militares como civis e científicas.

A história geológica das ilhas dos Açores tem registado importantes eventos sísmicos e vulcânicos, por isso, futuros eventos eruptivos dos seus vulcões ativos são expectáveis. Localizado no meio do Atlântico Norte, o arquipélago é uma excelente plataforma para desenvolver uma rede regional de monitorização por infrassons. A instalação de *arrays* de infrassons em caso de qualquer emergência, como a crise sismovulcânica de 2022 do Sistema Vulcânico Fissural de Manadas na Ilha de São Jorge, foi uma mais-valia para testar as redes de monitorização existentes do CIVISA/IVAR, particularmente para identificar sinais precursores da atividade vulcânica através da deteção de eventos sismo-acústicos, bem como uma ferramenta indispensável para monitorizar uma possível atividade eruptiva. De igual modo, o IVAR é responsável pela operação e manutenção da estação de infrassons IS42 do IMS, localizada na Ilha da Graciosa, e que desempenha um papel importante na deteção diversas fontes de infrassons no arquipélago dos Açores e globalmente. Assim sendo, a sua colaboração com outros *arrays* de infrassons torna-se fundamental em casos como o da crise de São Jorge relativamente ao *array* SJ1.

No entanto, antes instalação de qualquer *array* portátil de infrassons, devem ser avaliados e selecionados os locais com as melhores condições gerais, sobretudo com uma boa razão entre sinal e ruído. Portanto, este trabalho de investigação adaptou as metodologias conhecidas para os chamados *site surveys* direcionados para a instalação de *arrays* portáteis de infrassons nos Açores, hipotecando para isso cenários eruptivos nos vulcões centrais ativos nos Açores como fonte de infrassons de referência. Todas as etapas dos *site surveys* foram aqui detalhadas, nomeadamente (1) a seleção preliminar, (2) a avaliação *in situ* dos sítios pré-selecionados, que só foi possível na Ilha de São Miguel, e (3) o teste de sinal e consequente seleção final. Esta última etapa foi realizada na Ilha de São Jorge, dada a oportunidade que surgiu com a crise sismovulcânica. Assim, essa mesma metodologia foi adaptada para o Sistema Vulcânico Fissural de Manadas, tendo-se instalado o array SJ1 de modo a colaborar com as outras redes de monitorização, especialmente a sísmica, na deteção de eventos sismo-acústicos e, na eventualidade do início de atividade eruptiva.

Keywords: Infrassons; Monitorização vulcânica; Levantamentos de campo; Estação; São Jorge; Análise de ruído.

CHAPTER 1. INTRODUCTION TO INFRASOUND

1.1. Framework and objective of the work

1.1.1. Motivation

Following its geodynamic framework where the North American, Eurasian, and Nubian lithospheric plates interact, the Azores islands have remarkable seismic and volcanic activity along its geological history. Located on North Atlantic, they present very peculiar weather conditions, with frequent severe storms, strong winds and a record of many hurricanes. Nowadays, the volcanic activity is in a quiescence phase, despite the 2022 volcanic unrest on São Jorge Island. However, the eruptive history shows clearly that a potential local infrasound network is critical to support the other seismovolcanic monitoring techniques, already used in the archipelago, in future eruptive events, as it was applied to monitor the 2022 São Jorge Island seismovolcanic crisis.

The present research work comprises the importance of evaluating possible locations suitable for the deployment of infrasound mobile stations in the Azores Islands. The location of the archipelago provides an excellent environment to apply and learn from infrasound monitoring techniques for the study of extreme atmospheric events.

1.1.2. Study relevance

This study has a major contribution for a wider application of infrasound monitoring techniques in the Azores Islands, since this kind of monitoring is an essential tool to be combined along with seismic, geochemical, and geodetic ones, already applied on the *Instituto de Investigação em Vulcanologia e Avalição de Riscos* (IVAR), from the *Universidade dos Açores* and *Centro de Informação e Vigilância Sismovulcânica dos Açores* (CIVISA).

Since the Earth is an interconnected system, each source of data complements the weakness of the other. The symbiose between all monitoring fields mentioned above is very useful not only for a most deeply understanding of atmosphere and phenomena occurring within it but also to improve the risk management and mitigation of natural hazards, that has a huge potential to occur on these oceanic islands, as volcanic activity, high magnitude earthquakes, landslides, and severe storms.

The site surveys to be conducted in this work will allow the selection of the appropriated places around the Azores to temporally install an infrasound mobile stations network, especially in case of an emergency or crisis. These surveys aim for a future deployment of an Azorean infrasound network as the existing seismic, geodetic, geochemical, and meteorological. Only then it will be possible to apply infrasound monitoring in a more reliable and accurately way, always with the support of the IS42 infrasound station, located on Graciosa Island, as well as others from the International Monitoring System (IMS) of the Comprehensive Test-Ban Treaty Organisation (CTBTO). Several portable stations ready to be installed in pre-selected locations, near eminent eruption vents, are an essential support to the seismic and geochemical networks already existing on the archipelago. In 2022, the seismovolcanic crisis on São Jorge Island allowed to apply infrasound techniques as a contribution to the monitoring efforts, particularly together with the seismic, to monitor seismoacoustic events, being possible to correlated seismic activity related with the volcanic unrest to the infrasound detections of SJ1 array deployed on São Jorge Island and IS42 IMS station, located on Graciosa Island.

Furthermore, infrasound is a very important technique to be applied to open vent volcanic events, allowing to characterise the explosive eruptive phase of a volcanic eruption. It can be also used to follow North Atlantic atmospheric extreme events, such as the frequent hurricanes, or to characterize microbaroms, to understand the dynamic of the sea waves. It will be also very important to support the monitoring of the rockets launches from the centre that is projected to Santa Maria Island.

1.1.3. Research objectives

The main objectives of this work are to acquire the know-how and to implement methodologies and techniques to be applied on the Azores Islands for infrasound sites survey, considering its central volcanoes as a source reference. The purpose of the survey is to locate sites where it will be possible to deploy portable arrays for infrasound monitoring, considering important aspects such as topography, land cover, vegetation, noise sources as well as the logistic and environmental problems that might exist. After a first selection, the ideal approach is the evaluation of the signal-to-noise ratio *in* situ and the simulations of the detection capability of some sites tested at field will dictate which ones offer the best conditions for infrasound monitoring.

Also, it is present herein the study case of the 2022 São Jorge Island seismovolcanic crises, where a survey was conducted and consequently, a mobile infrasound array (SJ1) was deployed to monitor seismoacoustic events and a possible eruptive onset.

1.1.4. Dissertation structure and organization

The present study is organized in the following format: ***Chapter 1. Introduction to infrasound***, it describes the main objectives of this work and its structure, stating its relevance and contribution for the scientific field in hand. Also, contains all the important theoretical background necessary to understand the contents of an infrasound site survey, starting with general subchapters about the infrasound concept and definition as well as the way this acoustic wave propagates, mentioning its main sources, passing to more specific subchapters that describes some infrasound monitoring headlights and the main aspects on infrasound station components, design, and signal detection; ***Chapter 2. The Azores Islands*** briefly describes its geological framework as well as its standard wind patterns, which have a direct influence of infrasound waves propagation. Also, the 8 central volcanoes considered as the source of infrasound to apply the survey's methodologies were characterised regarding their tectonics and eruptive history; ***Chapter 3. Site survey methodology***, divided in few subchapters, starting with a rationale on the methods generally applied in infrasound site surveys. Next, the eruptive scenarios hypothetically chosen as the source references are present and justified. Then, it follows the characterization of the 3 steps of a survey, namely the (1) preliminary selection, (2) the assessment in situ, and (3) the field survey and final selection, as well as the discussion of the results from this chapter; ***Chapter 4. 2022 São Jorge Island seismovolcanic crises - study case***, describes in-depth the development of an infrasound survey and consequent deployment of an infrasound array to collaborate on the monitoring of the volcanic unrest that started in March 2022 on São Jorge Island, followed by data analysis of the noise as well as the discussion of the results; ***Final Considerations***, resume the fundamental outcomes achieved by this research study, also presenting work to be developed hereafter.

1.2. Infrasound concept and definition

Sound waves are longitudinal pressure waves in which the particle moves in the same direction as the wave propagation. They propagate in all phases of matter as plasmas, gases, liquids, and solids. However, this research work only focuses on the atmosphere (gases). When sound waves propagate trough a gas its equilibrium state is disturbed or deformed by the compression and rarefactions of these waves (Pain, 2005). The created disturbance or deformation on the air enables a large spectrum of frequencies for the acoustic waves, as seen in Figure 1.1.

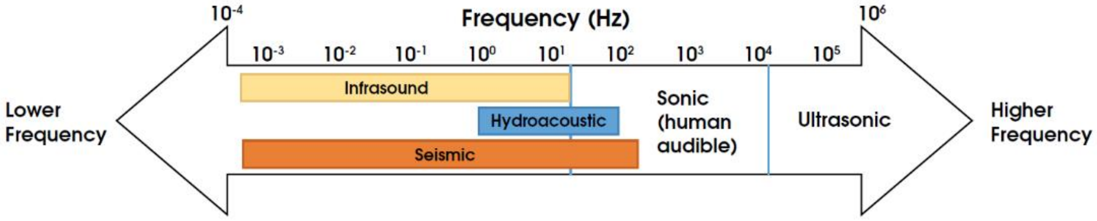

Figure 1.1 – Acoustic waveform spectrum (in Maceira *et al*., 2017).

The pressure waves with frequencies ranging from the cut-off frequency of sound (3.21 mHz for a 15°C isothermal atmosphere) to the lowest frequency of the human audible band (20 Hz) are called infrasound waves (Murayama *et al.*, 2014), illustrated in Figure 1.1 with yellow colour. This range of acoustic energy is produced by natural and man-made events, being globally spread through the atmosphere (Bedard and Georges, 2000) due to their longer wavelengths and consequent shorter frequencies.

Beside frequency, (infra)sound waves are characterized by propagation velocity and amplitude. The speed of sound at 20°C in the air is 343 ms^{-1}. This speed increases with temperature and downwind, depending as well on the type of gas. With respect to amplitude, infrasound signals used to range from hundredths to tens of pascals (Evers and Haak, 2010).

1.3. Infrasound waves: propagation and characteristics

The atmosphere has a such complex and dynamic system and its effects on the infrasound propagation environment are not that simple as the case for seismic waves, which propagate in a relatively stable medium, the Earth´s interior (Hedlin *et al*., 2012; Marty, 2019).

Infrasound was discovered when the Krakatoa eruption in 1883 occurred, which was registered on barometers around the world. In 1909, the well-known Tunguska event also produced a strong infrasound signal captured by barometers. Due to these two events, it was demonstrated that infrasound energy propagates with relatively little energy loss for thousands of kilometres, i.e., reasonably unattenuated, through refractive ducts in the atmosphere (Herrin *et al*., 2008).

Primarily, the two main factors that control the long-distance propagation of infrasound waves and its subsequently detections, in number and magnitude, are the temporal and spatial variations on the vertical gradients in the temperature and horizontal winds' velocity. Secondarily, it also can be influenced by density, average molecular weight, specific heat ratio, and air composition (de Groot-Hedlin *et al.*, 2010; Norris *et al.*, 2010).

Infrasound propagation depends on the effective sound speed, which relates the effect of the air temperature and the wind strength and direction. The acoustic velocity in atmosphere is directly proportional to the square root of absolute air temperature. Thus, the effective sound speed is ruled by the following equation:

$$\vec{c}_{eff} = 20.05\sqrt{T} + \vec{v}_w \cdot \hat{k}$$

Eq. 1.1

where $\vec{c}_{eff}$ is the effective sound speed, T is the Kelvin absolute air temperature, $\vec{v}_w$ is the wind velocity and $\hat{k}$ is the unit vector in the direction of sound propagation (Negraru and Herrin, 2009; Hedlin and Walker, 2013). Due to the existence of different layers in the atmosphere, the effective sound speed changes along with altitude, as shown in Figure 1.2.

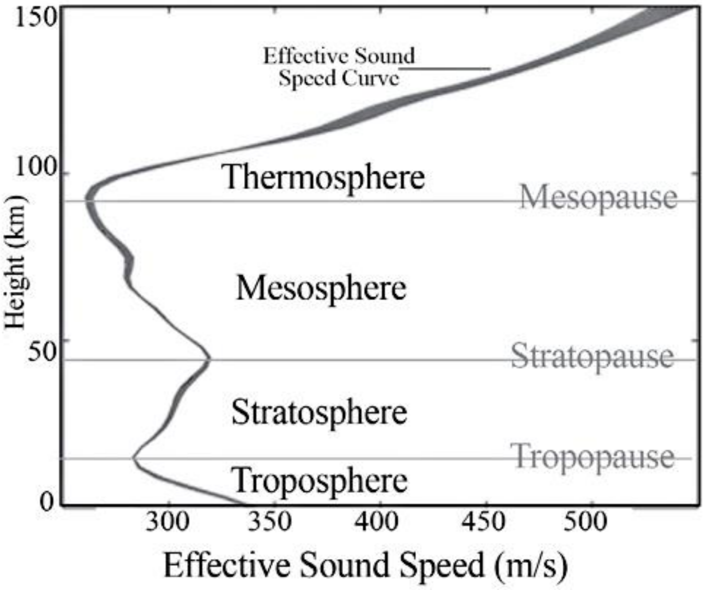

Figure 1.2 - Effective sound speed vertical gradient (Design World Staff, 2010).

1.3.1. Temperature

Generally, the structure of the Earth's atmosphere has been described by standard atmosphere profiles, regarding temperature as the main parameter. The most known is the *U.S. Standard Atmosphere of 1976* (USSA 1976) (Kambezidis, 2012). According to temperature gradients, the USSA 1976 divides the atmosphere into the following layers, named as *troposphere*, *stratosphere*, *mesosphere*, and *thermosphere* from bottom to top. Each layer is separated by correspondingly narrow regions of constant temperature, called *tropopause*, *stratopause*, and *mesopause* (Evers and Haak, 2010), represented in Figure 1.3. The temperature distribution in the atmosphere is controlled by solar radiation, as so it is the effective sound speed, subsequently. In the *troposphere*, temperature tends to decrease with altitude, since most of the heat transferences occurs on the Earth's surface. However, in the *stratosphere*, where takes place the absorption of ultraviolet radiation by the ozone layer, the temperature increases with altitude. It decreases again with altitude in *mesosphere*, up to around 100 km. In this boundary, where *thermosphere* starts, the temperature increases with the altitude because of direct ultraviolet radiation heating from the sun (Negraru *et al.*, 2010). The *boundary layer,* identified in Figure 1.3, corresponds to the *Planetary Boundary Layer* (PBL). This sub-layer is the portion of the atmosphere where the flow field is directly influenced by the interaction with Earth's surface, depending on molecular viscosity. The height of this sub-layer may range between 30 metres in conditions of large static stability, and more than 3 kilometres in highly convective circumstances due to surface heating. Despite being such a variable small sub-layer, it contains about 10 % of the mass of the atmosphere (Holton and Hakim, 2013).

It is important to mention that standard atmosphere profiles represent a global average atmospheric state. The atmosphere characteristics change widely, depending on latitude, longitude, season, and time of the day. For instance, the average temperature gradient in the Northern Hemisphere *troposphere* is much larger in winter than in summer whereas in the Southern Hemisphere this difference is smaller, due mostly to the large thermal inertia of the oceans along with the greater portion of the surface covered by oceans (Holton and Hakim, 2013). Also, the atmosphere becomes more stable after sunset. As obvious, its turbulence and convection are not influenced by solar heat fluxes as in the diurnal period.

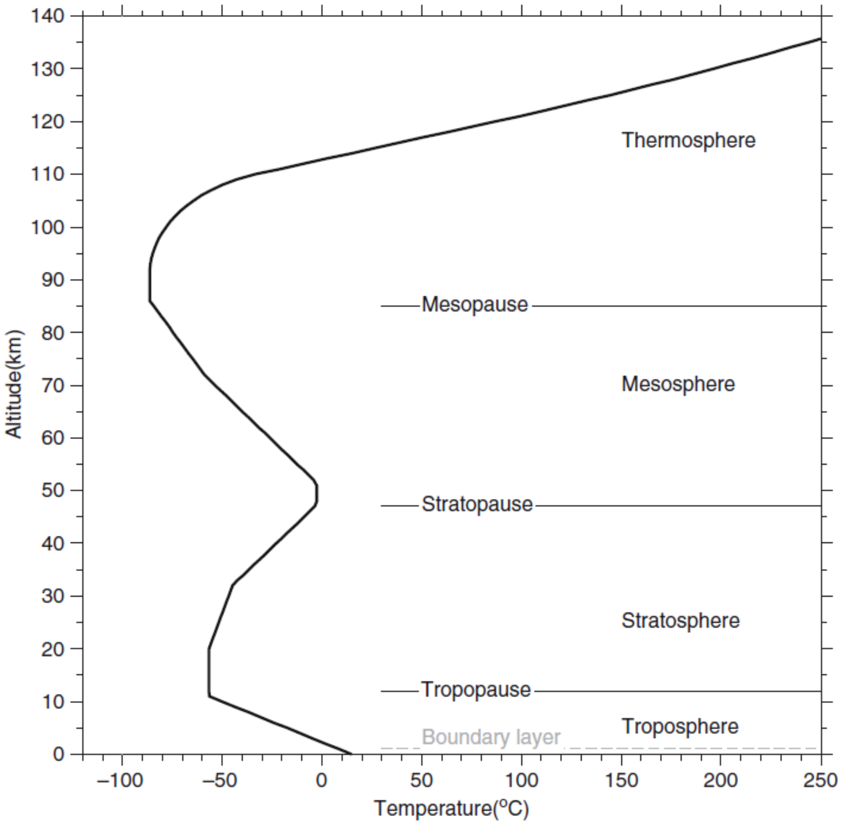

Figure 1.3 - Vertical gradient in average global atmospheric temperature. These variations are due to changes in the chemical and physical characteristics of the atmosphere with altitude, according to the USSA 1976 (adapted; in Evers and Haak, 2010).

1.3.2. Wind

The wind can be divided in two components: the zonal wind and the meridional wind. The term "zonal" is referent to the West-East direction, which is considered positive when blowing from the West to the East. On the opposite side, “meridional” represents the South-North direction, considered positive in the path from South to North (Holton and Hakim, 2013).

Regarding infrasound propagation, with respect to the wind influence, there are two regions in the atmosphere of such significance. One is the *jet stream*, laying just below the tropopause, caused by the temperature difference between the pole and equator, combined with the Coriolis force (Holton and Hakim, 2013). Consequently, the temperature gradient is much higher in winter than in summer and thus the winds variability is also much higher in winter than in summer, which makes the maximum zonal wind speed largest in winter (Georges and Beasley, 1977). The other one is the *zonal stratospheric wind*, which has different directions according to the season, reversing twice each year at midlatitudes in both hemispheres: an *easterly jet* (East-West) in the summer hemisphere and a *westerly jet* (West-East) in the winter hemisphere (Evers and Haak, 2010). Spring and fall are transition periods on this direction switch. In terms of daily wind variations, the wind speeds normally increase after sunrise, due to the solar heating of the surface (Herrin *et al.*, 2008).

Zonal stratospheric winds basically control the long-range infrasound propagation and its subsequently detections (de Groot-Hedlin *et al.*, 2010). The tropospheric wind jets, as the jet stream mentioned above can also have a significant role on regional and global infrasound propagation (McNutt *et al.*, 2015). Also, the winds in the troposphere and lower stratosphere affect the daily variability of infrasound observation (Garcés *et al.*, 2004).

Beside zonal winds, the surface winds also have an importance on infrasound detection since they are the ones responsible for the wind noise at the sensors of infrasound stations (de Groot-Hedlin *et al.*, 2010).

1.3.3. Ruling parameters for infrasound propagation

Factors that control infrasound propagation are mostly (1) the attenuation resulting on the absorbing properties of the atmosphere; (2) the refraction driven by sound-speed gradients; (3) the reflections by the ground terrain and vegetation; (4) the scatter due to atmospheric turbulence; and (5) the advection across a windy atmosphere (de Groot-Hedlin, 2008).

1.3.3.1. Infrasound attenuation: *absorption* and *dispersion*

The attenuation of a sound wave occurs by *absorption* and *dispersion*.

Absorption may be generalized as a heat dissipation within the particles, *i.e.*, each particle loses energy to the propagation medium.

There are major parameters with great impact on the *absorption* of sound within any gas, which are (1) the composition of the gas mixture; (2) the ambient pressure; (3) temperature; (4) sound frequency; and (5) relative humidity (Bass *et al.*, 1995; Dain and Lueptow, 2001).

At frequencies convenient to global infrasound propagation, between 0.02 and 5 Hz, the acoustic *absorption* (attenuation coefficient) in dB/m changes proportionally to the square of the propagation frequency plus a small constant term over altitudes up to 160 km. Atmospheric *absorption* increases with altitude. Consequently, high frequencies are more intensely attenuated while propagating upward from the source than downward (de Groot-Hedlin, 2008). At the lower atmosphere, considering its typical conditions, atmospheric *absorption* is usually insignificant (Sutherland and Bass, 2004).

Dispersion corresponds to a dependence of sound speed on frequency (Sutherland and Bass, 2004). Its effects are normally neglected for atmospheric propagation, except within the high absorption region of the thermosphere, where they might be important and considered for infrasound propagation (Norris *et al.*, 2010).

Since the resulting attenuation in atmosphere diminishes with the decrease of frequency, infrasound waves can be detected at distances of hundreds to thousands of kilometres from the source, due to their low frequency acoustic energy (de Groot-Hedlin *et al.*, 2010).

De Groot-Hedlin (2008) has developed a simulation for infrasound propagation, considering a heterogeneous absorptive atmosphere. The author also mentioned that gravitational forces are significant in computing infrasound propagation whereas the atmospheric vertical pressure and density gradients depend on gravity. These effects could change the waveform solutions at lower frequencies of interest to infrasound propagation.

1.3.3.2. Infrasound waveguides

Since scientific research has proved that acoustic propagation is controlled predominantly by fluctuations of winds and sound speed (directly proportional to temperature) the following infrasound studies contributed to support that acoustic energy is ducted between the ground and the lower, middle, or upper atmosphere, allowing the long-range distance propagation of infrasound waves through specific channels, known as waveguides (de Groot-Hedlin *et al.*, 2010).

Therefore, three important waveguides were identified as the tropospheric, stratospheric, and thermospheric ducts. They are established between the ground and high temperature and wind speed regions in the troposphere, stratosphere, and thermosphere (Le Pichon *et al.*, 2002). On downwind direction, infrasound energy can be trapped between (1) the ground and the troposphere and lower stratosphere, forming the tropospheric ducting; and (2) between the ground and stratosphere and lower mesosphere, representing the stratospheric ducting. Once the thermosphere has high temperatures, infrasound energy is refracted back to the ground by the thermospheric ducting, where the infrasound attenuation is naturally stronger (Garcés *et al.*, 2004).

In tropospheric and stratospheric waveguides, the absorption within the atmosphere is minimal. Also, the first one depends mainly on diurnal variations of sound and wind speeds. The last one is influenced by the seasonal variation of stratospheric winds, enhancing the propagation on this duct along the wind-bearing direction, e.g., from East to West in Summer hemisphere, and consequently decreasing it along with the opposite direction (de Groot-Hedlin *et al.*, 2011), which makes the long-range infrasound propagation predominantly dependent on the stratospheric duct.

1.3.3.3. Infrasound phases/arrivals

For each infrasound waveguides there are a type of wave phase correspondent, i.e., different categories of infrasound signal arrivals, detected on the ground, after their propagation from the source. In 1999, according to Pichon *et al.* (2002), David Brown nominated the phases concerned with waves returned from the troposphere, stratosphere, and thermosphere as *Iw*, *Is*, and *It*, respectively. Local atmospheric conditions have a strong impact on *Iw* phases, which may imply their extension not to very long ranges. *Is* phases depend on the season of the year, also they might fluctuate with the passing of extreme atmospheric events, such as storms and other types of massive atmospheric disturbances. At last, *It* phases are constantly expected, though they are rarely observed for frequencies above $\sim$ 1 Hz and their amplitudes may not be detectable due to the severe attenuation that occurs at thermosphere. Consequently, each one of these phases corresponds to different arrival times, depending on the waveguides in which the wave was propagated through (Blanc and Ceranna, 2009). Figure 1.4 illustrates a simulation of infrasound wave propagation in the atmosphere with its three types of signal arrivals.

According to the Classic Ray Theory, infrasound waves must reach a layer of effective sound speed greater than the velocity of sound at the source so that they can return to receivers (detectors) located on the Earth’s surface. The region where no infrasound returns are supposed is called shadow zone or “zone of silence” (Negraru *et al.*, 2010).

The tropospheric arrivals are dependent on the tropospheric winds as well as on the nature of the local weather below the tropopause, whereas the stratospheric and thermospheric returns are caused by the refraction of the atmospheric temperature gradient (Brown *et al.*, 2002). The refraction phenomena occur due to a combination of increased temperature and along-path wind speed. On the direction against the wind, infrasound may not return to the ground. However, when it does, the propagation is slower, and the amplitudes are as well usually smaller.

The thermospheric arrivals are predictable for every direction, independently of seasons, because of the steep sound gradients at altitudes over 90 km. Though, due to the increase of absorption within the upper atmosphere, only very large infrasound sources, as large volcanic eruptions, can originate detectable thermospheric returns (de Groot-Hedlin *et al.*, 2011). Also, they can be modified slightly by winds and solar effects. On the other hand, the stratospheric returns are seasonal arrivals due to the seasonal variation of the winds in the stratosphere (Brown *et al.*, 2002). In Spring and Autumn, the transitional periods in which the direction of stratospheric winds change, stratospheric arrivals may be completely non-existent.

Depending on the atmospheric conditions, a same source may generate multiple arrivals, one arrival or no arrival at a same measurement system on the ground.

Another way to explain and have a visual idea about the three signal phases mentioned above is to bracket the infrasound arrivals, considering the distance between the source and the detector, into three spatial categories, saying (1) local; (2) regional; and (3) global arrivals.

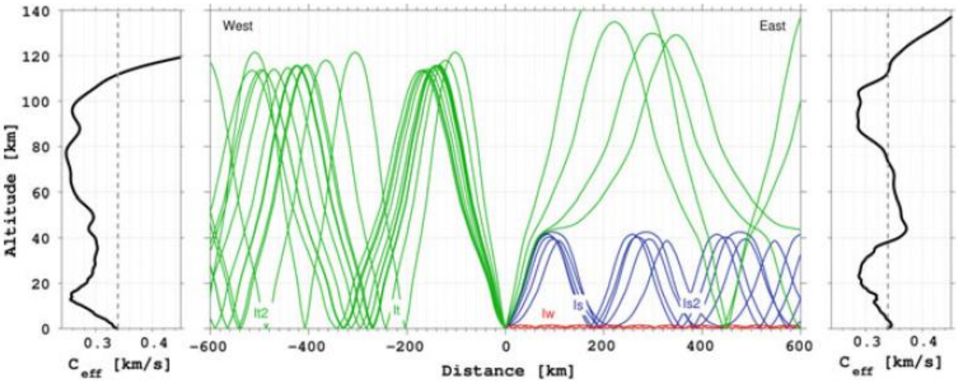

Figure 1.4 - Simulation of infrasound wave propagation for the meteor explosion observed offshore Portugal (40.5N, 18.0W) on March 9th, 2017. The red, blue, and green paths represent the tropospheric (*Iw*), stratospheric (*Is*), and thermospheric (*It*) arrivals, respectively. Correspondingly, the effective sound velocity models toward the West and the East are displayed in black on the left and right side of the figure, with the effective velocity at the ground represented by a gray-dashed line (in Marty, 2019).

Local infrasound arrivals correspond to near-field detections until about 10-15 km from the source, attributed to direct line-of-sight arrivals which are propagated exclusively through the lower troposphere. For this scenario, the atmosphere is often assumed as isotropic and so the acoustic wavefronts are represented by spherical shells, with a linearly decay of the pressure (amplitude) as the distance from the source increases. Upon this distance, the infrasound signals detected are considered as regional, being associated with the first stratospheric refractions. At last, global arrivals result from the ducting and consequent multiple refractions in the stratosphere and thermosphere (McNutt *et al.*, 2015).

1.3.3.4. Topography influence

The sound propagation along a surface can be reflected and diffracted by an irregular terrain morphology (hills, valleys, ridge, volcanic crater, etc.). The effect of topography on infrasound wavefield is mainly dependent on the source-receiver positions, having a major impact when the source and the receiver are close to the ground. Moreover, if a line-of-sight between the source and the receiver does not exist, waves may reach the receiver by diffraction or reflection/refraction of atmospheric upper layers, or a sort of shadow zone might be generated by topography itself. As a result, topography is an important factor on local detections. Thus, it should be considered in short-distance infrasound propagation modelling (Lacanna and Ripepe, 2012).

1.4. Infrasound sources

A myriad of atmospheric and shallow geophysical phenomena compresses a large volume of air, producing infrasound signals. According to its origin, these events can be divided in two categories of infrasound sources, saying (1) natural and (2) man-made sources.

Natural infrasound signals can be generated by (1) meteors; (2) auroras; (3) convective storms and lighting; (4) tornadoes; (5) microbaroms; (6) earthquakes; (7) icequakes; (8) landslides; (9) avalanches; (10) the calving of icebergs and glaciers; (11) continuously eruption and explosive volcanoes; (12) tsunamis; (13) waterfalls; (14) and coastal surf. On the other hand, man-made sources embrace (1) atmospheric nuclear tests; (2) mining and other chemical explosions; (3) the launch and re-entry of satellites, spacecraft and rockets, aircraft; (4) industrial sources such as exhaust fumes from industrial plants, oil and gas refinery flares, hydroelectric dams, wind generators; and (5) other cultural sources (Bass *et al*., 2003; Campus and Christie, 2010). Figure 1.5 illustrates several of these sources.

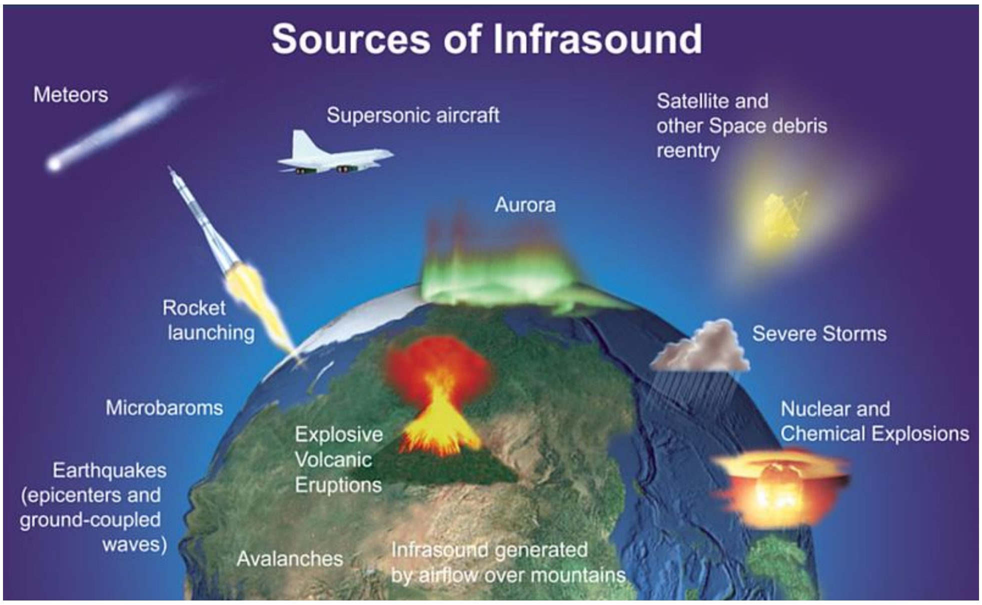

Figure 1.5 - Natural and man-made sources of infrasound (CTBTO, 2022).

All these signals have different characteristics that allowed their identification after the detection by infrasound arrays. They differ in frequency, amplitude, and period, having a recognized general pattern. Figure 1.6 shows some of the natural infrasound sources waveforms.

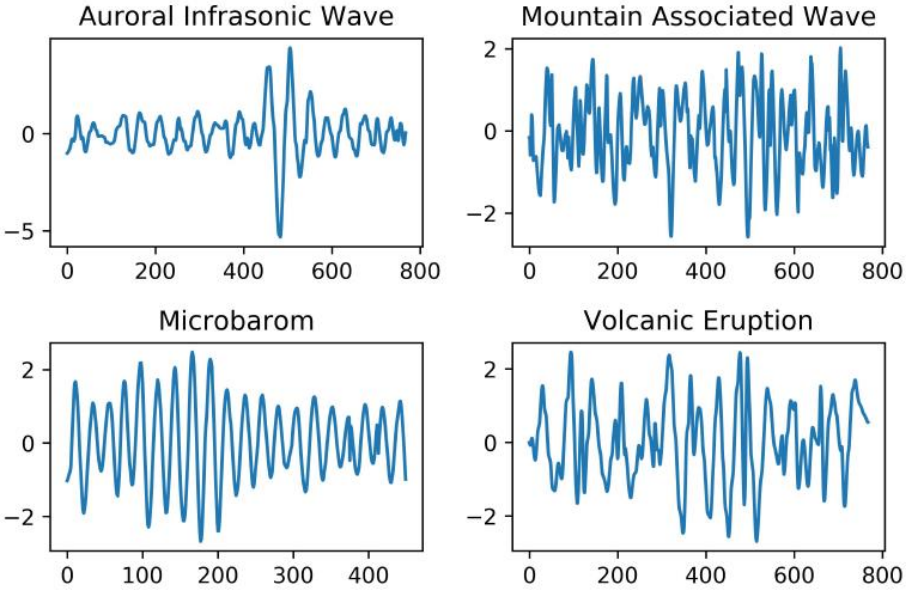

Figure 1.6 - Example waveforms of four naturals infrasound sources (in Soloman *et al.*, 2018).

In a nutshell, the following paragraphs describe some of the infrasound signals generated by natural sources that may be frequently detected in the Azores Islands, such as (1) microbaroms; (2) ocean swells and their surf-generated; (3) earthquakes; and (4) volcanic processes. Moreover, the sources firstly stated upward were already precisely described by Matos (2018).

Microbaroms are usually continuous infrasound waves over long periods of time, radiated into the atmosphere by standing waves caused by the nonlinear interaction of large-amplitude storm-generated waves on the surface of the ocean. Analogously, microbaroms are the atmospheric equivalent of microseisms. These signals are generally recorded anywhere around the globe at any time, with a frequency range between 0.12 and 0.35 Hz. Occurring as practically monochromatic wave trains with characteristic modulations in wave amplitude, microbaroms can be detected at distances unto 10,000 km (Campus and Christie, 2010). Thus, their origin is supposedly related with nonlinear interactions of ocean waves travelling in nearly opposite directions with similar frequencies (Arendt and Fritts, 2000) and not only exclusive from regions of marine storminess.

Ocean swells, i.e., breaking waves, may also generate continuous infrasound signals over long periods of time by (1) barreling (plunging); (2) slamming against a cliff; or (3) impacting against dry reef (Garcés *et al.*, 2003).

Earthquakes with large magnitudes produce associated infrasound waves through three distinct mechanisms: (1) the near vertical radiation of an acoustic wave away from the surface of the Earth during the passage of seismic body and surface waves; (2) a violent ground motion at the epicentre of a shallow earthquake which produce infrasound waves into the atmosphere; and (3) motions in high mountains, induced by seismic surface waves, radiating infrasound waves. Large earthquakes can be detected by infrasound arrays at distances unto 10,000 km or more (Campus and Christie, 2010). Therefore, it is particularly in mountain ranges and islands where a deep seismic event with a large magnitude might allow the phenomena ground to air coupling (Brachet *et al.*, 2010).

Volcanic eruptions are one of the most useful sources of infrasound waves. The explosive ejection of lava and gases from the crater and surrounding vents of the volcano cause atmospheric perturbations called volcanic infrasound. Its dominant frequency and amplitude from volcanic explosions depend on their size and the distance from the source at which are detected (Christie and Campus, 2010). Volcanic eruptions occur due to the excess pressure of volcanic fluids (Garcés *et al.*, 1998). The fluids may be composed by a combination of (1) magma; (2) water; (3) gas; (4) rock particles; and (5) mud, in some cases. The pressure is released once the fluids breach the surface of a volcano and this process may be recorded by microphones as (1) distinct explosions or bursts (Ripepe *et al.*, 1996), (2) jet noise or as (3) a continuous vibration of the atmosphere known as tremor. Landslides and pyroclastic flows also produce a unique acoustic signature that might be applied to track the flow deposits (Bass *et al.*, 2006).

Other new sources of infrasound are yet to be identified, since many of the detected infrasound signals still has an unknow origin (Campus and Christie, 2010).

1.4.1. Volcanic eruptions

The present research will focus on a site survey to deploy infrasound mobile stations towards the monitoring of central volcanoes, applying near-source detection, in the Azores Islands. In this subtopic, the characteristics of volcano infrasound signals are more elaborated.

Infrasound signals with volcanic origin have a wide variety of low frequencies between ∼0.01 Hz and 20 Hz. Explosive volcanic eruptions are one of the most powerful sources of infrasound recorded on Earth. Their energetic infrasound waves can propagate hundreds to thousands of kilometres in the atmospheric waveguides. However, not only explosive eruptions generate infrasound signals. Also, there are a consequence of other subaerial and shallow subsurface processes as (1) shallow degassing; (2) surface flow; and (3) mass wasting associated with volcanic phenomena (Matoza *et al*., 2019).

Infrasound sources mechanisms associated with different volcanic processes and their respective signals are widely varied. Waveforms of volcanic infrasound can range from short-duration events lasting ∼1 s to sustained tremor signals that may last months to years. Also, amplitudes present a wide-ranging dynamic, from small signals close to the noise level of infrasound sensors (mPa) to larger explosions that produce nonlinear shock waves with overpressures exceeding atmospheric pressure (>10^5 Pa). Furthermore, it is important to refer that topography and volcanic crater morphology can modify the signals and create extra diversity (Matoza *et al*., 2019).

According to several authors cited in Matoza *et al.* (2019), low-viscosity magmas, as the basaltic type, are notorious for their prolonged effusive eruptions staggered by short explosive bursts along with sporadic episodes of gas-rich lava fountains. It has been observed near-continuous broadband and/or harmonic infrasound. Additionally, cavities and gas-filled conduits above degassing bodies seem to significantly shape the infrasound wave signature. Hereinafter, Stromboli eruptions produce short-duration infrasound signals related to the gas overpressure and subsequence gas volume released. Their waveforms are characterized by an initial compressional onset followed by a rarefaction, with extended coda reverberation in some cases. In silicic volcanic systems, the viscous magmas create higher pressures within the conduit, forming pressurized solid lava plugs or domes. Therefore, when these formations crack, large explosions usually occur, with substantially ash plumes and ballistics. The resulted infrasound waveforms have lower frequency, higher amplitude, longer periods and are more complex than the ones from Strombolian eruptions. At last, hydrothermal, and magmatic-hydrothermal interaction processes might also generate infrasound signals.

1.5. Infrasound monitoring and its applications

The detection of infrasound signals to determine the location of a source as well as to estimate its size is the main goal of infrasound monitoring. Consequently, this type of monitoring is influenced by the infrasound propagation through the atmosphere. Therefore, the number and magnitude of the infrasound detections are affected by the temporal and spatial variations in atmospheric temperature and wind speed gradients (de Groot-Hedlin *et al*., 2010). Complemented with other type of signals, as seismic waves, infrasound detections can provide a better monitoring of the Earth activity (Brachet *et al.*, 2010).

1.5.1. The IMS infrasound network

Since the signing of the Comprehensive Nuclear-Test-Ban Treaty (CTBT) in 1996 and consequent establishment of the International Monitoring System (IMS) for treaty verification, infrasound monitoring technology has been experiencing an exponential development (Christie, 2007). Built for nuclear explosions monitoring purpose, when completely operational, the IMS consists of four networks of different technologies: 170 seismic stations; 11 hydroacoustic stations; 80 radionuclide stations; and 60 infrasound stations uniformly spread in pre-selected locations around the globe (Campus and Christie, 2010).

The IMS infrasound stations are deployed in diversified type of environments including (1) tropical equatorial rainforests; (2) semi-urban areas with high population densities; (3) semi-desert places; (4) exposed locations on remote islands; and (5) on ice-covered Polar regions of Artic and Antarctic (Campus and Christie, 2010), as seen on Figure 1.7.

These worldwide infrasound arrays network provide to record signals from energetic events occurred in the atmosphere as well as contribute to more detailed research on its dynamic processes. Also, together with the other monitoring techniques from the IMS, infrasound stations, in some places co-located with seismic stations, allow data fusion which enable a more precise and accurate monitoring (Bass *et al.*, 2003). Thus, this global data system employs modern electronics that make available a real time digitization of signals and their storage at a single location, at the International Data Centre (IDC) in Vienna (Bass *et al.*, 2006).

Also, the continuous improvement of IMS infrasound arrays has contributed to increase the quality and quantity of data available through scientific developments on instrumentation, such has microbarometers, with consequent advances in digital signal processing (Herrin *et al.*, 2008). As a global monitoring tool, the IMS infrasound network demands a scientific worldwide cooperation (Bass *et al*., 2006).

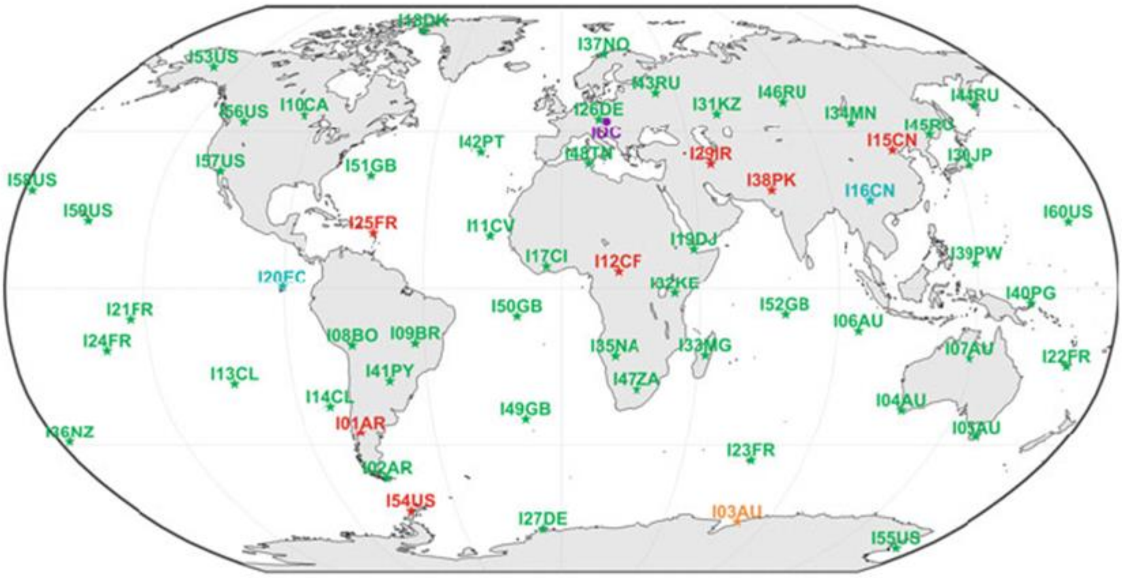

Figure 1.7 - IMS infrasound network, as of June 2017, with certified stations (green), installed stations (turquoise), stations under construction (orange), planned stations (red), and the IDC (purple) (in Marty, 2019).

1.5.2. Scientific and civil applications

With the growing network of infrasound arrays, in particularly due to the IMS infrasound stations deployment, what has started only for nuclear atmospheric tests monitoring purpose is now used for plenty of scientific and civil applications where infrasound data are of value. Automatically, the implementation of infrasound monitoring technology all around the Earth led to dynamic research programs in areas such as (1) evaluation of signal propagation codes; (2) atmospheric models; (3) nuclear explosions and natural hazards monitoring; (4) development of infrasound as a remote sensing tool, particularly in case of remote volcanoes; and (5) operational infrasound source location and characterization (Hedlin *et al*., 2012; Herrin *et al*., 2008).

On atmospheric models, infrasound tomography is applied to model the upper regions of atmosphere where the atmospheric profiles are not so accurate yet, which would be significant to improve source location estimates (Campus and Christie, 2010).

Also, infrasound data are valuable for various geophysical hazard warning systems around the world, contributing to evaluate potential damage of shallow earthquakes, landslides, and avalanches as well as global warming and global volcanic activity (Campus and Christie, 2010).

Signals from active volcanoes may infer the various source mechanisms for volcano-generated infrasound. Additionally, the IMS infrasound network has an essential contribution to monitor volcanic eruptions, particularly on remote areas, and can be employed on volcanic ash monitoring systems, resulting on reliable data in warning systems for aviation (Campus and Christie, 2010). Infrasound is a key advantage over satellites once clouds are transparent to sound and an impediment to satellites (Hedlin and Walker, 2013).

Furthermore, the infrasound generated from breaking of icebergs and the calving of glaciers at Artic and Antarctic are a useful indicator on global warming progress (Campus and Christie, 2010).

1.5.3. Volcano infrasound monitoring strategies

In the past 20 years, infrasound technology has become an established component to monitor volcanoes, complementing seismic, geodetic, and gas geophysical tools, enhancing the characterization, understanding and permanent volcano surveillance of volcanic physical processes (Johnson, 2019; Matoza *et al.*, 2019).

It is possible to know the present status of a volcano and to forecast eruptions, estimating their date and time; location; size and type; and even the probable duration. Infrasound allied with the above monitoring techniques may help to determine and establish time frames for whether a volcano (1) is in a background or restful state: (2) is restless; (3) shows precursory activity; (4) has begun to erupt; (5) is actively erupting; (6) is ending an eruption; or (7) is returning to a background state. Infrasound provides direct information about what is happening at the vent of a volcano. Infrasound sensors detect large explosions and the sensor arrays along with networks enable the identification and location of even low-energy eruptions. Also, changes in the eruptive style that may occur are recorded. For instance, the cessation of infrasound tremor before an eruption may represent a decrease in degassing due to conduit sealing. Moreover, the propagation of infrasound frequencies with low attenuation makes it possible to detect long-range signals and then to characterize explosive eruptions which in cases of remote eruptions offers the most detailed information. Additionally, recent research is focused on evaluate the relationship between infrasound pressure and frequency with plume heights (McNutt *et al.*, 2015).

One of the mandatory issues to be challenged in the next decades is the monitoring of volcanic activity in real time and on a global scale, once many volcanoes worldwide are poorly monitored or even unmonitored and most of the times satellite observations or by aeroplane pilots occur after the eruption (Marchetti *et al.*, 2019). An early warning system can be successfully implemented at a global scale to arrays located at several hundreds of kilometres from the volcano, particularly in remote volcanic places that are still lacking geophysical monitoring tools, allowing an automatically notification delivering of an ongoing eruption (Ripepe *et al.*, 2018).

Eruptions are well detected by arrays of infrasound sensors that can be deployed at local, regional, or global distances from the volcano (McNutt *et al.*, 2015), depending on the application purpose.

In local infrasound deployments, i.e., within < 15 km of the source, sensors are positioned near to and/or on the flanks of volcanoes, implying that sound transmission from the vent to receiver occurs in line-of-sight. This type of monitoring is ideal for detection of open-vent degassing, precision location of surface activity, and detection and tracking of moving flows (Johnson, 2019). In this scenario, the atmospheric effects on the sound propagation are small and can be neglected. Therefore, both amplitude and waveform of the acoustic pressure are considered as completely preserved and more representative of source processes (Lacanna and Ripepe, 2012). Then, locally recorded signals represent relatively undistorted source time motions and may be used to characterize volcanic activity through infrasound data analysis. Consequently, local arrays enhance the capability to identify minor activity and to locate and track sources with precision, detecting very small transients and low-amplitude tremor, which may not be energetic enough to propagate to distant recording sites (Johnson, 2019).

On the other side, regional and global infrasound data are applied for activity identification over a wider geographic domain and might be very effective at tracking activity at volcanoes which are either remote, too expensive to monitor locally, and/or where activity is not predicted (Matoza *et al.*, 2010). The global IMS infrasound network is a useful tool for identify large eruptions. However, it will be ideally to complement this global network with local and regional arrays capable of tracking early and less violent stages of eruptive sequences (McNutt *et al.*, 2015).

1.5.4. Monitoring strategies in oceanic islands

Monitoring in oceanic islands is a huge contribution to global infrasound monitoring. Though, the effectiveness of a typical oceanic site or even of a continental one is highly dependent on local meteorological conditions (Hedlin *et al.*, 2002).

The most significant difference between arrays located on islands and those on the continent is the increase in low frequency background noise (Park *et al.*, 2016). Sites located on islands are affected by the time-variant wind interactions with local topographic features, producing a complex relationship between noise power and wind speed (Hedlin *et al.*, 2002).

On the case of arrays near the ocean, the noise power density is influenced by additional local site affects related to the ocean environment. Infrasound detections from stations near the ocean are dependent on the seasonal variation of ocean energies (Park *et al.*, 2016).

In both locations on islands and near the coast the wind speeds are higher. Under conditions of low wind velocity, infrasound arrays can become sensitive to small, local events such as the movement of a vehicle, construction work or any of a variety of other human activities if they occur close to the array. For those arrays near the ocean this could include signals generated by ocean-atmosphere interactions. Under these conditions, the background noise level at low wind velocity is slightly higher than that observed for other arrays (Park *et al.*, 2016). In some islands there are a significant potential for signal blockage and noise-generated from turbulence due to wind flow over topography (Hedlin *et al.*, 2002). Therefore, for deployment of infrasound stations in these regions for certain monitoring purpose it is essential to survey the best possible sites, with lowers background noise levels. Forests and some topographic features are natural wind barriers that might minimize the infrasound noise on oceanic islands. Furthermore, infrasound noise reduction filters should be implemented on the arrays and should be designed to suit local needs at each of the windy sites.

1.6. Infrasound background noise

Infrasound background noise has been surveyed when selecting sites for new infrasound stations (Hedlin *et al.*, 2002).

Background noise consists of all energy measured by an infrasound sensor that was not generated by sources of interest. Its understanding is important since noise often limits the ability to detect and identify signals. Therefore, it is an important input for simulating the capability of infrasound networks. Background noise is characterized in the frequency band of 0.03 to 7 Hz. It is mainly dominated by long-range pressure fluctuations generated over the oceans, as microbaroms, and by short-range pressure fluctuations due to local eddies and winds, being highly variable over time and among stations. Some factors related to the station contribute to the noise, such as (1) climate; (2) station location relative to oceans; (3) local topography; (4) local noise sources; (5) vegetation or snow cover at the sensor sites; and (6) configurations of sensors and wind-noise reduction filters. Background noise at infrasound stations highly varies according to the season, time of the day and station. Noise spectra for an individual station may fluctuate by four orders of magnitude at any given frequency (Bowman *et al.*, 2005).

The background infrasound field is rich and diverse, consisting of many forms of coherent and incoherent noise that are simultaneously recorded with volcanic infrasound. It is used the term clutter to describe coherent infrasound from sources other than the one of specific interest (Matoza *et al.*, 2006).

Christie and Campus (2010) listed some of the primary sources of background noise. Considering volcano monitoring, from those sources, it is important to pay attention on the following ones:

(1) Wind-generated micropressure fluctuations associated with turbulent eddies in the atmospheric boundary layer (all frequencies).
(2) Microbarom infrasound waves in the 0.12 – 0.35 Hz passband.
(3) Surf-generated infrasound noise (usually at frequencies above 1 Hz).
(4) Infrasound noise generated by highway traffic, trains, aircraft, bridges, industry, and other cultural sources (usually high frequency).
(5) Oil and gas refinery flares (high frequency).
(6) Hydroelectric installations (high frequency).
(7) Wind turbines (usually high frequency).
(8) Mountain-generated infrasound waves (frequencies below 0.1 Hz).
(9) Long period pressure fluctuations and wind noise generated by mesoscale density currents.
(10) Pressure variations at the surface associated with shear instabilities in the upper tropospheric and boundary layer jet streams (low frequencies).

These weather systems, ocean waves, rivers, and cultural activities produce time dependent coherent and incoherent noise at infrasound arrays. The characterization and physical understanding as well as the spatial variability of these signals provides a basis for developing approaches for separating signals from both correlated and uncorrelated noise (Park *et al.*, 2016). Although noise and the signal of interest might have the same time-frequency, the noise is incoherent over shorter length scales. For example, at 0.25 Hz, wind noise is incoherent at spacing of tens of meters while acoustic waves at the same frequency can be coherent at > 1 km (Grover, 1971).

1.6.1. Wind-generated infrasound noise

The detection of infrasound waves is limited by the presence of a turbulent boundary layer at the surface of the Earth. The turbulent flow of the wind is the most significant source of infrasound noise in the band from 0.1 to 1 Hz (McDonald *et al.*, 1971), particularly at frequencies higher than the microbarom band (0.1 - 0.4 Hz) (Bowman *et al.*, 2005). The relationship between wind and infrasonic noise is given by Bernoulli’s Principle:

$$p + \frac{\rho v^2}{2} = C$$

Eq. 1.2

where p is pressure, ρ is density, v is wind velocity and C is a constant. Differentiation of this formula shows that there is a simple linear scaling between variations in wind speed and pressure (Hedlin *et al.*, 2000).

Wind-generated atmospheric turbulence can be divided into two categories: convective and mechanical (Walker and Hedlin, 2010). Mechanical turbulence is usually due to the interaction between the wind and the Earth's surface (topography, buildings, forests, etc.) Comprehending the interaction of wind with topographic irregularities that cause the turbulence that is concentrated in the atmospheric boundary layer (see Figure 4) is important for understanding the frequency dependence of infrasound noise (Hedlin *et al.*, 2000). Convective turbulence is primarily produced by the diurnal heating of the Earth's surface by solar radiation. When the upper winds are decoupled from the surface by a nocturnal boundary layer, the level of background noise is often very low at night. The onset of daytime convection usually leads to a rapid increase in wind noise as the upper-level winds are reconnected to the surface layer (Christie, 2007).

Furthermore, pressure variations across the ground result from turbulent eddies. Large turbulent eddies are generated by buoyancy driven convection, typically due to heating of the surface layer over land. Smaller eddies are then generated as wind shear in the boundary layer breaks up the large eddies, causing the decreasing of the power of wind-generated noise approximately inversely with frequency (Bowman *et al.*, 2005).

The wind velocity turbulence spectrum is heavily weighted to low frequencies. Therefore, the wind noise levels are higher at low frequencies (Raspet *et al.*, 2006).

Additionally, infrasound noise levels generally increase with wind speed over the frequency band of 0.02 – 5Hz (Hedlin *et al.*, 2002). At low wind speeds, the wind usually shows little effect on the observed infrasound noise. Though, above a usual threshold around 1-2 m/s, the infrasound noise increases dramatically with increasing wind speed (Bass *et al.*, 2006). Figure 1.8 represent the general characteristics of the functional relationship between wind and infrasound noise, for I31KZ IMS infrasound station, in Kazakhstan, where the season vegetation has influence as wind filtering effect evidenced by the seasonal variation of that function, even for the same wind speed.

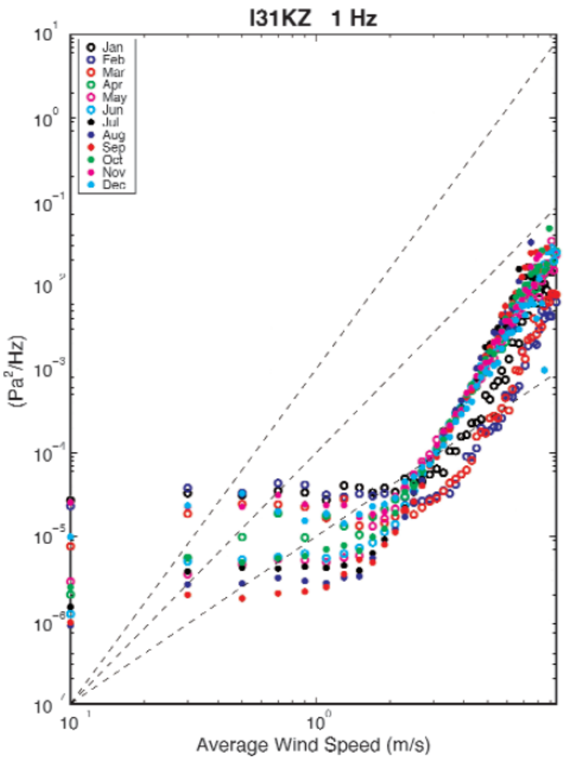

Figure 1.8 - Infrasound noise at 1 Hz as a function of average wind speed during 2004 for the IMS infrasound station I31KZ, Kazakhstan. The different coloured symbols represent the average values for each month of the year. Dashed lines, with slopes of 2, 3, and 4, are for reference (in Bass *et al*., 2006).

Since large pressure fluctuations originated by the wind can hide the weak signals from distant infrasound sources, in case of volcano monitoring, it is substantial to deploy infrasound instrumentation away from high-wind environments such as the upper slopes of a volcano. The sensors should be installed several kilometres from the vent, preferably in areas of thick vegetation to reduce wind noise (McNutt et al., 2015).

Many strategies have been applied to reduce the impact of wind-generated infrasound noise. The most common are described on sub-chapter 1.7, about infrasound stations. Despite the different techniques used in each strategy, all of them aim to mitigate the incoherence of wind-induce pressure fluctuations over length scales of tens of meters.

1.6.2. Power Spectral Density (PSD)

Before the deployment of an infrasound station, it is necessary to evaluate the infrasound background noise level at each selected site. After a certain time of data recording by a microbarometer, it is estimated the Power Spectral Density (PSD). The spectral amplitudes of the filtered data are calculated using Welch’s method, which gives a single power spectral estimate from an average of several taken at regular intervals in the time range of interest (Hedlin *et al*., 2002), through the overlapping of *Fast Fourier Transforms* (Bowman *et al*., 2005).

Bowman *et al*. (2005) defined preliminary infrasound noise models, illustrated in Figure 1.9, applied as baselines for evaluating background noise at current and new IMS infrasound stations.

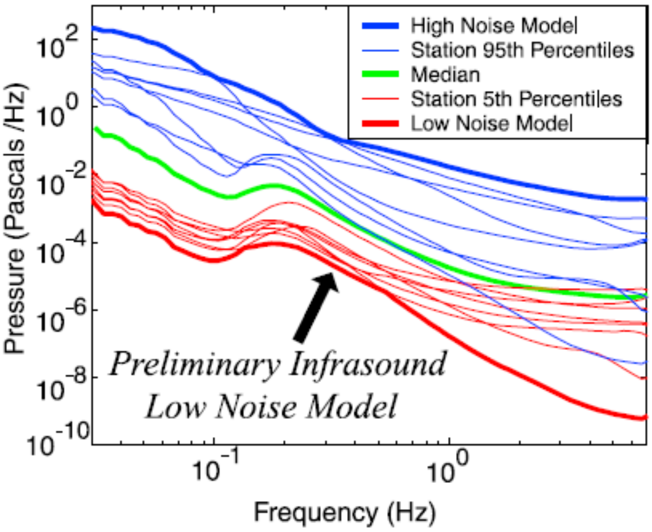

Figure 1.9 - Infrasound network noise models for all times and seasons for low-noise (heavy red line), median-noise (green) and high-noise (heavy blue line) conditions. The 5th (red) and 95th percentiles (blue) comprise a full year's data of tens stations (in Bowman *et al*., 2005).

The low-noise model (heavy red line) is defined as the minimum at each frequency of the 5th percentiles of all ten PSD distributions from individual stations. The high-noise model (heavy blue line) is defined similarly. The all-time network median (green) is the median of all PSD at each frequency. The infrasound noise models obtained can be used as a baseline against which relative changes in noise levels are measured. The microbarom peak is seen clearly in the low- and median-noise models but is washed out by wind in the high-noise model. The 95th percentile noise for some stations is lower than the 5th percentile noise for other stations above 1 Hz (Bowman *et al*., 2005).

Microbaroms are normally observed under relatively low wind noise conditions and the observation of a microbarom peak in the Power Spectral Density plot indicates that noise levels are low. Microbaroms are often observed at all times of the day and night at stations located mostly in tall dense forests (Campus and Christie, 2010).

During a 3-week survey occurred in November and December of 1998 on São Miguel Island, Azores, it was observed that wind speed and infrasound noise change rapidly. At this location, daily noise level swings from 40 to 50 dB at 0.1 Hz are not uncommon in the early winter and are caused by changes in wind speed and atmospheric turbulence. From the full three weeks of recording noise levels at all four selected sites it was calculated PSD at 454-time intervals. Each interval began at the turn of the hour and lasted 15 minutes. 10th, 50th and 90th percentile noise levels at all frequencies from 0.005 Hz to 10.0 Hz are shown in Figure 1.10. At times of relatively low noise, the microbarom peak is obvious at Chã das Mulas. Longer periods depend more strongly on time. For example, the spread between the 10th and 90th percentiles is 50 dB at 0.1 Hz and just 20 dB at 1 Hz (Hedlin *et al.*, 2002).

The spectral estimates that were used in this study were derived from an average of four estimates, each taken from consecutive 204.8 s intervals. The power spectral density taken from the filtered record (Figure 1.10) shows decay in power levels from the peak at 30 s to the corner of the anti-aliasing filter at 9 Hz. A strong microbarom peak is centred at 0.2 Hz. The peak at 30s is somewhat misleading as it does not reflect an intrinsic lack of noise power in the atmosphere at longer periods but is what remains after the sensor filter which bandpass the raw signal to exclude energy below 0.01 Hz. The fall-off energy bellow 0.01 Hz is due to the sensor filter (Hedlin *et al*., 2002).

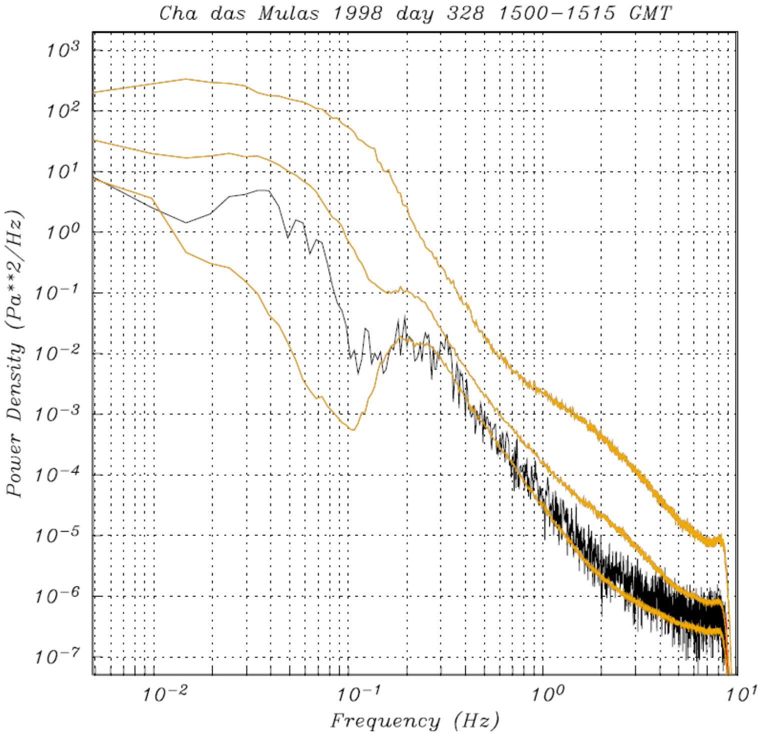

Figure 1.10 - Noise power density at Chã das Mulas, in São Miguel Island, Azores. In black is shown a single power density estimate taken from the filtered pressure data. The yellowish curves are the 10th, 50th and 90th percentile noise levels from the entire experiment. The 5 second microbarom is not observed at times of high noise (Hedlin *et al*., 2000).

The overall spectral shape is due to a well-known phenomenon in the atmosphere which receives a major input of energy at ~ 0.1 to 1 mHz, from large scale eddies cascades into smaller eddies, and consequent into higher frequencies, as the large eddies are fragmented (Kaimal and Finnigan, 1994).

1.6.3. Probability Density Function (PDF)

After that, PSD is converted into empirical noise-amplitude Probability Density Function (PDF). The noise PDF illustrates the distribution of noise and are valuable for predicting signal-to-noise ratio for signals of specified amplitude, important to estimate station and network detection capability (Bowman *et al.*, 2005).

The Probability Density Functions (PDF) as a function of noise power for each frequency band for four IMS stations is shown on Figure 1.11. It is possible to observe that the spectral background noise levels observed at station I49GB are in average much higher than the ones of station I06AU. Both stations are located on remote oceanic islands but station I49GB is located at a much windier location with no vegetation around and its WNRSs have a slightly reduced efficiency due to land constraints. In comparison, station I06AU is installed within a dense forest and include standard WNRSs (Marty, 2019).

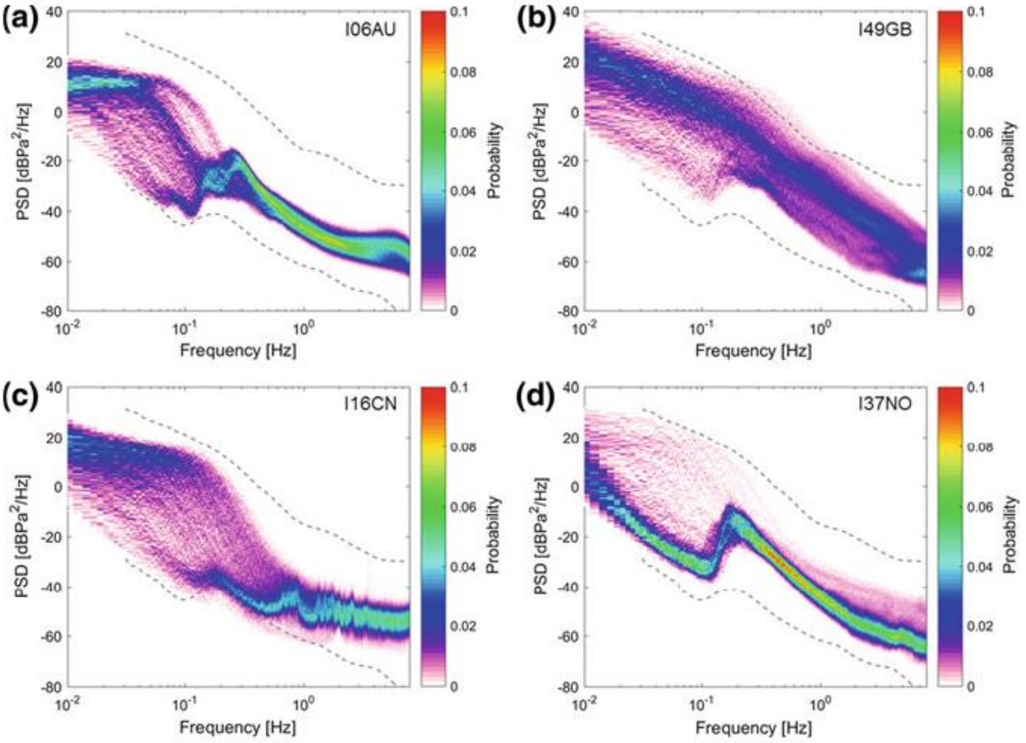

Figure 1.11 - PDFs in February 2017 for IMS infrasound stations a) I06AU (H6), b) I49GB (H2), c) I16CN (H3), and d) I37NO (H7). The Power Spectral Densities (PSDs) are computed over 1-h time-period using Welch's method and are corrected from the system response including WNRS, sensor, and data acquisition system. The grey-dashed lines represent a high- and low-noise model according to Bowman *et al*. (2005) infrasound noise models (in Marty, 2019).

1.7. Infrasound permanent stations

1.7.1. Infrasound arrays

Considering IMS infrasound network as an example, each infrasound station is characterized by (1) a Central Facility (CF); (2) an array of distant measurement sites, called array elements (Figure 1.12), located in a 1 - 4 km diameter area, and composed of four to fifteen sensors; (3) a data-transmission system between the elements on the infrasound array and the CF; (4) power supply systems, including backup power supplies, for the array elements and CF; and (6) an online satellite system, designed as Global Communications Interface (GCI), for the transmission of authenticated data in near real time to the International Data Centre (IDC) in Vienna, Austria. In most of the cases, a Virtual Private Network (VPN) system is used for transmitting authenticated data in near real time to the IDC (Christie and Campus, 2010; Marty, 2019).

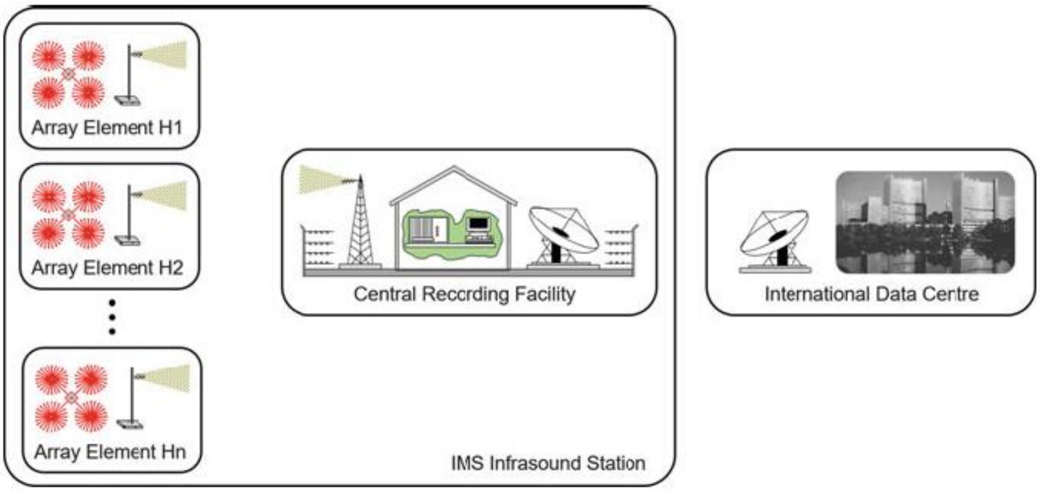

Figure 1.12 - Schematic illustration of an IMS infrasound station (in Marty, 2019).

1.7.1.1. Array elements

Most of the IMS infrasound stations have been constructed with 7- or 8-element arrays (Christie and Campus, 2010) spaced 1 to 4 km apart, which guarantees the best configuration for the optimal detection of infrasound signals (Blanc and Ceranna, 2009). IS42 in Graciosa has 8 elements. Each IMS array element consists of several components listed below:

(1) Equipment vault

All equipment at the array elements is installed inside the equipment vault, with the purpose to protect the equipment from the environment and vandalism. These chambers are secure, generally fire resistant, thermally insulated, and waterproof when necessary (Marty, 2019). They may be buried, partially buried, or located on the surface. The door on each vault is fitted with a tamper-sensing switch that transmits a signal to the CF and from there to the IDC in Vienna if the door to the vault is opened (Christie and Campus, 2010).

(2) Infrasound sensor

An infrasound sensor can be defined as a device sensitive to infrasound pressure oscillations that delivers an electric signal containing the measured information. It is associated with a digitizer and almost always to a wind noise reducer (Nief *et al*., 2019). Several types of infrasound sensors can be used to record these atmospheric pressure fluctuations above and below the ambient atmospheric pressure (McNutt *et al*., 2015), such as (1) absolute infrasound sensors; (2) differential infrasound sensors; and (3) Optical Fiber Infrasound Sensors (OFIS), among others (Ponceau and Bosca, 2010; Walker and Hedlin, 2010).

Absolute infrasound sensors are the most applied, particularly in the IMS infrasound network. An absolute infrasound sensor consists in an aneroid capsule deflected by atmospheric pressure changes inside a measuring cavity connected to atmospheric pressure, as shown by a schematic profile overview in Figure 1.13. A transducer converts the bellow deflection into a dynamic voltage signal adapted to the associated recorder (Ponceau and Bosca, 2010; Nief et *al*., 2019). For instance, the absolute pressure microbarometers MB2000/MB2005, designed by CEA and manufactured by *Martec Tekelec Systèmes*, have been widely used since 2000 due to their robustness and efficiency in a wide set of environments (Christie and Campus, 2010). MB2005 is represented in Photo 1.1.

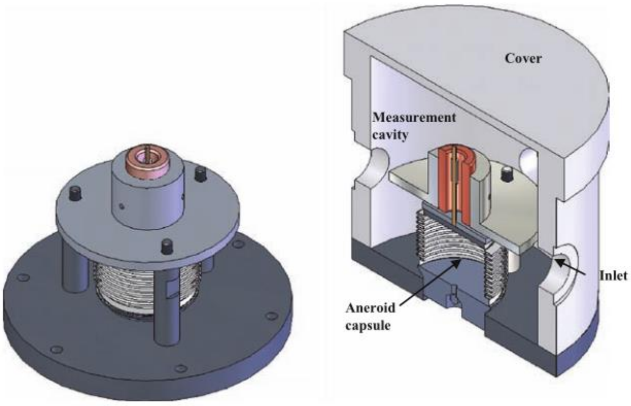

Figure 1.13 - Schematic overview of the absolute infrasound sensor MB2005 (in Ponceau and Bosca, 2010).

Recently, some infrasound sensors can be found in digital versions, *i.e*., the analog-to-digital conversion is realized inside the microbarometer case. The digitizer is then implanted and not externally connected to the sensor using cables. Nowadays, it is common to use the MB3 sensor, designed by CEA and marketed by *Seismowave* company, which has a remote calibration capability (Nief *et al*., 2019).

One microbarometer is installed inside each equipment vault (Christie and Campus, 2010). Infrasonic waves passing over these sensors will produce measurable changes in pressure propagating at acoustic velocities (~340 m/s at the ground surface), being generally reported in units of Pascal (Pa).

Photo 1.1 - MB2005 aneroide microbarometer, IS42 Graciosa, Portugal.

(3) Digitizer

A 24-bit digitizer with antialiasing filter and data authentication is deployed near the infrasound sensor inside the equipment vault. All infrasound data are sampled at 20 samples per second (Christie and Campus, 2010) in digital format (Marty, 2019).

(4) Meteorological equipment

A high-resolution sonic anemometer, temperature sensor, and absolute barometer are installed at one site in the infrasound array. The anemometer is installed at a height of 2.0 metres above the surface, and the temperature sensor and absolute barometer are installed at a height of 1.0 metres above the surface. All meteorological data are collected as well at 20 samples per second (Christie and Campus, 2010).

(5) GPS clock

GPS received time stamp and pulse per second (PTPS) allows to adjust the internal clock within an accuracy of less than 1ms (Christie and Campus, 2010).

(6) Wind-noise-reducing system (WNRS)

Forests are a natural reducer of noise since the vegetation does not allow the existence of large turbulent structures, refracting the wind field (Evers and Haak, 2004). However, they are not sufficient to control some aspects of noise environment, so that is necessary to apply wind-noise reduction filters along with the spatial configuration of infrasound sensors in an infrasound array (Bowman *et al.*, 2005).

Most part of wind-noise reducing systems have been based on a spatial averaging technique in which the pressure fluctuations at a series of inlets along a thin pipe are added to the microbarometer sensor (Christie, 2007). If the wind-generated noise is incoherent between inlet ports and if the signal is perfectly coherent, then this procedure results in an increase in the signal-to-noise ratio equal to the square root of the number of inlets (Christie 2007).

Noise reduction at each array element may be achieved by (1) wind barriers; (2) porous hoses; or (3) pipe arrays with discrete inlets (Hedlin *et al.*, 2003a).

Pipe array systems are the wind-generated noise reductor most used in IMS infrasound stations. They consist of several low-impedance air inlets, illustrated in Figure 1.14 and Photo 1.2, distributed over a spatial area that are linked to the infrasound sensor through a network of pipes and manifolds, as the schematic design showed in Figure 1.15.

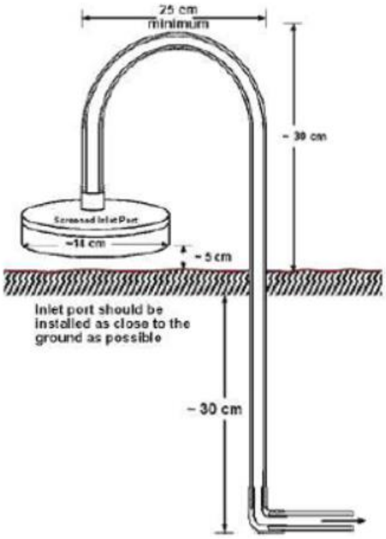

Figure 1.14 - Inlet port scheme (CTBTO, 2022) (left). **Photo 1.2** - Inlet port of noise reducing pipe array, IS42 Graciosa, Portugal (right).

IMS pipe arrays can be grouped into four categories: (1) rosette; (2) star; (3) hexagonal closed pack (HCP); and (4) radial, as represented in Figure 1.16. Nowadays, pipe arrays are made of stainless steel. Pipe array design are adapted to each environment. The development of solutions with flexible hoses has shown to be extremely useful. Also, the addition of gravel over air inlets can help further increasing the signal-to-noise ratio (Marty, 2019).

Nevertheless, pipe array systems show some disadvantages once they may be subject to unwanted resonances and may distort and attenuate higher frequency signals. The number of inlet ports and the size of existing pipe arrays has reached practical limits, thus a different approach to the problem of wind-generated noise is required (Christie, 2007).

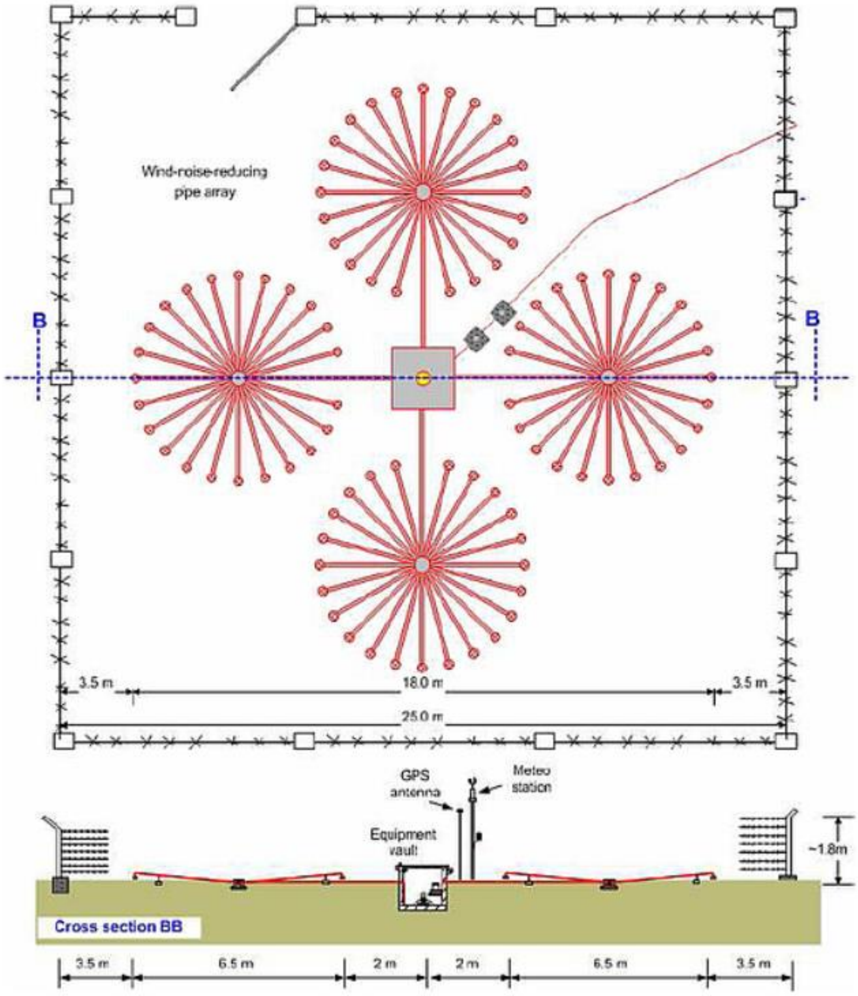

Figure 1.15 - Configuration of array element with pipe structures to reduce wind noise (CTBTO, 2022).

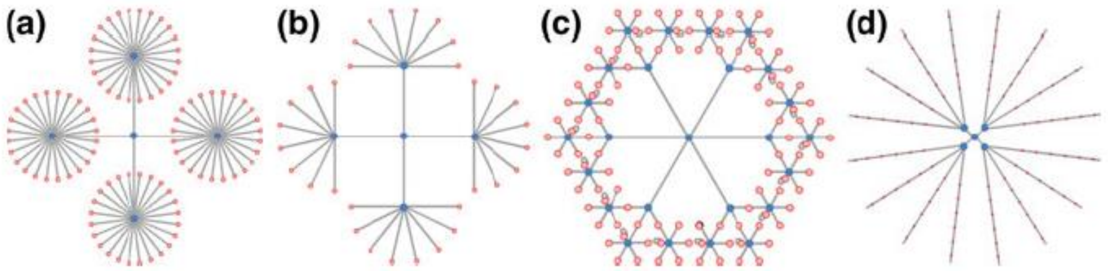

Figure 1.16 - Four most common types of pipe array configurations installed at IMS infrasound stations: a) rosette; b) star; c) hexagonal closed pack; and d) radial (in Marty, 2019).

New techniques that have been designed over the past 40 years (Raspet *et al.*, 2019), consisting of wind protection structures, aim to isolate the measurement system from wind turbulence (Walker and Hedlin, 2010), with different sizes, shapes, and porosity. Research are being made on spherical windscreening devices such as (1) wind fence enclosures; (2) fabric wind domes; and (3) porous metal domes (Raspet *et al.*, 2019). Depending on the structure porosity, spatial averaging can also occur over the surface of the structure leading to further attenuation of wind-generated noise (Hedlin and Raspet, 2003). Also, these wind protection structures are considered for open field locations on the top of existing pipe arrays (Hedlin *et al.*, 2003).

These new methodologies and systems are still in phase of testing and validating the associated data processing technique. The acoustic response of such systems must be well characterized, and it should be demonstrated that it remains stable through time. Additionally, is required an evaluation of the system lifetime in operational conditions (Marty, 2019). These studies will demonstrate if these wind structures are good to be deployed, especially in infrasound arrays located in small and windy islands (Raspet *et al.*, 2019).

(7) Power supply

Power for the equipment at each array element is supplied using buried cables connected to the central facility power supply, in cases where a power grid is not available. Also, additional batteries are installed to provide backup power when the main power supply fails (Christie and Campus, 2010).

In the case of IS42, the energy for the vault equipment is supplied by three 12V 100Ah batteries, which are charged by grid energy. Energy is independent for each site, supplied by power grid.

(8) Data transmission system

Authenticated data from the digitizer at the array elements are usually transmitted to the central processing system via a buried/aerial optical fibre transmission system or UHF telemetry. Both systems are immune to lightning strikes (Christie and Campus, 2010).

Figure 1.17 illustrates the general design of an array element, with all components identified. Furthermore, Photo 1.3 is a capture of the element H1 from the IMS infrasound station IS42. This element array is the one that includes the meteorological equipment.

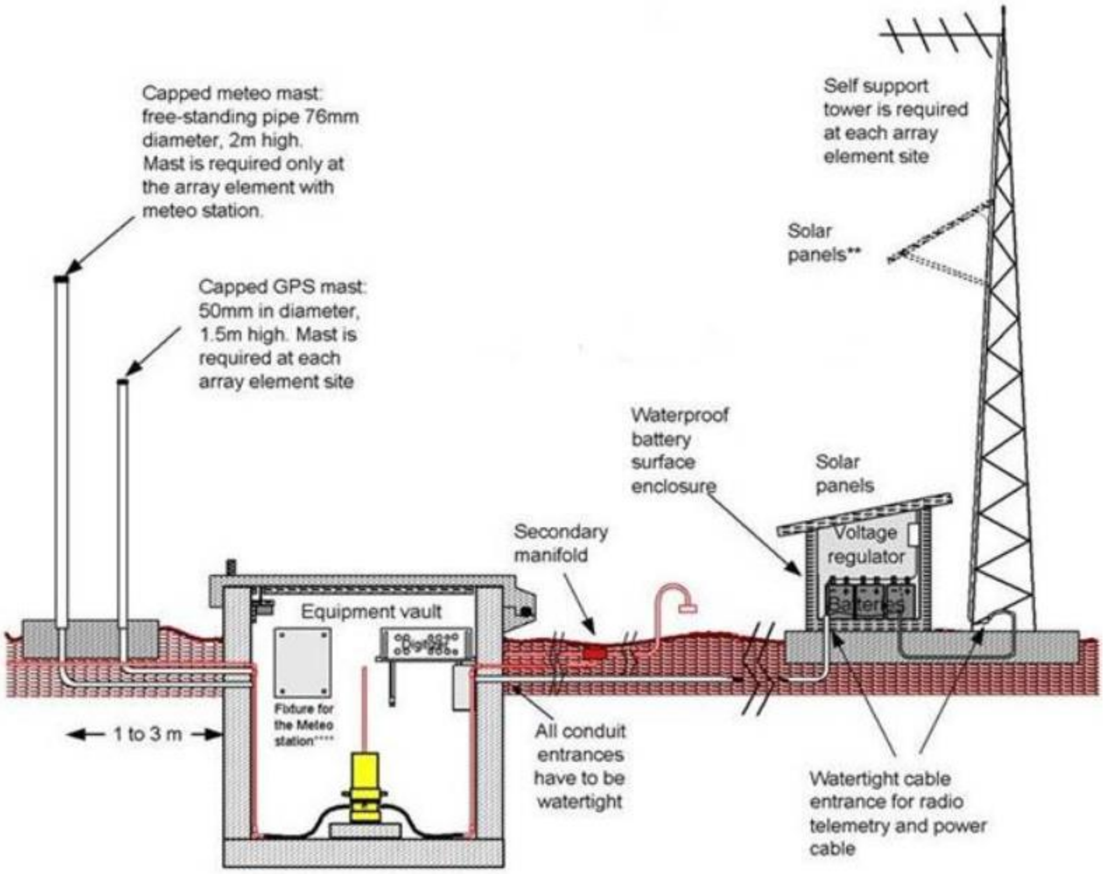

Figure 1.17 - Infrasound array element general design (ARISE, 2013).

Photo 1.3 - Element H1 from IS42 Graciosa, Azores, Portugal.

1.7.1.2. Central Facility (CF)

Central facility equipment includes hardware and software for data acquisition, buffering, formatting, digital signature, and transmission to the IDC (Marty, 2019). It is usually less sheltered than array elements and requires a more stable and cleaner operating environment. Apart from critical equipment, CF usually includes a small workbench, a data analysis computer, and an adequate storage environment for spare equipment. Therefore, it demands more power than array elements and are usually powered through a combination of diesel generators, photovoltaic systems, or main power when available (Marty, 2019). The central facility from IS42 is shown below in Photo 1.4.

Photo 1.4 - CF from IS42 Graciosa, Azores, Portugal.

1.7.1.3. Global Communications Interface (GCI)

The GCI is commonly implemented through satellite communication and GCI equipment at the CF and consists of an integrated services router, satellite router, and VSAT antenna (Marty, 2019). In the case of IS42 the backup connection is supplied by Fibre Optic fast internet access.

1.7.2. Array Design

A successfully application of infrasound as a monitoring technique is strongly dependent on the array design (Evers and Haak, 2004).

A proper design for an infrasound array must provide an accurate estimate of signal azimuth for use in source location algorithms. The design of an infrasound monitoring array depends on several factors, including (1) the number and configuration of the array elements; (2) the spatial coherence of signals between array elements; and (3) the amplitude and coherence properties of background noise. Consequently, there is an absence of a standard configuration, but most of these designs comprises a larger aperture main array with a smaller aperture subarray (Christie and Campus, 2010).

The stations from the IMS infrasound network were recommended to be built with more than 4 array elements, 8 elements, when possible, which allows a station to be resilient to the loss of array elements, despite its good combination between detection capability, and construction and operational costs. A wide range of array geometries can be found in the IMS infrasound network, since there are not any specified requirements for element positioning for stations with more than four elements. These geometries can be defined by the following groups: (1) triangle with an element at the centre, a configuration that had been shown to be optimal (Haubrich, 1968) ; (2) small aperture array surrounded by a larger aperture triangle; (3) small aperture triangle embedded inside a larger aperture pentagon; (4) small aperture array outside a larger array; and (5) other distributions (Marty, 2019). Figure 1.18 illustrates five different configurations for an IMS infrasound array.

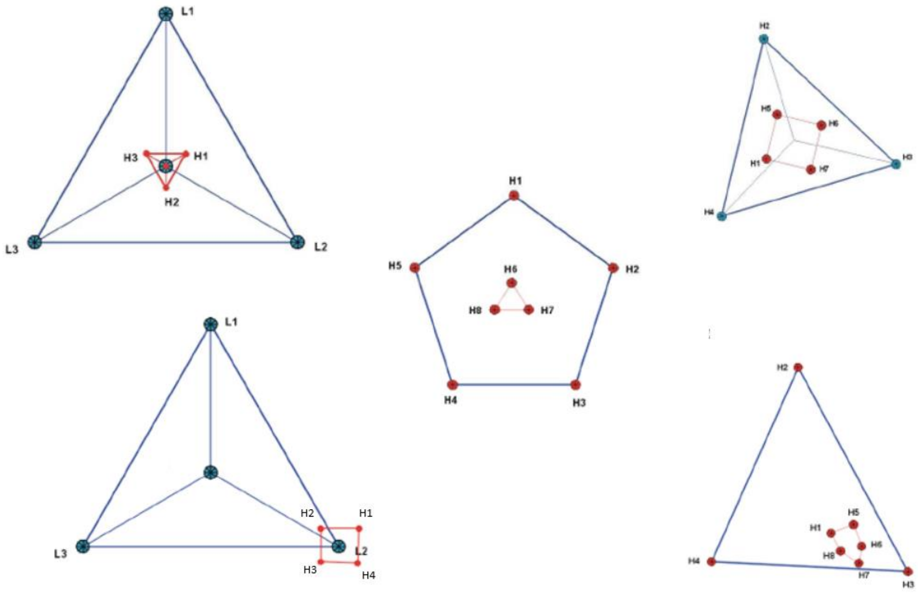

Figure 1.18 - Possible configurations of infrasound arrays (CTBTO, 2022).

It is important to note that the lower the noise conditions are at a specific site, the larger the array aperture can be, and thus the better wave parameters can be estimated. Therefore, installing array elements at locations with background noise as low as possible is of much higher importance than designing the optimal theoretical array geometry. Then, before the choice about the array geometry, firstly is required to identify locations in dense forests wherever it is possible (Marty, 2019).

Moreover, the spacing of sensors, or array elements, is generally tuned to the wavelength of the expected signal, even when being small compared with propagation distances from the vent. Considering volcano monitoring, typical 1 Hz infrasound has a wavelength of ∼ 330 - 350 m, thus many volcano infrasound arrays have apertures of 75 - 100 m, approximately a quarter to half wavelength (McNutt *et al.*, 2015). In case of IMS array elements, the aperture ranges from 1 to 4 km, which enhance the detection of a wide spectrum of infrasound frequencies and the possibility to record infrasound waves from sources at global distances.

1.7.2.1. Small apertures

In general, small aperture sub-arrays have a much better performance than large aperture sub-arrays because of the loss of spatial coherence of infrasound data verified on the larger ones. However, large aperture sub-arrays operate slightly better than small aperture sub-arrays in relation to accuracy (Evers and Haak, 2004).

Nevertheless, the application of small aperture infrasound arrays represents a major tool in volcano monitoring. The analysis of infrasound signals from volcanic explosions or degassing activity allows a precise source location of explosive events. At short ranges, pressure fluctuations propagate through atmosphere with almost no constraints by path effects, containing direct information about the source process. Therefore, a small aperture array can easily track the position of the volcano-generated infrasound source (Ripepe and Marchetti, 2002).

1.7.3. Signal detection and processing

Infrasound arrays are designed to ensure that wind-generated background noise is incoherent between array elements (Christie and Campus, 2010), allowing the detection of coherent signals when they cross the array. The information received through the detection of coherent signals is useful to infer the direction from which the signals have originated (azimuth) and to estimate the speed of propagation across the infrasound array (apparent wave velocity). Thus, both information helps to identify and characterize the source of the signals (Blanc and Ceranna, 2009).

The most substantial coherent signal detections by each sensor are called *phases*, as opposed to *noise*. These phases are grouped to form and locate an event. They are identified by the Progressive multi-channel correlation (PMCC) method, created by Cansi in 1995, one of the most employed techniques in signal processing. The PMCC, considering the number of sensors participating in the detection, may distinguishes the coherent signals originated by natural and anthropogenic sources from incoherent background noise (Brachet *et al.*, 2010; Drob *et al.*, 2010). In volcano monitoring, the Progressive Multi-Channel Correlation (PMCC) is used to separate volcanic signals from the background *clutter* (Matoza *et al*., 2006). As McNutt *et al*. (2015) mentioned, PMCC measures the time-lags between pairs of array elements associated with maximum cross-correlation and finds the best fitting sound propagation vector associated with all inter array time-lags.

The three main infrasound wave phases mentioned in subtopic 1.3.3.3. (Tropospheric (*Iw*), stratospheric (*Is*), and thermospheric (*It*)) are predicted to arrival at an infrasound array with a different value of (1) horizontal trace-velocity; (2) back azimuth deviation; (3) frequency content; (4) amplitude; (5) celerity; (6) consistency; and (7) correlation values. Trace-velocity relates with the incidence angle of signal arrivals at an array. While *Iw* have lower trace-velocities and higher celerity due to its almost horizontally propagation along the ground, *It* are characterized by higher trace-velocities and lower celerity. Also, differences in back-azimuth deviation are a result of the propagation path exposure to crosswinds (Matoza *et al.*, 2010; Brachet *et al*., 2010).

Furthermore, in volcano monitoring beyond local distances it is necessary to avoid the deployment of an infrasound station in a region where the shadow zones are predicted, otherwise infrasound sensors will not detect any signal of potential volcanic activity, between a few tens to few hundreds of kilometres from the volcano. Also, local topography and the volcano crater morphology might disturb the signal recording (McNutt *et al*., 2015).

Nevertheless, in the case of IMS infrasound network, infrasound data are recorded at 20 samples per second. The Nyquist frequency (10 Hz) limits the frequency of detected signals at these stations to less than about 8 Hz. All data are analysed in near real time and archive at the International Data Centre (Campus and Christie, 2010).

1.7.3.1. Signal-to-Noise Ratio (SNR) and detection capability

Arrays are more significant advantageous than single sensors. The combination of multiple recordings increases the ratio of coherent signal to incoherent noise due to wind, *i.e*., signal-to-noise ratio (SNR). Therefore, it can be essential for extracting weak signals from noise at more distant stations or improving understanding of the signal structure at all distances (Herrin *et al*., 2008).

The configuration and number of elements from an array might affect the number of detections. The signal recording strongly increases with the number of elements (Evers and Haak, 2004). Consequently, the SNR is increased by the square root of the number of array elements (Christie and Campus, 2010).

Moreover, the detection capability of an infrasound array it is not only dependent on the number of elements. It is ruled as well by (1) the position of the elements that controls the resolution and the total aperture of the array (Evers and Haak, 2004); (2) the background noise level at each site;

(3) the efficiency of the WNRS applied ; (4) the sensitivity of the infrasound sensors at all frequencies of interest (Christie and Campus, 2010); and (5) the seasonal variations in the atmospheric winds (Le Pichon *et al.*, 2008).

1.8. Infrasound mobile stations

In recent times, the development and deployment of portable infrasound arrays that are small, lightweight and can be rapidly set-up and torn down are essential for several application field such as military use, search-and-rescue teams operating in GPS-denied environments, volcanology research, among others (McIntire *et al.*, 2017).

Mobile infrasound arrays are used to identify sources to extend the database for the study of infrasound wave properties to new sources and source distances, to measure the properties of background noise, and to test procedures that can be used to minimize background noise (Christie *et al.*, 2006). Also, they are a helpful tool to improve the accuracy and robustness of the atmospheric corrections in the detected signals by several techniques, including the measured azimuth deviations (Le Pichon *et al.*, 2005a).

Several research groups around the world have been developing projects to establish local infrasound networks of portable infrasound stations. These temporary networks have been instrumental for observation of events recorded at local and regional distances. Additionally, they have been complementing the data gathered through the IMS infrasound network (Campus *et al.*, 2010). Such portable equipment together with IMS permanent arrays is so valuable to study and understand local and regional infrasound background activity (Mialle *et al.*, 2010). Mobile infrasound arrays are an auxiliary tool to the existing permanent infrasound arrays installations of IMS and non-IMS, performing an essential role in increasing the density of infrasound stations worldwide, as well as, consequently, improving their detection capability (Campus *et al.*, 2010).

In general, infrasound arrays consist of 3 or more pressure sensors distributed in a configuration whose aperture is far smaller than the propagation distance between the source and the array. According to the purpose of each deployment, the aperture of an infrasound array may be hundreds to thousands of meters, commonly adjusted to the wavelength of infrasound signals expected (Johnson, 2019). Aiming especially local monitoring, temporary arrays present shorter apertures than permanent infrasound stations, consisting of 3 to 5 array elements with a spatial distance around 100 to 300 meters (Herrin *et al.*, 2008).

1.8.1. Application in volcano monitoring

Mobile arrays have a useful application in volcano monitoring and can be locally deployed within distances less than 15 km from the volcanic source. However, their installation will always be variable and dependent on field site accessibility and the resources available to the volcano observatory or scientific team. In general, arrays of closely spaced sensors are optimal. Even an array of two sensors allows critical distinction between volcano signal, infrasound generated by non-volcanic sources, and background noise such as wind-generated infrasound (Johnson, 2019).

1.8.2. Examples of temporary infrasound arrays

1.8.2.1. CTBTO portable array

The CTBTO portable array has been applied all around the world. In the experiment realized in South Central Chile, from March to July 2009, with this portable station composed by four microbarometers arranged in a triangular geometry with a central element, the sides of this equilateral triangle were 450 - 500 metres apart, with inter-sensor distances of 280 metres. Noise reduction was achieved by 15 m porous hoses, arranged in a spatial configuration to the inlet manifold on each microbarometer. Deployed approximately 55 km away from Villarica and Llaima volcanoes, the most active volcanoes in the Southern Volcanic Zone, the temporary array aimed to observe for the first time volcanic-associated infrasound waves in Chile (Riquelme *et al*., 2009). Photos 1.5 and 1.6 illustrate the CTBTO portable array applied temporarily in Japan and Bermuda, respectively.

Photo 1.5 - Installation of CTBTO portable array in Tsukuba, Japan, in March 2010 (in Mialle *et al*., 2010).

Photo 1.6 - Portable site equipment ready for deployment in Bermuda, 2019 (in Robertson *et al.*, 2021).

1.8.2.2. Temporary infrasound UniFI arrays

The University of Firenze (UniFI) has been deploying temporary and permanent infrasound arrays in several places (see Figure 1.19) and for different purposes. For instance, to monitor volcanoes in South America intending volcanic early warning issuance, UniFI installed the small aperture CHP array, near Copahue volcano, in Argentina, at approximately 380 km away from Calbuco volcano, Chile. Also, the TNG array was implemented near the Tungurahua volcano, in Ecuador (Campus *et al.*, 2017). Furthermore, UniFi has been permanently performing real-time monitoring of the Italian volcanoes of Etna (*e.g.*, Ripepe *et al.*, 2018) and Stromboli (Ripepe and Marchetti, 2002), since 2003.

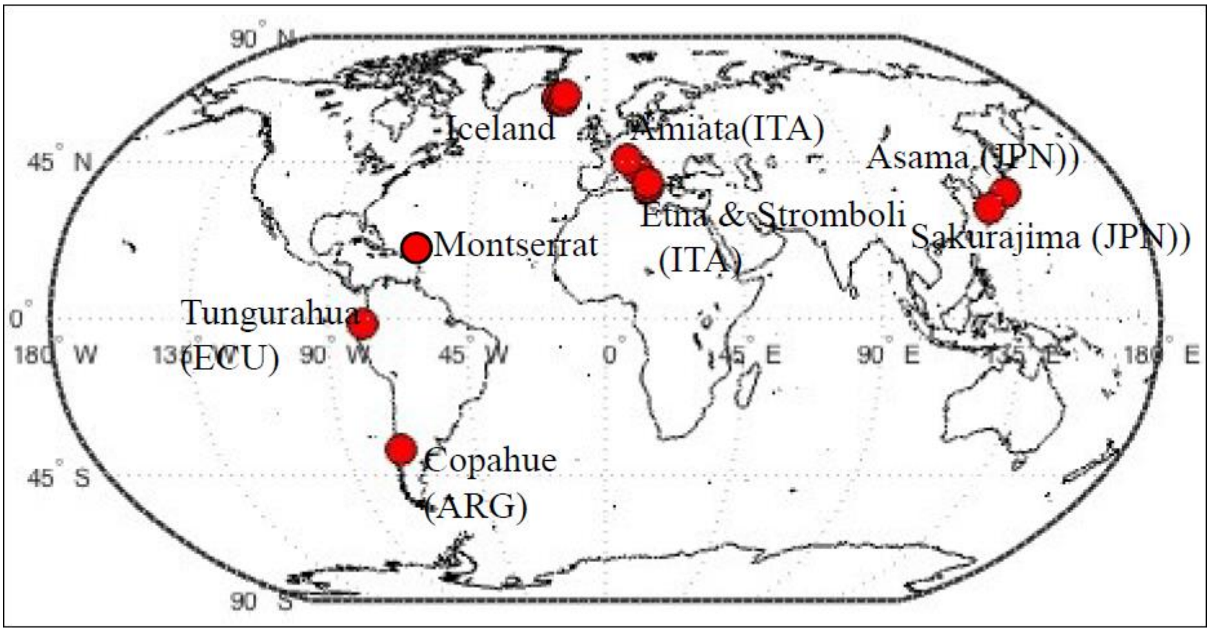

Figure 1.19 - Infrasound arrays operated by UniFI around the world (in Campus *et al.*, 2017).

1.8.2.3. Temporary infrasound arrays at Volcán de Fuego, Guatemala

Temporary deployments took place between 18th - 23rd May 2018 and 26th November -3rd December to gather infrasound data from activity at Volcán de Fuego, in Guatemala. In May 2018 it was deployed a temporary network of six infrasound sensors located between 1 and 9 km from the active vent. In the period between 26 November and 3 December 2018 it was deployed again a temporary network, also consisting of six infrasound sensors (Diaz-Moreno *et al.*, 2020). Figure 1.20 shows de layout of these mobile arrays around Vólcan de Fuego.

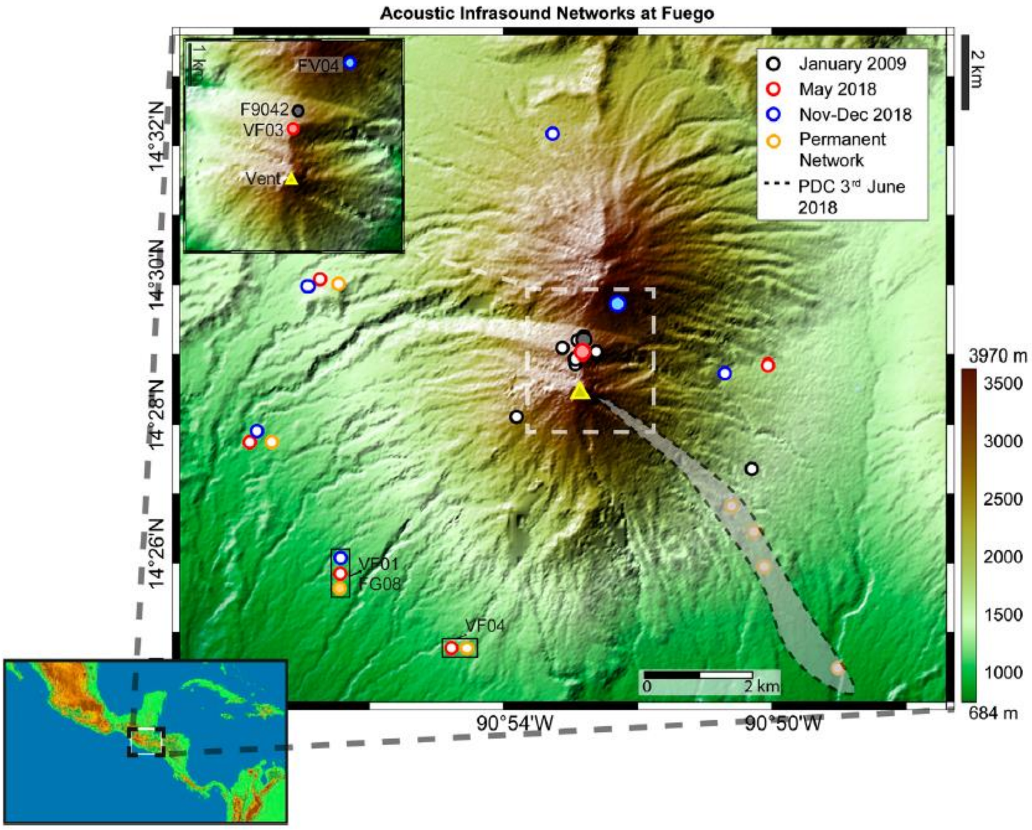

Figure 1.20 - Temporary and permanent infrasound monitoring networks at Volcán de Fuego. Red (May 2018) and blue circles (November-December 2018) are temporary deployments; orange circles indicate the permanent seismo-acoustic network. The grey-filled area illustrates, qualitatively, the footprint of the 3rd, June 2018 Pyroclastic Density Current (PDC) (in Diaz-Moreno *et al.*, 2020).

CHAPTER 2. THE AZORES ISLANDS

This chapter relies on the general settings of the Azorean archipelago, describing its geological framework, followed by a brief resume on the wind patterns of this region, once they represent a conditional factor on the propagation of infrasound waves, and then a topic about its central stratovolcanoes, as it is the focus of this research project.

2.1. General settings of the Azores Islands

2.1.1. Geological framework

The Azores Islands form an archipelago composed of nine volcanic islands and some islets, with location in the middle of North Atlantic Ocean, between latitudes 36°55’ and 39°44’ N and longitudes 24°46’ and 31°17’ W, around 1400 km west of mainland Portugal.

The nine islands are disposed along approximately 600 km in a NW-SE trend, defining three geographical groups: (1) Western (Flores and Corvo); (2) Central (Graciosa, Terceira, São Jorge, Pico, and Faial); and (3) Eastern (São Miguel and Santa Maria). They are the result of the rise of large submarine volcanic edifices from the Azores Plateau (Lourenço *et al*., 1998), roughly limited by the 2000 m bathymetric curve (Needham and Francheteau, 1974).

The geodynamic setting of the archipelago is particularly unique once this area is where the Eurasian, African and North American lithospheric plates interact, forming the so well-known Azores Triple Junction (Miranda *et al*., 2015). Several magnetic anomalies are verified in this region, due to the nature of magmatic sources, which may be caused by the existence of a mantle plume (Silveira *et al*., 2006, Miranda *et al*., 2015). Significant structures define the plate boundaries of the Azores Triple Junction, as it is shown in Figure 2.1 The Mid-Atlantic Ridge (MAR) divides the Eurasian and African lithospheric plates to the east from the North American plate to the west. The Terceira Rift (TR) is the westernmost segment of the Eurasian plate, characterized by a WNW-ESE-orientated alignment of alternating basins and volcanic edifices (islands and seamounts). From east of the TR, the Eurasian-African plates boundary is expressed by the Gloria Fault (GF). At last, located from west of the GF towards east of the MAR, the East Azores Fracture Zone (EAFZ) is an abandoned fault segment that probably represents the ancient limit of the Eurasian-Nubian boundary (Searle, 1980).

Such complex geological framework is responsible for significant seismic and volcanic activity mainly located at the actual lithospheric plate boundaries (Gaspar *et al*., 2015b). While Corvo and Flores lie to the west of the MAR and emerge from a current relatively stable geological setting, the other islands are situated on an important seismic and volcanically active zone corresponding to the boundary between the Eurasian and Nubian tectonic plates. (Gaspar *et al*., 2015*a*).

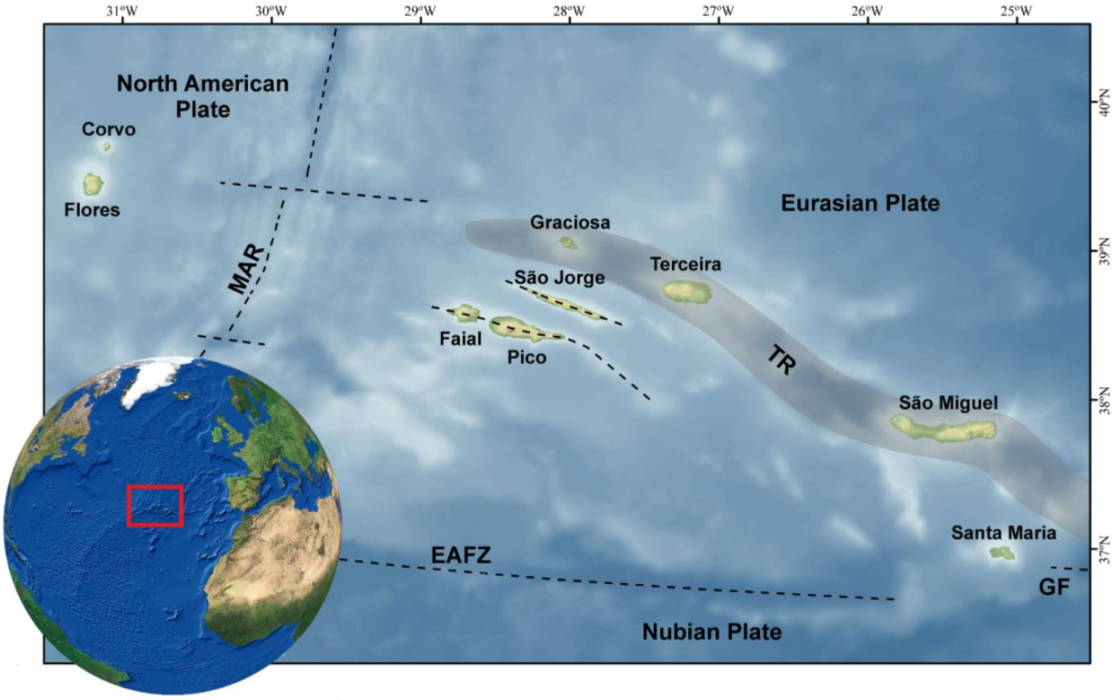

Figure 2.1 – Geological framework of the Azores Islands. MAR – Mid-Atlantic Ridge; TR – Terceira Rift; EAFZ – East Azores Fracture Zone; GF – Gloria Fault (modified by Pimentel (2015) from Lourenço *et al*. (1998), Vogt and Jung (2004), Beier *et al*. (2008)), and Georgen and Sankar (2010)).

Since its settlement in the 15th century, 31 destructive earthquakes and 28 volcanic eruptions were registered in the Azores archipelago. The biggest earthquakes have reached magnitudes > 7. On the other hand, subaerial volcanic eruptions have ranged from Hawaiian to sub-Plinian character, while submarine ones have been mainly of Surtseyan type (Gaspar *et al*., 2015*b*).

2.1.1.1. Seismicity

Since the settlement, the Azores region was affected by about 15 major earthquakes and 16 seismic crises, which had cause considerable damage and plentiful deaths (Gaspar *et al*., 2015*b*). These geological events are associated with the structural system that extends from GF to the MAR.

The first registered destructive earthquake occurred on 22nd October 1522, with epicentre on north of Vila Franca do Campo, the capital of São Miguel Island at that time, and reached intensity X on the EMS-98 scale (Silveira *et al*., 2003). On 9th July 1757 it has occurred the strongest earthquake until present-day, with epicentre close to the north coast of São Jorge Island. With a magnitude of 7.4, the event had reached intensity X on the EMS-98 scale (Silva, 2005). The epicentral locations of the registered destructive earthquakes in the Azores are shown in Figure 2.2.

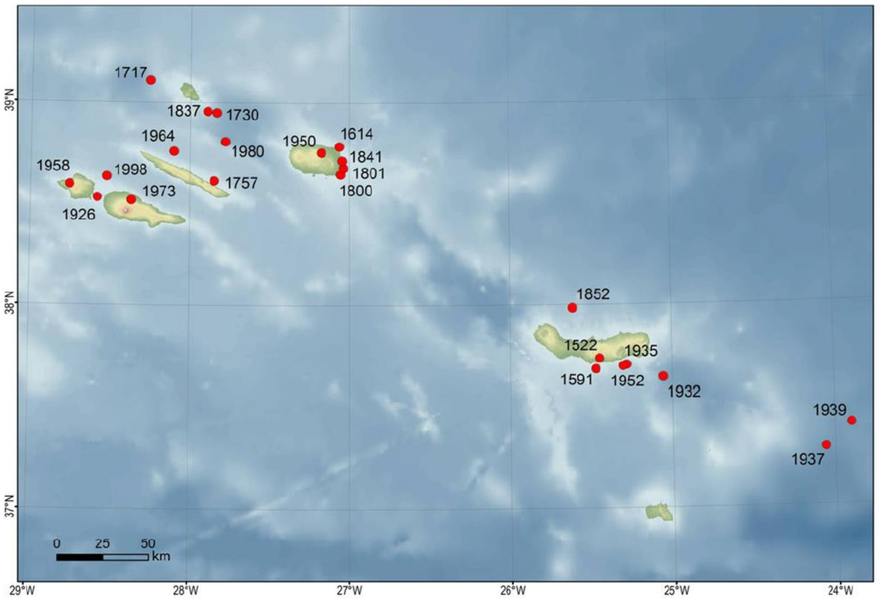

Figure 2.2 - Epicentral locations of destructive earthquakes during historical times (in Gaspar *et al*., 2015b).

2.1.1.2. Volcanism

As well as seismicity, volcanic activity in the Azores Islands coincides with the NW-SE regional tectonic trend that extends from GF to the MAR. Since the settlement, at least 28 volcanic eruptions have already occurred in the region, which 15 of them were subaerial, *i.e*., located on land, namely on the islands of São Miguel, Terceira, São Jorge, Pico, and Faial (Gaspar *et al*., 2015*b*).

The observed volcanic eruptions have a wide spectrum of eruptive styles, from Hawaiian to sub-Plinian, sometimes with a hydromagmatic signature. Basaltic eruptions have occurred on the 5 islands: (1) São Miguel, in 1563 and 1811 (offshore); (2) Terceira, in 1761 and 1998 (offshore); (3) São Jorge, in 1580 and 1808; (3) Pico, in 1562-64, 1718 and 1720; and (3) Faial, in 1672-73 and 1957-58. The effusive activity has been related to active fissure volcanic systems, as for example the one of Manadas Fissure Volcanic System (Forjaz and Fernandes, 1975) in São Jorge Island (see chapter 4). Associated with central volcanos, trachyte explosive eruptions were registered on São Miguel Island at (1) Furnas volcano, in 1439-45 and 1630 (Cole et al., 1999); and (2) Fogo, in 1563 (Wallenstein, 1999). Both included phreatomagmatic phases caused by magma-water interaction from caldera lakes. Figure 2.3 illustrates the historical volcanic events, subaerial and submarine, registered in Azores archipelago.

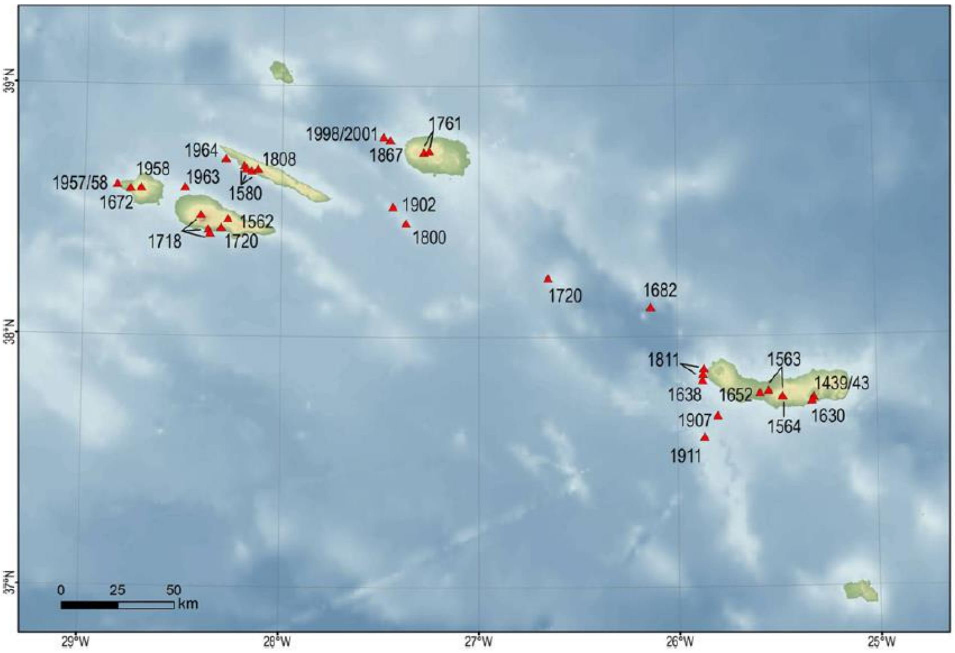

Figure 2.3 - Location of historical subaerial and submarine eruptions (in Gaspar *et al*., 2015b).

2.1.2. Wind patterns

As Madruga *et al*. (2015) have referred, the Azores region sits at north of the predominant influence of the trade winds (east-west direction) and on the influence of the subtropical high-pressure belt, well-known as the Azores High, in an area of transition and confrontation between air masses from the tropics and colder masses from the north. Consequently, the wind is a prevalent component on the islands, showing an increased speed from the eastern group to the western one. Along the year, the wind blows regularly, but more vigorously in the winter months than in the summer ones. In winter, the fragmented evolution of the low-pressure systems at north of the archipelago allows the winds to circumvent the islands by north and from the west to the east. In this season, the average velocity approaches 20 km/h (5.56 ms^{-1}). Nevertheless, gusts are felt almost every year and may reach 100 km/h (27.78 ms^{-1}). In summer, the high-pressure systems move to superior latitudes and their influence on the islands becomes weaker, allowing the decrease of the wind speed to values under 10 km/h (2.78 ms^{-1}). Thus, southwest winds encircle the islands. Nevertheless, the wind speed increases with altitude and as the atmospheric circulation releases itself gradually from the friction of the planetary boundary layer.

Tropospheric winds are the most influent for the propagation of infrasound waves on a local scale(Brown *et al.*, 2002; Garcés *et al.*, 2004; de Groot-Hedlin *et al*., 2011; McNutt *et al.*, 2015).. Therefore, they are a crucial factor to be considered on the analysis of signals detected by infrasound stations deployed near central volcanoes.

2.2. Active central volcanoes

Volcanoes that have been active within the last 10,000 years are considered as active volcanoes (Rymer, 2015). Thus, 8 of the Azorean central volcanoes, 9 fissure volcanic systems and 8 submarine volcanoes are active (IVAR, 2022), although they seem to be in a quiescence stage once the estimate recurrence interval (e.g., Gaspar *et al*., 2015*c*) has already been exceed.

Polygenetic or central volcanoes are located at the intersection of two fault systems. Therefore, the tectonic structure is responsible for controlling volcanism (Madeira, 1998; Madeira *et al*., 2015), which is characterized by erupted basaltic to trachytic magmas in the Azores Islands (Zanon, 2015).

Possible eruptive scenarios were considered in this work for the active subaerial volcanoes of São Miguel (Sete Cidades, Fogo and Furnas), Terceira (Pico Alto and Santa Bárbara), Faial (Caldeira), and Pico (Montanha do Pico) to select the best sites for monitoring those eruptive scenarios through infrasound techniques (see chapter 3). In spite of Caldeira volcano in Graciosa Island (Gaspar, 1996), be assumed as active, even without any historical eruptive events, it was not considered hereinafter, once the IS42 infrasound station is deployed in its vicinity. Therefore, this monitoring method has already been applied there permanently.

2.2.1. São Miguel Island

On the largest island of the Azorean archipelago, São Miguel, 3 central volcanoes with calderas - Sete Cidades, Fogo and Furnas - and 2 basaltic fissure systems - Picos and Congro - are still considered as active and had been the place for several eruptions in the last 5 ka. Hence, this island is known as the most volcanically active (Gaspar *et al*., 2015*a*). During the last 5 ka, around 57 volcanic eruptions took place on this island. Half of them were trachytic and the other half of basaltic character. The trachytic eruptions were mainly explosive, originating from vents within the calderas. On the other hand, basaltic eruptions have produced lava flows and pyroclastic products (Booth *et al*., 1978). Around 5 ka BP, the Plinian eruption of Fogo A covered a large part of the island, providing a convenient stratigraphic reference horizon to distinguish recent eruptive activity (< 5 ka) from the ones of pre-Fogo A period (Walker and Croasdale, 1970; Booth *et al*., 1978; Wallenstein *et al.*, 2015).

From basaltic to trachytic character, all range of volcanic eruptions styles were identified here, involving Hawaiian, Strombolian, Vulcanian, sub-Plinian and Plinian eruptive styles type events. Trachytic explosive activity is mostly associated with central volcanoes of Sete Cidades, Fogo and Furnas, which confirms the presence of plumbing systems connected to well-developed magma chambers. This kind of events on São Miguel Island has a recurrence interval of nearly 147 years during the last 5 ka. Regarding sub-Plinian explosions, Sete Cidades volcano shows moderate eruption frequency and a recurrence interval of about 300 years, but a reduced frequency of Plinian eruptions, being considered as the most active volcano of the island. Furnas and Fogo volcanos exhibit low frequency of sub-Plinian eruptions, with return intervals of around 550 and 1000 years, respectively. Furthermore, exclusively Fogo volcano had a Plinian eruption in the last 5 ka (Gaspar *et al*., 2015*c*).

In historical times, *i.e.*, since settlement by the Portuguese, this island had already been transformed as result of 6 subaerial volcanic eruptions (Gaspar *et al*., 2015*b*). Figure 2.4 shows all volcanic systems of São Miguel Island, including the oldest and inactive ones of Nordeste and Povoação.

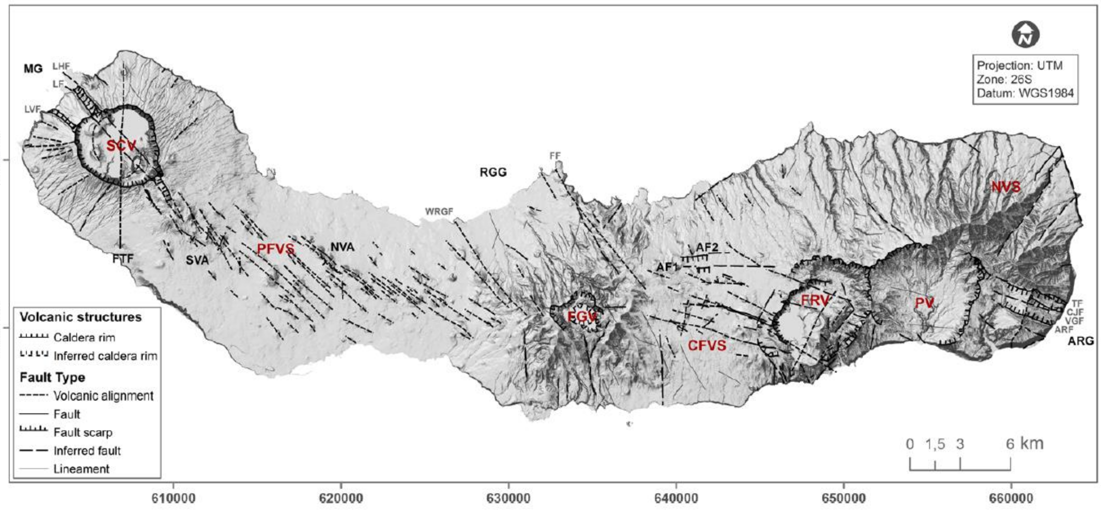

Figure 2.4 - Location of volcanic systems on São Miguel Island, identified by red colour. SCV - Sete Cidades volcano; PFVS - Picos fissural volcanic system; FGV - Fogo volcano; CFVS - Congro fissural volcanic system; FRV - Furnas volcano; PV - Povoação volcano; NVS - Nordeste volcanic system (in Madeira *et al*., 2015).

2.2.1.1. Sete Cidades volcano

On western region of São Miguel Island stands the volcano massif of Sete Cidades, formed by an active central volcano with a well-developed nearly circular caldera at its summit, as illustrated by

Photo 2.1. This volcano was originated from a central vent through to plentiful eruptions of diversified styles, magnitudes, and durations, with the consequent accumulation of pyroclastic deposits and lava flows (Queiroz *et al*., 2015). The eastern limit of Sete Cidades volcano is defined by its boundary with Picos Fissural Volcanic System (Ferreira *et al*., 2015).

Photo 2.1 - Caldera of Sete Cidades volcano (photo courtesy of Nicolau Wallenstein).

2.2.1.1.1. Tectonics

The intersection of two main fracture systems lead to the formation of Sete Cidades volcano, namely (1) the dominant fracture system of NW-SE trend (Carmo *et al*., 2015), which is related to the regional tectonic regime of Terceira Rift (*e.g.*, Beier *et al.*, 2008); and (2) E-W fractures, that are associated with deep faults in the oceanic crust, parallel to the direction of the Azores-Gibraltar fracture zone (Searle, 1980). The NW-SE fault system has its expression through Mosteiros graben on the NW sector that cuts the caldera and extends towards SE, controlling the alignment of numerous scoria cones (Queiroz, 1997). Moreover, the E-W direction is represented by several alignments of trachytic domes and scoria cones on the western flank of Sete Cidades volcano. Also, on southern and southwestern flank, NE-SW trending faults control the direction of some valleys (Queiroz *et al.*, 2015). At last, the distribution of pumice cones and maars inside the caldera may be evidence of arcuated faults on that area. The vents responsible for those volcanic forms are then assumed to be located at the intersection of these arcuated faults with the regional NW-SE trend and E-W faults (Queiroz, 1997).

2.2.1.1.2. Eruptive history

Since settlement no eruptions on land were recorded, although 3 events have occurred offshore near the west coast of Sete Cidades volcano. Regardless, large paroxysmal eruptions related to caldera-forming stages had marked the volcano over its history. In the last 5 ka, Sete Cidades was the Azorean volcano with more volcanic events geologically registered. 17 trachytic sub-Plinian eruptions occurred inside the caldera with strong hydromagmatic character. Therefore, it was considered as the most active central volcano in the Azores Islands in the last 5 ka. Additionally, trachytic effusive eruptions have occurred either inside caldera or on its western flank, which are represented by domes and associated lava flows (Queiroz *et al*., 2015). The most recent event that occurred within the caldera was estimated around 700 years BP, and it was a trachytic explosive eruption of sub-Plinian type (VEI 4), showing a hydromagmatic character, on which had resulted the Caldeira Seca tuff ring (Queiroz *et al*., 2008; Cole *et al.*, 2008).

Also, more than 12 subaerial basaltic events, producing basaltic scoria and lava flows, were found out to have happened on its outer slopes in the same period, from effusive to moderately explosive eruptions of Hawaiian or Strombolian styles, reflecting a clear tectonic control (Queiroz *et al*., 2015). The most recent flank eruption is estimated to have occurred around 800 years ago (Moore and Rubin, 1991), at the top of the western sea cliffs of Sete Cidades, producing a scoria cone, named as Pico das Camarinhas, and lava flows that formed the lava delta of Ponta da Ferraria (Queiroz *et al*., 2008).

2.2.1.2. Fogo volcano

Fogo volcano is located on the centre of São Miguel Island, occupying the widest area, and representing the most rugged morphology when compared to the other two central volcanos of the same island. Its summit caldera resulted from explosive and collapse events (Wallenstein *et al*., 2015). Its borders intersect on west and east sides with the two fissural volcanic systems of São Miguel Island, Picos and Congro, respectively.

Photo 2.2 - Caldera of Fogo volcano (photo courtesy of Nicolau Wallenstein).

2.2.1.2.1. Tectonics

The intersection of three main fault systems of (1) NW-SE, (2) NE-SW, and (3) E-W trends (Wallenstein et al., 2015) had contributed for the rise of Fogo volcano. On the northern flank, a predominant NW-SE to NNW-SSE direction (Carmo, 2013) reflects the dominant tectonic regime of the Azores region, expressed by the Terceira Rift, as in Sete Cidades volcano. These faults are well-defined by the alignment of scoria cones and lava domes on the flanks, confirming its tectonic control. The NW-SE direction fault corresponds to the well-known Ribeira Grande graben (Muecke *et al.*, 1974), mostly characterised by a fault system that crosses the summit caldera of Fogo volcano. N-S trend is expressed through an important set of structures in the direction of valleys on the southern flank. Furthermore, the curved distribution of trachytic domes in the north of Lombadas may indicate a possible circular tectonic structure associated with the outer caldera (Wallenstein, 1999).

2.2.1.2.2. Eruptive history

During the last 5 ka, after the paroxysmal event of Plinian type named as Fogo A (Walker and Croasdale, 1971), the eruptive history record of Fogo volcano can be characterized in (1) trachytic explosive eruptions and (2) basaltic eruptions.

Designated by Booth *et al.* (1978) as Fogo B, Fogo C and Fogo D, these 3 trachytic explosive events were of much smaller magnitude than Fogo A. Dated around 3242 years BP (Shotton *et al.*, 1970), Fogo B eruption was the only one of these three with eruptive centre located outside the summit caldera, having formed a crater that cuts part of Mata do Botelho trachytic dome. Fogo B started with the emission of fine materials, which was followed by an increase in the eruptive intensity and its final phase had resulted on the collapse of the eruptive column, originating surges. On the contrary, Fogo C and D occurred within the caldera, but showed two distinct aspects. Fogo C was mainly a hydromagmatic eruption, while Fogo D was mostly magmatic, with some hydromagmatic explosions (Wallenstein, 1999).

The basaltic activity of Fogo volcano has been located exclusively on the flanks for at least more than 40 000 years, ranging from effusive of Hawaiian style to moderately explosive of Strombolian style, originating scoria cones and associated lava flows. In the last 5 ka and before the Portuguese settlement, at least 2 eruptions of this type have occurred, namely (1) Pico Arde, formed around 1800 years BP (Moore and Rubin, 1991), whose lava flows had created the lava delta that separates Ribeira Grande and Santa Bárbara Beaches, at north of Ribeira Seca, and (2) Pico da Nossa Senhora das Angústias, whose scoria cone was responsible for the emission of lavas that created the lava delta of Caloura (Wallenstein, 1999).

At last, the most recent eruption of Fogo volcano took place in 1563. The island was already occupied by the Portuguese, and it was the first time that an eruption from Fogo volcano was recorded on site. The event had two different phases: (1) the first one was an intracaldera eruption of sub-Plynian type (VEI 4), firstly with hydromagmatic character and then passing to a strong magmatic phase, developing a large eruptive column; (2) the second one comprised an effusive basaltic eruption of Hawaiian style that occurred 4 days later in the north-western lower flank, on Pico do Sapateiro, ejecting blocks and bombs during the initial explosions with the opening of the first vent, and later on producing *pahoehoe* lava flows that reached the sea (Wallenstein *et al.*, 2015). Moreover, a probable phreatic eruption may have occurred in 1564, inside caldera in the same location as the 1563 event. However, the records about it are contradictory and the field data is very scarce or inexistent, not allowing to validate them (Wallenstein, 1999).

2.2.1.3. Furnas volcano

Furnas volcano is the easternmost of the 3 trachytic active central ones of São Miguel Island. Also, its topography is the least impressive since it does not have a well-defined cone-like shape as Sete Cidades and Fogo volcanoes. However, its caldera-complex is morphologically unique, particularly when viewed from its rim, formed by a nested inner caldera complex, roughly elliptical (Guest *et al.*, 1999), surrounded by a steeply outer caldera to the north and north-east, where Furnas leans against the western rim of Povoação Caldera. To the west and south, the caldera boundary is not well defined due to the overlay of deposits inter-fingered with those from the Congro Fissural Volcanic System (Guest *et al.*, 2015).

Photo 2.3 - Caldera of Furnas volcano: parish of Furnas (left) and Lagoa das Furnas (right) (photo courtesy of Nicolau Wallenstein).

2.2.1.3.1. Tectonics

One of the most dominant fracture systems that crosses the volcanic massif of Furnas volcano shows a WNW-ESE trend and appears to control some volcanic alignments (Guest *et al.*, 1999), especially the ones that extend from the Congro Fissural Volcanic System, on the western slope of Furnas volcano (Carmo *et al.*, 2015). There are other important fault systems, as the NE-SW orientated tectonic structures that are prolonged through all Furnas caldera and seem to have a significant part on its outlines (Carmo *et al.*, 2015). Moreover, a N-S fracture system is well-defined on the south flank, between Amora beach and Ribeira Quente, where it controls the drainage pattern (Guest *et al*., 1999; Carmo *et al*., 2015). Furthermore, a set of NW-SE trending fractures parallel to the well-known regional fault system of Terceira Rift are represented likewise (Guest *et al*., 1999).

2.2.1.3.2. Eruptive history

Throughout the last 5 ka, Furnas volcano erupted at least 10 times and all of them had the eruptive centre within its caldera (Booth *et al*., 1978), 6 of which have occurred in the last 2 ka, including the two historic events in 1439-43 and 1630. The eruptions were explosive of trachytic nature and sub-Plinian in magnitude, mostly involving both magmatic and hydromagmatic activity (Guest *et al*., 2015). At least three eruptions on this period, counting with both historical ones, had effusive final phases, with extrusion of trachytic lava domes (Cole *et al*., 1999).

Having occurred around 1900 years BP, Furnas C was the bigtest eruption on the last 5 ka, thus originating the depression where the village of Furnas has developed (Pacheco *et al*., 2012; Guest *et al*., 2015).

After the first arrival at São Miguel Island, somewhere around 1439, an e-ruption started and in the second visit with the first settlers, around 1443, the final stage of an ongoing explosive eruption at Furnas volcano was witnessed, ending with the extrusion of a trachytic dome named as Pico do Gaspar (Pacheco *et a*l., 2012).

In 1630, the last eruption of Furnas volcano occurred in the southern part of caldera, and it was characterized two distinctive phases. The first one was explosive, starting with magmatic activity of sub-Plinian type, and then oscillating between magmatic and phreatomagmatic activity, ending with a sustained magmatic stage. The last phase was purely magmatic and of effusive in style, with the extrusion of a trachytic lava dome over at least the following two months (Cole *et al*., 1995).

Regarding basaltic activity, there is no evidence of this type of eruption on Furnas volcano at least during the last 5 ka (Booth *et a*l., 1978), as well as is very unlikely that a basaltic event may occur within its caldera (Guest *et al*., 1999; Cole *et al*., 1999).

Beside eruptive situations, it is noteworthy to mention that Furnas volcano has an active geothermal system. Its fumarolic fields continuously discharge high levels of CO_2, which represents a permanent health risk for the population of Furnas village (e.g., Viveiros *et al*., 2010).

2.2.2. Terceira Island

Terceira Island is formed by five main volcanic systems: 4 central volcanoes, named (1) Cinco Picos; (2) Guilherme Moniz; (3) Pico Alto; and (4) Santa Bárbara; and 1 basaltic fissure system, known as Fissure Zone. Though, only the trachytic central volcanoes of Pico Alto and Santal Bárbara, as well as the Fissure Zone, remain active (Self, 1976; Madeira, 2005; Zanon and Pimentel, 2015). The 4 central volcanos are identified in Figure 2.5. These main eruptive centres are aligned in a WNW-ESE to NW-SE trend (Self, 1974), which may express the subaerial influence of Terceira Rift (Machado, 1959a).

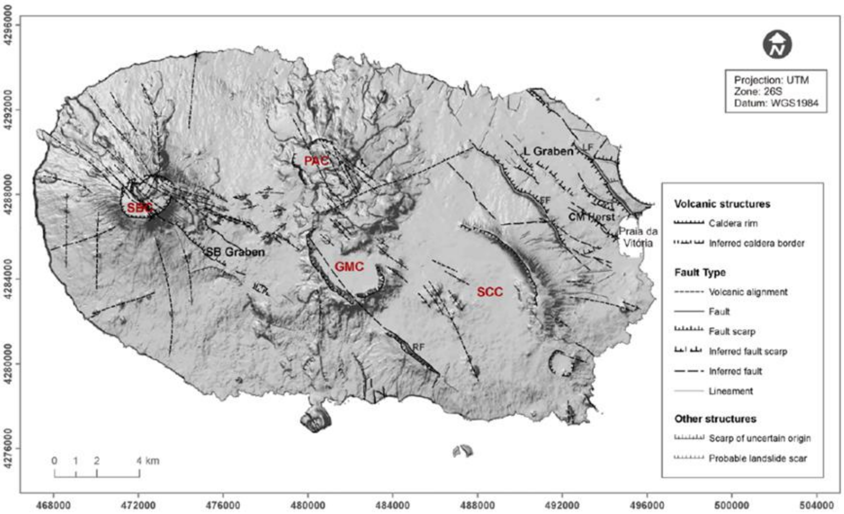

Figure 2.5 - Location of the 4 central volcanoes on Terceira Island, identified by red colour. SBC - Santa Bárbara caldera; PAC - Pico Alto caldera; GM - Guilherme Moniz caldera; SCC - Serra do Cume caldera, *i.e.*, Cinco Picos caldera (in Madeira *et al.*, 2015).

The recent eruptive history of this island is defined by the last 23 ka to 20 ka. Around this time, two extensive ignimbrites had erupted from Santa Bárbara and Pico Alto volcanoes, which covered a large part of the island, thus forming an important stratigraphic reference horizon demarcated as the base of the most recent volcanic group, i.e., Upper Terceira Group (UTG) (Self, 1976). Therefore, during the last 23 ka, at least 116 distinct eruptions of several styles have released a diversified range of volcanic products, namely (1) trachytic lava effusions, producing coulees and domes, (2) sub-Plinian explosive trachytic eruptions, producing pumice fall deposits, (3) trachytic pyroclastic-flow eruptions, forming ignimbrites, as well as (4) strombolian basaltic eruptions, originating scoria cones, scoria fall deposits and lava flows (Self, 1974, 1982; Pimentel, 2015).

Undoubtedly, trachytic lavas, especially domes and coulees, were the most predominant of these volcanic products from Pico Alto and Santa Bárbara volcanoes. Moreover, these products are unique characteristic of Terceira Island when compared to the other Atlantic ones (Pimentel, 2006). They resulted from effusive volcanism or of reduced explosivity, that is common preceded by sub-Plinian eruptions of lower explosivity than those which occur in other Atlantic islands (Self, 1976).

During the extrusion of lavas, the trachytic type tends to accumulate around the emission centre. Hence, depending on the conditions, they might (1) originate domes, or (2) form coulees, if they sediment and flow along greater slopes of the terrain forming (Pimentel, 2006). Basaltic activity is almost exclusive at the Fissure zone (Self, 1976; Madeira, 2005; Zanon and Pimentel, 2015).

There are no known dates between 2 ka and 18 ka. On the last 2 ka, there have been at least 21 eruptions (Self, 1974). Historically, a basaltic eruption with pyroclasts emission had occurred on a central part of the island of the Fissure Zone, in 1761. Furthermore, on Serreta submarine crest, offshore Santa Bárbara volcano, in 1867 a volcanic event was recorded, and more recently another one in the same area was registered between 1998-2001 (Gaspar *et al*., 2003; Pimentel, 2006).

2.2.2.1. Pico Alto volcano

Located on the N sector of Terceira Island, Pico Alto is an active central volcano with a caldera nearly filled by an important cluster of trachytic domes and coulees. Moreover, several lava extrusions of trachytic character are dispersed along its northern and north-eastern flanks (Self, 1976). However, the eruptive products from this volcano seem to differ from the pattern of fissure-controlled eruptions, in contrast to Santa Bárbara volcano (Self, 1974). These kinds of eruption-generated evolved products are clearly dominant, showing that Pico Alto volcano has been the stage of several violent eruptive events (Pimentel, 2015). Contemporaneously with Santa Bárbara volcano, Pico Alto volcano grew on the northern flank of the current extinct Guilherme Moniz volcano and may be an exclusive type of parasitic, trachytic volcano complete with its own caldera (Self, 1974).

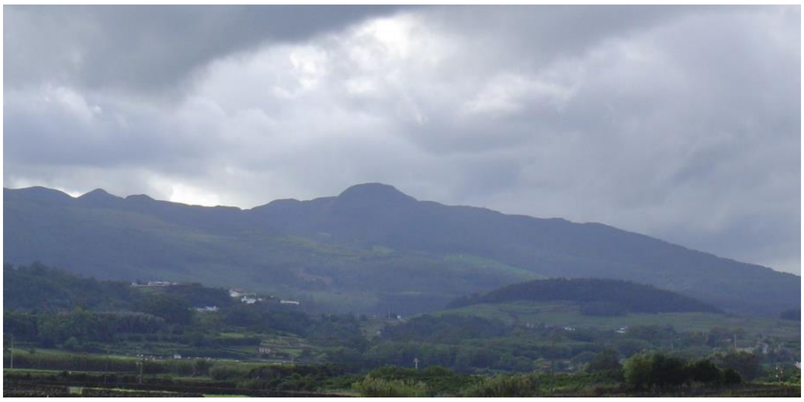

Photo 2.4 - Pico Alto volcano (photo courtesy of Adriano Pimentel).

2.2.2.1.1. Tectonics

In this volcanic system it is possible to distinguish two main alignments, namely (1) of general NW-SE and NNW-SSE trend, as the Biscoito Rachado alignment, and (2) of general ENE-WSW orientation (Pimentel, 2006).

2.2.2.1.2. Eruptive history

On the last 23 ka, both Pico Alto and Santa Bárbara have exhibited eruptions characterised by the following phases, starting with sub-Plinian blasts that ejected vesiculated magma of trachytic composition from a vent, succeeded after a short period by effusion of lava of similar composition from the same or a nearby vent (Self, 1974).

The occurrence of basaltic activity on this volcanic system is practically unlikely, since no basalts have been found in its subaerial edifice (Self, 1974, 1982).

Despite the non-existence of any historical eruption related to Pico Alto volcano, the last eruptions were estimated of about 1000 years B.P. or less (Self, 1982; Calvert *et al.*, 2006).

2.2.2.2. Santa Bárbara volcano

The north-western end of Terceira Island is dominated by Santa Bárbara volcano, the youngest central volcanic system of this island (Self, 1976). Its conical-shape edifice is truncated by two nested calderas filled with lava domes and coulees. Its slopes are marked by several structurally controlled alignments of (1) lava domes and coulees; (2) trachytic lava extrusions; and (3) several dispersed adventive basalt scoria cones (Self, 1976; Pimentel, 2006).

Photo 2.5 - Santa Bárbara volcano (photo courtesy of Adriano Pimentel).

2.2.2.2.1. Tectonics

The distribution of domes and coulees from the outer slopes of Santa Bárbara volcano suggests the existence of a tectonic structure control expressed by alignments of general trend WNW-ESE to NW-SE. Furthermore, it is possible to recognize some N-S-orientated alignments, like Pico Rachado alignment (Pimentel, 2006).

2.2.2.2.2. Eruptive history

Santa Bárbara volcano was firstly a large, basaltic stratovolcano before its caldera collapse and the beginning of trachytic eruptions. Such as Pico Alto volcano, eruptions from Santa Bárbara volcano during the last 23 ka have typically started with sub-Plinian blasts, ejecting vesiculated magma of trachytic composition from a vent, followed by lava effusion of similar composition from the same or a nearby vent, after a short period (Self, 1974). Its fissure controlled eruptive sites are largely distributed on the N, NW, and E slopes, as well inside its caldera (Self, 1974; Pimentel, 2006).

It is difficult to certainly know the absolute ages for the most recent events from this volcano. Nevertheless, Self (1974) has characterized its youngest pumice fall deposit as member H, formed by an explosive phase that was followed by the trachytic coulee of Pico do Carneiro extrusion. It is known that the age of member G, from other explosive eruption just before member H, is younger than 2040 years BP (Self, 1974).

2.2.3. Faial Island

Faial Island is formed by 4 distinct geomorphological regions, specifically (1) Pedro Miguel Graben, (2) Central volcano, (3) Horta Platform, and (4) Capelo Peninsula (Madeira, 1998). These regions roughly overlap respectively with the spatial expression of the 4 volcanic systems that have originated the current edifice of Faial Island, in particular the central volcanoes of (1) Ribeirinha and (2) Caldeira, which is represented on Figure 2.6, and the basaltic fissural systems of (3) Horta Plataform and (4) Capelo Peninsula (Serralheiro *et al*., 1989; Pacheco, 2001; Pacheco *et al.*, 2012). However, Ribeirinha, a shield volcano located on the north-eastern part of the island, is the only one of the 4 volcanic systems considered as inactive. On the western flank of Ribeirinha volcano sits Caldeira volcano, the current active central volcano of Faial (Madeira *et al*., 2015).

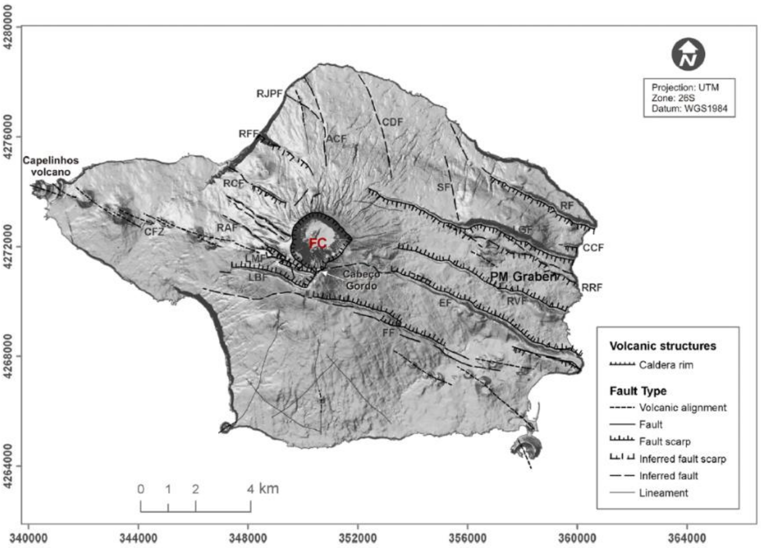

Figure 2.6. - Location of the only active central volcano on Faial Island, identified by red colour. FC - Faial caldera, *i.e.*, Caldeira volcano (in Madeira *et al*., 2015).

The volcanic systems of (1) Capelo and (2) Caldeira are the ones with higher probability of producing future eruptive events, such as (1) basaltic effusive and strombolian eruptions, and (2) explosive trachytic activity as well as hydromagmatic explosions, respectively (Pacheco, 2001).

Since settlement, 3 eruptions occurred on this island, 2 of them on Capelo Peninsula, related to Capelo fault, namely (1) an eruption with intense effusive activity and some strombolian phases at Cabeço do Fogo, in 1672-73, and (2) the well-known Capelinhos eruption occurred between 1957 and 1958 (Machado, 1959b; Madeira, 1998; Pacheco, 2001). At last, in 1958, contemporaneously to Capelinhos event, Caldeira volcano had a phreatic explosion centred on its caldera (Machado, 1959b).

2.2.3.1. Caldeira volcano

Occupying the central part of Faial Island, Caldeira volcano is a polygenetic volcanic edifice with a roughly circular truncated caldera at the top. Inside caldera two volcanic forms can be found, namely a dome, called domo do Altar, and a small pyroclastic cone with around 40 m height. Its volcanic products range from basaltic to trachytic nature (Pacheco, 2001).

Photo 2.6 - Caldeira volcano (left) (photo courtesy of Adriano Pimentel) and its caldera (right) (photo courtesy of Nicolau Wallenstein).

2.2.3.1.1. Tectonics

Several tectonic systems of WNW-ESE, NNW-SSE to NW-SE, and NE-SW orientation converge on the central region of Caldeira volcano, which have contributed to its installation on that area. Also, it is possible to identify some radial faults, especially expressed where adventive cones from Caldera volcano were built upon them, as well as concentric structures concordant with the caldera's edge, represented by lineaments with weak morphological expression (Madeira, 1998).

2.2.3.1.2. Eruptive history

Around 16 ka BP, the eruptive style of Caldeira volcano has change from a medium or low basaltic explosive activity to a dominant explosive activity of trachytic character, which marked the division between the products from the recent eruptive activity and from the older events. The products from the last 16 ka belong to the Upper Group of Cedros Volcanic Complex, thus emitted by at least 14 eruptions at Caldeira Volcano. One of them is correlated with the opening of the actual caldera, about 1200 years BP. It was an eruption that produced the most important pyroclastic flows and surges of this period (Pacheco, 2001; Pimentel *et al.*, 2015), beside other 11 trachytic explosive events of sub-Plinian type that were also originated within the crater (Pacheco, 2001).

All in all, the eruptive events from Caldeira volcano of this last 16 ka were strictly magmatic (62%) and strictly hydromagmatic (38 %). However, some have shown both magmatic and hydromagmatic phases, being the later ones associated to initial or final stages of the eruptions (Pacheco, 2001).

Furthermore, apart from the almost exclusively explosive activity of trachytic nature, there was an event that formed a scoria cone inside caldera, which is considered as the most recent deposit in the eruptive sequence (Pacheco, 2001).

Nevertheless, the most recent eruption on Caldeira volcano was historic and characterized by a phreatic explosion inside its caldera in 1958 (Machado, 1959b). This eruption produced a thin layer of very fine light ash deposited in the bottom of the caldera and on the ESE flank of the volcano. After that, a fumarolic field had emerged inside the caldera with several vapour steams and mud jets. This eruption is believed to be a consequence of the violent seismic crises of 12-13 May 1958, associated with the ongoing volcanic activity of Capelinhos at that time.

Regarding all this, sub-Plinian or Plinian events are the most probable type of volcanism to occur within Caldeira volcano (Pacheco, 2001).

2.2.4. Pico Island

Pico Island is composed of 3 main volcanic complexes, specifically (1) Topo-Lajes Volcanic Complex, where belongs the older central shield volcano of Topo; (2) São Roque-Piedade Volcanic Complex, where the volcanic fissure system of Planalto da Achada is present, characterised by basaltic activity; and (3) Montanha Volcanic Complex, with the dominance of Montanha do Pico volcano (Nunes, 1999), which is identified on Figure 2.7.

The volcanic eruptions on this island have been of Hawaiian to Strombolian type, particularly with lava flows effusions and low explosivity associated. According with the available data, it is estimate that 14 eruptions have occurred in the last 1 ka, and more than 35 eruptions in the last 2 ka (Nunes, 1999).

In historical times, 4 eruptions have already occurred on this island in the following years: (1) 1562-64 (Praínha) in São Roque Volcanic Complex; (2) 1718 (Santa Luzia and São João) and (3) 1720 (Silveira), associated with Pico Mountain volcano; and (4) 1963, at NW offshore. All of them resulted from Hawaiian to Strombolian events, showing low to moderate explosivity, with a clear dominance of effusive phases, and the most recent eruption was of Surtseyan style (Nunes, 1999; Madeira, 2005; Madeira *et al.*, 2015).

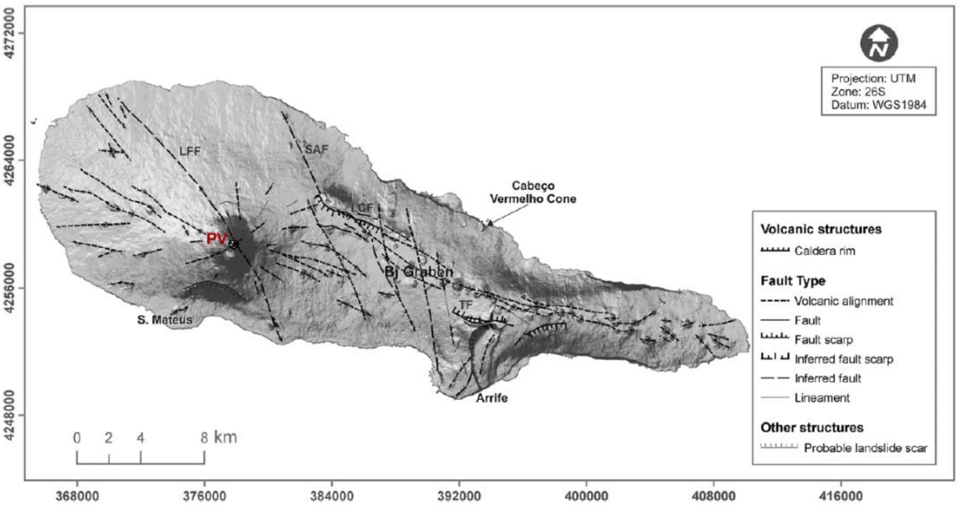

Figure 2.7 - Location of Pico Mountain volcano on Pico Island, identified by red colour. PV - Pico volcano (in Madeira *et al.*, 2015).

2.2.4.1. Montanha do Pico volcano

On the western part of Pico Island emerges Montanha do Pico volcano, a central basaltic volcano with a maximum altitude of 2351 m, the highest point of Portugal. At the top, its semi-circular crater is covered by *pahoehoe* lavas emerging from a lava cone of 125 m high, well-known as Piquinho (Machado, 1959a; Nunes, 1999). Also, several adventive scoria or spatter cones are dispersed on its flanks, aligned at radial structures (Madeira, 1998).

Montanha do Pico is the only one of the Azorean central volcanoes that has not yet reached the stage of caldera forming, typically of eruptive phases of acid magmas (Madeira, 2007), once this stratovolcano is a juvenile volcanic edifice whose magma is still of mafic nature. Hence, explosive activity of trachytic nature is unlikely to occur.

Photo 2.7 - Montanha do Pico volcano (photo courtesy of Nicolau Wallenstein).

2.2.4.1.1. Tectonics

Montanha do Pico volcano comprises an important set of radial fractures, whose development could be dependent on the main tectonic directions, WNW-ESE and NNW-SSE (Madeira, 1998).

The WNW-ESE alignments are more numerous and reach greater extension on its western and south-eastern flanks, being almost entirely expressed by volcanic alignments, cones, craters, and eruptive vents and fissures. Also, the NNW-SSE trending fault is represented by several volcanic alignments (Nunes, 1999).

The radial structures of this volcano show many trends, as the WSW-ENE trending fracture that cuts the bottom of the crater and continues to the outside (Madeira, 1998).

2.2.4.1.2. Eruptive history

According with the work of Nunes (1999), the most recent history of Montanha do Pico volcano can be divided into three phases. The first and second stage comprise the formation of the older crater at 2050 m a.s.l. and the present crater, respectively. The last one was dated around 1700 years B.P. The third stage included eruptive events from Piquinho lava cone, as well as from an eruptive fissure of WSW-ENE trend on the crater. The eruption of Piquinho was dated about 1300 years B.P. Furthermore, several eruptions had occurred on its flanks mainly from adventive cones on the western an easter slopes.

At least 22 volcanic episodes took place in the last 1.5 ka. The eruptions were of Hawaiian and Strombolian character, mostly effusive of low magnitude (VEI < 1) and centred on the top or along fissures, mainly on the western and eastern flanks. Therefore, the main basaltic products from this volcano are scoria and spatter cones, as well as *pahoehoe* lava flows (Nunes, 1999).

The historical eruptions of 1718 and 1720 are the most recent events associated with Montanha do Pico volcano. With VEI 2, those eruptions had predominant effusive phases (Nunes, 1999). The eruption of 1718 had at least 3 vents, the first one started on the northern flank of Montanha do Pico volcano, the second vent on the southern flank, and the third one was offshore on further south (Madeira, 2005), all of them along a general NNW-SSE orientated fault (Madeira, 1998). The eruption of 1720 took place on the southern slope of Montanha do Pico volcano and was localised on a WNW-ESE trending fault marked by an alignment of craters. It was a Hawaiian/Strombolian event that produced *aa* lava flows and great amount of ash. Lasting 5 months, it is believed that 16 vents had opened (Madeira, 2005).

A study by Capello *et al*. (2015) has showed that the most probable area to host new eruptions is along a WNW-ESE trend centred on the volcano. Consequently, the areas with the highest susceptibility to be affected by future lava flows are the ones near the coasts, on the NW and SE flanks of the central volcano.

CHAPTER 3. SITE SURVEY METHODOLOGY

3.1. Introduction to site surveys

Site surveys are a fundamental key before the establishment of any infrasound array, even if it is permanent or portable. They aim to find locations with the best overall conditions, most importantly with the lowest possible background noise, to detect infrasound signals of interest with good quality, above noise, thus being possible to locate and characterise its sources (Hedlin *et al*., 2002, 2003b). Therefore, to evaluate the suitability of a site to host an infrasound station is essential to follow three main general procedures, namely (1) to do a preliminary sites' selection, regarding several constraints and their needed requirements, (2) to assess in *situ* the pre-selected sites, and then (3) to field survey the chosen sites and finally select the one with best signal-to-noise ratio.

On the preliminary sites' selection, by knowing the most important constraints (described on subchapter **3.2.2.1. *Constraints and their requirements***) that affect the detection of infrasound signals, their respective requirements are pre-evaluated in the lab using GIS software, namely Google Earth Pro® and QGIS®. While choosing a site, if we identify parameters such as dense forests, good accessibility, good available infrastructures, and low potential background noise sources in one specific location, it would be a strong candidate for a field survey.

Secondly, the potential sites are checked on the terrain. Thus, the locations showing the best suitable features will be field surveyed.

At last, during field surveys we measure noise levels using 4 infrasound sensors disposed on an array, for a great evaluation. Nevertheless, this kind of test requires a minimum of 2 sensors, but ideally 3 sensors should be used. Then data are processed, and their spectral analysis will verify which site shows the best signal-to-noise ratio, *i.e.*, the prime location among the others to deploy an infrasound station.

3.2. Monitoring volcanic eruptions in the Azores Islands

Regarding the objectives of the present research study, a methodology was applied to survey sites in the vicinities of the seven central volcanoes of the Azores Islands (see chapter **2. *The Azores Islands***) such is the importance to have an infrasound monitoring network prompt to be activated in case of any eminent volcanic eruption, as was the case of the 2022 São Jorge volcanic unrest (see chapter **4. *São Jorge Island volcanic unrest - Study case***).

Forasmuch as the infrasound signals of interest for this monitoring purpose are volcanic and seismoacoustic, the survey methodology herein implemented has involved 4 main steps, specifically by order (1) the definition of hypothetic eruptive scenarios for each one of the active central volcanoes of the Azorean archipelago, (2) a preliminary selection of ideal sites around each volcanic scenario where an infrasound site survey can be conducted with optimal conditions, also simulating the deployment of a theoretical infrasound array, using GIS®, (3) the assessment *in situ* of those pre-selected sites, checking the real features of each location and if it would be possible to install an infrasound mobile station in case of a favourable field survey, and finally (4) the field survey itself, using an array of 4 infrasound sensors configurated within a specific geometry, to collect noise data to be analysed in the office whose evaluation will define the finest sites to deploy infrasound mobile stations around each central volcano.

3.2.1. Eruptive scenarios

Several eruptive scenarios were established for the 7 active central volcanoes in the Azores Islands, considering (1) the main bibliography, especially about their tectonics and eruptive history, and thus (2) signalizing probable eruptive emission centres on QGIS®. It is important to notice that this was just a hypothetically simulation of possible eruptive emission centres and an eruptive model for each case was not implemented.

Therefore, the first stage of this methodological step consisted in researching on the bibliography the most frequent types of volcanic episodes on the last 10 ka as well as the respective tectonic fault systems where they have occurred (see subchapter **2.2. *Active central volcanoes***). Soon after, the existing maps of main tectonic and volcanic structures (e.g., Carmo *et al*., 2015; Madeira *et al*., 2015) were analysed and then a draft for eruptive scenarios was made to further discussion.

Afterwards, the existing shapefiles of the tectonic faults for each island were upload to a QGIS® project, where also the accepted eruptive emission centres were marked. Each case was described and justified hereafter and the maps of their locations were also integrated in Annex A.

In the following subchapters, each eruptive scenario was identified with an ID name and characterised by its location associated with tectonic faults intersection and its type of predictable eruptive activity scenarios.

3.2.1.1. Sete Cidades volcano (São Miguel Island)

Despite no historical on land eruptions have been recorded in Sete Cidades volcano since the settlement, there were considered two different contemporaneous eruptive scenarios, one of sub-Plinian type (SC1) and the other of Strombolian type (SC2).

SC1 is an event equivalent to the last eruption of this volcano that formed Caldeira Seca tuff ring around 700 years BP (Cole *et al*., 2008; Queiroz *et al*., 2008). It is located inside the caldera near the intersection of an arcuated fault (inferred volcanic alignment) with the regional NW-SE trend (inferred fault) (Queiroz, 1997; Carmo *et al*., 2015) (see Figure 3.1 and Annex A.1.1). The eruptive activity is characterized by a trachytic explosive sub-Plinian eruption of VEI 4 (Newhall and Self, 1982), essentially hydromagmatic with sporadic short magmatic pulses and an oscillating convective column with high probability of collapse. A distinctive range of volcanic products may be formed such as tephra and lapilli fallout, ballistic projectiles and, in the worst assumption, pyroclastic density currents (PDCs) that may get out of the caldera and extend down the eastern and north-eastern flank (Queiroz et *al*., 2008; Cole *et al*., 2008).

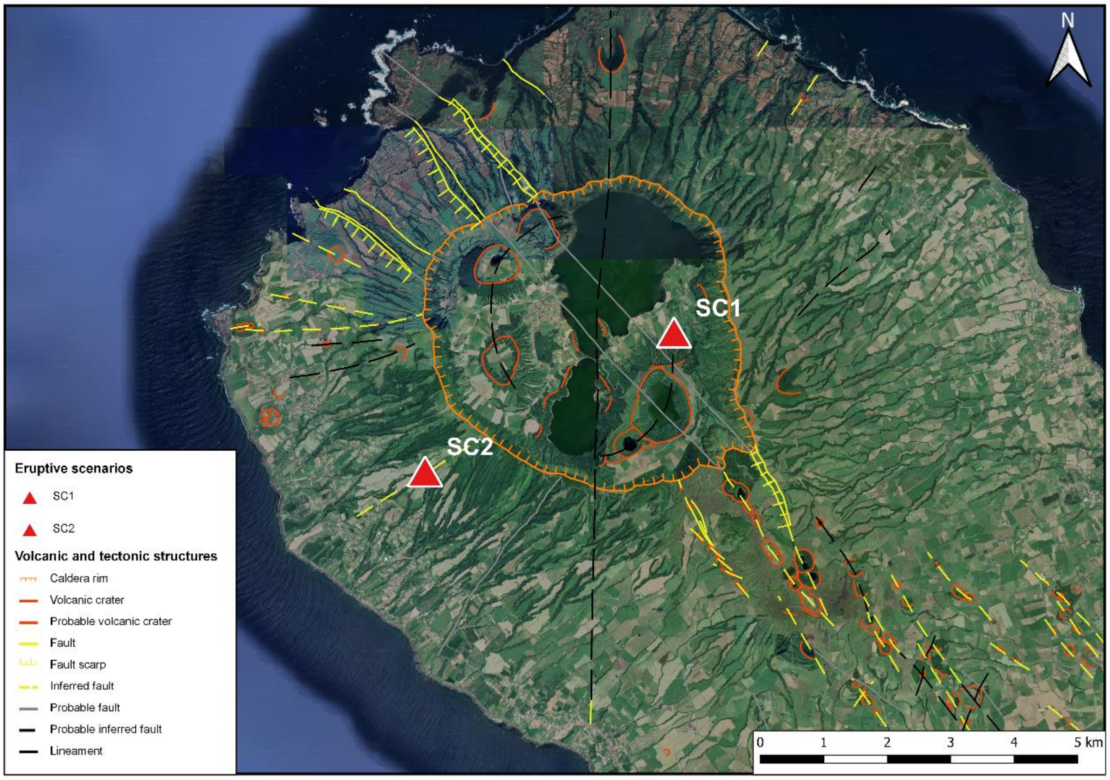

Figure 3.1 - Eruptive scenarios SC1 and SC2, Sete Cidades volcano. Volcanic and tectonic structures are from Carmo (2013), modified by CIVISA.

SC2 is an event comparable to the last flank eruption occurred on this volcano that had formed Pico das Camarinhas scoria cone and Ponta da Ferraria lava delta around 800 years BP (Queiroz *et al.*, 2008). It is located on the outer southwestern flank of the volcano at a volcanic alignment trending NE-SW (Queiroz *et al.*, 2015; Carmo *et al.*, 2015) (see Figure 3.1 and Annex A.1.1). The eruptive activity is characterized by a basaltic Strombolian eruption of VEI 2 (Newhall and Self, 1982), with moderate explosivity, producing basaltic scoria and lava flows towards the sea at south, with high probability of forming a lava delta(Queiroz *et al.*, 2008).

3.2.1.2. Fogo volcano (São Miguel Island)

For Fogo volcano there were considered two different contemporaneous eruptive scenarios, one of sub-Plinian type (FO1) and the other of Hawaiian type (FO2), in a similar way to what had happened in 1563 where an intracaldera sub-Plinian eruptive event was succeeded 4 days later by a Hawaiian eruption on the northern flank.

In our case FO1 is would be located outside the summit caldera and have a VEI equivalent to Fogo B eruption that formed a crater cutting Mata do Botelho trachytic dome around 3 ka BP (Wallenstein, 1999), although it would start by an important hydromagmatic activity. It would be located at the intersection of an E-W orientated fault with the continuity of a NE-SW inferred fault (Carmo *et al.*, 2015; Wallenstein *et al.*, 2015) (see Figure 3.2 and Annex A.2.1) The eruptive activity is characterized by a trachytic explosive sub-Plinian eruption of VEI 3-43 (Newhall and Self, 1982), with magmatic character and an oscillating convective column with high probability of collapse. A distinctive range of volcanic products may be formed such as tephra and lapilli fallout, ballistic projectiles and, in the worst assumption, pyroclastic density currents (PDCs) (Wallenstein, 1999).

FO2 is an event comparable to the historical eruption in 1563 which occurred on the northern flank of Fogo volcano at Pico do Sapateiro, forming lava flows that reach the sea at north (Wallenstein, 1999, Wallenstein *et al.*, 1998, 2015). It is located on the north-western flank of the volcano near the intersection of two lineaments trending NE-SW and NW-SE (Wallenstein *et al.*, 2015; Carmo *et al.*, 2015) (see Figure 3.2 and Annex A.2.1). The eruptive activity is characterized by a basaltic Hawaiian eruption of VEI 2 (Newhall and Self, 1982), with moderate explosivity in the beginning, producing basaltic scoria and lava flows towards the sea at north, with high probability of forming a lava delta (Wallenstein *et al.*, 2015).

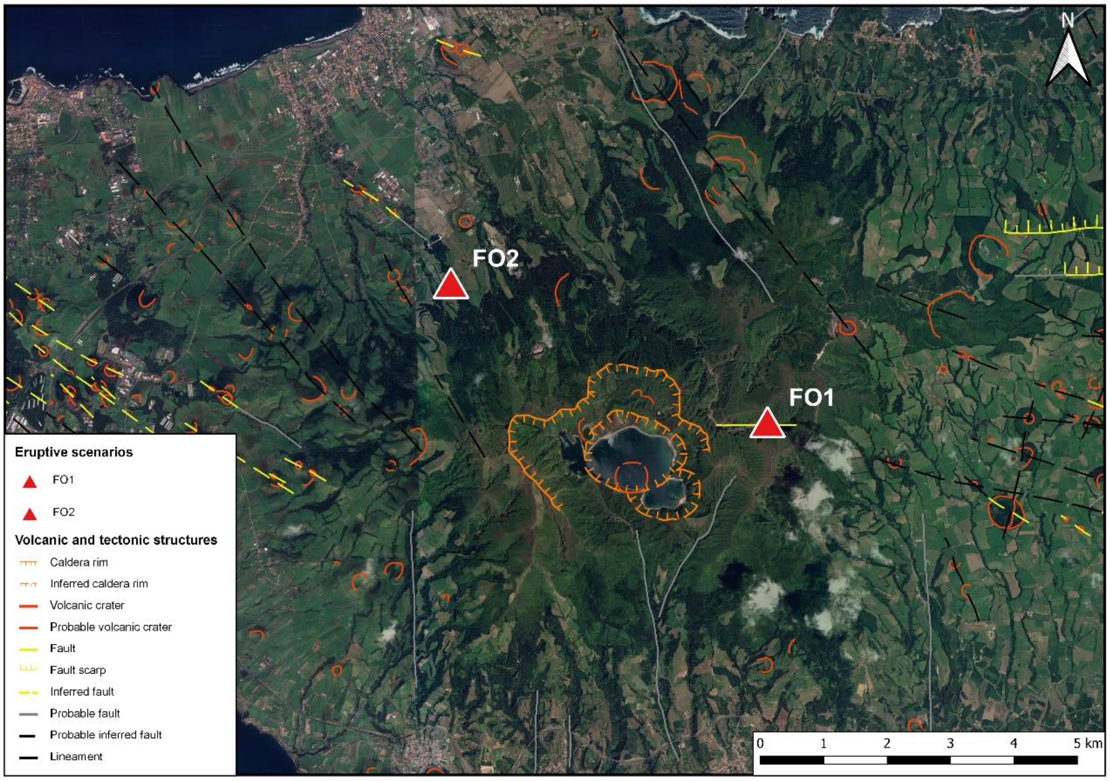

Figure 3.2 - Eruptive scenarios FO1 and FO2, Fogo volcano. Volcanic and tectonic structures are from Carmo (2013), modified by CIVISA.

3.2.1.3. Furnas volcano (São Miguel Island)

Once there is no evidence of basaltic eruptions on Furnas volcano during the last 5 ka, it was merely considered one eruptive scenario (FU1), in contrast to Sete Cidades and Fogo volcanoes. Nevertheless, FU1 shows a very complex and irregular trend.

FU1 is an event equivalent to the historical eruption of Furnas volcano in 1630 (Cole *et al.*, 1995). It is located inside the inner caldera complex at the intersection of a NE-SW orientated inferred volcanic alignment (Carmo *et al.*, 2015) with an inferred fault of WNW-ESE trend (Guest *et al.*, 1999), precisely where the fumarolic field of Furnas village is located (see Figure 3.3 and Annex A.3.1). The eruptive activity is characterized by two distinctive phases. On the first phase, the eruption is pulsatory, oscillating between trachytic explosive, with strong magmatic character, sub-Plinian episodes of VEI 4 (Newhall and Self, 1982) and phreatomagmatic stages, generating an oscillating eruptive column with high probability of collapse. This phase may finish with a sustained magmatic episode. Then, the second and last phase follows up the previous explosive activity, consisting of an entirely magmatic effusive phase (VEI 2) with a trachytic lava dome formation. Additionally, distinctive range of volcanic products may be generated during the explosive phase, such as tephra and lapilli fallout, ballistic projectiles and, in the worst assumption, pyroclastic density currents (PDCs) (Cole *et al.*, 1995).

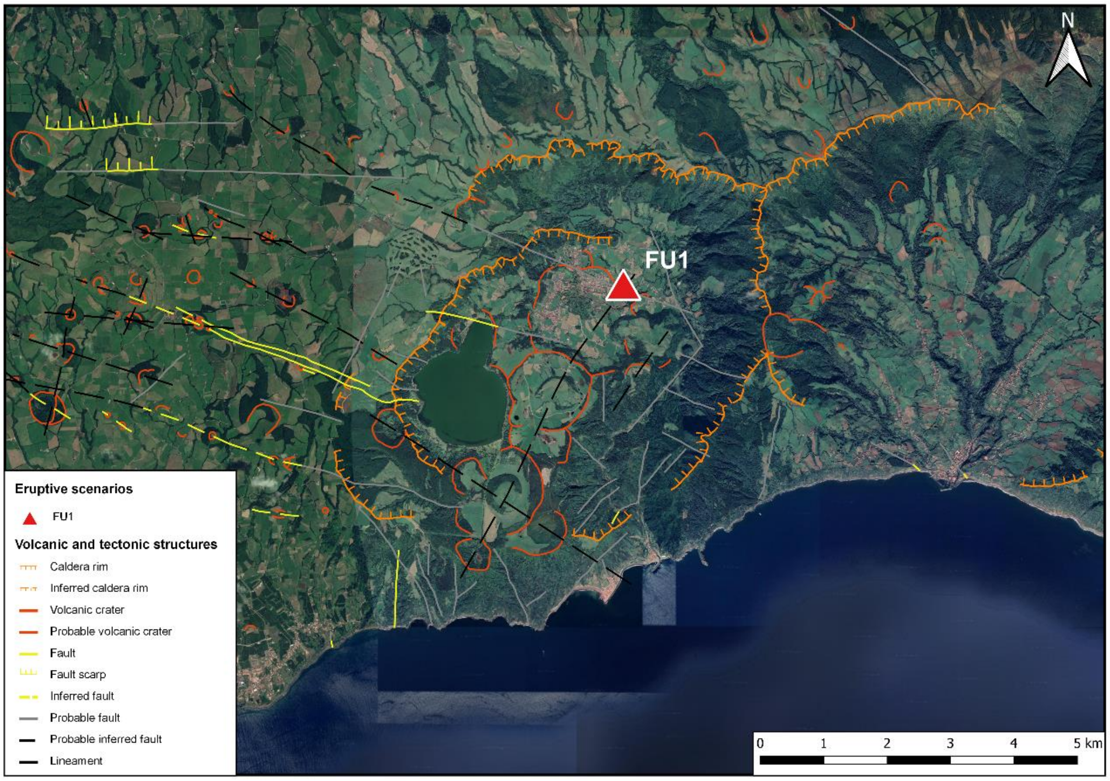

Figure 3.3 - Eruptive scenario FU1, Furnas volcano. Volcanic and tectonic structures are from Carmo (2013), modified by CIVISA.

3.2.1.4. Pico Alto volcano (Terceira Island)

Once basaltic activity is unlikely to occur at Pico Alto volcano, it was merely considered one eruptive scenario (PA1) characterized by explosive and effusive stages.

PA1 is an event equivalent to the most common type of eruption at Pico Alto volcano during the last 23 ka (Self, 1974). It is located at NW outside the northern border of Pico Alto caldera at an NW-SE orientated volcanic alignment (Madeira *et al.*, 2015; Pimentel, 2006) (see Figure 3.4 and Annex A.4.1). The eruptive activity is characterized by two distinctive phases. The eruption starts with lower explosivity sub-Plinian blasts of VEI 3 (Newhall and Self, 1982), forming a sustained eruptive column and ejecting vesiculated magma of trachytic composition as well as pumice fallout (Self, 1974, 1976). Continuously, the eruptive event finalises with trachytic lava effusions of VEI 2 from the same or a nearby vent. The extrusions tend to accumulate around the emission centre and might originate coulees and/or domes (Self, 1974, 1976; Pimentel, 2006).

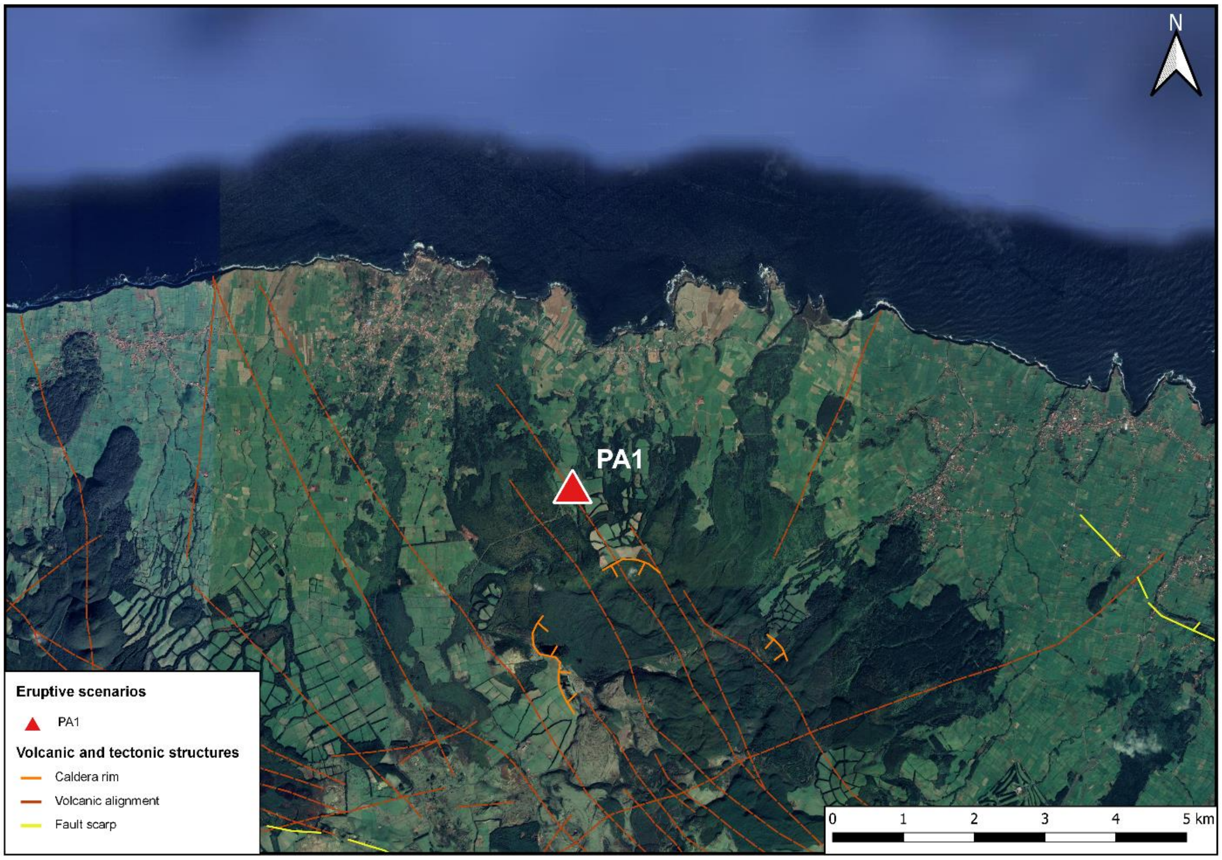

Figure 3.4 - Eruptive scenario PA1, Pico Alto volcano. Volcanic and tectonic structures are from Madeira (2005), modified by CIVISA.

3.2.1.5. Santa Bárbara volcano (Terceira Island)

Basaltic activity has not been so much frequent at Santa Bárbara volcano. It was only considered one eruptive scenario (SB1) characterized by explosive and effusive stages.

SB1 is an event equivalent to the most common type of eruption at Santa Bárbara volcano during the last 23 ka (Self, 1974). It is located on the volcano's NW flank at a volcanic alignment trending NW-SE (Madeira *et al.*, 2015; Pimentel, 2006) (see Figure 3.5 and Annex A.5.1) The eruptive activity is characterized by two distinctive phases. The eruption starts with lower explosivity sub-Plinian blasts of VEI 3 (Newhall and Self, 1982), forming a sustained eruptive column and ejecting vesiculated magma of trachytic composition as well as pumice fallout (Self, 1974, 1976). Continuously, the eruptive event finalises with trachytic lava effusions of VEI 2 from the same or a nearby vent. The extrusions tend to accumulate around the emission centre and might originate coulees and/or domes (Self, 1974, 1976; Pimentel, 2006).

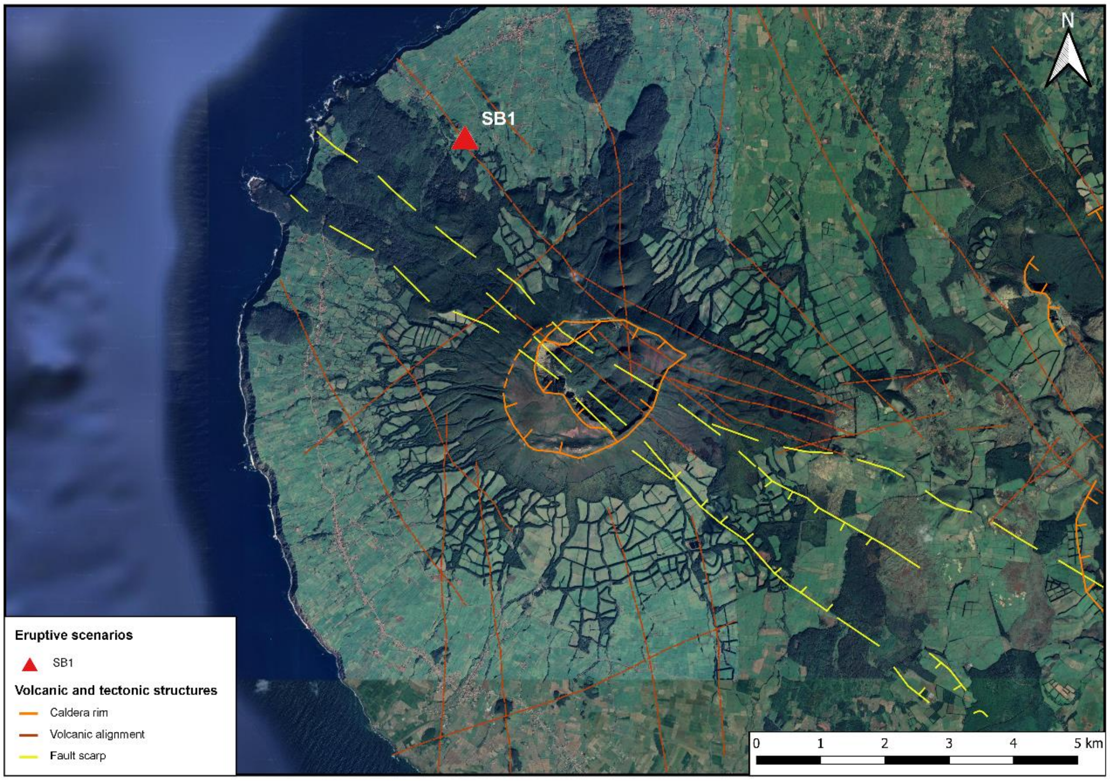

Figure 3.5 - Eruptive scenario SB1, Santa Bárbara volcano. Volcanic and tectonic structures are from Madeira (2005), modified by CIVISA.

3.2.1.6. Caldeira volcano (Faial Island)

Once Caldeira volcano has mostly shown explosive eruptive activity on the last 16 ka, it was merely considered one eruptive scenario (CA1) of trachytic explosive nature.

CA1 is an event equivalent to the most common type of eruption at Caldeira volcano during the last 16 ka (Pacheco, 2001). It is centred inside the caldera (see Figure 3.6 and Annex A.6.1). The eruptive activity is characterized by a trachytic explosive sub-Plinian eruption of VEI 4 (Newhall and Self, 1982), purely magmatic, forming an oscillating convective column with high probability of collapse. A distinctive range of volcanic products may be formed such as tephra and lapilli fallout, ballistic projectiles and, in the worst assumption, pyroclastic density currents (PDCs) that might be driven through tectonics structures such as Pedro Miguel Graben (Pacheco, 2001).

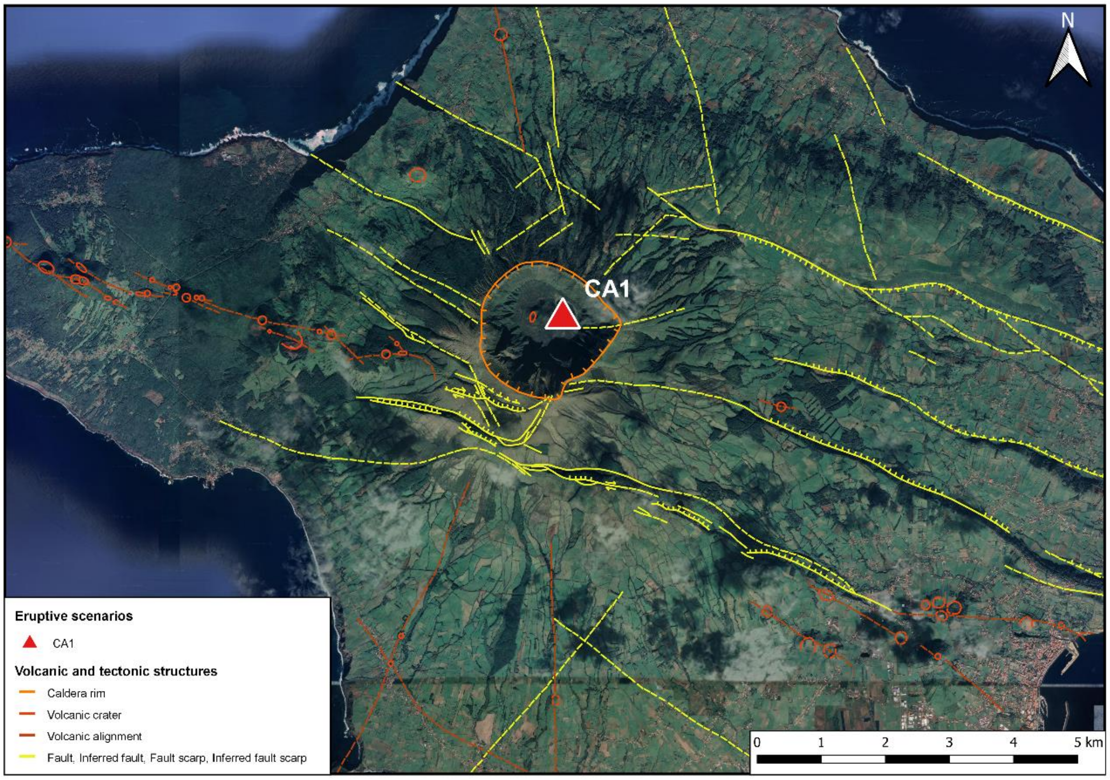

Figure 3.6- Eruptive scenario CA1, Caldeira volcano. Volcanic and tectonic structures are from Madeira (1998), modified by CIVISA.

3.2.1.7. Montanha do Pico volcano (Pico Island)

Once explosive activity of trachytic nature is unlikely to occur at Montanha do Pico volcano, it was merely considered one eruptive scenario (MP1) of basaltic effusive character.

MP1 is an event comparable to the historical eruption of Silveira in 1720, which occurred on the south-eastern flank of Montanha do Pico volcano, generating lava flows emitted from several vents (Madeira, 2005). Since Capello *et al*. (2015) mentioned that the most probable eruptive scenario to take place on this volcano is along a WNW-ESE trending fault, MP1 is located on the WNW flank of the volcano at a WNW-ESE orientated volcanic alignment (Madeira, 1998; Madeira *et al*., 2015) (see Figure 3.7 and Annex A.7.1). The eruptive activity is characterized by a basaltic Hawaiian to Strombolian eruption of VEI 2 (Newhall and Self, 1982), with *aa* lava flow effusions and low explosivity associated, producing as well basaltic scoria and great amount of tephra (Nunes, 1999; Madeira, 2005). Nevertheless, there is a possibility of other vents opening along the same fault trending, even on the ESE side. Thus, lava flows might particularly affect not only the NW flank but also the SE one (Capello *et al*., 2015).

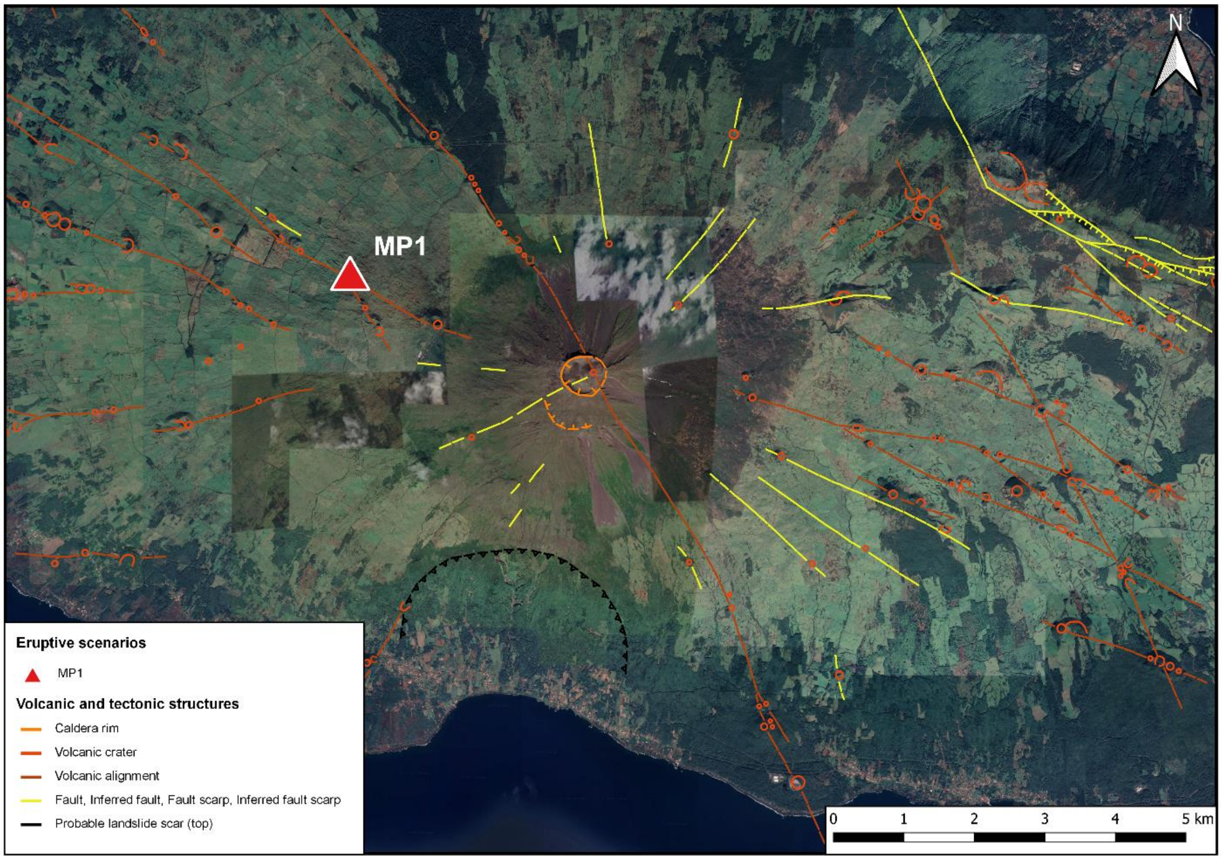

Figure 3.7- Eruptive scenario M1, Montanha do Pico volcano. Volcanic and tectonic structures are from Madeira (1998), modified by CIVISA.

3.2.2. Preliminary selection

The next step after defining the above eruptive scenarios was to pre-select sites around them that gather the best overall conditions to do an infrasound survey and where a mobile array can possibly be deployed the in future.

This preliminary selection considered the most significant constraints of a site that affect the detection of infrasound signals, namely (1) nearby sources of infrasound background noise, (2) field aspects, such as topography, size, and land cover, as well as (3) the logistics, security and environmental conditions associated. To face those constrictions, it was necessary to evaluate the respective requirements while searching for good quality locations on Google Earth Pro®, such as (1) dense forests, that are natural filters for background noise; (2) flat terrains with enough area to deploy an infrasound array or an independent sensor with its wind noise reducing system; and (3) good accessibility and available infrastructures nearby.

With this in mind, the most convenient sites for each eruptive scenario were pre-selected and a hypothetically infrasound array per each location was a designed, firstly using Google Earth Pro® and then mapped on QGIS® (see subchapter **3.2.2.2. *Pre-selected sites in the Azores Islands*).**

3.2.2.1. Constraints and their requirements

The Provisional Technical Secretariat (PTS), assisting the Preparatory Commission of the CTBTO in supervising and coordinating the provisional operation of the International Monitoring System (IMS) and the International Data Centre (IDC) in establishing a global verification regime to monitor compliance with the comprehensive ban on explosive nuclear testing, has conducted hundreds of site surveys in order to install 60 infrasound stations around the world (CTBTO, 2022). Therefore, the most consolidated existing guidelines about the essential and ideal conditions to perform an infrasound field testing are undoubtedly the procedures applied by the PTS (*e.g.*, Hedlin and Berger, 2000), which were also herein employed and described below.

3.2.2.1.1. Infrasound background noise

The influence of noise on a specific location is a major concern while surveying sites to deploy future infrasound stations, once if the noise is lower their detection capability will be much higher. Undoubtedly, the spectral properties of noise levels recorded during a survey is the most valuable weighting factor on the site's final decision as well as on the configuration of the array geometry (Hedlin *et al*., 2002; Marty, 2019).

Accordingly with the survey guidelines from PTS, a good site is characterised by low infrasonic noise between 0.02 and 4 Hz. (*e.g.*, Hedlin and Berger, 2000). Therefore, the first step of a survey should be to select sites far enough from background noise sources, natural or man-made, such as waterfalls, rivers, coastal areas (surf noise), airports, industrial activities, major highways, among others (see subchapter **1.6. *Infrasound background noise***). Nevertheless, wind is by far the most critical noise source (see subchapter **1.6.1*. Wind-generated infrasound noise***). To face its effects, the sites to survey should be in areas with little wind as possible, also protected from local wind turbulence, which it will enhance the detection of signals with low signal-to-noise ratios (SNRs) (Marty, 2019) (see subchapter **1.7.3.1. *Signal-to-Noise Ratio (SNR) and detection capability***). Thus, dense forests with tall trees and thick ground cover are the ideal best locations as they form a natural acoustic filtering of much more significance than the single use of a wind noise reducing system (Marty, 2019; Hedlin and Berger, 2000).

Nonetheless, it is not always possible to find an available place far enough from local noise sources, particularly on small oceanic islands (Marty, 2019), as is the case of the Azores archipelago. For instance, surf noise is inevitable here, because is not easy to find ideal sites located at least 5 km away from the coast (Hedlin and Berger, 2000), mostly because the Azorean Islands are small and narrow. But the most predominantly and impactful source of noise by far on oceanic islands is the wind, which is constant along all year, particularly in autumn and winter.

Also, in situations when it is not possible to find forest areas, small bushes come in handy to help on noise reduction (Marty, 2019).

3.2.2.1.2. Topography, area, and land cover

Topography is another relevant aspect to be considered in the process of selecting sites to survey. It is important that sensor sites do not have significant differences in altitude (*e.g.*, Hedlin *et al.*, 2002). According with the PTS (*e.g.*, Hedlin and Berger, 2000), it is required a relatively flat terrain where view to horizon is not obstructed by more than 20°. However, this is not always possible, namely on topographically rugged islands, as the case of the present research study. Furthermore, it is necessary to pay attention to the surrounding topography between the potential source and each site, due to a sort of shadow zones that might be generated by terrain morphology (see subchapters **1.3.3.3. *Infrasound phases/arrivals*** and **1.3.3.4. *Topography influence***) thus blocking the signal at some azimuths (*e.g.*, Hedlin *et al.*, 2002).

Additionally, each site must have enough space to accommodate (1) an array of 4 sensors set apart up to 150 m and connected to a digitizer with cables of 100 m (see chapter **4. *São Jorge Island volcanic unrest - study case***), or (2) and individual array element, in case of using independent sensors, including its wind noise reducing system with a diameter around 6 m (*e.g.*, Hedlin and Berger, 2000). If the main gold of the survey is to deploy an array with similar results to those of IMS infrasound stations, the aperture between individual sensors should be at least 1 km. However, this is very difficult to implement, especially on small islands facing a volcanic unrest, being urgent to deploy an array, as the case described on chapter 4. Therefore, the use of a small aperture array is the most practical solution in this type of scenario where the focus is on monitoring potential volcanic activity and seismoacoustic events, thus the aperture can be limited to some hundred metres to guarantee the detection of minimum frequency of 1 Hz.

Furthermore, land cover maps of the involved region are a great complement to the survey. If available, their classified information allows to identify areas of interest to deploy an infrasound station, such as forests and bushes, as well others to avoid, such as urban spaces, farm areas and mining/quarry industries.

3.2.2.1.3. Logistics, security, and environmental conditions

Logistics is also a significant constraint in the decision of selecting sites to survey. The availability of infrastructure nearby, such as airports, power lines and road accesses, is a fundamental requirement to evaluate the potentiality of each site in install an infrasound array with the most optimized costs as possible (Hedlin *et al*., 2002).

Also, each site should be in areas easily accessed at all times of the year, particularly with low risk of environmental hazards (Hedlin and Berger, 2000).

Where possible, it is easier as well to get permission to conduct a survey if the selected sites are of public domain. Otherwise, if the land is private, the owners might not always be willing to accept the conditions.

At last, security is always a concern. The equipment for an infrasound survey and future array is very expensive. In some areas with more criminality this is an issue to considered. In those cases, safety measurements should be applied, as the installation of electric fences, cameras, and lockers.

3.2.2.2. Pre-selected sites in the Azores Islands

Two different approaches were carried out to select sites for survey around each eruptive scenario mentioned above. Both aim to identify places according with the necessary requirements for an ideal site survey, although they rely on distinct infrasound instrumentation and array configuration as follow outlined.

The first approach intended to deploy low-cost infrasound arrays of small aperture, between 5 and 7.5 km from the source. Widely applied in several infrasound monitoring networks of **UniFI** (Università Degli Studi Firenze) around the world (Campus *et al*., 2017; iTem, 2022) these arrays are composed of 4 differential pressure transducers, built by ***iTem*** (Integrated Technologies for Environmental Monitoring - UniFI). These are individually connected to a digitizer by 100 m-electric cables. This type of array can only have an acceptable performance up to a maximum aperture of ~ 140 m between sensors. Therefore, it will just detect infrasound signals above 1 Hz. Consequently, these arrays should be displaced as near as possible to the hypothetic vents, to record higher infrasound frequencies. Also, since their cost are lower, we could risk deploying arrays such close to the source, even knowing that there is a high probability of losing them. These arrays were herein labelled as ***LC*** (low-cost).

The second approach sought to install arrays of independent infrasound sensors, between 7.5 and 15 km from the source. The idea is to deploy 4 individual array elements, as the product sell by ***SEISMOWAVE*** company called **SISTEM** (SEISMOWAVE, 2022). Each **SISTEM** is an easy-to-deploy and transportable infrasound station composed of 1 absolute infrasound sensor with an embedded digitizer with ethernet socket, a GSM/3G/4G modem, a GPS antenna and power supply, that may include solar panels. It is important to include, when possible, a weather station and a wind noise reduction system (SEISMOWAVE, 2022). Therefore, the 4 **SISTEMS** would form an infrasound array, thus its records are processed to assess infrasound detections. To get similar results to those of IMS infrasound stations, the aperture between individual sensors should be at least 1 km. Hence, these arrays can detect infrasound signals in a wider range of frequencies, recording above 0.1 Hz. As these individual array elements are very expensive, they should be displaced far enough from the theoretical eruptive sources. This type of array was herein labelled as ***IS*** (independent sensors).

In this context, it was developed a rudimental methodology using Google Earth Pro® to search for ideal locations where is possible to deploy two distinct types of infrasound mobile station for volcano monitoring. Following below, this method is mainly qualitative. Nevertheless, it is intended to transform it in the future into a quantitative and automatic interface for sites' selection in cases of eminent eruptions.

Google Earth Pro® was the tool used because of its practicality to see 3D terrain and rotate its plan views. Also, it allows to observe the influence of topography with certain back azimuths from the source and a consequent sort of shadow zones that might exist and interfere, which facilitates the selective process of sites for survey. The selected Google Earth Pro® options to visualise the area in study are illustrated bellow on Figure 3.8. The use of vertical aerial photographs with stereoscopy would be ideal but the coverage of all the areas were not available, and so the same technique was used to all the cases.

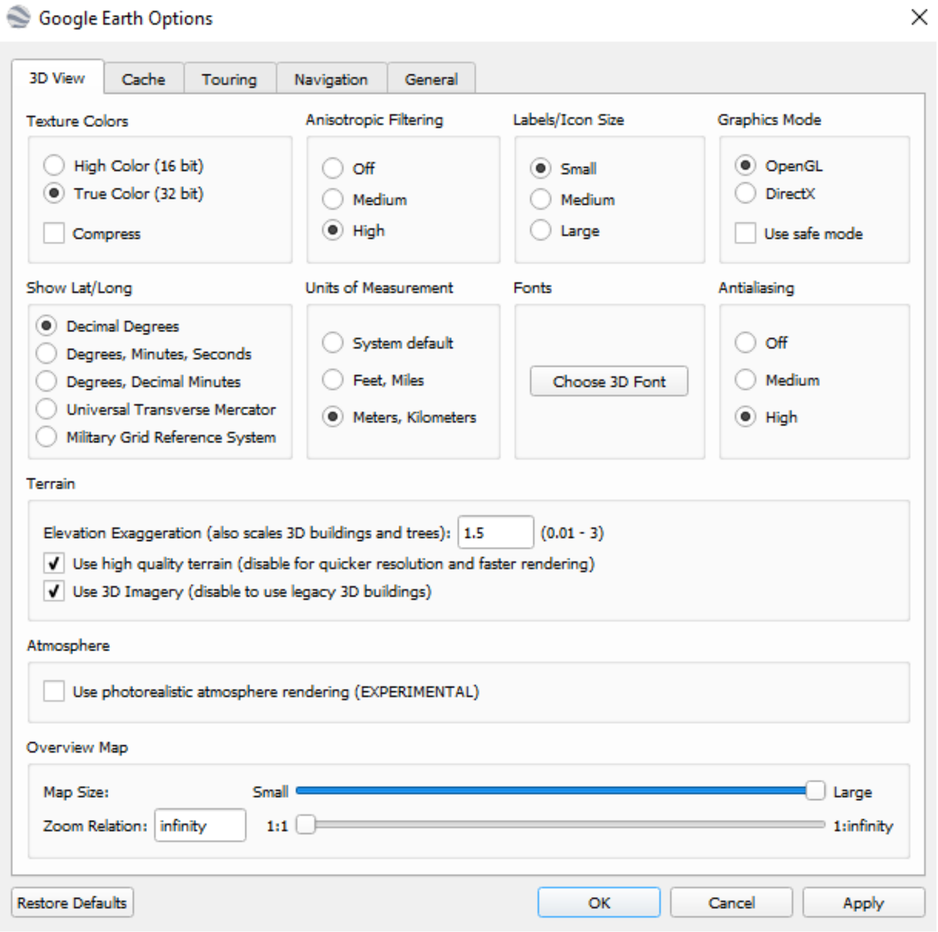

Texture Colors
○ High Color (16 bit)
● True Color (32 bit)
☐ Compress

Anisotropic Filtering
○ Off
○ Medium
● High

Labels/Icon Size
● Small
○ Medium
○ Large

Graphics Mode
● OpenGL
○ DirectX
☐ Use safe mode

Show Lat/Long
● Decimal Degrees
○ Degrees, Minutes, Seconds
○ Degrees, Decimal Minutes
○ Universal Transverse Mercator
○ Military Grid Reference System

Units of Measurement
○ System default
○ Feet, Miles
● Meters, Kilometers

Fonts

Antialiasing
○ Off
○ Medium
● High

Terrain
Elevation Exaggeration (also scales 3D buildings and trees): 1.5 (0.01 - 3)
☑ Use high quality terrain (disable for quicker resolution and faster rendering)
☑ Use 3D Imagery (disable to use legacy 3D buildings)

Atmosphere
☐ Use photorealistic atmosphere rendering (EXPERIMENTAL)

Overview Map
Map Size: Small – Large
Zoom Relation: infinity 1:1 – 1:infinity

Figure 3.8 - Options of Google Earth Pro® that were selected to visualise the area in study.

Several steps were defined in the used methodology, as follows:

Step 1

The theoretical eruptive centres already characterised in subchapter **3.2.1. *Eruptive scenarios*** and signalized on QGIS® (see Annexe A) were as well marked on Google Earth Pro®. Each one was classified by the names related to each volcano as shown on Table 3.1.

Nevertheless, it is important to mention that wind direction was not considered on the eruptive scenarios, thus the only areas excluded from the selection of sites were the ones with back azimuth equivalent to the back azimuth from IMS infrasound station IS42 on Graciosa Island to each scenario. Each back azimuth (IS42 - SOURCE) was identified on Table 3.1. This feature was laid out on the map by a straight line of blue colour (see Figure 3.9 and 3.10). This station would be considered as a supporting infrasound station to the local portable ones to be deployed in case of eminent eruptions. Therefore, there was no need to look for sites in areas of this same back azimuth.

Table 3.1 - Classification of the eruptive scenarios in the Azores Islands and respective back azimuths from IS42 station.

ID NAME	DESCRIPTION	BACK AZIMUTH IS42 - SOURCE (°)
SC1	Eruptive scenario 1 of Sete Cidades volcano (São Miguel Island)	123.4
SC2	Eruptive scenario 2 of Sete Cidades volcano (São Miguel Island)	124.4
FO1	Eruptive scenario 1 of Fogo volcano (São Miguel Island)	121.7
FO2	Eruptive scenario 2 of Fogo volcano (São Miguel Island)	121.9
FU1	Eruptive scenario 1 of Furnas volcano (São Miguel Island)	120.1
PA1	Eruptive scenario 1 of Pico Alto volcano (Terceira Island)	113.9
SB1	Eruptive scenario 1 of Santa Bárbara volcano (Terceira Island)	117.2
CA1	Eruptive scenario 1 of Caldeira volcano (Faial Island)	230.7
MP1	Eruptive scenario 1 of Montanha do Pico volcano (Pico Island)	211.2

Step 2

Three circular buffers were created to measure distances from each eruptive source, namely (1) the 5 km buffer (red colour), (2) the 7.5 km buffer (white colour), and (3) the 15 km buffer (purple colour), as displayed on Figure 3.9, regarding the example of the eruptive scenario FU1 for Furnas volcano. The area within the 5 km buffer was considered as the critical zone for every eruption and no infrasound station should be deployed in here. The area between 5 and 7.5 km was attributed for *LC* arrays and the one between 7.5 and 15 km was designated for *IS* arrays. It is recalled that the distance of 15 km was the maximum considered once infrasound deployments for local monitoring purpose are within < 15 km from the source (see subchapter **1.5.3. Volcano infrasound monitoring strategies**).

Additionally, there are two situations, for Sete Cidades and Fogo volcano, where the eruptive scenarios were considered contemporaneous, specifically SC1 and SC2 as well as FO1 and FO2, respectively. Therefore, the limits of the 5 km, 7.5 km, and 15 km-buffers were the joining of every simple buffer around each scenario individually, as shown by the SC1 and SC2 example on Figure 3.10. Also, the situation of CA1 in Faial Island requires to locate IS arrays at about 20 km away, on Pico Island, once this island is very small, and its coast is right after 7.5 km away from the source.

Figure 3.9 - Step 1 and 2 for FU1 (Furnas volcano), showing the source location, the IS42 back azimuth (blue) and the buffers of 5 km (red), 7.5 km (white) and 15 km (purple).

Figure 3.10 - Step 1 and 2 for contemporaneous eruptive scenarios of SC1 and SC2 (Sete Cidades volcano), showing the two sources' location, the two IS42 back azimuths (blue) and the two buffers of 5 km (red), 7.5 km (white) and 15 km (purple).

Step 3

After defining the areas, the search for sites started, trying to follow the above requirements described on subchapter **3.2.2.1. Constraints and their requirements** wherever was possible, but simply looking for green areas with low gradient. Firstly, it was selected several sites in the LC arrays' area, then the same was done in the IS arrays' area. Note that for MP1 in Pico Island, the North, East, and South parts were not considered, once there is a high probability of lava flows from the basaltic eruption reach those flanks.

For LC array cases each site should have a sufficient forested area to deploy 4 sensors with a maximum aperture of ~140 m. Conversely, for IS array cases each site simply needs a small, forested area to install only one individual sensor element, with it is own energy supply and communication device, and between elements the distances should de around 1 km.

It was chosen the simplest array configuration for both LC and IS arrays, namely the centred triangular design, with 3 sensors forming a triangle and 1 sensor on the middle, as display on Figure 3.11, always with the biggest aperture "open" to the source, *i.e.*, perpendicular to the azimuth from the source. Nevertheless, this azimuth from the source to the chosen site was traced as an auxiliary reference to arrange the position of each sensor within the array configuration, defining somehow its middle (see Figure 3.11). Then, a rudimental simulation was made to define the final position of each sensor. It consisted in drawing a circle, using the ruler tool of Google Earth Pro®, with centre on each eruptive scenario. The circle was enlarged until the array as a simulation of spherical sound waves' propagation passing through the array with origin on the volcanic eruption, as exemplified on Figure 3.11. Consequently, it was possible to confirm that each sensor point would receive the wave at different arrival times, allowing to settle a theoretical array design. Remind that in local monitoring the detections are direct line-of-sight arrivals whose acoustic wavefronts are represented by spherical shells (McNutt *et al*., 2015 (see subchapter **1.3.3.3. Infrasound phases/arrivals**).

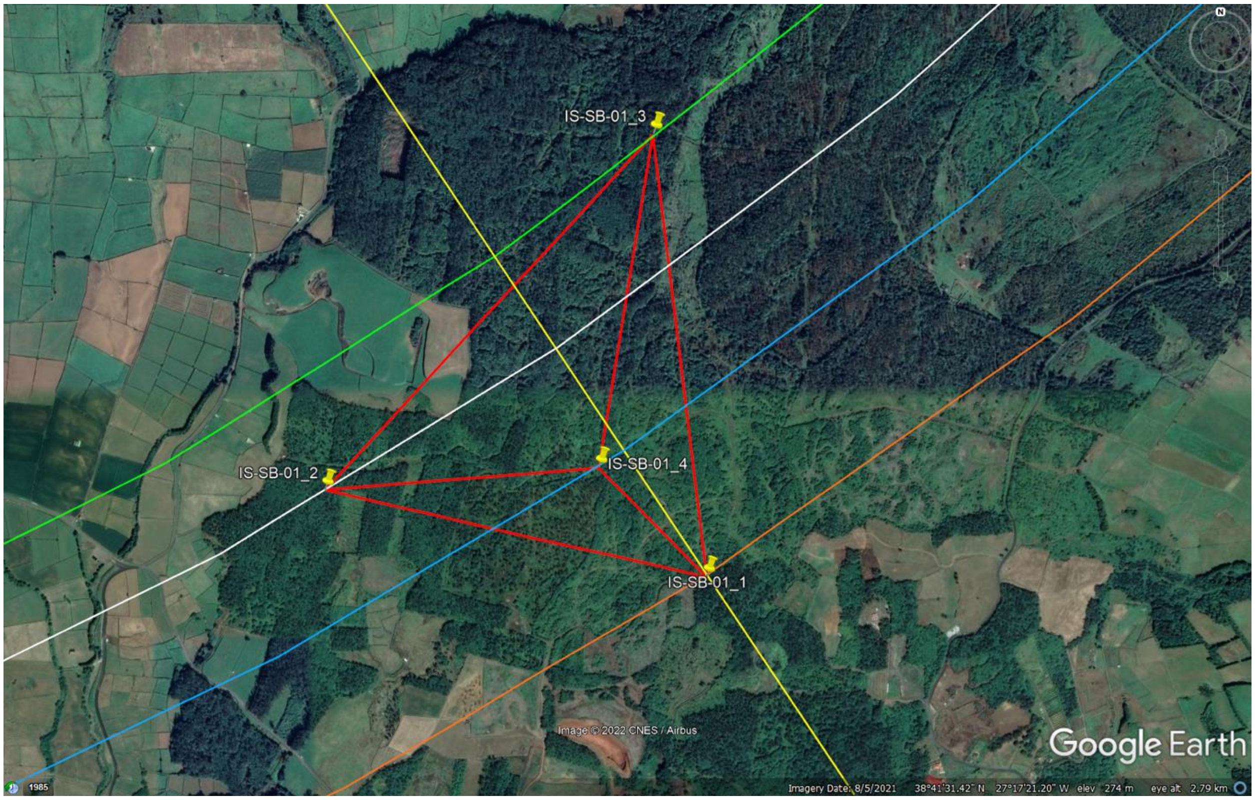

Figure 3.11 - Step 3 for one IS array to monitor the eruptive scenario SB1 of Santa Bárbara volcano, in Terceira Island. The yellow stretch represents the azimuth from the source (NNW); the yellow points illustrate each sensor, and the 4 sensors form a centred triangular configuration marked in red colour. The 4 colourful arcs of circles show the same spherical acoustic wavefront propagating through time and space. In ascending order of time, this wavefront arrives to IS-SB-01_3 (green), IS-SB-01_2 (white), IS-SB-01_4 (blue), and at last to IS-SB-01_1 (orange).

The final arrays for all central volcanoes are listed and characterized in Annex A, with a table for each volcano with their respective arrays. These are identified by an ID, as shown on Figure 3.11, whose first letters represent the type of array (*e.g.*, IS), follow by the volcano's code (*e.g.*, SB) and the number of the array (*e.g.*, 01). The maximum aperture and the back azimuth to the source from each array are also listed on the same table. Note that all arrays have 4 elements (*e.g.*, _1; _2; _3; and _4).

Furthermore, all the final pre-selected sites marked by the respective arrays were added to a QGIS® project, whose maps can be found in Annex A.

3.2.3. Assessment in *situ* of the pre-selected sites - São Miguel Island

This phase of the survey consisted in assess the pre-selected sites on field. However, this stage was only possible to conduct it on São Miguel Island.

Therefore, major essential parameters were evaluated to know if each site was good for signal-testing, accordingly with the following check list:

- **Land cover**: description of the type of rock formation beneath the soil and respective vegetation.
- **Surrounding environment**: all potential sources of background noise nearby each site were noted, such as roads, urban areas, and farms.
- **Gradient**: qualitative and quantitative evaluation of each terrain's declivity; firstly, the flatness of each site was qualitatively observed; then, it was quantitatively estimate through the measurement of the highest and lowest point's altitudes of the site, using a small pressure altimeter device and a mobile application called *GPS Satellites Viewer* (ver. 3.0.0, Stathis D. Stathakis, S.F. Applicality Ltd., 2016). Later, the average slope's values were determined for the sites already selected during this assessment, using Google Earth Pro®.
- **GSM**: measurement of GSM signal using a mobile application named *GSM Signal Monitor* (version 1.6.12, VMSoft, 2014-2022), to check the conditions to broadcast data to remote servers through GSM transmission.
- **Road accesses**: qualitative characterization of the accesses to the sites according to the season, mentioning the required vehicle's features.
- **Ownership**: for cases where was not possible to contact the owners on the local, the registration numbers of the selected lands were consulted on the existing website of SiRGIC (Recolha e Gestão de Informação Cadastral, https://cadastro.azores.gov.pt/Default.aspx) of the Azores Government.
- **Security**: the level of security in each site was analysed, considering their surroundings and the type of roads facilities to access each place.

Annex B.1 comprises a map with the location of all the sites checked in *situ* on São Miguel Island. In Annex B.2, the respective field tables of each site detail all parameters above discriminated, followed by illustrative photos. At last, Annex B.3 represents a map identifying the sites selected during the assessment for the signal testing phase. The survey's results are further discussed on subchapter **3.3. Discussion of the results**.

3.2.4. Field survey and final selection

In this stage, the local noise conditions should be evaluated at all sites selected during the assessment in *situ*. Therefore, the analysis of noise levels dictates whether a site is suitable (or not) for an infrasound array, or its aperture should be optimised (in case of being suitable).

Field survey comprises five main steps, namely (1) final definition in *situ* of the array configuration, (2) gathering and calibration of all necessary equipment to be installed, (3) deployment of an infrasound array at a selected site, (4) signal recording for a previous determined period, and (5) analysis of the data recorded on that period and final selection of the sites to effectively install an infrasound array.

Despite the different apertures and other features between LC and IS arrays, both are deployed with the same basic principles. Hence, these are briefly characterized in a general basis down below, according to the existent bibliography on the subject.

However, field survey was not carried out on São Miguel Island, once it came out the opportunity to do it during the 2022 São Jorge Island seismovolcanic crisis, where an infrasound LC array from **UniFI** was deployed for local monitoring purposes. All procedures of the field survey applied on São Jorge Island are detailed on chapter **4. 2022 São Jorge Island seismovolcanic crises - study case**.

3.2.4.1. Final definition in *situ* of the array configuration

The disposition of all elements of an infrasound array are finally marked on the field, which includes the spots for 4 sensors; digitizer (communications); batteries and south orientated solar panels (energy), as well as GSM and GPS antennas, in accordance with the respective pre-defined configuration (see example on Figure 3.11).

3.2.4.2. Gathering and calibration and of all necessary equipment

The portable equipment to be installed must be previously configurated and calibrated before going to the field.

Firstly, digitizer is configurated on its parameters, such as sample rate, compression, gain, among others (*e.g.*, Robertson *et al*., 2021). Data is locally recorded, but optionally a GSM modem is also prepared with a serviceable SIM card and linked to the digitizer.

The pressure calibration of infrasound sensors, irrespective of their type (Ponceau and Bosca, 2010; Nief *et al*., 2019), is fundamental to be performed on the laboratory and/or field to certify that all devices are working properly as well as are emitting equal digitized signals for equal input (Hedlin and Berger, 2000; Hedlin *et al*., 2002).

Furthermore, all necessary equipment for the array should be gather and prepared, such as cables; batteries, solar panels; GSM and GPS antennas; pelicases; WNRSs, and other auxiliary tools to help on the installation (see subchapter **4.2.2. Gathering and calibration of all necessary equipment and Annex D.2** for an extensive checklist in the case of a LC array).

3.2.4.2.3. Deployment of an infrasound array

All in all, the installation of an infrasound array comprises three main sectors: (1) infrasound sensors; (2) data converter and transmission equipment (communications); and (3) energy supply. At all sites, the equipment to be installed should have the same specifications (Hedlin and Berger, 2000).

Regardless the type of sensor already selected, accordingly to Marty (2019), it is required that the sensor self-noise must be at least 10 dB below a standard worldwide low noise model, as the one defined by Bowman *et al*. (2005), already described in subchapter **1.6.2. Power Spectral Density (PSD)**. Moreover, it is particularly important to use a microporous wind noise reducing system on each sensor, in order to effectively reduce background noise and improve signal detection (Hedlin and Berger, 2000).

The atmospheric pressure variations measured by each sensor are then conducted by electric cables or optical fibre to a central facility where signals are sampled (from analog to digital signal) through a digitizer, locally recorded and eventually transmitted through a GSM modem for remote access.

The mains or rechargeable batteries connected to solar panels supply energy to the central facility.

Optionally, a digital meteorological station can be masted at each site to record continuous wind speed and direction data (*e.g*., Roberston *et al*., 2021), as well as temperature conditions.

Thereafter, all necessary equipment to deploy an IS array is described below, using, as an example, the portable station created by SEISMOWAVE called SISTEM. An example of a LC array is specified on the next chapter.

IS array - SISTEM by SEISMOWAVE

As referred before, SEISMOWAVE (2022) has recently developed an easy solution to deploy a mobile infrasound station (see datasheets in see Annex D.1) well-known as SISTEM. Each SISTEM can be connect to the mains, to external batteries or to solar panels, depending on what is required and on field constraints. Also, it can be easy connected with a weather station and a flexible wind noise reduction system for more efficient measurements. It requires 4 SISTEMS to deploy an IS array of 4 elements.

One SISTEM is composed by the following elements:

- 1 digital microbarometer infrasound sensor (MB3d version): includes a 24-bits digitizer with 1 GB data storage (it is possible to choose the analog version, MB3a, with digitizer separated from the sensor).
- 1 data transmission equipment: includes a GSM/3G/4G modem; RS232 to ethernet converter that allows the remote transmission of the MB3d data; and a 450 MHz cellular antenna.
- 1 GPS antenna.
- 1 power supply: includes a rechargeable Li-ion battery, solar charge controller and Li-ion battery chargers.
- 1 collocated weather station (optional).
- 1 flexible wind noise reduction system (optional).
- 1 solar panel (optional).

The MB3d sensor (see Annex D.1) enhances the requirements of a survey, especially because it incorporates a digitizer, simplifying the work on field and enabling data conversion and transmission.

The selection of this sensor provides the following characteristics and advantages:

- Allows the recording of very low-frequency acoustic signals over a broad frequency band (from 0.01 to 28 Hz), with a sensitivity of 20mV/Pa, an excellent resolution (1.75 mPaRMS from 0.02 to 4Hz) and a large dynamic range (111 dB @ f<106 Hz to 109 dB @ f=4 Hz).
- Can be remotely calibrated through MLS, pulse, or sine waves.
- Has an extremely low level of instrumental noise (<-80 dB relative to 1 Pa^2/Hz at 1 Hz), allowing the sensor to resolve more than 10 dB under Low Noise Model (Bowman *et al.*, 2005).
- Encapsulates a low-noise 24-bit digitizer (ADC, with a calibration board, a timecard, and a storage capacity of 1 GB).
- Has its specifically developed software (Dionisos), where is possible to (1) graphically visualise data, in real and deferred time; (2) remotely calibrate the sensor; (3) configure and monitor the states of health of the sensor; as well as (4) choose the sampling rate (20, 50 or 100 Hz).

3.2.4.2.4. Signal testing and recording

In a standard site survey, pressure variations (infrasonic noise) and weather conditions (wind velocity, air temperature, and humidity) are collected for a minimum of 15 continuous days at the selected sites (*e.g.*, Hedlin and Berger, 2000; Hedlin *et al*., 2002; Robertson *et al*., 2021). This period provides a preview of the full range of meteorological phenomena that may occur through the year at each site, being sufficient to indicate which site is the best to deploy an infrasound array (Hedlin *et al*., 2002). Also, this is an important step to assess the detection capability during day and night (Paola Campus, personal communication).

3.2.4.2.5. Data analysis and final selection of the sites

Recorded data on the period above is then and analysed using a software (*e.g*., MATLAB®; DTK-(G)PMCC®), allowing to view the waveforms, as well as to plot the meteorological data recorded at the portable site. Therefore, Power Spectral Density (PSD) plots are processed (see subchapter **1.6.2. Power Spectral Density (PSD)**) and the acoustic noise levels at each site are evaluated (*e.g*., Robertson *et al*., 2021) in comparison with the standard Noise Model of Bowman *et al*. (2005).

Finally, PSDs are converted into PDFs (empirical noise amplitude Probability Density Function), to estimate signal-to-noise ratio and thus the detection capability of the array (see subchapter **1.6.3. Probability Density Function (PDF)**).

The sites with less background noise would be the ones with the most significant signal-to-noise ratio, hence better detection capability.

After the results of the signal testing, there are two options for the sites with not so good results: (1) they are excluded; or (2) the array configuration is changed and/or the aperture is optimised.

3.3 Discussion of the results

The aim of this study was not to model any future eruptive activity, but to present eruptive scenarios as examples of possible locations and general eruptive styles based on events that occurred in the last 10 ka years BP, to constrain possible sites to deploy infrasound arrays.

Only three scenarios were determined as basaltic effusive/moderately explosive style of Hawaiian/Strombolian eruptive styles, namely SC2 (comparable to the 800-year BP eruption of Pico das

Camarinhas), FO2 (comparable to the 1563 eruption of Pico do Sapateiro), and MP1 (comparable to the 1720 eruption of Silveira).

On the other hand, the remaining 6 scenarios were considered as trachytic explosive of sub-Plinian type, namely SC1 (comparable to the 700-year BP eruption of Caldeira Seca), FO1 (comparable to 3 ka years BP eruption of Fogo B), FU1 (comparable to the 1630 eruption), PA1 (comparable to the most common type of eruption during the last 23 ka, whose the most recent dated eruption is believed to have occurred around 1000 years BP), SB1 (comparable to the most common type of eruption during the last 23 ka, whose the most recent dated eruption is believed to have occurred around 2000 years BP), and CA1 (comparable to the most common type of eruption during the last 16 ka years BP, whose the most recent eruption occurred at 1200-year BP, being correlated with the opening of the actual caldera).

Sete Cidades and Fogo volcanoes are the only central volcanoes in the Azores Islands that have records on basaltic eruptions on their recent volcanism, apart from the trachytic explosive ones. Therefore, both scenarios for each of these volcanoes were considered contemporaneous.

These eruptive scenarios were considered as potential sources to conduct a site survey to deploy infrasound mobile stations aiming their monitoring. The selected technique relies on using two types of arrays of different equipment. LC arrays consist in differential pressure transducers within a small aperture (maximum of 140 metres), while IS arrays use microbarometers sensors with integrated digitizer within an extended aperture (around 1 Km). Due to the different distances between sensors within each array, LC arrays are useful to detect higher frequencies of infrasound, between 1-4 Hz, in a closer distance to the source, while IS are more robust an able to detect frequencies within a wider range of values, especially the lowest ones below 1 Hz. As expected, IS arrays are far more expensive than LC arrays. Therefore, it was decided to allocate them to different areas defined by 3 buffers around the hypothetical source.

Without considering other parameters on the scenarios, particularly wind intensity and direction, the buffers were concentric to the source. The sites for the arrays should be between 5 to 15 km away from the source, being sites for LC arrays closer to the source between 5-7.5 Km. It is preferably to lose a LC array than an IS array.

The pre-selection of areas with the required characteristic within those areas was a hard challenge due to the rugged geology of the islands surrounded by a very dynamic ocean and under windy weather conditions with frequently extreme atmospheric events (EAE). Wind and surf noise will always be a constant on every site selected. Fortunately, the islands still preserve several forested areas, which were of a great importance and contribution for the selection of sites.

Although the array sites were chosen for each volcano individually, some of the pre-selected sites are apparently able, in terms of distance from the source, to monitor several volcanoes simultaneously, as in the following situations:

- On São Miguel Island: the sites IS-SC-02, IS-FO-02, IS-FO-03 and IS-FO-05 for Sete Cidades and Fogo volcanoes; the sites LC-FO-04, LC-FU-04, and LC-FU-05 for Fogo and Furnas volcanoes.
- On Terceira Island: the sites IS-PA-01 and IS-SB-01, IS-PA-02 and IS-SB-02, LC-PA-08 and IS-SB-03, LC-PA-01 and IS-SB-05 for Pico Alto and Santa Bárbara volcanoes. When the same site was chosen for LC and IS, it is preferable to select the deployment of an LC array adapted for both volcanoes, if the site would be approved during the survey.

In small island volcanoes as the case of Faial, to implement an IS array is impossible. Fortunately, Pico Island is nearby by and that can be a solution in case of an eruption as CA1 event. LC array sites were difficult to select in here and would always be in great risk in a case as this type of scenario.

Furthermore, in situations where sites have a similar back azimuth to the considered source, after the assessment and possible signal testing, it is only necessary to choose the one with the best overall conditions.

Due to logistic and financial limitations, it was decided to only visit the pre-selected sites on São Miguel Island, to test work methodologies, leaving for later opportunities to access and test sites from other islands. From the 37 sites assessed, 15 have passed for the signal testing phase. However, two of these 15 sites (IS-FO-02_1 and _4) are still needed to be checked, once they are within private residential properties/farms, even knowing that each one has a good, forested area.

Several sites were being discard along the process and in the case of being IS array sites, it was necessary to look up for other sites on field to substitute them and complete the array in hand, as for IS-FO-05, which it was possible two find 2 more places (IS-FO-05_New1 and _New2). Nevertheless, it was verified the site LC-FU-05 would be potentially better for an IS element. Therefore, it is still needed to look up for more 3 sites around that place (between Fogo and Furnas volcanoes).

Regarding the evaluated parameters, generally, it was possible to verify the following along the assessment:

- Land cover: the type of rock formation beneath the soil (basaltic lava or pumice) has a straight influence on the type of vegetation: for instance, where the ground is formed by pumice, trees are most of all *cryptomeria japonica*, and this kind of tree uses to rise near waterlines, which are not good spots particularly for LC arrays. This is a common situation in the area between Fogo and Furnas volcano; also, several other sites were excluded for being waterline valleys, as was the case of LC-FO-01, LC-FO-04, LC-

FU-05, IS-FU-05, and IS-FO-07, meaning that the pre-selection part of the survey could have considered waterlines as parameter to be excluded.

- Background noise: despite natural background noise, sites like LC-FO-06 and LC-FO-05 nearby industrial activities were still selected for signal testing, once they showed great conditions to allocate a LC array, just in case of belonging to a security exclusion zone during a volcanic unrest of Fogo volcano.
- Gradient: even using the above-mentioned devices on field, their precision was not reliable, thus its measurement used the Elevation Profile's tool on Google Earth Pro to get the values of the highest and lowest points and distance between them for the calculation; flat terrains are particularly found in the central part of the island, between Sete Cidades and Fogo volcanoes.
- GSM: almost all sites showed a good GMS signal, for broadcast data to the server; for the good places in the other parameters but with poor GSM signal, radio communications with repeaters should be a viable option; several sites, mainly the ones between Fogo and Furnas, may present an issue regarding the charge of solar panels during the winter, once they have scoria cones blocking the sunrays.
- Road accesses: almost every site requires a 4 x 4 car.
- Ownership: practically every piece of land on São Miguel Island is private. Only on LC-FO-05 it was possible to speak with the tenants of the site. The ownership registration of the remaining sites will be consulted in a posterior phase on the platform above-mentioned.

Security: most of the sites are highly secure since they are very hidden and only known almost by the owners.

CHAPTER 4. 2022 SÃO JORGE ISLAND SEISMOVOLCANIC CRISIS - STUDY CASE

4.1. Background of the seismovolcanic crises

On 19 March 2022, seismic activity suddenly increased on São Jorge Island, being associated with a possible unrest of Manadas fissure volcanic system, where subaerial historical eruptions occurred in 1580 and 1808 (Madeira, 1998; Wallenstein *et al*. 2018, Zanon & Viveiros, 2019, CIVISA, 2022a, b).

4.1.1. São Jorge Island - geological framework

With a rugged and steep terrain, São Jorge Island is particularly different from the other 8 islands that form the Azorean archipelago, once the island itself is a WNW-ESE orientated fissure volcanic system (Madeira *et al*., 2015).

As referred in Madeira *et al*. (2015), the island is composed of 4 volcanic units, namely (1) São João Volcanic Complex (~ 1.3 - 1.2 ka (Hildenbrand *et al*., 2008)); (2) Topo Volcanic Complex (~ 740 - 690 ka (Forjaz and Fernandes, 1970, 1975 in Madeira, 1998; Hildenbrand *et al*., 2008)); (3) Rosais Volcanic Complex (370 - 270 ka (Hildenbrand *et al*., 2008)) that represents a WNW-ESE linear chain of scoria cones and associated lava flows; and (4) overlying the preceding unit, Manadas Volcanic Complex, the youngest volcanic sequence (< 5.6 ka (Madeira, 1998)) located on the centre of the island and where the historical eruptions of 1580 and 1808 took place. Hildenbrand *et al*. (2008) believe that Rosais and Manadas complexes form a single main eruptive complex. All volcanic units, except the oldest one, are illustrated on Figure 4.1 and Annex C.1.

The volcanic activity on São Jorge Island has been characterized by basaltic volcanism related with effusive and moderately explosive fissure eruptions, from Hawaiian to Strombolian style, respectively, originating linear chains of scoria cones and associated lava flows (*e.g.*, Madeira *et al*., 2015). Also, the occurrence of PDCs (pyroclastic density currents) (Wallenstein *et al*. 2018) seems to be common, even though they are infrequent in regions of low explosivity volcanism as the case (Madeira, 1998).

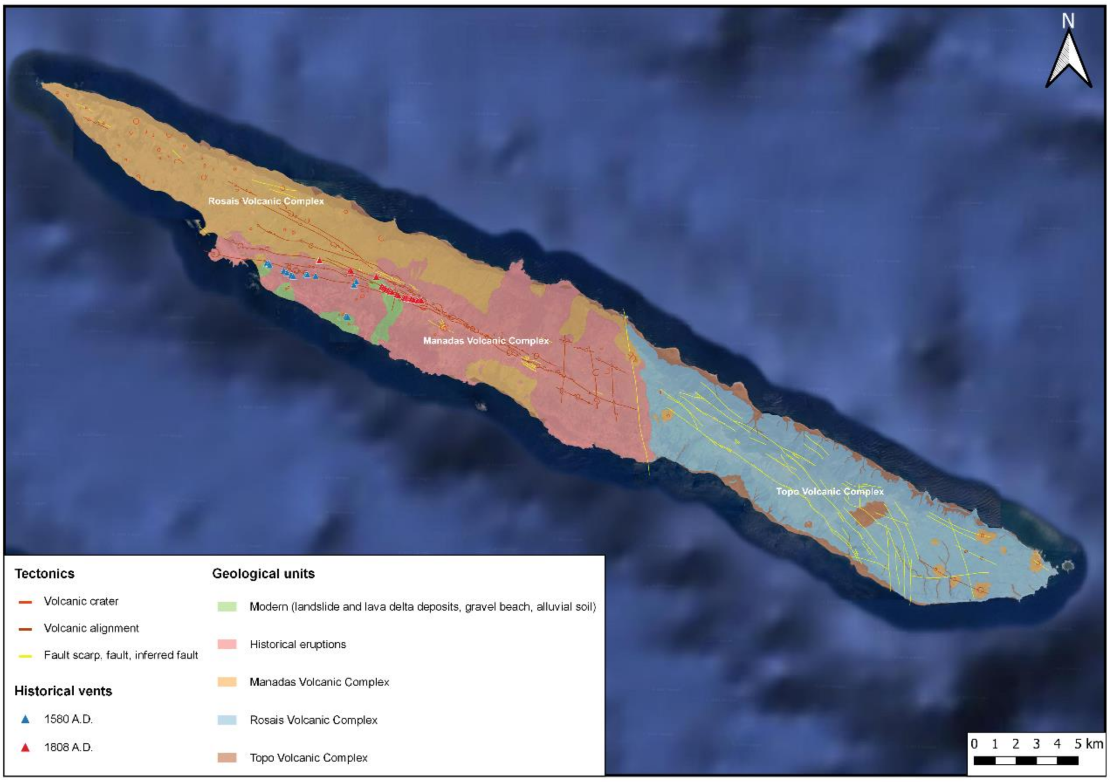

Figure 4.1 - Geological framework of São Jorge Island, illustrating its (1) volcanic complexes, (2) tectonics, as well (3) the vents of both historical eruptions at Manadas fissure volcanic system (modified by CIVISA from: (1) Madeira and Brum da Silveira, 2003, (2) Madeira, 1998, and (3) Zanon and Viveiros, 2019).

4.1.1.1. Manadas fissure volcanic system

According to Madeira and Brum da Silveira (2003), the young sequence of Manadas Volcanic Complex is also a fissure volcanic unit - Manadas fissure volcanic system (CIVISA, 2022b) - formed by 2 alignments of Hawaiian/Strombolian cones and respective lava flows, as surtseyan tuffs, as illustrated by Photo 4.1. One alignment is WNW-ESE orientated and the other trends almost east-west (Madeira *et al.*, 2015). Moreover, there are other volcanic edifices along NNW-SSE alignments (Madeira, 1998).

In the last 5.6 ka, at least 12 eruptions have occurred associated with this volcanic system (Madeira, 1998), including the subaerial eruptions of 1580 and 1808 (*e.g.*, Wallenstein *et al.*, 2018; Zanon and Viveiros, 2019), as well as a probable submarine event in 1964 (Madeira, 1998; Madeira and Brum da Silveira, 2003). The eruptions of 1580 and 1808 were firstly characterised by basaltic lava flows and tephra fallout emitted from many fissures simultaneously active and opening for several kilometres, related to WNW-ESE orientated fissures (*e.g.*, Zanon and Viveiros, 2019). On a second stage, hydromagmatic events and the occurrence of lava front collapses when reaching a steep cliff have triggered fatal PDCs (Madeira, 1998; Wallenstein *et al.*, 2018; Zanon and Viveiros, 2019).

Photo 4.1 – Partial view of the eastern section of the Manadas fissure volcanic system, from west to east (photo courtesy of Nicolau Wallenstein).

4.1.2. 2022 Seismovolcanic crisis - current situation

Accordingly with the status of the crisis made on 2 November 2022 at 10:00 am UTC in the web Portal of CIVISA/IVAR (CIVISA, 2022a,b), the seismovolcanic activity that has been recorded on São Jorge Island since 5:05 pm UTC of 19 March 2022 is still ongoing, remaining above the standard, generally concentrated along a WNW-ESE orientated range (see Figure 4.2 and Annex C.2), from Ponta dos Rosais to the area of Norte Pequeno - Silveira. Until this day, around 332 earthquakes have been felt by the population, among a total of 54,832 registered low magnitude tectonic events. The most energetic earthquake occurred on 29 March 2022, at 09:56 pm UTC, with epicentre at about 2 km SSW from Velas and a magnitude of 3.8 (Richter).

Since the first day, CIVISA and IVAR developed a monitoring network on the island composed of several distinct monitoring techniques from various scientific domains, namely seismicity, geochemistry (gases), hydrogeology, geodesy, and infrasound. The integration of data from those monitoring fields has allowed to assume that Manadas fissure volcanic system was reactivated, having occurred a magmatic intrusion in depth in the beginning of this crises (CIVISA, 2022a).

During the crises, scientific alerts (Gaspar *et al.*, 2012) were activated to characterise the status of seismovolcanic activity, useful for Civil Protection measurements. In a scale from V0 ("quiescent state") to V6 ("eruption of VEI 4 or superior in course"), on 20 March at 00:40 UTC, the alert has rose to V2 ("possible reactivation of the system"). Two hours after, at 02:40 UTC, the level increased again to V3 ("confirmation of the system reactivation"). Three days after, on 23 March at 15:30 UTC, the alert level reached V4 ("threat of a magmatic or hydromagmatic eruption") (CIVISA, 2022a). During the next 2 months, seismicity has slowly diminished and no other anomalous signs from the remaining techniques were identified. Therefore, on 9 June at 09:20 UTC, CIVISA has dropped down the Scientific Alert Level from V4 to V3 for São Jorge Island. During the following weeks until 2 November 2022, seismic activity has slightly decreased, sometimes interrupted by short periods of higher hourly frequency and/or release of energy The correspondent hypocentres were presumably located at more than 5 km depth (CIVISA, 2022b). The daily frequency of recorded earthquakes since the start of this seismovolcanic crises (CIVISA, 2022c) is represented on Figure 4.3.

Currently, CIVISA is still maintaining high monitoring levels at São Jorge Island as well as enhancing the permanent seismovolcanic observation network, once eruptive precursor signs can suddenly reappear (CIVISA, 2022b).

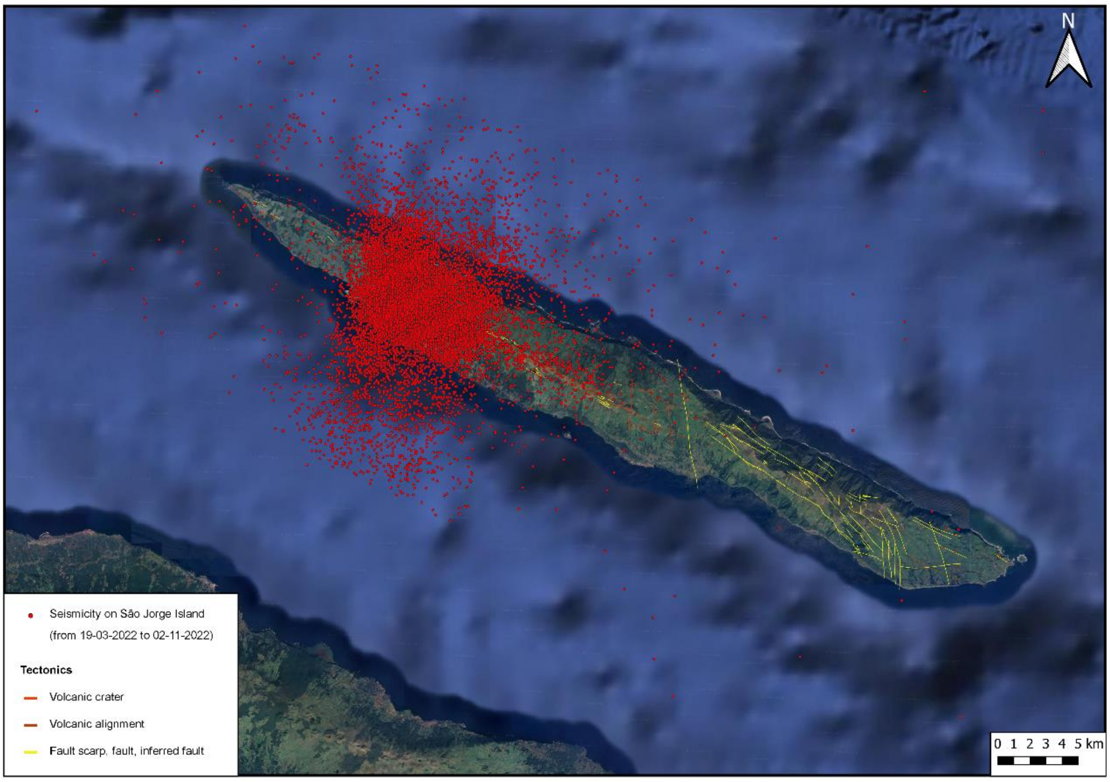

Figure 4.2 - Seismic activity on São Jorge Island since 19 March 2022 until 2 November 2022 (data from CIVISA, 2022).

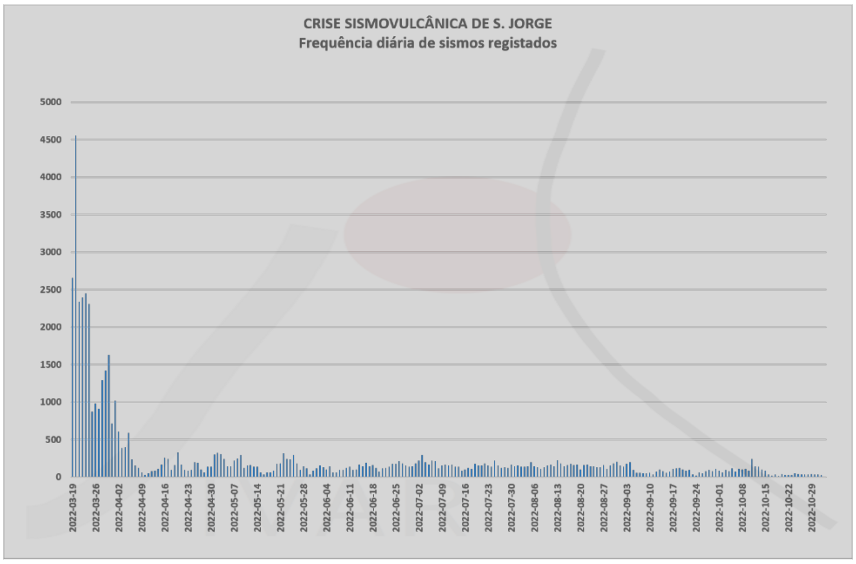

Figure 4.3 - Daily frequency of recorded earthquakes during the current seismovolcanic crises (in CIVISA, 2022d).

4.2. Site survey and deployment of a mobile infrasound array

To locally support the established seismovolcanic monitoring network on following the evolution of seismicity, as well as eventual eruptive activity, the Infrasound Operational Unit from IVAR immediately started a site survey to deploy a mobile infrasound array (SJ1) around the epicentral area of the seismovolcanic crises on São Jorge Island.

In a pre-eruptive stage, the array, SJ1, alongside with the IMS infrasound station IS42, located in Graciosa Island at around 40 km distance from São Jorge Island, were expected to possibly detect seismoacoustic events, through a symbiose between seismic and infrasound networks that would enable to correlate seismic data with infrasound detections.

Thankfully, on the one hand, this situation has matched with the arrival of two members from UniFI (University of Florence, Italy) that were here to perform an internship at the Infrasound Operational Unit from IVAR and have brought an infrasound array with them to support this dissertation in São Miguel Island field tests. Therefore, this seismovolcanic crises was a fantastic one-time-opportunity to conduct a field survey on São Jorge Island, as the one described on **Chapter 3. Site survey methodology**. Even though Manadas fissure volcanic system is obviously not a central volcano of the Azores Islands, hence not considered in the previous chapters, the major difference and value between doing the field survey in São Jorge or in São Miguel was respectively the circumstances, once it was possible to do it on a situation with possible eruptive activity, rather than a hypothetic eruptive scenario with no emerging risk associated.

Due to the situation of a possible eruption, the site survey undertaken on São Jorge Island was more simplified and not so rigorous than the standard one of **Chapter 3. Site survey methodology**. Briefly, in first place and immediately after the starting of the crises, several sites were pre-selected on São Jorge Island, around the epicentral area, using a terrain imagery software. Then, on 1 April 2022, those spots were evaluated *in situ.* At the most ideal site, the team has deployed a 4-element infrasound array (SJ1), firstly configurated in a diamond geometry with an aperture of ∼ 115 m. After 1 month, the array was rearranged into a centred triangular design, extending the aperture to ∼ 130 m. Since the beginning, SJ1 has been remotely acceded by GSM transmission and data are broadcasted in real time to IVAR and UniFI servers. Data of several 24-h periods were collected and processed to analyse PSDs for both array configurations, which are herein compared and discussed on subchapter **4.3. Data processing and analysis from SJ1**.

4.2.1. Preliminary selection of sites on São Jorge Island

Several sites were pre-selected on São Jorge Island, at a distance around 4 km from the main epicentral area with the most frequent seismicity over Manadas fissure volcanic system, using Google Earth Pro®.

Already described on subchapter **3.2.2. Preliminary selection,** all constraints and requirements to be considered during a site survey were also applied in this pre-selection.

The mobile infrasound array to be deployed on the final site is a low-cost infrasound array of small aperture (LC array), which was previously detailed on subchapter **3.2.2.2. Pre-selected sites in the Azores Islands**.

4.2.1.1. Constraints and requirements

The search for sites with good overall conditions for an infrasound survey is a particular challenge on São Jorge Island comparatively with the remaining islands, due to its tapered morphology only with a maximum width of 6.7 km (Madeira and Brum da Silveira, 2003). Hereafter, the specific constraints for this island are highlighted.

4.2.1.1.1. Infrasound background noise

São Jorge is a quiet island mostly dedicated to agriculture, livestock, and fishery. Therefore, the main sources of infrasound background noise are undoubtedly wind and surf noise, as it is a small oceanic island, as well as farming and quarry activities. On a land with maximum width of 6.7 km, it is a rough task to select a site at more than 5 km from the coast. Nevertheless, the island is formed by extremely high cliffs of around 300 metres *a.s.l.* (Madeira, 1998), excluding lava delta areas, which might, for one side, attenuate the surf noise, and on the other side, intensify even more the turbulence of winds, especially in winter months. Fortunately, São Jorge still preserves some areas of endemic forest distributed all over the island, which became the priority choice for site selection during the survey.

4.2.1.1.2. Topography, size, and land cover

Finding relatively flat terrains was also a hard challenge on São Jorge Island due to its rugged topography condensed over a very long but too narrow space. However, it was possible to identify some forested sites around 4 km from the main probable eruptive fissure, with lower gradient and enough space to accommodate an LC array.

4.2.1.1.3. Logistics, security, and environmental conditions

In a normal situation, São Jorge Island have all necessary infrastructures and services that an island of its size and population requires, having (1) a main town, Velas, with practically all main resources, including the main harbour of the island; (2) a small airport with daily flights, nearby Velas; as well as (3) two major roads, in south and north, and dirt tracks, with great accessibility to everywhere on the island.

However, due to this seismovolcanic crises, in the event of an eruptive onset, the Velas area and surroundings (including the harbour and the airport) could be seriously affected by the eruption. Moreover, every spot outside this eventual exclusive zone would probably become inaccessible, with the east part of the island isolated from the west. The only possibility to reach those places would be through small harbours at lava deltas and/or by helicopter.

Sao Jorge is a very familiar island with strong sense of community. Therefore, during this emergency, all population were responsive and prompted to help CIVISA and IVAR teams and have temporarily lent terrains and houses/structures to deploy equipment. Furthermore, security would not be a problem in a place with low criminality. Sometimes, fences are needed, but to protect the equipment from cattle.

Environmental conditions are always a concern in the Azores Island, but specially on São Jorge. Mainly in winter, this island is scoured by hurricanes, heavy rain, thunderstorms, intense wind gusts and consequent landslides. Then, it is crucial to select a site that even under those weather conditions would still be accessible.

4.2.1.2. Pre-selected sites on São Jorge Island

The sites to deploy a LC array were pre-selected applying the qualitative methodology described on subchapter **3.2.2.2. Pre-selected sites in the Azores Islands**, using Google Earth Pro® and then mapped on QGIS®. However, since São Jorge was facing a volcanic unrest, it was urgent to deploy the infrasound array, thus the method for the survey was simplified, as described below.

Step 1

Considering that IS42 infrasound station, located on Graciosa Island around 40 km from São Jorge, can also be used to support monitoring on this island, the initial idea was to design a small infrasound monitoring network together with a LC array. Nevertheless, differently from the methodology of subchapter **3.2.2.2. Pre-selected sites in the Azores Islands** that was applied for central volcanoes, here it was not so simple to exclude sites that might have similar back azimuths of IS42, considering that the eventual source or sources are not central points, instead is a segment that represents the most probable eruptive fissure at Manadas fissure volcanic system. Therefore, the area between the IS42 back azimuths at east of the probable eruptive fissure (around 190°) and at west (around 206°) cannot be excluded from the pre-selection, since the probability of the back azimuths from a chosen site and IS42 be the same is extremely low, as illustrated on Figure 4.4 and Annex C.3.

Step 2

As an eventual eruption may occur along the fissure already mentioned, a buffer of 4 km around that segment was marked using QGIS® (Figure 4.4 and Annex C.3). Thus, the area within the 4 km buffer was considered as the critical zone for the eventual eruption and any deployment of infrasound station should be avoid in here. However, some apparent ideal spots are at around 3 km from the fissure. On a very long and narrow island like São Jorge it is necessary to adapt for the respective situation. Where possible, sites were selected outside the buffer area.

Step 3

Continuously the sites were finally pre-selected. The previously mentioned buffer was used as reference on the selection. Also, the requirements for an ideal site were respected as much as possible, but the first parameter to observe using Google Earth Pro® was forested spots with sufficient space to deploy an LC array of 4 sensors with a maximum of 150 metres as well as a south orientated open area to install a solar panel to charge the batteries.

The array configuration was only defined on the local, after the final decision during the assessment in *situ*.

The map with all pre-selected sites can be found in Figure 4.4 and Annex C.3. Additionally, the ID Name of each site as well as the back azimuth to the probable eruptive fissure are indicated on the following table (Table 4.1).

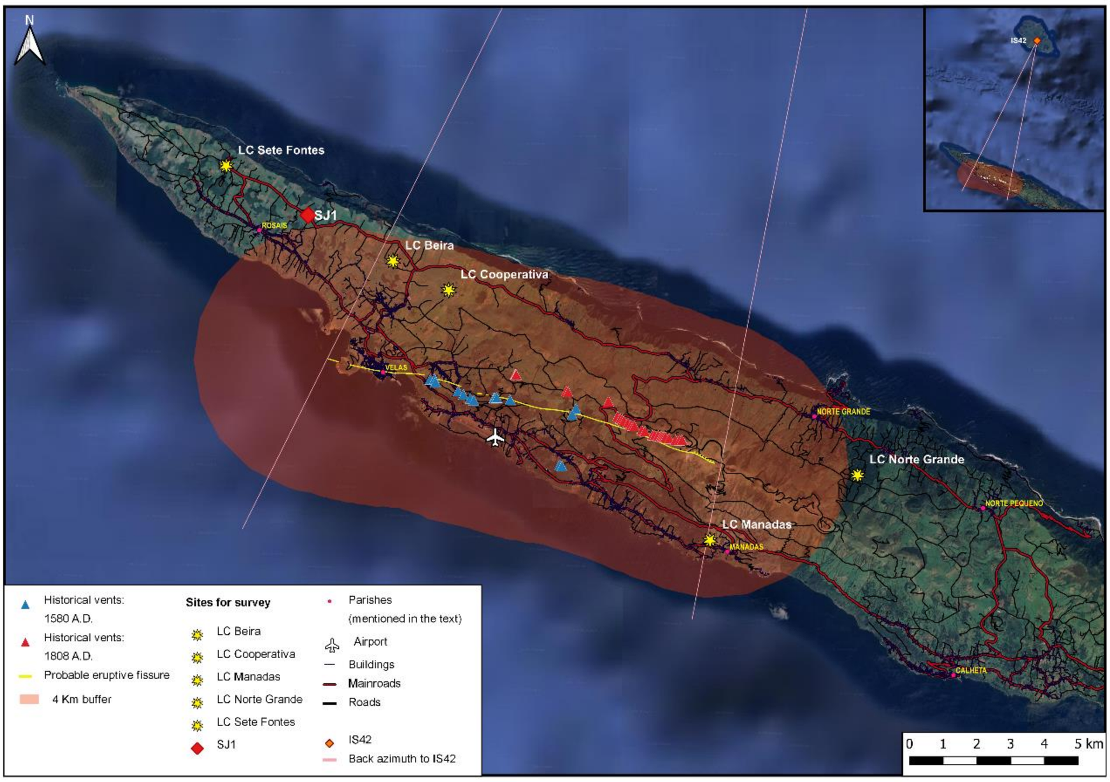

Figure 4.4 - Pre-selected sites for survey at São Jorge Island, with the back azimuths from the eruptive fissure considered to IS42 station. Historical vent's locations are from Zanon and Viveiros (2019) and probable eruptive fissure is from Madeira (1998), all data modified by CIVISA.

Table 4.1 - Back azimuths from the pre-selected sites to the probable eruptive fissure.

ID NAME	BACK AZIMUTH (°)
LC Manadas	5 - 295
LC Norte Grande	273 - 282
LC Cooperativa	222 - 240
LC Beira	121 - 214
LC Sete Fontes	120 - 152

4.2.2. Gathering and calibration of all necessary equipment

Before traveling to São Jorge, all necessary material has been collected.

SJ1 mobile infrasound array is composed of the following main components, namely:

- **4 Differential pressure transducers**: with sensitivity of 400 mV/Pa and frequency response between 0.01 Hz and 200 Hz, for a maximum distance between sensors of ~ 140 m; built by iTem (UniFI); differently from absolute microbarometers that records very small changes of pressure in atmosphere through aneroid deformation, the sensors herein measure small changes in pressure in relation with a reference pressure.
- **Digitizer**: Güralp GDM-DM24 configurated in a sampling rate of 100 Hz, where data is recorded at a local hard disk,
- **Data transmission equipment**: GSM/3G modem for remote access.
- **GPS antenna**: for time synchronization.
- **Power supply**: lead-acid rechargeable batteries connected to solar panels.
- **Wind noise reduction system**: 50-cm rubber hoses, functioning as air inlets.
- **Electric cables**: for all connections between components.

This equipment was prepared to be deployed, according with the following methodology (see photos on Annex C.5):

1. All sensors and communications equipment were tested and kept inside a protective Pelicase® type box.

2. The 4 differential pressure transducers, as well both spares, were connected by electric cables to the digitizer. As they are differential pressure transducers, and not absolute microbarometers, it is important to always have the screw opened, until the sensor is still on its final place and connected to the electrical cables. By this point, the screw must be tightened.

3. The digitizer (Güralp GCM-DM24) was configurate, setting the sampling rate at 100 Hz. Therefore, the signal from the sensors were checked as well as GPS antenna reception.

4. A 3G modem with SIM card (MEO) was configurated to test GSM transmission.

5. The energy supply equipment composed by batteries with their accessories, as well as solar panels was prepared.

6. Other components for the main equipment were also added, such as electric cables; connectors; hoses for an improvised wind noise reduction system; barrels and buckets, to keep the sensors protected on the terrain; auxiliary tools to held on deployment tasks; among others.

All equipment was sent by cargo ship and airplane to the island, for when the team arrives the cargo would be already there. A full list of SJ1's materials can be found on Annex D.2.

4.2.3. Assessment in *situ* of the pre-selected sites

On São Jorge, the evaluation of sites was not so rigorous compared with the one performed on São Miguel Island. The seismovolcanic crises enabled an urgent deployment of an infrasound array. Therefore, the qualitative checklist described on subchapter **3.2.3. Assessment in *situ* of the pre-selected sites - São Miguel Island** needed to be simplified. Then, the first decisive factor on the selection was GSM signal, beside land cover and relative altimetry.

This part of the survey started since the moment the team as arrived at São Jorge Island, on 1 April 2022. It was an extremely rainy, windy, and foggy day. Obviously, these severe weather conditions would complicate the assessment, not allowing to check all the pre-selected sites. After leaving the airport, the team follow the road up to Calheta's village to leave the bags at the hotel that was the chosen base for the operations of CIVISA/IVAR. On the way, the team has passed nearby **LC Manadas** in Manadas parish, but the weather conditions didn´t allow to check it. After Calheta, the team went to Norte Pequeno to pick up the necessary material previously sent to the island. Continuously, the road towards west was followed in direction to **LC Norte Grande** in Norte Grande parish. However, the creeping fog continued to deter from checking the site. Still, GSM signal was measured on the main road, but the reception was particularly bad. Thereafter, the team went directly to LC Beira in Velas parish, once the only access **to LC Cooperativa** was out of the way and the team didn't check it. So, **LC Beira**, which was the promising site on the pre-selection, turned out to be a disappointment. It was a steeply terrain cover by a dense bush and difficult to penetrate it. By this time, the fog has lift and the rain has stopped for a while. Afterwards, following the road towards LC Sete Fontes and analysing simultaneously on Google Earth Pro® other potential spots, the team found the perfect site (later named SJ1), between LC Beira and LC Sete Fontes, in Rosais Parish. **LC Sete Fontes** was not event checked at that time, because after assessing this new spot it was decided to install the array in here. Moreover, it has the advantage of having good accessibilities and available infrastructures only 10-min drive to Velas. Also, SJ1 is located around 5 km from Manadas fissure volcanic system. Below, Table 4.2 shows the results of SJ1 site assessment in *situ*.

Table 4.2 - Site characterization of SJ1.

EVALUATED PARAMETERS	**DESCRIPTION**
Land cover	Basaltic lava flow under dense heather vegetation (*Erica Azorica*).
Surrounding environment	Road at 25 m from the closest sensor. Nearest cliff at 580 m, with ~ 370 m of height. Closest village at ~ 1500 m. Possible milking machine on pastures around SJ1.
Gradient	~14 % (Google Earth Pro®)
GSM	Good (GSM Signal Monitoring)
Road accesses	Very good, all over the year. Asphalt roads. Accessed with a regular car.
Ownership	Permission given in person by the owner, the moment the team found the site.
Security	High
Back azimuth to the probable eruptive fissure	120° - 173°

4.2.4. Field survey - deployment of SJ1 array

SJ1 was deployed in a forested area of endemic vegetation commonly known as heather vegetation (*Erica Azorica*), at an elevation of around 368 metres *a.s.l*.

After the brief assessment described above, the team started to do the field testing by collecting noise data to be analysed back in the lab, using an array of 4 differential pressure transducers configurated within a specific geometry. The procedures for the deployment of SJ1 array were based on the ones described on subchapter **3.2.4. Field survey and final selection**. Due to the emergency status, the team decided to install the array on this location, without checking the remaining sites. Therefore, the noise level test was only made here. Moreover, in contrast to the previous chapter, the array configuration was only defined on site simultaneously as the team was deploying the array. Then, the results from PSDs analysis of 24-h periods would denote if the array design should be rearranged.

4.2.4.1. Deployment of SJ1 array

After finding a good site to deploy SJ1 array, the team has immediately started the installation process. Therefore, from mid-afternoon of 1 April 2022 until late afternoon of 2 April 2022 the deployment has been completed and SJ1 array became operational (Figure 4.5 and Annex C.4). Nevertheless, 1 month later, having more time and resources, namely longer electric cables to extend the connections, the team went back to São Jorge Island to upgrade the array and rearranged its geometry into a new one (Figure 4.6 and Annex C.4). Both array deployments geometries can be compared on Figure 4.7 and Annex C.4, in a map with the overlapping of SJ1 elements for both configurations, which enables an effective and visual comparison between them. Furthermore, the works were documented by photos (see Annex C.5).

<u>1st visit (1 - 4 April 2022)</u>

After having defined the spots for each element in an imprecisely way, the team started by extending the electric cables from the digitizer to each sensor spots. The fourth sensor stayed inside the digitizer's protective Pelicase® type box. The remaining three sensors were stored inside their respective barrel that was buried on the ground. After the connection of the sensors to the digitizer, a hose was added to each barrel and then covered by a bucket with a rock on top. This was the most practical approach to keep the sensors protected, specially from noise background.

Moreover, a GSM modem was connected to the digitizer inside the Pelicase® type box, as well as its antenna on a mast and GPS antenna on a tree branch on a south-orientated open area.

Also, batteries were deployed inside a box close to digitizer's protective Pelicase® type box and connected to it, as well as to 40 W solar panel, that was set orientated to south, through a charger controller. Kindly, the parish of Rosais installed a fence around the solar panel to protect the device from the cattle on the pasture. Furthermore, a spare battery was left with a local CIVISA's operator to replace the consumed one and recharge it, every time solar panel is not capable of recharging the batteries, particularly due to consecutive cloudy days.

A last, GPS points of each array's element were taken, and it was noticed that the array geometry was not centred triangular as expect. Instead, it was a diamond shape configuration.

Back in the lab, all elements were marked using QGIS® and the distance between sensors were measured, as illustrated by Figure 4.5. The aperture of the array was 115.09 metres, between sensors 1 and 3.

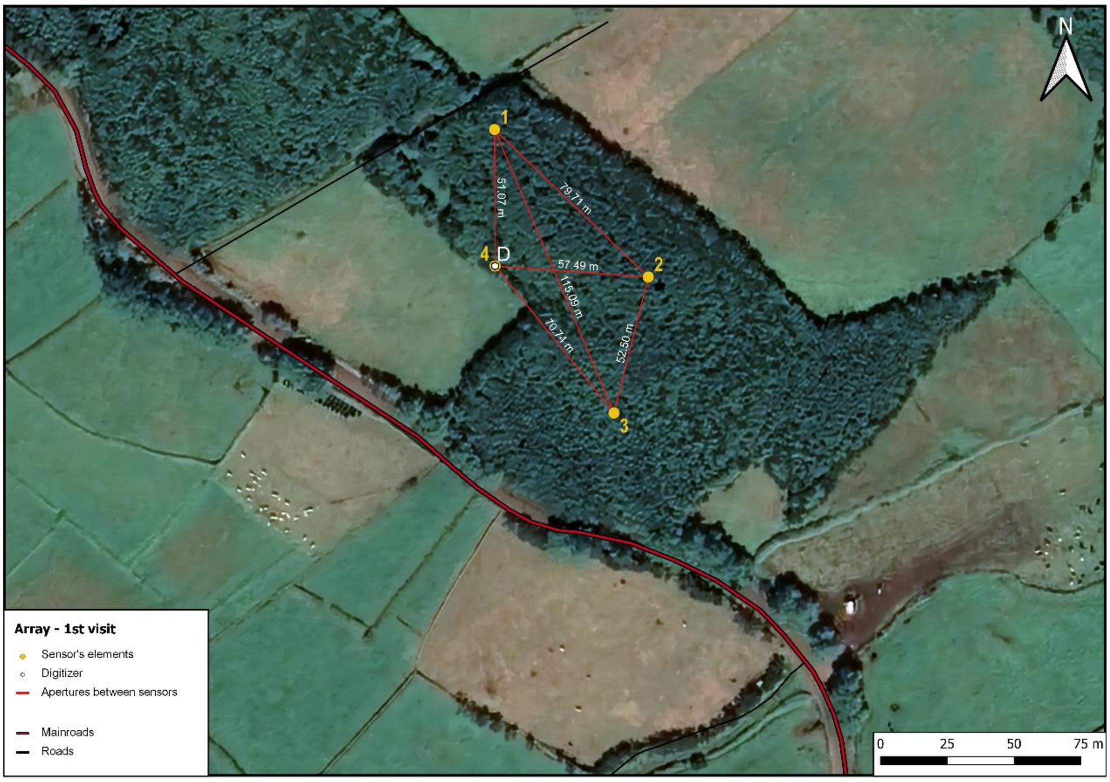

Figure 4.5 - Configuration of SJ1 from the 1st visit.

2nd visit (3 - 5 May 2022)

After 1 month, the team has returned do São Jorge Island to upgrade SJ1 array and rearrange its geometry. By that time, the seismovolcanic crisis has decreased from the initial peak and has been showing some stabilisation, albeit above the standard, as shown of Figure 4.3.

Most of all, this 2nd visit comprised the following main tasks:

- Changing the electric cables by other with 100 metres long.
- Protecting those electric cables with protection tubes.
- Extending the distance of sensors 2 and 3 from the digitizer, to increase their apertures with sensor 1.
- Removing sensor 4 from the digitizer's protective Pelicase® type box, placing it in the middle of the array, and deploying it in the same way as the reimaging.

Therefore, a centred triangular design was set up, with sensor 4 in the middle, as well the aperture was extended up to 129.08 metres, between sensor 1 and 3, as illustrated on Figure 4.6.

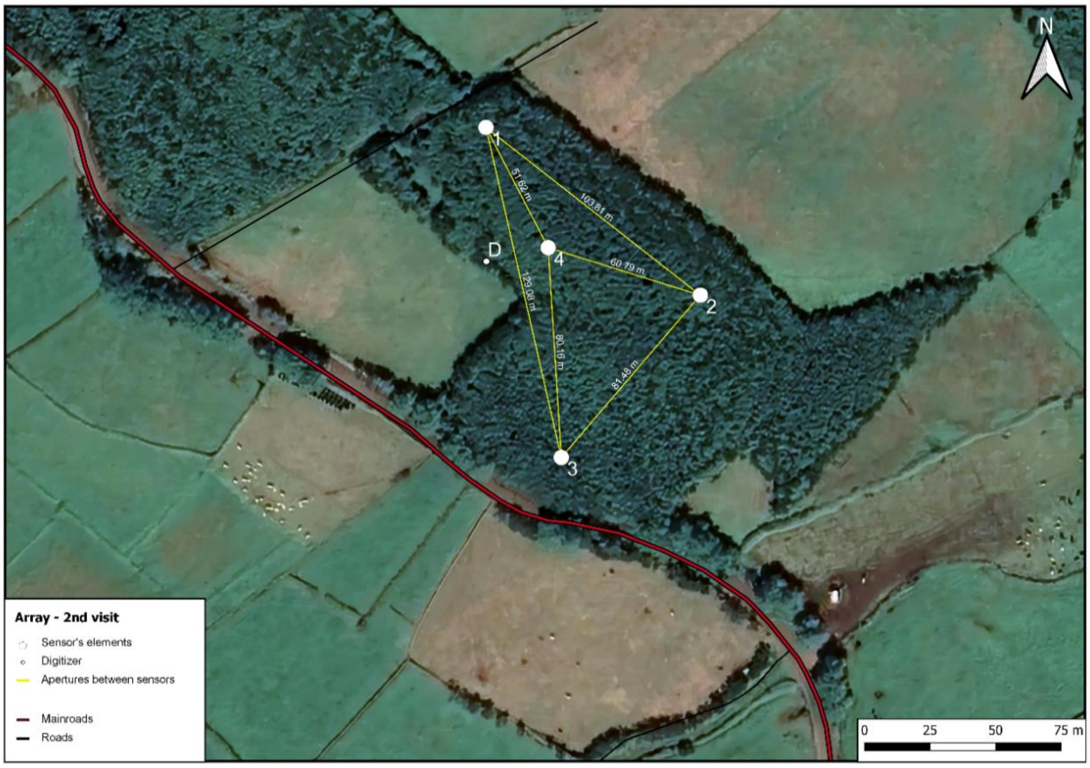

Figure 4.6 - Configuration of SJ1 after the 2nd visit.

Afterwards, a second solar panel of 115 W was added to the one with 40 W, as well as and a second battery (100 Ah each) to reinforce the energy supply for the cloudy days. We kept then 2 other batteries as spares at Velas.

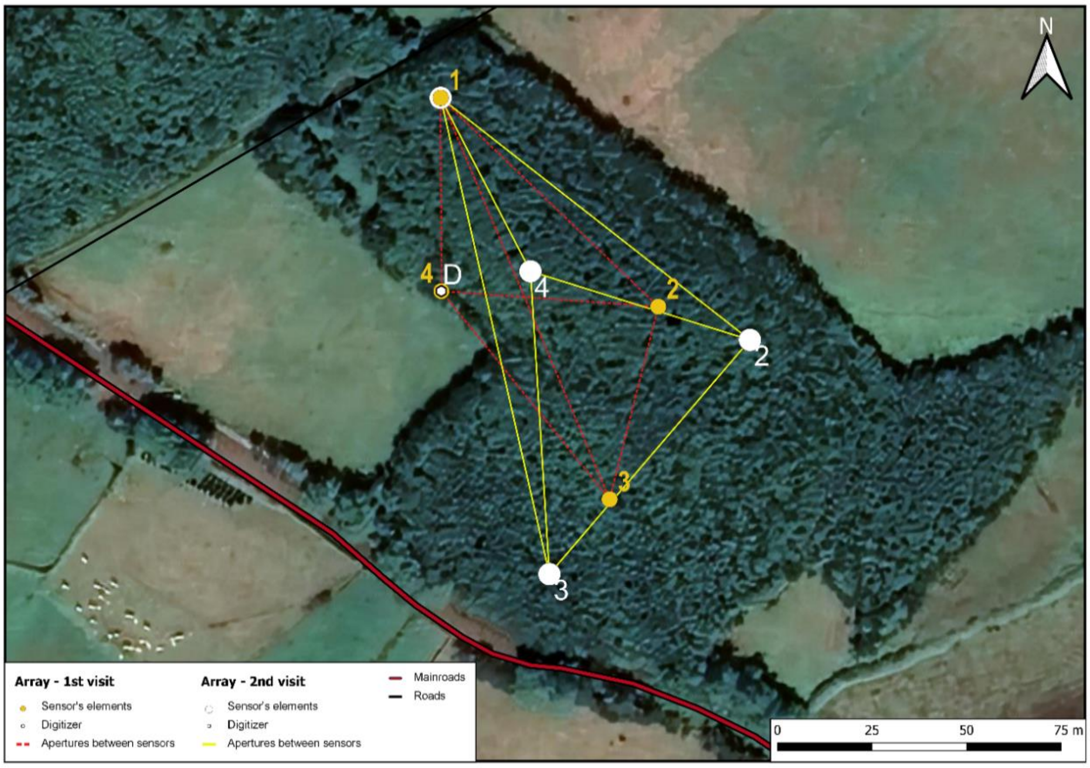

Figure 4.7 – SJ1 arrays deployments compared geometries.

4.2.4.3. Signal testing and recording

At the end of each of the deployments, a laptop was connected to the digitizer to confirm if the signals from the sensors were being recorded as well as to detect possible anomalies.

During the 1st visit, 24-h data were collected, since late afternoon of 2 April 2022 until late afternoon of 3 April 2022, in order to be further analysed in the lab.

The remote access to data only was possible after a week from the first visit once the GSM CARD had to be changed. Thereafter, all periods of 24-h data could be remotely accessed through a server located in Florence (UniFI). Those were analyse using MATLAB® to evaluate the behaviour of noise during day and night-time. Therefore, the processing was distinguished for both arrays, as extensively described below.

Additionally, the local pen-disk was already replaced by an empty one, in May and September.

4.3. Data processing and analysis from SJ1

An initial assessment of performance for both arrays is presented below, consisting in a rudimental PSD analysis from 24-h period of data for each array in similar meteorological conditions.

4.3.1. Meteorological conditions on São Jorge Island

Since meteorological conditions have a major influence on the propagation and consequently record of micro pressure fluctuations by the sensors, the meteorological data recorded at Velas with 1-h interval (IPMA, 2022) was plotted using MS Excel® from 02/04/2022 08:00 PM to 01/06/2022 06:00 PM (see Figure 4.8 and Annex E). Data since 03/05/2022 08:00 PM corresponds to the second visit array. Afterwards, to evaluate noise from 24-h periods of data at each one of the arrays, two 24-periods of meteorological data with similar conditions were selected, particularly with low influence of wind parameters, as shown in Figure 4.8 (see complete plot in Annex E). both PSDs would be under the same weather circumstances.

For the 1st array, it was selected the period between 19/04/2022 12:00 AM to 20/04/2022 12:00 AM, characterized by (1) a mean wind direction (DD_MED, blue colour) ranging from 60° up to 160°; (2) a prevailing wind direction (DD_PRE , dark blue colour) varying from NE, E, and SE ; (3) an average wind intensity (FF_MED , brown colour) from 2 ms^{-1} to 4 ms^{-1}; (4) an average air temperature (T_MED, orange colour) ranging from 13°C up to 15°C; as well as (5) an average pressure at sea level (P_M_MD, light blue colour) of -990 hPa.

For the 2nd array, it was selected the period between 23/05/2022 12:00 AM to 24/05/2022 12:00 AM, characterized by (1) a mean wind direction (DD_MED, blue colour) ranging from 60° up to 160°; (2) a prevailing wind direction (DD_PRE , dark blue colour) varying from NE, E, and SE; (3) an average wind intensity (FF_MED , brown colour) from 1 ms^{-1} to 3 ms^{-1}; (4) an average air temperature (T_MED, orange colour) ranging from 15°C up to 18°C; as well as (5) an average pressure at sea level (P_M_MD, light blue colour) of -990 hPa.

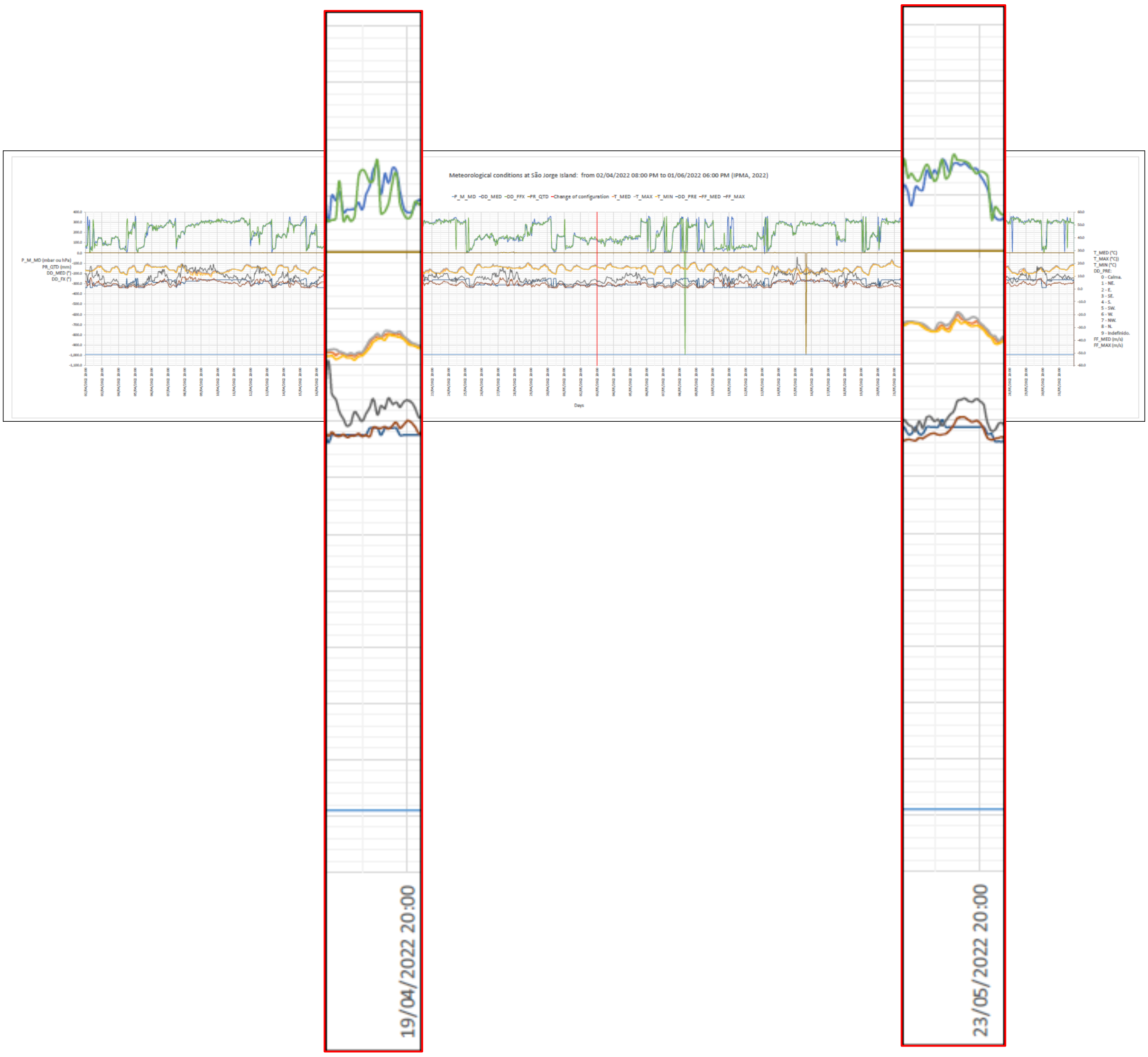

Figure 4.8 – Meteorological data (IPMA, 2022) of the periods selected to analyse PSDs: 19/04/2022 12 AM - 20/04/2022 12 AM for the 1st array (left) and 23/05/2022 12 AM - 24/05/2022 12 AM for the 2nd array (right) (see complete plot in Annex E).

4.3.2. Power Spectral Density (PSD)

PSDs were evaluated from infrasonic data recorded by the four differential pressure transducers of SJ1 array. They were processed individually for 24-hours period from 12:00 AM – 12:00 AM and 12:00 PM – 12:00 PM, overlapping 12 hours in each day. 42 individual PSDs were processed for the 1st array, from 10-04-2022 12:00 AM to 03-05-2022 12:00 PM, as well as 92 for the 2nd array, from 04-05-2022 12:00 AM to 22-06-2022 12:00 AM.

MATLAB® scripts developed by UniFI were used to calculate each PSD, applying the following MATLAB® the function:

[S, F, T, P] = spectrogram (X, WINDOW, NOVERLAP, NFFT, Fs)

Eq. 4.1

where,

- **X** is a vector in the matrix **S**, *i.e.*, it corresponds to the pressure fluctuations values in Pa (**X**), recorded during a previously selected period of 24-h data, from the four sensors (**S**) that are processed through the function, which returns the respective short-time Fourier transforms.
- **WINDOW** is an integer (1000 s in this case) that the function uses to divide **X** into segments of length equal to that integer value and windows each segment with a Hamming window (Harris, 1987).
- **NOVERLAP** samples of overlap between adjoining segments and must be an integer smaller than **WINDOW** if **WINDOW** is an integer, in this case **NOVERLAP** is 50% of the **WINDOW**, i.e., 500 s.
- **NFFT** specifies frequency points used to calculate the discrete Fourier transforms, in this case corresponds to 2^{10}.
- **Fs** specifies the sample rate in Hz, in this case is 100 Hz.

and,

- **S** contains an estimate of the short-term, time-localized frequency content of **X**.
- **F** is a vector of frequencies at which the spectrogram is computed.
- **T** is a vector of times at which the spectrogram is computed.
- **P** is a matrix representing the Power Spectral Density (PSD) of each segment. For real signals, spectrogram returns the one-sided modified periodogram estimate of the PSD of each segment.

The resultant values of **F** and **P** are then plotted into a logarithmic plot to represent the values of PSD (**P**, Pa^2/Hz) depending on the values of frequency (**F**, Hz), which is represented in Figure 4.10

(left), for the 1st array during the period between 19/04/2022 12:00 AM to 20/04/2022 12:00 AM, and Figure 4.12 (left), for the 2nd array during the period between 23/05/2022 12:00 AM to 24/05/2022 12:00 AM.

However, it is only presented here a single PSD processed from the first array and another from the second one. Figures 4.9 and 4.11 illustrate the raw and filtered data of the periods above-mentioned used to calculate the PSDs for the 1st and 2nd array, respectively. Figures 4.10 and 4.12 represent the PSD plot and the spectrogram of sensor 1 for the 1st and 2nd array, respectively.

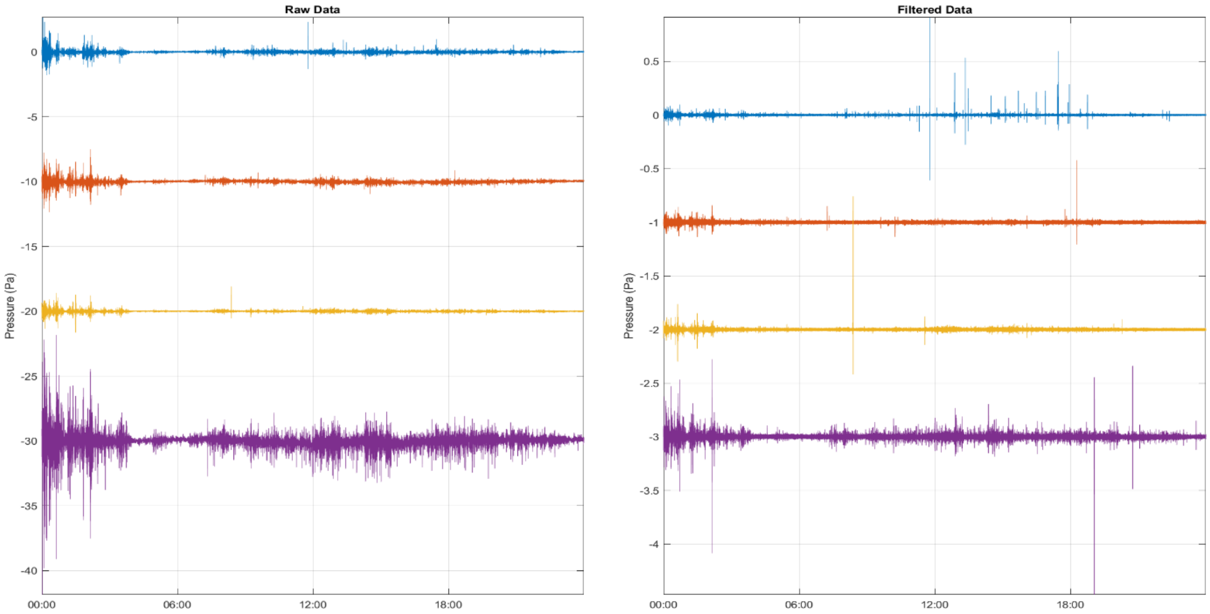

Figure 4.9 – Raw (left) and filtered (right) data of the period between 19/04/2022 12 AM to 20/04/2022 12 AM (1st array).

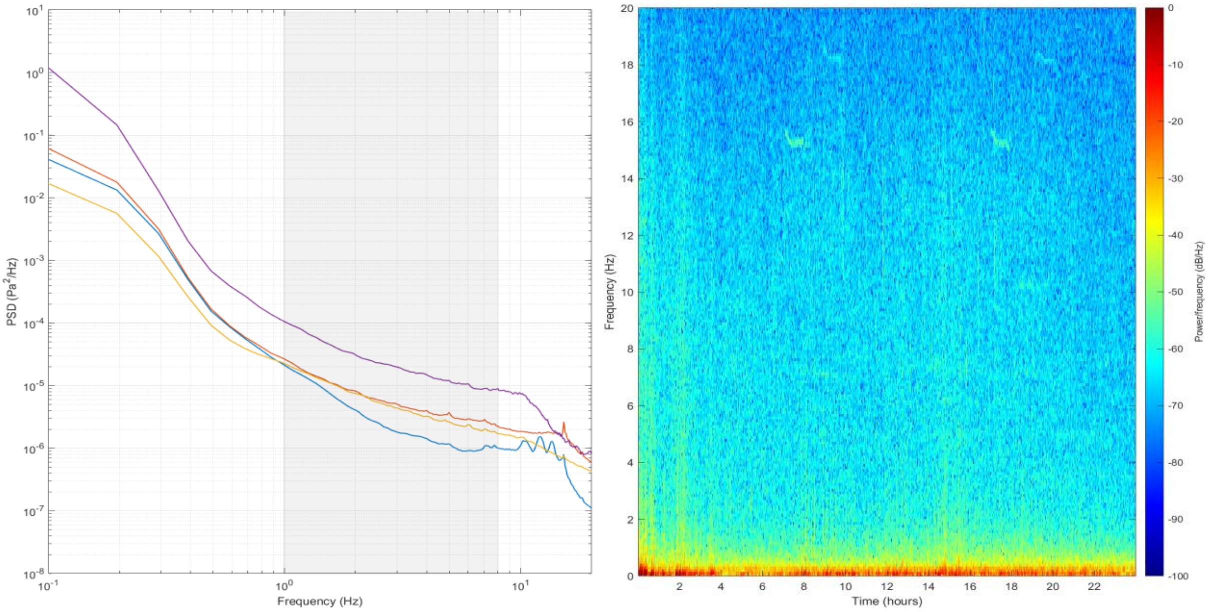

Figure 4.10 – PSD plot (left) and spectrogram of sensor 1 (right) from the data of the period between 19/04/2022 12 AM to 20/04/2022 12 AM (1st array) (blue transparency represents the interval of frequencies between 1 and 8 Hz).

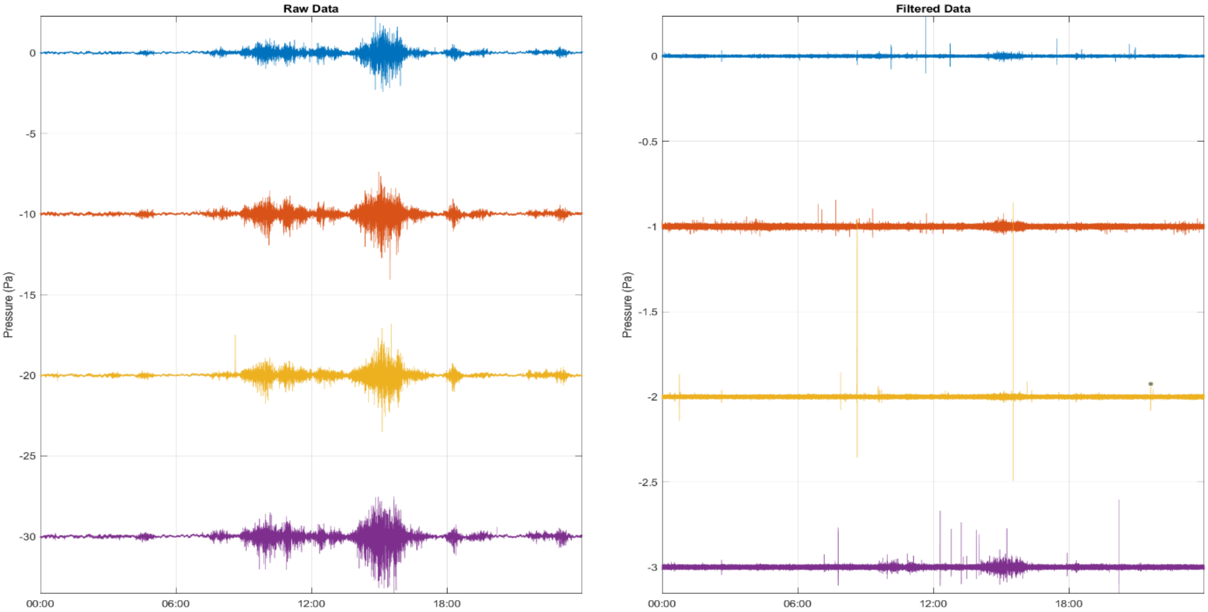

Figure 4.11 – Raw (left) and filtered (right) data of the period between 23/05/2022 12 AM to 24/05/2022 12 AM (2nd array).

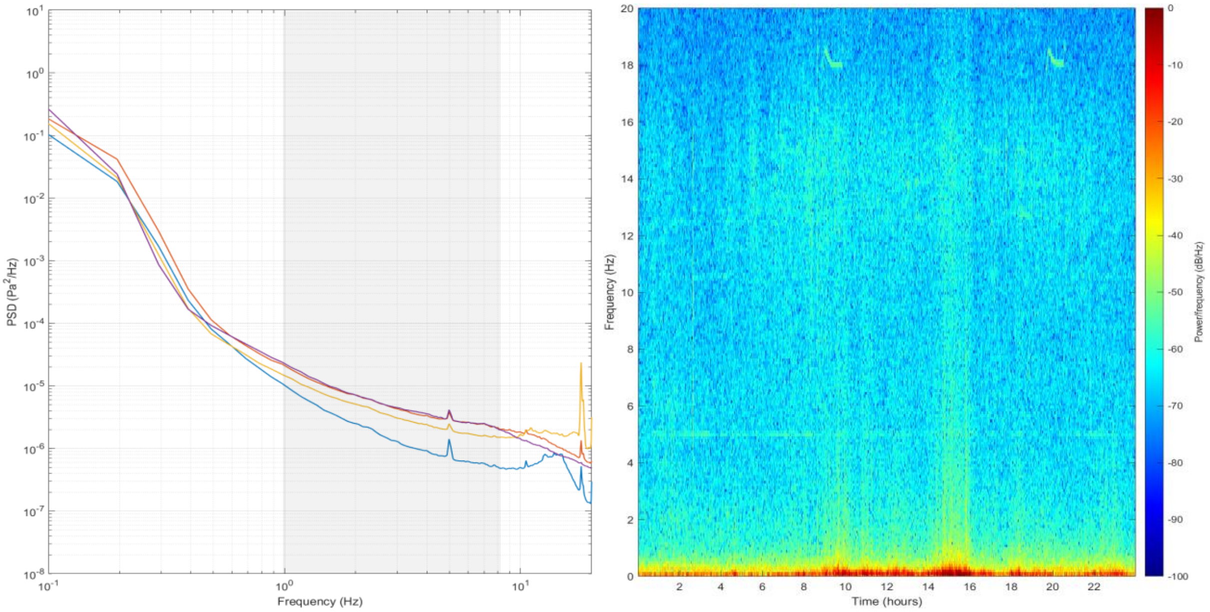

Figure 4.12 – PSD plot (left) and spectrogram of sensor 1 (right) from the data of the period between 23/05/2022 12 AM to 24/05/2022 12 AM (2nd array) (blue transparency represents the interval of frequencies between 1 and 8 Hz).

4.4. Discussion of the results

Regarding the meteorological data, it is important to mentioned that the values plotted are unfiltered. Also, they were measured at a meteorological station of IPMA (Instituto Português do Mar e da Atmosfera) in Velas, located at sea level, and SJ1 is located around 368 metres *a.s.l.*, which means that the values used should have a significant difference than the real ones at SJ1. Furthermore, it is possible to verify from the data presented herein that the only parameter with a major difference between both periods analysed for each array is the average air temperature, once after the 2nd array was configurated the weather was in transition from spring to summer seasons. Thus, the average air temperature is higher for the period of the 2nd array.

In terms of instrumentation, the comparison of both PSDs, represented in Figure 4.13, confirms that the 2nd array, configurated within a centered triangular geometry, shows a greater coherence of signal and response resemble between the 4 sensors of SJ1 than the 1st array.

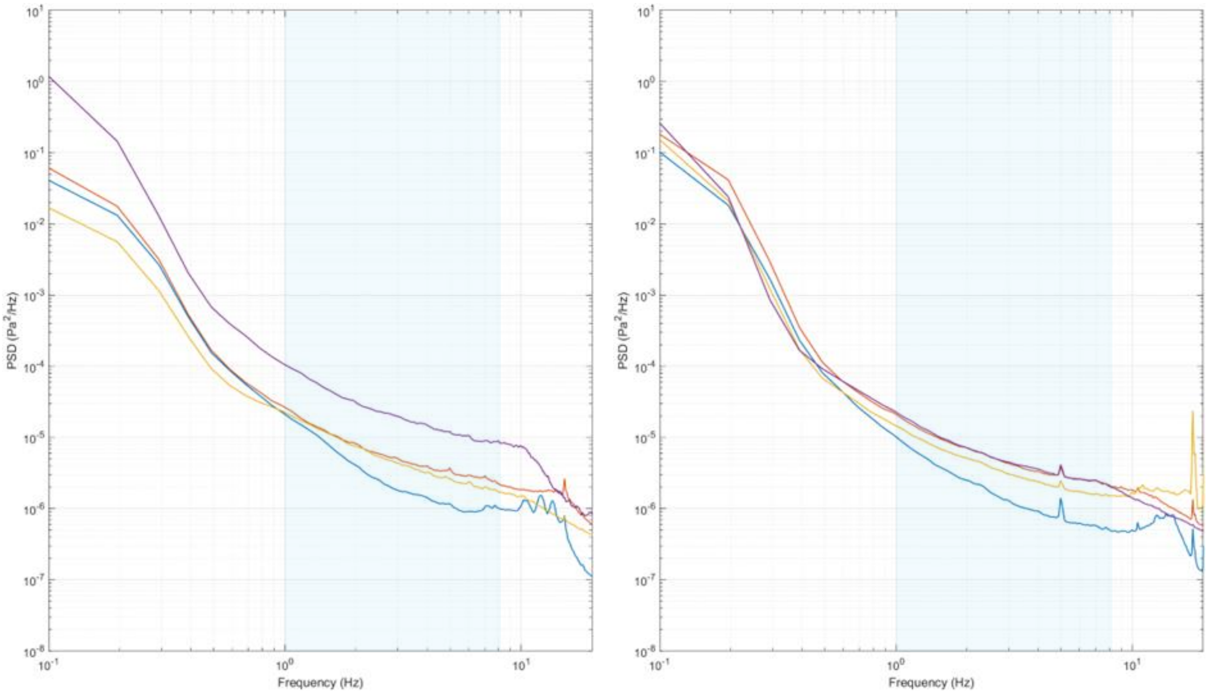

Figure 4.13 – PSD plots for the 1st array (left) 2nd array (right) from the data of the periods between 19/04/2022 12 AM to 20/04/2022 12 AM, and 23/05/2022 12 AM to 24/05/2022 12 AM, respectively (blue transparency represents the interval of frequencies between 1 and 8 Hz).

Regarding the analysis of noise at the array, we know by the theoretical background on the subject, as written in Marty *et al*. (2021), that above the cut-off frequency of infrasound (3.21 mHz, see subchapter **1.2. Infrasound concept and definition**), (1) wind turbulence is the major source of most of the spectral energy (Bowman *et al*., 2005; Walker and Hedlin, 2010); (2) for low wind conditions, acoustic waves as the microbarom frequency band (0.1 - 4 Hz) are dominant in the pressure spectra (Willis *et al*., 2004; Le Pichon *et al*., 2006), as well as above 1 Hz, in case of existing local sources such as surf or man-made activities (Garcés *et al*. 2006; Brachet *et al*. 2010).

Nevertheless, the present research study has only processed individually PSD of 24-h data. It would be necessary a further and more complex integration of all PSDs, requiring computing the mean PSD for both arrays and consequent analysis of the PDFs (probability density function) in order to evaluate the probability of a given frequency range be detected by each array. Thus, it would be possible to firmly discuss the results as well as get valid conclusions on signal-to-noise ratio and detection capability.

Nonetheless, a quick way to check a good signal-to-noise ratio would be to observe its best indicator on PSDs, *i.e*, the microbarom peak (0.1 - 4 Hz) (Paola Campus, *personal communication*). However, once SJ1 array has only a 130 metres aperture, it is only able to detect frequencies above 1Hz. Therefore, for this scenario it would be important to identify other know common source to infer the signal-to-noise ratio. As see in Figure 4.13, the PSD for the 2nd array (right) has a peak around 4 Hz, that is constant in all the rest of PSDs from the same array configuration. However, it is yet to be identified.

One way to have a robust noise analysis would be to apply the same methodology developed by Marty *et al.* (2021). The new noise models proposed, illustrated in Figure 4.14, can be used in diverse applications, such as in (1) assessing the quality of measured pressure fluctuations; (2) verifying the validity of modelled pressure fluctuations, as well as (2) supporting the design, testing, and calibration of a new generation of measurement systems (Marty *et al*., 2021).

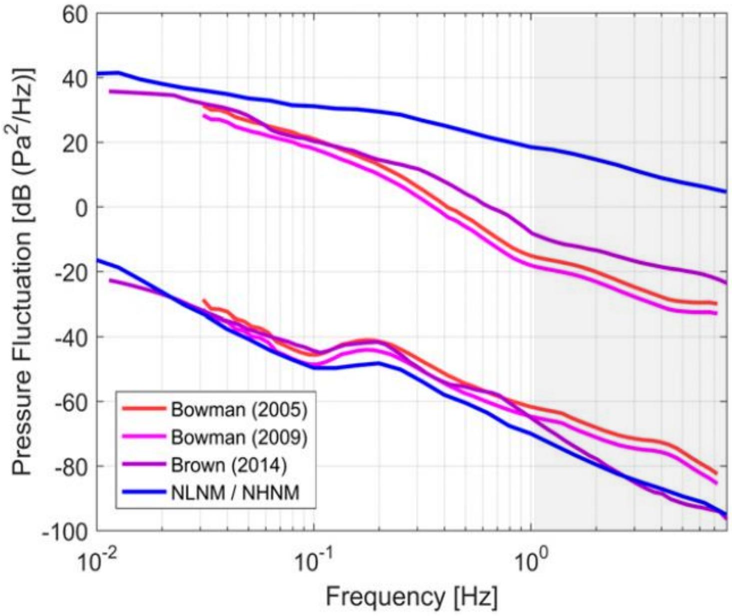

Figure 4.14 - Comparison of the NLNM (New Low Noise Model) and NHNM (New High Low Noise Model) with previously proposed models between 0.01 and 8 Hz (Marty *et al*.,2021). A blue transparency was added to represent the interval of frequencies between 1 and 8 Hz.

Differently from the approach used in MATLAB in this study to compute the PSDs, Marty *et al*. (2021) applied the Welch's (1967) technique with a Hann function and 9 time windows with 50% overlap for each PSD segment. Then, the resultant PSDs were processed for each of these measurement systems on six frequency bands, considering a period of a year, which corresponds to a total of around 150 million PSDs computed. Hence, those PSDs were used as inputs to compute monthly probability density functions (PDFs) over the full frequency range for each measurement system, in order to illustrate the probability of a PSD to fall within a particular range of values at each given frequency, thus being possible a more detailed analysis on the detection capability of signals in the range of interest.

However, Marty *et al*. (2021) developed these models using several IMS infrasound stations. Therefore, once UniFI arrays have different instruments (iTem) with different sensitivities, those noise models presented above could not apply in the same way. Then, it would be interesting to apply the same methodology for all UniFI infrasound arrays and develop their own noise models to compare them later with the ones from Marty *et al*. (2021), also using the same MATLAB® function (*pwelch*) instead of the one used herein (*spectrogram* (Eq. 4.1)).

FINAL CONSIDERATIONS

The geological history of the Azores Islands and the 2022 volcanic unrest of Manadas fissure volcanic system on São Jorge Island showed the importance of the development of a strategy to complement the existing seismovolcanic monitoring efforts with the infrasound techniques.

The references to the works of site surveys methodologies to which it was possible to have access date back to about 20 years ago. , which were an incentive to the development of this research study since its beginning, with its application to the demanding environment of oceanic islands.

Also, even though the eruptive scenarios were just hypothetically without further complex simulations, they have required a lot of further research in order to be reliable.

Once the survey methodology developed was basically qualitative, after the definition of the 3 buffers, it was very exhaustive selection using basically an eye view, instead of automatic tools through GIS software due to the beginner experience with this type of software.

At last, the approach during the assessment in *situ* using a check list of the parameters to be evaluated had shown efficient results to select the sites for the signal testing phase in quantitative and practical way.

Considering these topics, it would be interesting to develop the following subjects in future works:

- Simulate more complex eruptive scenarios, particularly the worst possible case scenarios including the direction of the lava and/or pyroclastic flows as well as tropospheric and stratospheric wind, to have a complete idea in the level of safety regarding the distance of the sensors to the source, and if necessary, change the distances of the buffers in relation to the VEI estimated for an eruptive scenario. Also, further studies would be considered intersection buffer areas from the volcanoes simultaneously, because if, in reality, one volcano on an island begin to erupt, we have to pay attention to the remaining volcanic systems, event central or fissural. However, in the Azores Islands, it is practically impossible in the cases referred to choose sites in inactive areas. Normally the arrays are located within eruptive active fissure systems areas, or others where materials can flow/deposit there, or on the flanks of the volcano.
- Modelling of non-linear local infrasound propagation, considering winds on the turbulent boundary layer and troposphere, as well as topography barriers to simulate near-reality the arrivals of direct waves to the sites, and then configurated to best array design to detect them.
- Modelling an automatic, efficient, fast site selection, considering the main constraints and requirements for an infrasound site survey, such as forests, topography, eruptive scenarios, infrastructures, high noise backgrounds, in order to exclude immediately the areas that don´t serve

those necessities for a good site survey and further deployment of an infrasound array. It would be valuable to integrate date from terrain imagery (remote sensing techniques), as well as aerial photography through drone imagery techniques. Also, the input on this modelling of land registration would facilitate the processes to contact the owners of each selected site.

- Move forward with the signals testing phase, firstly on São Miguel Island and later for the remaining ones, which would need an extensive knowledge and training of the device SISTEM® from SEISMOWAVE (IS arrays).
- Design a mobile infrasound monitoring network, firstly for São Miguel Island and then, after testing all sites in the rest of the Islands, for all the Azorean archipelago, to function mainly as a regional infrasound monitoring network integrated with other regional monitoring networks, as the seismic one of CIVISA.

The 2022 São Jorge volcanic unrest was a benefit exercise within a real crisis to conduct an infrasound site survey to deploy faster as possible an infrasound array on an island with unfavourable geological features to select a good site for local infrasound detections.

The major limitation on this topic was the data processing on MATLAB®, once it was the first introduction to programming, and with the results presented herein it was not possible to get firm conclusion mostly regarding background noise at SJ1, and consequently about signal-to-noise ratio and detection capability. However, the results show that the 2nd array design (centred triangular) have an optimal response between the 4 sensors.

Furthermore, the meteorological data presented are unfiltered and recorded on a location at sea level, and SJ1 array is located more than 300 a.s.l, where those data would be slightly different.

Therefore, considering these topics, it would be necessary to improve the data processing analysis from SJ1 by developed the following issues:

- Add a meteorological station to the array, to know the values in *situ*. It would be valuable to learn how to integrate weather data with infrasound on MATLAB® and, consequently, interpretate the results and the meteorological influence on the PSDs.
- Gather information on anthropogenic noise, *e.g.* roads, wind generators, mechanical milking, etc., once they are regular spikes that show up on PSDs.
- Characterize the already identified known sources for both arrays as a sort of calibration signal, to infer signal-to-noise ratio, once SJ1 array is not able to detect frequencies below 1 Hz, thus the microbarom peak would not be identifiable. The first array has detected one low magnitude earthquake, whose work is already being prepared by the lab team, and the second array has been recording ground-truth events of blasts in a basaltic quarry in Pico Island as well as a meteor north

offshore of São Miguel Island, which was also detect by IS42 and the seismic network of CIVISA on São Miguel Island.

- Apply the methodology of Marty *et al*. (2021) in order to continuously compute all PSDs, through Welch's Method, for a further PDFs processing, where several pass-band filters would be applied, similarly to what is done with the IMS data. This would facilitate the comparison between data from SJ1 array and IS42.
- Further research on the optimal and ideal array design to face the constrains of the high noise of all year windy weather conditions in the Azores Islands.

.

REFERENCES

Bibliography

Arendt S. and Fritts D. C. (2000). Acoustic radiation by ocean surface waves. J. Fluid Mech., vol. 415, pp. 1-21. Cambridge University Press, United Kingdom.

Bass H. E., Sutherland L. C., Zuckerwar A. J., Blacstock D. T., Hester D. M. (1995). Atmospheric absorption of sound: Further developments. J. Acoust. Soc. Am., 97, 680–683.

Bass *et al*. (2003). Infrasound monitoring of Atmospheric Events. 25th Seismic Research Review - Nuclear explosion Monitoring: Building the Knowledge Base, 577-586.

Bass H. E., Bhattacharyya J., Garcés M., Hedlin M., Olson J. V., Woodward R. L. (2006). Infrasound. Acoustics Today, Vol. 2, Issue 1, 9-19. Acoustical Society of America.

Bedard A. and Georges T. M. (2000). Atmospheric infrasound. Physics Today 53, 3, 32. DOI: 10.1063/1.883019.

Beier C., Haase K. M., Abouchami W., Krienitz M-S., Hauff F. (2008). Magma genesis by rifting of oceanic lithosphere above anomalous mantle: Terceira Rift, Azores. Geochem. Geophys. Geosyst., 9, Q12013. DOI:10.1029/2008GC002112.

Blanc E. and Ceranna L. (2009). Infrasound in Science for Security: Verifying the Comprehensive Nuclear-Test-Ban Treaty. Paper presented at International Scientific Studies Conference (Austria), Vienna (pp. 1-16). Vienna, Austria: Preparatory Commission for the Comprehensive Nuclear-Test-Ban Treaty Organization (CTBTO).

Booth B., Croasdale R., Walker G. P. L. (1978). A Quantitative Study of Five Thousand Years of Volcanism on São Miguel, Azores. Phil. Trans. R. Soc. Lond. A, 288. DOI: 10.1098/rsta.1978.0018.

Brachet N., Brown D., Le Bras R., Cansi Y., Mialle P., Coyne J. (2010). Monitoring the Earth's Atmosphere with the Global IMS Infrasound Network. In: Le Pichon A., Blanc E., Hauchecorne A. (eds) Infrasound Monitoring for Atmospheric Studies. Springer, Dordrecht. DOI: 10.1007/978-1-4020-9508-5_3.

Bowman J. R., Baker G. Eli, Bahavar M. (2005). Ambient infrasound noise. Geophysical Research Letters, vol. 32, L09803. DOI: 10.1029/2005GL022486.

Brown D. J., Katz C. N., Le Bras R., Flanagan M. P., Wang J., Gault A. K. (2002). Infrasonic Signal Detection and Source Location at the Prototype International Data Centre. Pure and Applied Geophysics, Vol. 159, 1081-1125.

Calvert A. T., Moore R. B., McGeehin J. P., Silva A. M. R. (2006). Volcanic history and $^{40}Ar/^{39}Ar$ and ^{14}C geochronology of Terceira Island, Azores, Portugal. Journal of Volcanology and Geothermal Research 156, 103-115. Elsevier. DOI: 10.1016/j.jvolgeores.2006.03.016.

Campus P. and Christie D. R. (2010). Worldwide Observations of Infrasonic Waves. In: Le Pichon A., Blanc E., Hauchecorne A. (eds) Infrasound Monitoring for Atmospheric Studies. Springer, Dordrecht. DOI: 10.1007/978-1-4020-9508-5_6.

Campus P., Ripepe M., Marchetti E., Le Pichon A., Vergoz J., Fyen J., Kvaerna T., Ceranna L., Liszka L., Evers L. (2010). Infrasound detections and calibration experiments. Poster communication.

Campus P., Ripepe M., Marchetti E., Genco R. (2017). Near-field detections of UniFI arrays, synergies with IMS infrasound arrays. Poster communication.

Cansi Y. (1995). An automatic seismic event processing for detection and location: The P.M.C.C. method. Geophysical Research Letters, Vol. 22, No 9, 1021-1024. American Geophysical Union.

Capello A., Zanon V., Del Negro C., Ferreira T. J. L., Queiroz M. G. P. S. (2015). Exploring lava-flow hazards at Pico Island, Azores Archipelago (Portugal). Terra Nova, Vol 27, No. 2, 156-161. John Wiley & Sons.

Carmo R. L. (2013). Estudos de Neotectónica na Ilha de S. Miguel, uma Contribuição para o Estudo do Risco Sísmico no Arquiélago dos Açores. PhD dissertation in Geology, specialty in Volcanology. Departamento de Geociências, Universidade dos Açores.

Carmo R., Madeira J., Ferreira T., Queiroz G., Hipólito A. (2015). Volcano-tectonic structures of São Miguel, Azores. In: Gaspar J. L., Guest J. E., Duncan A. M., Barriga F. J. A., S., Chester D. K. (eds) Volcanic Geology of São Miguel Island (Azores Archipelago). Geological Society, London, Memoirs, 44, 65-86. DOI: 10.1144/M44.6.

Christie D. R., Kennett B. L. N., Tarlowski C. (2006). Detection of atmospheric explosions at IMS monitoring stations using infrasound techniques. 28th Seismic Research Review: Ground-Based Nuclear Explosion Monitoring Technologies.

Christie D. R. (2007). Verification science - Recent developments in infrasound monitoring technology: application to CTBT verification. CTBTO Spectrum 10, 18-24.

Christie D. and Campus P. (2010). The IMS Infrasound Network: Design and Establishment of Infrasound Stations. In: Le Pichon A., Blanc E., Hauchecorne A. (eds) Infrasound Monitoring for Atmospheric Studies. Springer, Dordrecht. DOI: 10.1007/978-1-4020-9508-5_2.

Cole P. D., Queiroz G., Wallenstein N., Gaspar J. L., Duncan A., M., Guest J. E. (1995). An historic subplinian/phreatomagmatic eruption: the 1630 AD eruption of Furnas volcano, São Miguel, Azores. Journal of Volcanology and Geothermal Research, 69, 117-135. Elsevier.

Cole P. D., Guest J. E., Queiroz G., Wallenstein N., Pacheco J. M., Gaspar J. L., Ferreira T., Duncan A., M. (1999). Styles of volcanism and volcanic hazards on Furnas volcano, São Miguel, Azores. Journal of Volcanology and Geothermal Research, 92, 39-53. Elsevier.

Cole P. D., Pacheco J. M., Gunasekera R., Queiroz G., Gonçalves P., Gaspar J. L. (2008). Contrasting styles of explosive eruption at Sete Cidades, São Miguel, Azores, in the last 5000 years: Hazard implications from modelling. Journal of Volcanology and Geothermal Research, 178, 574-591. Elsevier. DOI: 10.1016/j.jvolgeores.2008.01.008.

Dain Y. and Lueptow R., M. (2001). Acoustic attenuation in a three-gas mixture: Results. J. Acoust. Soc. Am., 110, 2974-2979. DOI: 10.1121/1.1413999.

de Groot-Hedlin C. (2008). Finite-difference time-domain synthesis of infrasound propagation through an absorbing atmosphere. J. Acoust. Soc. Am., 124, 1430-1441. DOI: 10.1121/1.2959736.

de Groot-Hedlin C. D., Hedlin M. A. H., Drob D. P. (2010). Atmospheric Variability and Infrasound Monitoring. In: Le Pichon A., Blanc E., Hauchecorne A. (eds) Infrasound Monitoring for Atmospheric Studies. Springer, Dordrecht. DOI: 10.1007/978-1-4020-9508-5_15.

de Groot-Hedlin C., Hedlin M. A. H., Walker K. (2011). Finite difference synthesis of infrasound propagation through a windy, viscous atmosphere: application to a bolide explosion detected by seismic networks. Geophys. J. Int., 185, 305–320. DOI: 10.1111/j.1365-246X.2010.04925.x.

Diaz-Moreno A., Roca A., Lamur A., Munkli B. H., Ilanko T., Pering T. D., Pineda A., De Angelis S. (2020). Characterization of Acoustic Infrasound Signals at Vólcan de Fuego, Guatemala: A Baseline for Volcano Monitoring. Front. Earth Sci. 8:549774. DOI: 10.3389/feart.2020.549774.

Drob D. P., Garcés M., Hedlin M., Brachet N. (2010). The Temporal Morphology of Infrasound Propagation. Pure and Applied Geophysics, 167, 437-453. US Government. DOI: 10.1007/s00024-010-0080-6.

Evers L. G. and Haak H. W. (2004). The detectability of infrasound in the Netherlands from the Italian volcano Mt. Etna. Journal of Atmospheric and solar-Terrestrial Physics, 67, 259-268. Elsevier. DOI: 10.1016/j.jastp.2004.09.002.

Evers L. and Haak H. (2010). The Characteristics of Infrasound, its Propagation and Some Early History. In: Le Pichon A., Blanc E., Hauchecorne A. (eds) Infrasound Monitoring for Atmospheric Studies. Springer, Dordrecht. DOI: 10.1007/978-1-4020-9508-5_1.

Ferreira T., Gomes A., Gaspar J. L., Guest J. E. (2015). Distribution and significance of basaltic eruptive centres: São Miguel, Azores. In: Gaspar J. L., Guest J. E., Duncan A. M., Barriga F. J. A., S., Chester D. K. (eds) Volcanic Geology of São Miguel Island (Azores Archipelago). Geological Society, London, Memoirs, 44, 135-146. DOI: 10.1144/M44.10.

Forjaz V. H., Fernandes, N. A. M. (1975). Notícia explicativa da folha “A” e “B”: Ilha de S. Jorge (Açores), Carta Geológica de Portugal. Serviços Geológicos de Portugal, Lisboa.

Garcés M., Hagerty M. T., Schwartz S. Y. (1998). Magma acoustics and time-varying melt properties at Arenal Volcano, Costa Rica. Geophysical Research Letters, Vol. 25, No 13, 2293-2296. American Geophysical Union.

Garcés M., Hetzer C., Merrifield M., Willis M., Aucan J. (2003). Observations of surf infrasound in Hawai'i. Geophysical Research Letters, Vol. 30, No 24, 2264. American Geophysical Union. DOI: 10.1029/2003GL018614.

Garcés M., Willis M., Hetzer C. (2004). On using ocean swells for continuous infrasonic measurements of winds and temperature in the lower, middle, and upper atmosphere. Geophysical Research Letters, Vol. 31, L19304. American Geophysical Union DOI: 10.1029/2004GL020696.

Garcés M., Aucan J., Fee D., Caron P., Merrifield M., Gibson R., Bhattacharyya J., Shah S. (2006). Infrasound from large surf. Geophysical Research Letters, Vol. 33, L05611. American Geophysical Union DOI: /10.1029/2005GL025085.

Gaspar J. L. R. B. (1996). Ilha Graciosa (Açores). História Vulcanológica e Avaliação do Hazard. PhD dissertation in Geology, specialty in Volcanology. Departamento de Geociências, Universidade dos Açores.

Gaspar J. L., Queiroz G., Pacheco J. M., Ferreira T., Wallenstein N., Almeida M. H., Coutinho R. (2003). Basaltic lava balloons produced during the 1998-2001 Serreta Submarine Ridge eruption (Azores). In: White J., Clague D., Smellie J. (eds.) Subaqueous Explosive Volcanism. Geophysical Monograph, 140, 205-212. American Geophysical Union.

Gaspar J. L., Queiroz G., Ferreira T. (2012). Escala de alertas científicos para a caracterização do estado de actividade sismovulcânica na região dos Açores. CIVISA.

Gaspar J. L., Guest J. E., Duncan A., Chester D., Barriga F. (2015a). Volcanic geology of São Miguel Island (Azores Archipelago): introduction. In: Gaspar J. L., Guest J. E., Duncan A. M., Barriga F. J. A., S., Chester D. K. (eds) Volcanic Geology of São Miguel Island (Azores Archipelago). Geological Society, London, Memoirs, 44, 1-3. DOI: 10.1144/M44.1.

Gaspar J. L., Queiroz G., Ferreira T., Medeiros A. R., Goulart C., Medeiros J. (2015b). Earthquakes and volcanic eruption in the Azores region: geodynamic implications from major historical events and instrumental seismicity. In: Gaspar J. L., Guest J. E., Duncan A. M., Barriga F. J. A., S., Chester D. K. (eds) Volcanic Geology of São Miguel Island (Azores Archipelago). Geological Society, London, Memoirs, 44, 33-49. DOI: 10.1144/M44.4.

Gaspar J. L., Guest J. E., Queiroz G., Pacheco J., Pimental A., Gomes A., Marques R., Felpeto A., Ferreira T., Wallenstein N. (2015c). Eruptive frequency and volcanic hazards zonation in São Miguel Island, Azores. In: Gaspar J. L., Guest J. E., Duncan A. M., Barriga F. J. A., S., Chester D. K. (eds) Volcanic Geology of São Miguel Island (Azores Archipelago). Geological Society, London, Memoirs, 44, 155-166. DOI: 10.1144/M44.12.

Georges T. M. and Beasley W. H. (1977). Refraction of infrasound by upper-atmospheric winds. J. Acoust. Soc. Am., Vol. 61, No. 1.

Grover F. H. (1971). Experimental Noise Reducers for an Active Microbarograph Array. Geophys. J. R. astr. Soc., 26, 41-52.

Guest J. E., Gaspar J. L., Cole P. D., Queiroz G., Duncan A. M., Wallenstein N., Ferreira T., Pacheco J. M. (1999). Volcanic geology of Furnas Volcano, São Miguel, Azores. Journal of Volcanology and Geothermal Research, 92, 1-29. Elsevier.

Guest J. E., Pacheco J. M., Cole P. D., Duncan A. M., Wallenstein N. W., Queiroz G., Gaspar J. L., Ferreira T. (2015). The volcanic history of Furnas Volcano, São Miguel, Azores. In: Gaspar J. L., Guest J. E., Duncan A. M., Barriga F. J. A., S., Chester D. K. (eds) Volcanic Geology of São Miguel Island (Azores Archipelago). Geological Society, London, Memoirs, 44, 125-134. DOI: 10.1144/M44.9.

Harris F. J. (1987). Multirate FIR Filters for Interpolating and Desampling. In: Elliott D. F. (ed) Handbook of Digital Signal Processing. Academic Press, 173-287. DOI: 10.1016/B978-0-08-050780-4.50008-4.

Haubrich R. A. (1968). Array Design. Bulletin of the Seismological Society of America, vol. 58 nº 3, 977-991.

Hedlin M. and Berger J. (2000). Report on Infrasound Site-Survey at IS56, Newport, WA. 43-78.

Hedlin M. A. H., Berger J., Zumberge M. (2000). Evaluation of Infrasonic Spatial Filters. Report. Defense Threat Reduction Agency.

Hedlin M. A. H., Berger J., Vernon F. L. (2002). Surveying Infrasonic Noise on Oceanic Islands. Pure and Applied Geophysics, vol. 159, 1127-1152. Birkhäuser Verlag, Basel.

Hedlin A. H., Alcoverro B., D'Spain G. (2003a). Evaluation of rosette infrasonic noise-reducing spatial filters. J. Acoust. Soc. Am. 114 (4), 1807-1820. Acoustical Society of America. DOI: 10.1121/1.1603763.

Hedlin M. A. H., Berger J., Vernon F. L. (2003b). Reconnaissance of Background Infrasound at Selected Future IMS Locations, Atlantic Ocean. Technical Report. Defense Threat Reduction Agency.

Hedlin M. A. H. and Raspet R. (2003). Infrasonic wind-noise reduction by barriers and spatial filters. J. Acoust. Soc. Am. 114 (3), 1379-1386. Acoustical Society of America. DOI: 10.1121/1.1598198.

Hedlin M. A. H., Walker K., Drob D. P., de Groot-Hedlin C. D. (2012). Infrasound: Connecting the Solid Earth, Oceans, and Atmosphere. Annual Review of Earth and Planetary Sciences, 40:327-54. DOI: 0084-6597/12/0530-0327$20.00.

Hedlin M. A. H. and Walker K. T. (2013) A study of infrasonic anisotropy and multipathing in the atmosphere using seismic networks. Philosophical Transactions of the Royal Society. DOI: 10.1098/rsta.2011.0542.

Herrin E. T., Golden P. W., Bass H. E., Norris D. E., Andre B., de Groot-Hedlin C., Woodward R. L., Walker K. T., Drob D. P., Szuberla C. A. L., Hedlin M. A. H., Whitaker R. W., Garcés M. A., Shields F. D. (2008). High-altitude Infrasound Calibration Experiments. In: Acoustics Today, Volume 4, Issue 2. Acoustical Society of America.

Hildenbrand A., Madureira P., Marques Ornelas F., Cruz I., Henry B., Silva P. (2008). Multi-stage evolution of a sub-aerial volcanic ridge over the last 1.3 Myr: S. Jorge Island, Azores Triple Junction. Earth and Planetary Science Letters 273, 289-298. Elsevier. DOI: 10.1016/j.epsl.2008.06.041.

Holton J. R. and Hakim G. J. (2013). An Introduction to Dynamic Meteorology, Fifth Edition. Elsevier.

Johnson J. (2019). Local Volcano Infrasound Monitoring. In: Le Pichon A., Blanc E., Hauchecorne A. (eds) Infrasound Monitoring for Atmospheric Studies - Challenges in Middle Atmosphere Dynamics and Societal Benefits. Springer, Cham. DOI: 10.1007/978-3-319-75140-5_32.

Kaimal J. C. and Finnigan J. J. (1994). Atmospheric Boundary Layer Flows - Their Structure and Measurement. Oxford University Press, New York.

Kambezidis H. D. (2012). The Solar Resource. In: Sayigh A. (ed) Comprehensive Renewable Energy, Volume 3: Solar Thermal Systems: Components and Applications. Elsevier. DOI:10.1016/B978-0-08-087872-0.00302-4.

Lacanna G. and Ripepe M. (2012). Influence of near-source volcano topography on the acoustic wavefield and implication for source modelling. Journal of Volcanology and Geothermal Research, 250, 9-18. DOI: 10.1016/j.jvolgeores.2012.10.005.

Le Pichon A., Blanc E., Barthélémy M., Drob D. P. (2002). Acoustic propagation and atmosphere characteristics derived from infrasonic waves generated by the Concorde. J. Acoust. Soc. Am., Vol. 111, No. 1, Pt. 2., 629-641. DOI: 10.1121/1.1404434.

Le Pichon A., Blanc E., Drob D., Lambotte S., Dessa J. X., Lardy M., Bani P., Vergniolle S. (2005a). Infrasound monitoring of volcanoes to probe high-altitude winds. Journal of Geophysical Research, Vol. 110, D13106. American Geophysical Union. DOI: 10.1029/2004JD005587.

Le Pichon A., Ceranna L., Garcés M., Drob D., Millet C. (2006). On using infrasound from interacting ocean swells for global continuous measurements of winds and temperature in the stratosphere. Journal of Geophysical Research, Vol. 111, D11106. American Geophysical Union. DOI: /10.1029/2005JD006690.

Le Pichon A., Vergoz J., Herry P., Ceranna L. (2008). Analyzing the detection capability of infrasound arrays in Central Europe. Journal of Geophysical Research, Vol. 113, D12115. American Geophysical Union. DOI: 10.1029/2007JD009509.

Lourenço N., Miranda J. M., Luis J. F., Ribeiro A., Mendes Victor L. A., Madeira J., Needham H. D. (1998). Morpho-tectonic analysis of the Azores Volcanic Plateau from a new bathymetric compilation of the área. Marine Geophysical Researches 20, 141-156. Kluwer Academic Publishers, Netherlands.

Maceira M., Blom P. S., MacCarthy J. K., Marcillo O. E., Euler G. G., Begnaud M. L., Ford S. R., Pasyanos M., E., Orris G. J., Foxe M. P., Arrowsmith S. J., Merchant B. J., Slinkard M. E. (2017). Trends in Nuclear Explosion Monitoring Research & Development – A Physics Perspective. U.S. Department of Energy. DOI:10.2172/1355758.

Machado F. (1959a). Submarine pits of the Azores plateau. Bull. Volcanol., Série II, Tome XXI, 109-116.

Machado F. (1959b). Actividade vulcânica da ilha do Faial (Mai/Ago 1958). Atlântida, III, 40-55.

Madeira J. (1998). Estudos de Neotectónica nas ilhas do Faial, Pico e S. Jorge: uma contribuição para o conhecimento geodinâmico da junção tripla dos Açores. PhD dissertation. Universidade de Lisboa.

Madeira J., and Brum da Silveira A. (2003). Active tectonics and first paleoseismological results in Faial, Pico and S. Jorge islands (Azores, Portugal). Annals of Geophysics, Vol. 46, N. 5, 733-761.

Madeira J. (2005). The volcanoes of Azores Islands: a world-class heritage, examples from Terceira, Pico and Faial Islands - Field Trip Guide Book. IV International Symposium ProGEO on the Conservation of the Geological Heritage.

Madeira J. (2007). A erupção dos Capelinhos e o vulcanismo nos Açores. Boletim do Núcleo Cultural da Horta, 16: 29-44.

Madeira J., Brum da Silveira A., Hipólito A., Carmo R. (2015). Active tectonics in the central and eastern Azores islands along the Eurasia-Nubia boundary: a review. In: Gaspar J. L., Guest J. E., Duncan A. M., Barriga F. J. A., S., Chester D. K. (eds) Volcanic Geology of São Miguel Island (Azores Archipelago). Geological Society, London, Memoirs, 44, 15-32. DOI: 10.1144/M44.3.

Madruga J., Azevedo E. B., Sampaio J. F., Fernandes F., Reis F., Pinheiro J. (2015). Analysis and definition of potential new areas for viticulture in the Azores (Portugal). SOIL, 1, 515-526. Copernicus Publications, European Geosciences Union.

Marchetti E., Ripepe M., Campus P., Le Pichon A., Vergoz J., Lacanna G., Mialle P., Héreil P., Husson P. (2019). Long range infrasound monitoring of Etna volcano. Sci Rep 9, 18015. DOI: 10.1038/s41598-019-54468-5.

Marty J. (2019). The IMS Infrasound Network: Current Status and Technology Developments. In: Le Pichon A., Blanc E., Hauchecorne A. (eds) Infrasound Monitoring for Atmospheric Studies, 2nd Edition. Springer, Dordrecht. DOI: 10.1007/978- 3-319-75140-5_1.

Marty J., Doury B., Kramer A. (2021). Low and High Broadband Spectral Models of Atmospheric Pressure Fluctuation. Journal of Atmospheric and Oceanic Technology, 38, 1813-1822. American Meteorological Society. DOI: 10.1175/JTECH-D-21-0006.1.

Matos S. B. (2018). The use of infrasound in volcano monitoring. Contribution for future application in the Azores Islands. MSc dissertation in Volcanology and Geological Risks, University of the Azores, Ponta Delgada.

Matoza R. S., Hedlin M. A. H., Garcés M. A. (2006). An infrasound array study of Mount St. Helens. Journal of Volcanology and Geothermal Research, 160, 249-262. Elsevier. DOI: 10.1016/j.jvolgeores.2006.10.006.

Matoza R. S., Le Pichon A., Vergoz J., Herry P., Laland J-M., Lee H-i., Che I-Y., Rybin A. (2010). Infrasonic observations of the June 2009 Sarychev Peak eruption, Kuril Islands: Implications for infrasonic monitoring of remote explosive volcanism. Journal of Volcanology and Geothermal Research 200, 35-48. DOI: 10.1016/j.jvolgeores.2010.11.022.

Matoza R., Fee D., Green D., Mialle P. (2019). Volcano Infrasound and the International Monitoring System. In: Le Pichon A., Blanc E., Hauchecorne A. (eds) Infrasound Monitoring for Atmospheric Studies - Challenges in Middle Atmosphere Dynamics and Societal Benefits. Springer, Cham. DOI: 10.1007/978-3-319-75140-5_33.

McDonald J. A., Douze E. J., Herrin E. (1971). The Structure of Atmospheric Turbulence and its Application to the Design of Pipe arrays. Geophys. J. R. astr. Soc., 26, 99-109.

McIntire J. P., Nguyen D. K., Vinande E. T., Webber F. C. (2017). A Portable Tactical Field Sensor Array for an Infrasound Direction-Finding and Positioning System. U.S. Air Force Research Laboratory.

McNutt S. R., Thompson G., Johnson J., De Angelis S., Fee D. (2015). Chapter 63 - Seismic and Infrasonic Monitoring. In: Sigurdsson H. (ed) The Encyclopedia of Volcanoes (Second Edition). Academic Press. DOI: 10.1016/B978-0-12-385938-9.00063-8.

Mialle P., Brachet N., Brown D., Bittner P., Coyne J., Given J. (2010). Verification science - A unique global network: that detects very low frequency sound waves in the atmosphere. CTBTO Spectrum 15, 30-35.

Miranda J. M., Luis J. F., Lourenço N., Fernandes R. M. S. (2015). The structure of the Azores Triple Junction: implications for São Miguel Island. In: Gaspar J. L., Guest J. E., Duncan A. M., Barriga F. J. A., S., Chester D. K. (eds) Volcanic Geology of São Miguel Island (Azores Archipelago). Geological Society, London, Memoirs, 44, 5-13. DOI: 10.1144/M44.2.

Moore R. B. and Rubin M. (1991). Radiocarbon dates for lava flows and pyroclastic deposits on São Miguel, Azores. Radiocarbon, Vol. 33, No. 1, 151-164. DOI: 10.1017/S0033822200013278.

Muecke G. K., Ade-Hall J. M., Aumento F., MacDonald A., Reynolds P. H., Hyndamn R. D., Quintino J., Opdyke N., Lowrie W. (1974). Deep drilling in an active geothermal area in the Azores. Nature, Vol. 252, 281-285.

Murayama T., Kanao M., Yamamoto M-Y., Ishihara Y., Matsushima T., Kakinami Y. (2014). Infrasound array observations in the Lützow-Holm Bay region, East Antarctica. Polar Science 9, 35-50. Elsevier. DOI: 10.1016/j.polar.2014.07.005.

Needham H. D. and Francheteau J. (1974). Some characteristics of the rift valley in the Atlantic Ocean near 36°48' North. Earth and Planetary Science Letters, 22, 29-43. North-Holland Publishing Company, Amsterdam.

Negraru P. T. and Herrin E. T. (2009) On Infrasound Waveguides and Dispersion. Seismological Research Letters, Volume 80, Number 4. DOI: 10.1785/gssrl.80.4.565.

Negraru P. T., Golden P., Herrin E. T. (2010) Infrasound Propagation in the “Zone of Silence”. Seismological Research Letters, Volume 81, Number 4. DOI: 10.1785/gssrl.81.4.615.

Newhall C. G. and Self S. (1982). The Volcanic Explosivity Index (VEI): An Estimate of Explosive Magnitude for Historical Volcanism. Journal of Geophysical Research, Vol. 87, No. C2, 1231-1238. American Geophysical Union.

Nief G., Talmadge C., Rothman J., Gabrielson T. (2019). New Generations of Infrasound Sensors: Technological Developments and Calibration. In: Le Pichon A., Blanc E., Hauchecorne A. (eds) Infrasound Monitoring for Atmospheric Studies - Challenges in Middle Atmosphere Dynamics and Societal Benefits. Springer, Cham. DOI: 10.1007/978- 3-319-75140-5_2.

Norris D., Gibson R., Bongiovanni K. (2010). Numerical Methods to Model Infrasonic Propagation Through Realistic Specifications of the Atmosphere. In: Le Pichon A., Blanc E., Hauchecorne A. (eds) Infrasound Monitoring for Atmospheric Studies. Springer, Dordrecht. DOI: 10.1007/978-1-4020-9508-5_17.

Nunes J. C. (1999). A actividade vulcânica na ilha do Pico do Plistocénico Superior ao Holocénico: mecanismo eruptive e hazard vulcânico. PhD dissertation in Geology, specialty in Volcanology. Departamento de Geociências, Universidade dos Açores.

Pacheco J. M. R. (2001). Processos associados ao desenvolvimento de erupções vulcânicas hidromagmáticas explosivas na ilha do Faial e sua interpretação numa perspectiva de avaliação do hazard e minimização do risco. PhD dissertation in Geology, specialty in Volcanology. Departamento de Geociências, Universidade dos Açores.

Pacheco J. M., Ferreira T., Queiroz G., Wallenstein N., Coutinho R., Cruz J. V., Pimental A., Silva R., Gaspar J. L., Goulart C. (2012). Notas sobre a geologia do arquipélago dos Açores. In: Dias R., Araújo A., Terrinha P., Kullberg J. C. (eds) Geologia de Portugal, vol. 2. Escolar Editora, 596-690.

Pain H. J. (2005). The Physics of Vibrations and Waves, Sixth Edition. John Wiley & Sons Ltd, England. DOI:10.1002/0470016957.

Park J., Stump B. W., Hayward C., Arrowsmith S. J., Che I-Y., Drob D. P. (2016). Detection of regional infrasound signals using array data: Testing, tuning, and physical interpretation. J. Acoust. Soc. Am. 140 (1), 239-259. Acoustical Society of America. DOI: 10.1121/1.4954759.

Pimentel A. H. G. (2006). Domos e coulees da ilha Terceira (Açores): Contribuição para o estudo dos mecanismos de instalação. MSc dissertation in Volcanology and Geological Risks. Departamento de Geociências, Universidade dos Açores.

Pimentel A. H. G. (2015). Pyroclastic Density Current-Forming Eruptions on Faial and Terceira Islands, Azores. PhD dissertation in Geology, specialty in Volcanology. Departamento de Geociências, Universidade dos Açores.

Pimentel A., Pacheco J., Self, S. (2015). The ∼ 1000-years BP explosive eruption of Caldeira Volcano (Faial, Azores): the first stage of incremental caldera formation. Bull. Volcanol., 77:42. Springer. DOI: 10.1007/s00445-015-0930-2.

Ponceau D. and Bosca L. (2010). Low-Noise Broadband Microbarometers. In: Le Pichon A., Blanc E., Hauchecorne A. (eds) Infrasound Monitoring for Atmospheric Studies. Springer, Dordrecht. DOI: 10.1007/978-1-4020-9508-5_4.

Queiroz M. G. P. S. (1997). Vulcão das Sete Cidades (S. Miguel, Açores). História Eruptiva e Avaliação do Hazard. PhD dissertation in Geology, specialty in Volcanology. Departamento de Geociências, Universidade dos Açores.

Queiroz G., Pacheco J. M., Gaspar J. L., Aspinall W. P., Guest J. E., Ferreira T. (2008). The last 5000 years of activity at Sete cidades volcano (São Miguel Island, Azores): Implications for hazard assessment. Journal of Volcanology and Geothermal Research, 178, 562-573. Elsevier. DOI: 10.1016/j.jvolgeores.2008.03.001.

Queiroz G., Gaspar J. L., Guest J. E., Gomes A., Almeida M. H. (2015). Eruptive history and evolution of Sete Cidades Volcano, São Miguel Island, Azores. In: Gaspar J. L., Guest J. E., Duncan A. M., Barriga F. J. A., S., Chester D. K. (eds) Volcanic Geology of São Miguel Island (Azores Archipelago). Geological Society, London, Memoirs, 44, 87-104. DOI: 10.1144/M44.7.

Raspet R., Webster J., Dillion K. (2006). Framework for wind noise studies. J. Acoust. Soc. Am. 119 (2), 834-843. Acoustical Society of America. DOI: 10.1121/1.2146113.

Raspet R., Abbott J-P., Webster J., Yu J., Talmadge C., Alberts II K., Collier S., Noble J. (2019). New Systems for Wind Noise Reduction for Infrasonic Measurements. In: Le Pichon A., Blanc E., Hauchecorne A. (eds) Infrasound Monitoring for Atmospheric Studies - Challenges in Middle Atmosphere Dynamics and Societal Benefits. Springer, Cham. DOI: 10.1007/978- 3-319-75140-5_3.

Ripepe M., Poggi P., Braun T., Gordeev E. (1996). Infrasonic waves and volcanic tremor at Stromboli. Geophysical Research Letters, Vol. 23, No 2, 181-184. American Geophysical Union.

Ripepe M. and Marchetti E. (2002). Array tracking of infrasonic sources at Stromboli volcano. Geophysical Research Letters, Vol. 29, No 22, 2076, 181-184. American Geophysical Union. DOI: 10.1029/2002GL015452.

Ripepe M., Marchetti E., Delle Donne D., Genco R., Innocenti L., Lacanna G., Valade S. (2018). Infrasonic Early Warning System for Explosive Eruptions. Journal of Geophysical Research: Solid Earth, 123, 9570–9585. DOI: 10.1029/2018JB015561.

Riquelme F., Barrientos S., Brachet N., Kramer A., Campus P. (2009). Infrasonic Signals Generated by the Villarrica and Llaima Volcanoes in Southern Chile. XII Congreso Geológico Chileno, Santiago, 22-26 Noviembre.

Robertson J., Mialle P., Sapsford J. (2021). Deployment of Portable Infrasound Sites to Assess Feasibility of Additional Elements, I51GB, Bermuda, UK. CTBT: Science and Technology Conference - SnT 2021. Poster Communication.

Rymer H. (2015). Part II Eruptions. In: Sigurdsson H. (ed) The Encyclopedia of Volcanoes 2nd Edition. 237-238. Academic Press. DOI: 10.1016/B978-0-12-385938-9.02004-6.

Searle R. (1980). Tectonic pattern of the Azores spreading centre and triple junction. Earth and Planetary Science letters, 51, 415-434. Elsevier Scientific Publishing Company, Amsterdam.

Self S. (1974). Recent volcanism on Terceira, Azores. PhD dissertation. Geology Department, Imperial College, London.

Self S. (1976). The Recent volcanology of Terceira, Azores. Jl geol. Soc. Lond. Vol. 132, pp. 645-666, Northern Ireland.

Self S. (1982). Excursion guide for field trip V2, Island of Terceira. Symposium on the activity of ocean volcanoes.

Serralheiro A., Matos Alves C. A., Forjaz V. H., Rodrigues, B. (1989). Carta vulcanológica dos Açores - ilha do Faial à escala 1:15000. Edição do Serviço Regional de Protecção Civil, Universidade dos Açores e Centro de Vulcanologia do INIC, 4 folhas.

Shotton F. W., Blundell D. J., Williams R. E. G. (1970). Birmingham University Radiocarbon Dates IV. Radiocarbon, Vol. 12, No. 2, 385-399. DOI: 10.1017/S0033822200008158.

Silva M. A. (2005). Caracterização da sismicidade histórica dos Açores com base na reinterpretação de dados de macrossísmica: contribuição para a avaliação do risco sísmico nas ilhas do Grupo Central. MSc dissertation in Volcanology and Geological Risks. Departamento de Geociências, Universidade dos Açores.

Silveira G., Stutzmann E., Davaille A., Montagner J-P., Mendes-Victor L., Sebai A. (2006). Azores hotspot signature in the upper mantle. Journal of Volcanology and Geothermal Research, 156, 23-24. Elsevier. DOI: 10.1016/j.jvolgeores.2006.03.022.

Silveira D., Gaspar J. L., Ferreira T., Queiroz G. (2003). Reassessment of the historical seismic activity with major impact on S. Miguel Island (Azores). Natural hazards and Earth System Sciences, 3: 615-623. European Geosciences Union.

Solomon M. L., Bryan K. J., Smith K. E., Clauter D. A., Smith A. O., Peter A. M. (2018). Infrasound threat classification: a statistical comparison of deep learning architectures. Proc. SPIE 10629, Chemical, Biological, Radiological, Nuclear, and Explosives (CBRNE) Sensing XIX, 1062917, Orlando, Florida, United States. DOI: 10.1117/12.2304030.

Sutherland L. C. and Bass H. E. (2004). Atmospheric absorption in the atmosphere up to 160 km. J. Acoust. Soc. Am., 115, 1012–1032. DOI: 10.1121/1.1631937.

Viveiros F., Cardellini C., Ferreira T., Caliro S., Chiodini G., Silva C. (2010). Soil CO_2 emissions at Furnas volcano, São Miguel Island, Azores archipelago: Volcano monitoring perspectives, geomorphologic studies, and land use planning application. Journal of Geophysical Research, Vol. 115, B12208. American Geophysical Union. DOI: 10.1029/2010JB007555.

Walker G. P. L. and Croasdale R. (1970). Two Plinian-type eruptions in the Azores. JL geol. Soc. Vol. 127, pp. 17-55. Northern Ireland.

Walker K. T. and Hedlin M. A. H. (2010). A Review of Wind-Noise Reduction Methodologies. In: Le Pichon A., Blanc E., Hauchecorne A. (eds) Infrasound Monitoring for Atmospheric Studies. Springer, Dordrecht. DOI: 10.1007/978-1-4020-9508-5_5.

Wallenstein N., Duncan A., Almeida H., Pacheco J. (1998). Novo esquema estratigráfico dos últimos 15.000 anos do Vulcão do Fogo, S. Miguel (Açores). I Asemblea Hispano Portuguesa de Geodesia Y Geofísica (Abstract Volume), Almeria, 329.

Wallenstein N. M. B. A. (1999). Estudo da História Recente e do Comportamento Eruptivo do Vulcão do Fogo (S. Miguel, Açores) - Avaliação Preliminar do Hazard. PhD dissertation in Geology, specialty in Volcanology. Departamento de Geociências, Universidade dos Açores.

Wallenstein N., Duncan A., Guest J. E., Almeida M. H. (2015). Eruptive history of Fogo Volcano. In: Gaspar J. L., Guest J. E., Duncan A. M., Barriga F. J. A., S., Chester D. K. (eds) Volcanic Geology of São Miguel Island (Azores Archipelago). Geological Society, London, Memoirs, 44, 105-123. DOI: 10.1144/M44.8.

Wallenstein N., Duncan A., Coutinho R., Chester D. (2018). Origin of the term *nuées ardentes* and the 1580 and 1808 eruptions on São Jorge Island, Azores. Journal of Volcanology and Geothermal Research, 358, 165-170. Elsevier. DOI: 10.1016/j.jvolgeores.2018.03.022.

Willis M., Garcés M., Hetzer C., Businger S. (2004). Infrasonic observations of open ocean swells in the Pacific: Deciphering the song of the sea. Geophys. Res. Lett., 31, L19303. DOI: 10.1029/2004GL02067610.1029/2004GL020696.

Welch P.D. (1967). The use of fast Fourier transform for the estimation of power spectra: A method based on time-averaging over short, modified periodograms. IEEE Trans. Audio Electroacoust., AU-15, 70–73. DOI: 10.1109/TAU.1967.1161901.

Zanon V. (2015). The magmatism of the Azores islands. In: Gaspar J. L., Guest J. E., Duncan A. M., Barriga F. J. A., S., Chester D. K. (eds) Volcanic Geology of São Miguel Island (Azores Archipelago). Geological Society, London, Memoirs, 44, 51-64. DOI: 10.1144/M44.5.

Zanon V. and Pimentel A. (2015). Spatio-temporal constraints on magma storage and ascent conditions in a transtensional tectonic setting: The case of the Terceira Island (Azores). American Mineralogist, 100, 795-805. DOI: 10.2138/am-2015-4936.

Zanon V. and Viveiros F. (2019). A multi-methodological re-evaluation of the volcanic events during the 1580 CE and 1808 eruptions at São Jorge Island (Azores Archipelago, Portugal). Journal of Volcanology and Geothermal Research, 373, 51-67. Elsevier. DOI: 10.1016/j.jvolgeores.2019.01.028.

Webography

ARISE (2013). ARISE technologies - Infrasound network. Available at http://arise-project.eu/infrasound.php [accessed on 29/11/2022].

CIVISA (2022a). Crise Sismovulcânica de São Jorge - Ponto de Situação - 02-11-2022. Available at http://www.ivar.azores.gov.pt/sjorge/Paginas/ponto-situacao.aspx [accessed on 02/11/2022].

CIVISA (2022b). Crise Sismovulcânica de São Jorge - Comunicado CIVISA para VONA. Available at http://www.ivar.azores.gov.pt/sjorge/Paginas/comunicados.aspx [accessed on 02/11/2022].

CIVISA (2022c). Crise Sismovulcânica de São Jorge - Frequência Sísmica (FSH e FSD). Available at http://www.ivar.azores.gov.pt/sjorge/Paginas/frequencia-sismica.aspx [accessed on 02/11/2022].

CTBTO (2022). Infrasound Monitoring. Available at https://www.ctbto.org/our-work/monitoring-technologies/infrasound-monitoring [accessed on 21/11/2022].

Design World Staff (2010). Using FEM for Infrasound Propagation. Available at https://www.designworldonline.com/using-fem-for-infrasound-propagation/ [accessed on 19/07/2021].

IVAR (2022). Vulcões Activos. Available at http://www.ivar.azores.gov.pt/vulcoes-activos/Paginas/vulcoes-activos.aspx [accessed on 16/12/2022].

iTem (2022). Products. Available at https://www.item-geophysics.it/products/ [accessed on 14/10/2022].

SEISMOWAVE (2022). SISTEM. Available at http://seismowave.com/produit/produit-sistem-ready-to-use-portable-infrasound-station/ [accessed on 27/07/2022].

Data

CIVISA (2022d). Dados da sismicidade no arquipélago dos Açores desde 19/03/2022 a 02/11/2022.

IPMA, IP (2022). Dados Meteorológicos - EMA510 - Abril-Junho 2022-2 [cedidos via email por Carlos Ramanho dirigente da Delegação Regional dos Açores do IPMA].

ANNEXES

A. Preliminary selection of sites in the Azores Islands

A.1. Sete Cidades volcano (São Miguel Island)

A.1.1. Eruptive scenarios SC1 and SC2 (Map)

Eruptive scenarios SC1 and SC2, Sete Cidades volcano. Volcanic and tectonic structures are from Carmo (2013), modified by CIVISA.

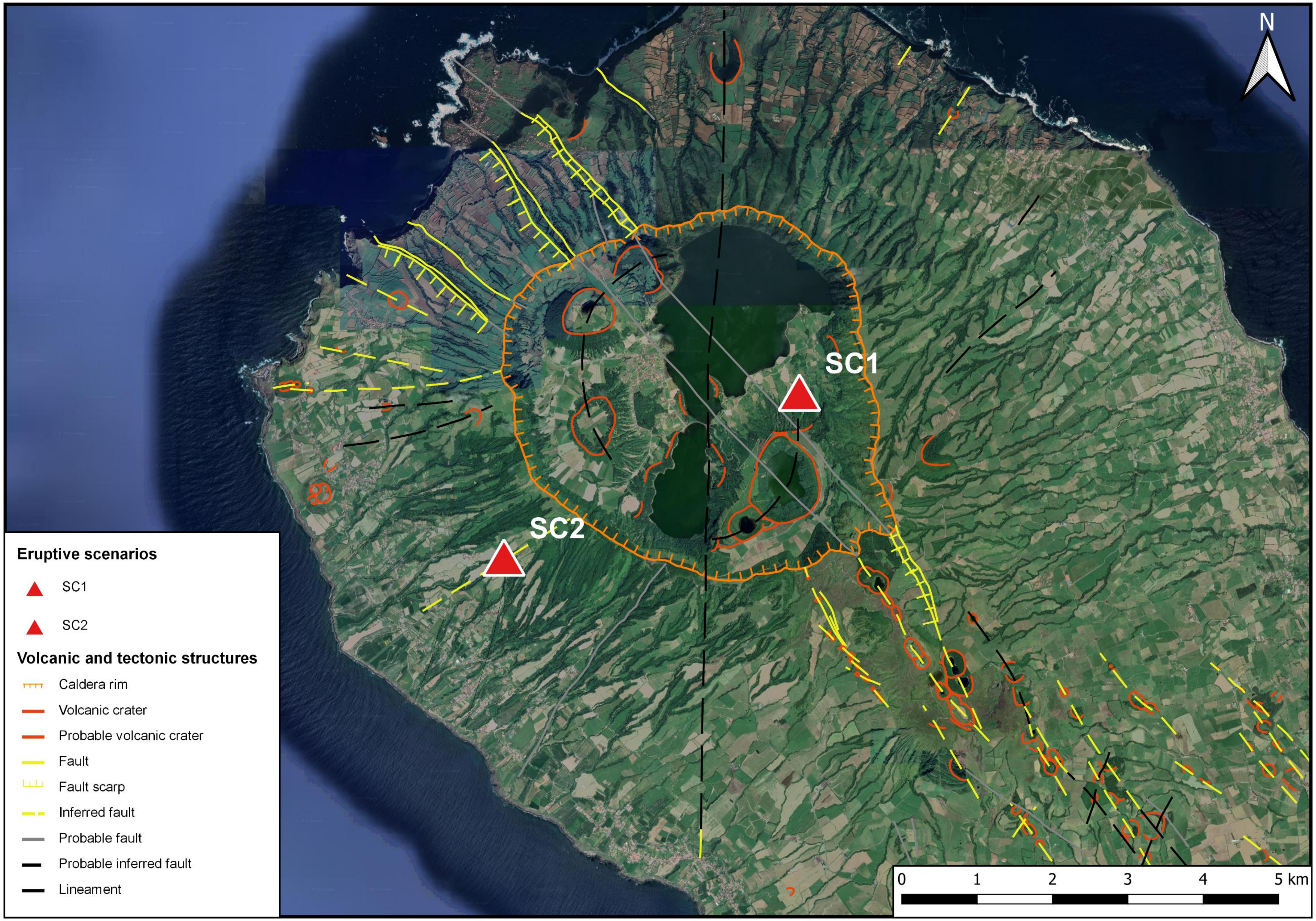
N
SC1
SC2
Eruptive scenarios
SC1
SC2
Volcanic and tectonic structures
Caldera rim
Volcanic crater
Probable volcanic crater
Fault
Fault scarp
Inferred fault
Probable fault
Probable inferred fault
Lineament
0
1
2
3
4
5 km

A. Preliminary selection of sites in the Azores Islands

A.1. Sete Cidades volcano (São Miguel Island)

A.1.2. LC and IS arrays (Map)

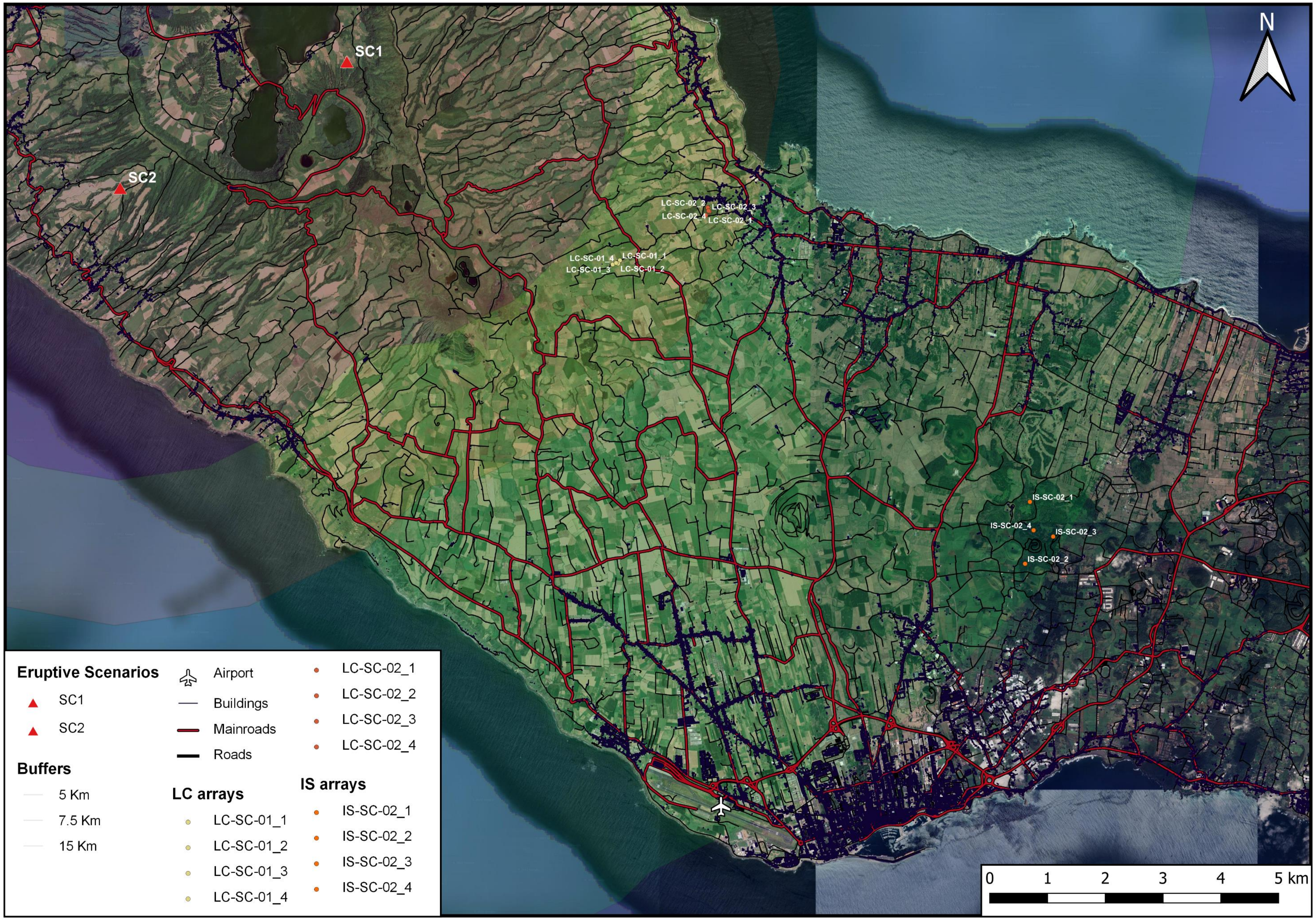
N
SC1
SC2
LC-SC-02_2
LC-SC-02_3
LC-SC-02_4
LC-SC-02_1
LC-SC-01_4
LC-SC-01_1
LC-SC-01_3
LC-SC-01_2
IS-SC-02_1
IS-SC-02_4
IS-SC-02_3
IS-SC-02_2
Eruptive Scenarios
SC1
SC2
Buffers
5 Km
7.5 Km
15 Km
Airport
Buildings
Mainroads
Roads
LC arrays
LC-SC-01_1
LC-SC-01_2
LC-SC-01_3
LC-SC-01_4
LC-SC-02_1
LC-SC-02_2
LC-SC-02_3
LC-SC-02_4
IS arrays
IS-SC-02_1
IS-SC-02_2
IS-SC-02_3
IS-SC-02_4
0
1
2
3
4
5 km

A. Preliminary selection of sites in the Azores Islands

A.1. Sete Cidades volcano (São Miguel Island)

A.1.3. Features of the LC and IS arrays (Table)

ID	Aperture (m)	Back azimuth to the source (°)	Parish	County	Island
LC-SC-01	142	**SC1**: 306.36 **SC2**: 278.35	Capelas	Ponta Delgada	São Miguel
LC-SC-02	135	**SC1**: 292.23 **SC2**: 271.94	Capelas	Ponta Delgada	São Miguel
IS-SC-02	1066	**SC1**: 304.14 **SC2**: 290.53	Fajã de Cima	Ponta Delgada	São Miguel

A. Preliminary selection of sites in the Azores Islands

A.2. Fogo volcano (São Miguel Island)

A.2.1. Eruptive scenarios FO1 and FO2 (Map)

Eruptive scenarios FO1 and FO2, Fogo volcano. Volcanic and tectonic structures are from Carmo (2013), modified by CIVISA.

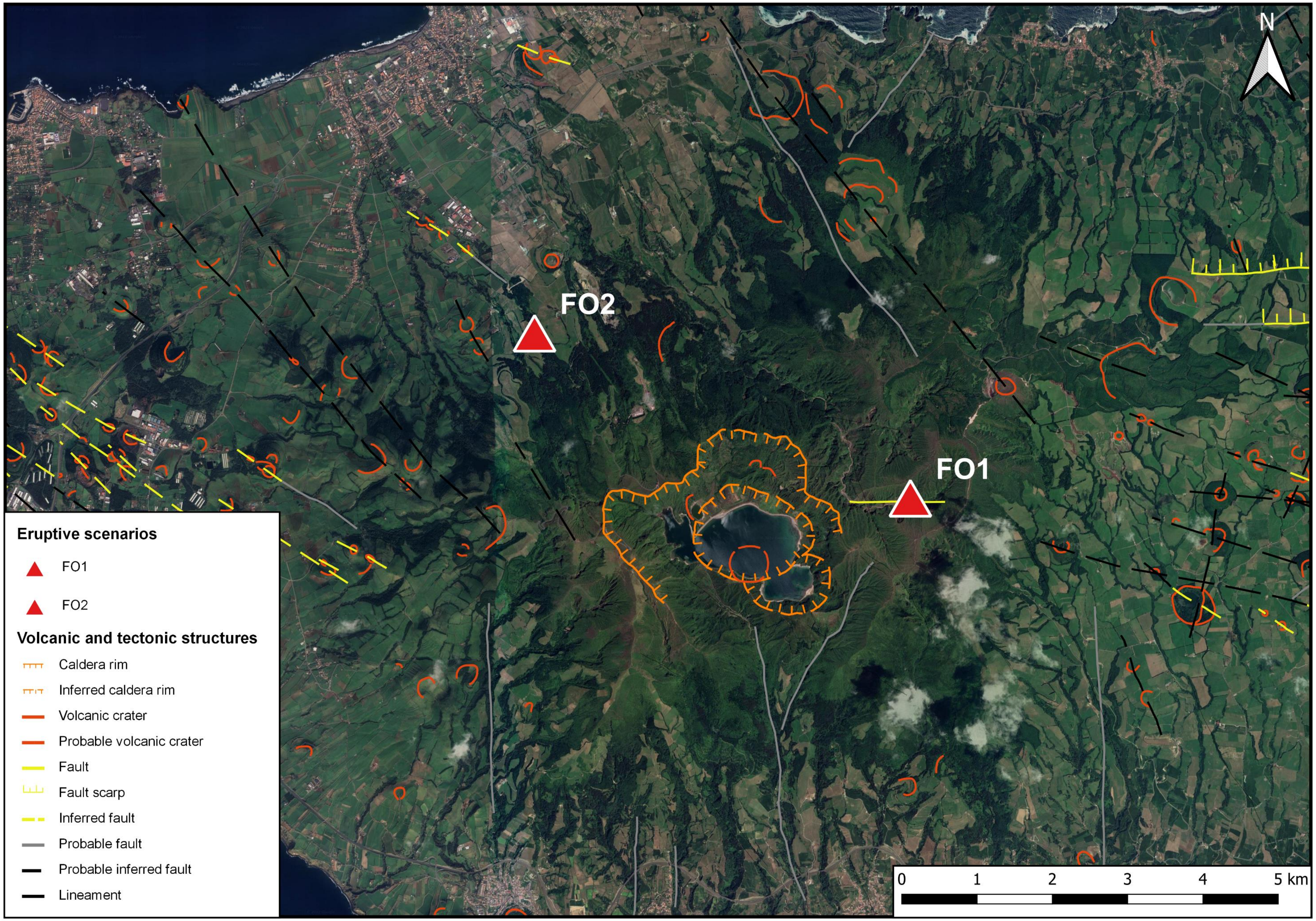
N
FO2
FO1
Eruptive scenarios
▲ FO1
▲ FO2
Volcanic and tectonic structures
Caldera rim
Inferred caldera rim
Volcanic crater
Probable volcanic crater
Fault
Fault scarp
Inferred fault
Probable fault
Probable inferred fault
Lineament
0
1
2
3
4
5 km

A. Preliminary selection of sites in the Azores Islands

A.2. Fogo volcano (São Miguel Island)

A.2.2. LC and IS arrays (Map)


N
FO1
FO2
IS-FO-05_2
IS-FO-05_3
IS-FO-05_1
IS-FO-05_4
IS-FO-03_1
IS-FO-03_2
IS-FO-03_4
IS-FO-03_3
IS-FO-02_3
IS-FO-02_4
IS-FO-02_1
IS-FO-02_2
LC-FO-06_1
LC-FO-06_2
LC-FO-06_4
LC-FO-06_3
LC-FO-05_1
LC-FO-05_3
LC-FO-05_2
LC-FO-01_1
LC-FO-01_2
LC-FO-01_3
LC-FO-01_4
LC-FO-04_3
LC-FO-04_2
LC-FO-04_4
LC-FO-04_1
IS-FO-07_3
IS-FO-07_4
IS-FO-07_2
IS-FO-07_1
Eruptive Scenarios
▲ FO1
▲ FO2
Buffers
5 Km
7.5 Km
15 Km
Buildings
Mainroads
Roads
LC arrays
● LC-FO-01_1
● LC-FO-01_2
● LC-FO-01_3
● LC-FO-01_4
● LC-FO-04_1
● LC-FO-04_2
● LC-FO-04_3
● LC-FO-04_4
● LC-FO-05_1
● LC-FO-05_2
● LC-FO-05_3
● LC-FO-05_4
● LC-FO-06_1
● LC-FO-06_2
● LC-FO-06_3
● LC-FO-06_4
IS arrays
● IS-FO-02_1
● IS-FO-02_2
● IS-FO-02_3
● IS-FO-02_4
● IS-FO-03_1
● IS-FO-03_2
● IS-FO-03_3
● IS-FO-03_4
● IS-FO-05_1
● IS-FO-05_2
● IS-FO-05_3
● IS-FO-05_4
● IS-FO-07_1
● IS-FO-07_2
● IS-FO-07_3
● IS-FO-07_4
0 1 2 3 4 5 km

A. Preliminary selection of sites in the Azores Islands

A.2. Fogo volcano (São Miguel Island)

A.2.3. Features of the LC and IS arrays (Table)

ID	Aperture (m)	Back azimuth to the source (°)	Parish	County	Island
LC-FO-01	139	**FO1**: 58.96 **FO2**: 5.42	Água de Pau	Lagoa	São Miguel
LC-FO-04	136	**FO1**: 282.52 **FO2**: 287.42	Ponta Garça	Vila Franca do Campo	São Miguel
LC-FO-05	140	**FO1**: 89.72 **FO2**: 68.95	Cabouco	Lagoa	São Miguel
LC-FO-06	141	**FO1**: 102.18 **FO2**: 91.62	Rabo de Peixe	Ribeira Grande	São Miguel
IS-FO-02	1143	**FO1**: 91.02 **FO2**: 80.43	Fajã de Baixo	Ponta Delgada	São Miguel
IS-FO-03	1326	**FO1**: 94.55 **FO2**: 85.96	Fajã de Cima Fajã de Baixo	Ponta Delgada	São Miguel
IS-FO-05	1558	**FO1**: 98.98 **FO2**: 93.44	Fajã de Cima São Vicente Ferreira	Ponta Delgada	São Miguel
IS-FO-07	1083	**FO1**: 247.02 **FO2**: 262.62	Lomba da Maia	Ribeira Grande	São Miguel

A. Preliminary selection of sites in the Azores Islands

A.3. Furnas volcano (São Miguel Island)

A.3.1. Eruptive scenario FU1 (Map)

Eruptive scenario FU1, Furnas volcano. Volcanic and tectonic structures are from Carmo (2013), modified by CIVISA.

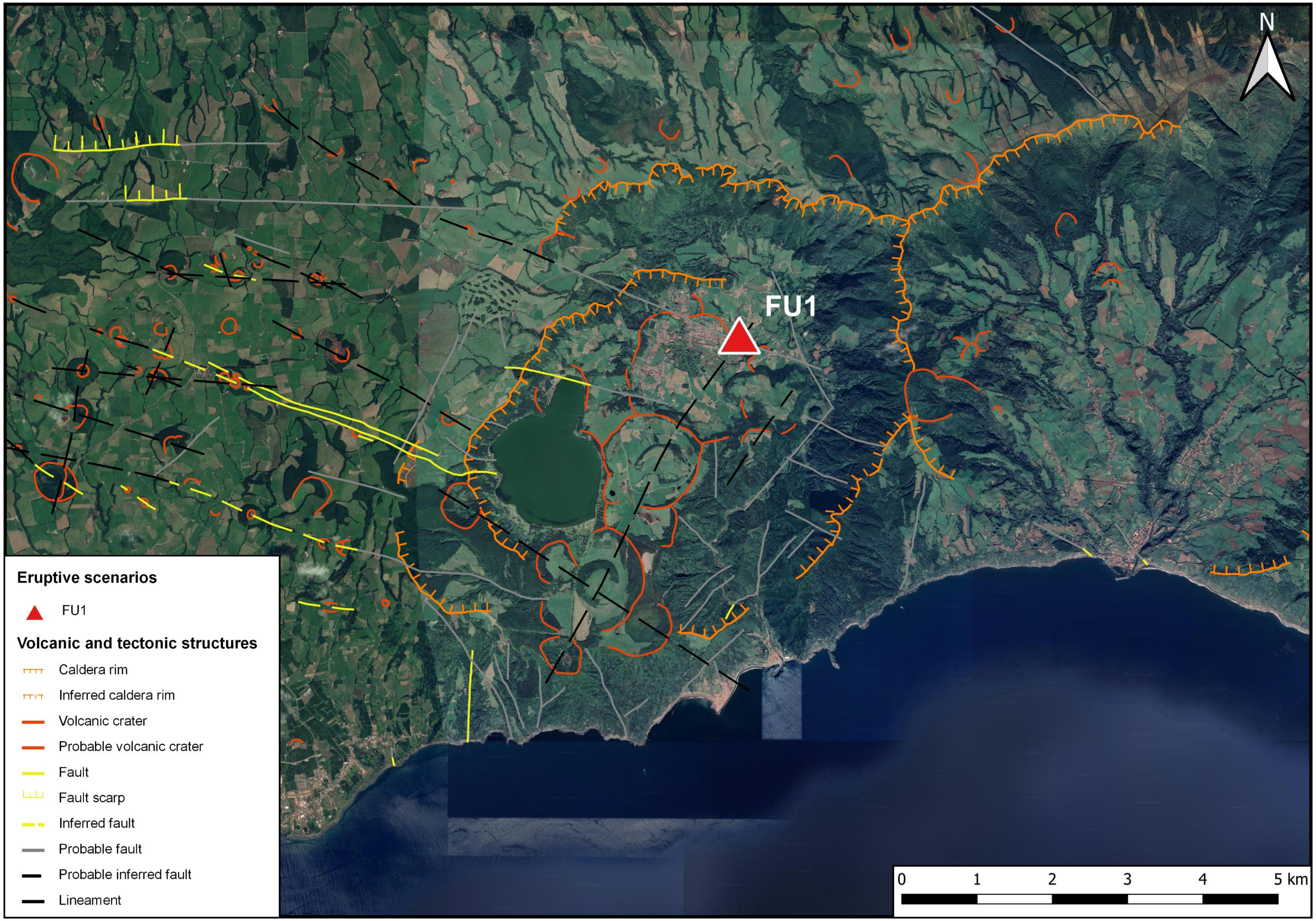
N
FU1
Eruptive scenarios
FU1
Volcanic and tectonic structures
Caldera rim
Inferred caldera rim
Volcanic crater
Probable volcanic crater
Fault
Fault scarp
Inferred fault
Probable fault
Probable inferred fault
Lineament
0
1
2
3
4
5 km

A. Preliminary selection of sites in the Azores Islands

A.3. Furnas volcano (São Miguel Island)

A.3.2. LC and IS arrays (Map)

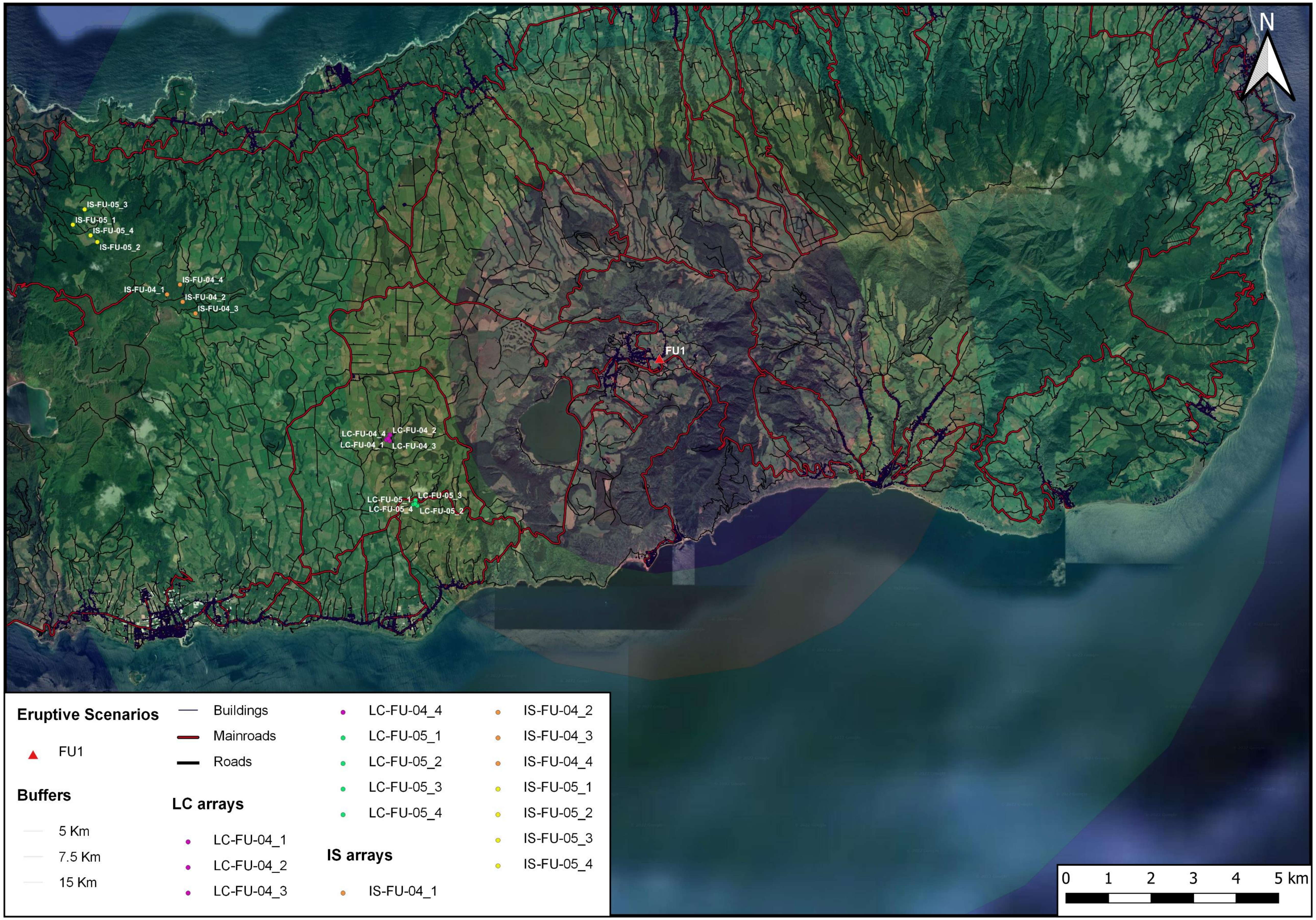
N
IS-FU-05_3
IS-FU-05_1
IS-FU-05_4
IS-FU-05_2
IS-FU-04_4
IS-FU-04_1
IS-FU-04_2
IS-FU-04_3
FU1
LC-FU-04_4
LC-FU-04_2
LC-FU-04_1
LC-FU-04_3
LC-FU-05_1
LC-FU-05_3
LC-FU-05_4
LC-FU-05_2
Eruptive Scenarios
FU1
Buffers
5 Km
7.5 Km
15 Km
Buildings
Mainroads
Roads
LC arrays
LC-FU-04_1
LC-FU-04_2
LC-FU-04_3
LC-FU-04_4
LC-FU-05_1
LC-FU-05_2
LC-FU-05_3
LC-FU-05_4
IS arrays
IS-FU-04_1
IS-FU-04_2
IS-FU-04_3
IS-FU-04_4
IS-FU-05_1
IS-FU-05_2
IS-FU-05_3
IS-FU-05_4
0 1 2 3 4 5 km

A. Preliminary selection of sites in the Azores Islands

A.3. Furnas volcano (São Miguel Island)

A.3.3. Features of the LC and IS arrays (Table)

ID	Aperture (m)	Back azimuth to the source (°)	Parish	County	Island
LC-FU-04	137	**FU1**: 73.89	Ponta Garça	Vila Franca do Campo	São Miguel
LC-FU-05	132	**FU1**: 59.68	Ponta Garça	Vila Franca do Campo	São Miguel
IS-FU-04	789	**FU1**: 96.67	Porto Formoso São Brás São Miguel	Ribeira Grande Vila Franca do Campo	São Miguel
IS-FU-05	818	**FU1**: 103.17	Ribeirinha	Ribeira Grande	São Miguel

A. Preliminary selection of sites in the Azores Islands

A.4. Pico Alto volcano (Terceira Island)

A.4.1. Eruptive scenario PA1 (Map)

Eruptive scenario PA1, Pico Alto volcano. Volcanic and tectonic structures are from Madeira (2005), modified by CIVISA.

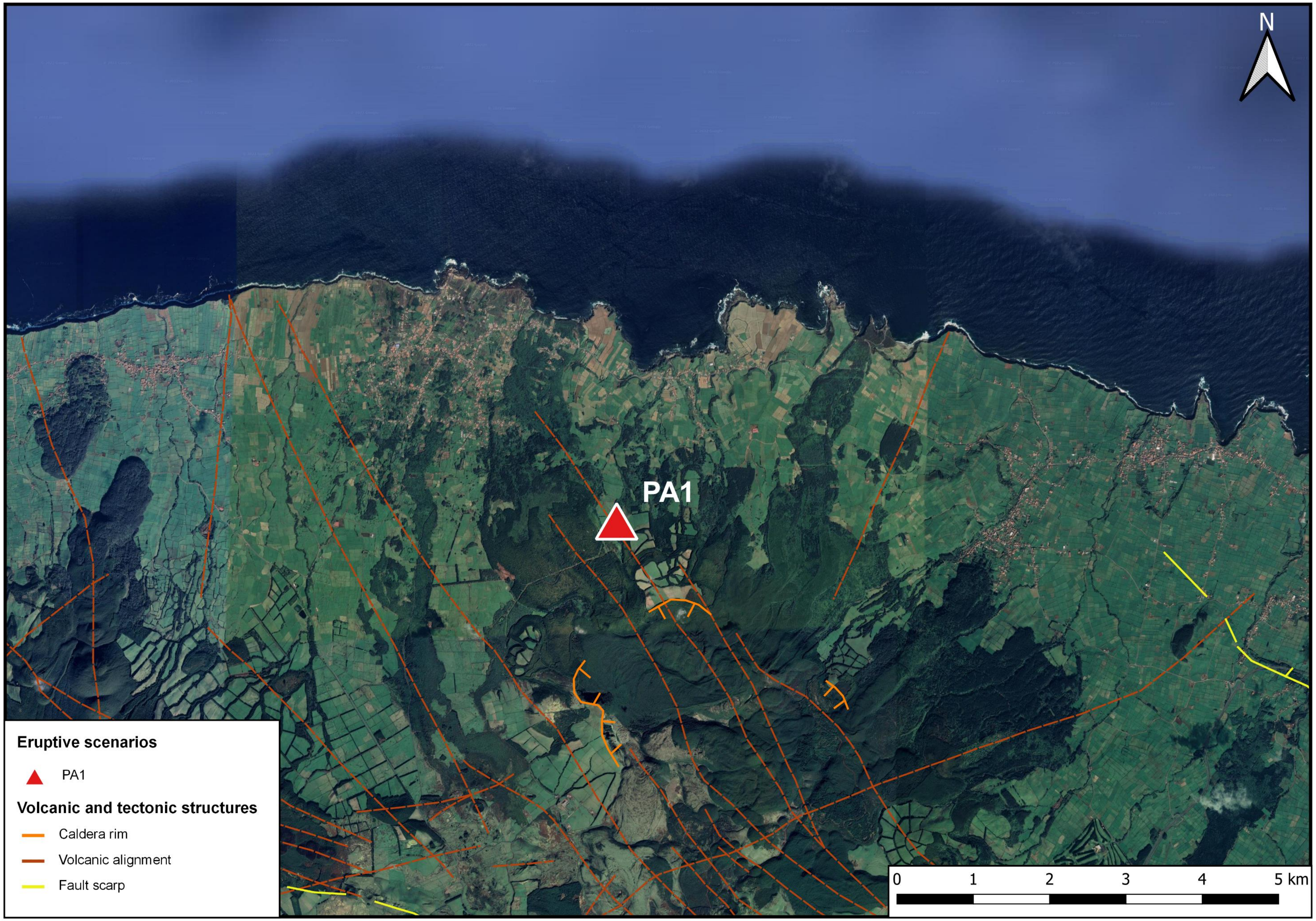
N
PA1
Eruptive scenarios
PA1
Volcanic and tectonic structures
Caldera rim
Volcanic alignment
Fault scarp
0
1
2
3
4
5 km

A. Preliminary selection of sites in the Azores Islands

A.4. Pico Alto volcano (Terceira Island)

A.4.2. LC and IS arrays (Map)

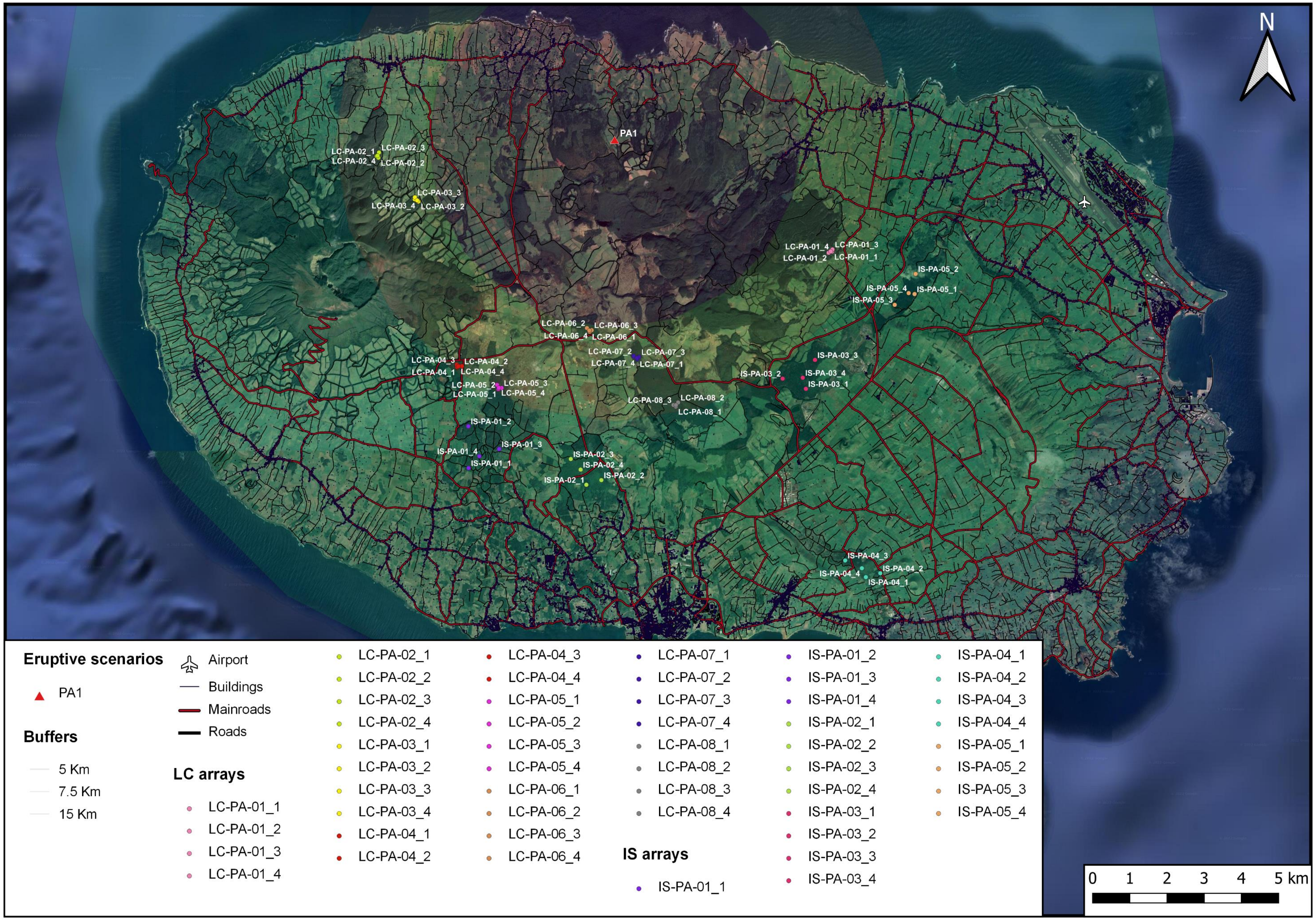
N
PA1
LC-PA-02_1
LC-PA-02_3
LC-PA-02_4
LC-PA-02_2
LC-PA-03_3
LC-PA-03_4
LC-PA-03_2
LC-PA-01_4
LC-PA-01_3
LC-PA-01_2
LC-PA-01_1
IS-PA-05_2
IS-PA-05_4
IS-PA-05_1
IS-PA-05_3
LC-PA-06_2
LC-PA-06_3
LC-PA-06_4
LC-PA-06_1
LC-PA-07_2
LC-PA-07_3
LC-PA-07_4
LC-PA-07_1
LC-PA-04_3
LC-PA-04_2
LC-PA-04_1
LC-PA-04_4
LC-PA-05_2
LC-PA-05_3
LC-PA-05_1
LC-PA-05_4
IS-PA-03_3
IS-PA-03_2
IS-PA-03_4
IS-PA-03_1
LC-PA-08_3
LC-PA-08_2
LC-PA-08_1
IS-PA-01_2
IS-PA-01_3
IS-PA-01_4
IS-PA-01_1
IS-PA-02_3
IS-PA-02_4
IS-PA-02_1
IS-PA-02_2
IS-PA-04_3
IS-PA-04_2
IS-PA-04_4
IS-PA-04_1
Eruptive scenarios
PA1
Buffers
5 Km
7.5 Km
15 Km
Airport
Buildings
Mainroads
Roads
LC arrays
LC-PA-01_1
LC-PA-01_2
LC-PA-01_3
LC-PA-01_4
LC-PA-02_1
LC-PA-02_2
LC-PA-02_3
LC-PA-02_4
LC-PA-03_1
LC-PA-03_2
LC-PA-03_3
LC-PA-03_4
LC-PA-04_1
LC-PA-04_2
LC-PA-04_3
LC-PA-04_4
LC-PA-05_1
LC-PA-05_2
LC-PA-05_3
LC-PA-05_4
LC-PA-06_1
LC-PA-06_2
LC-PA-06_3
LC-PA-06_4
LC-PA-07_1
LC-PA-07_2
LC-PA-07_3
LC-PA-07_4
LC-PA-08_1
LC-PA-08_2
LC-PA-08_3
LC-PA-08_4
IS arrays
IS-PA-01_1
IS-PA-01_2
IS-PA-01_3
IS-PA-01_4
IS-PA-02_1
IS-PA-02_2
IS-PA-02_3
IS-PA-02_4
IS-PA-03_1
IS-PA-03_2
IS-PA-03_3
IS-PA-03_4
IS-PA-04_1
IS-PA-04_2
IS-PA-04_3
IS-PA-04_4
IS-PA-05_1
IS-PA-05_2
IS-PA-05_3
IS-PA-05_4
0 1 2 3 4 5 km

A. Preliminary selection of sites in the Azores Islands

A.4. Pico volcano (Terceira Island)

A.4.3. Features of the LC and IS arrays (Table)

ID	Aperture (m)	Back azimuth to the source (°)	Parish	County	Island
LC-PA-01	136	**PA1**: 296.88	Agualva	Praia da Vitória	Terceira
LC-PA-02	142	**PA1**: 85.99	Altares	Angra do Heroísmo	Terceira
LC-PA-03	145	**PA1**: 74.04	Altares	Angra do Heroísmo	Terceira
LC-PA-04	146	**PA1**: 34.86	São Bartolomeu de Regatos	Angra do Heroísmo	Terceira
LC-PA-05	145	**PA1**: 25.20	São Bartolomeu de Regatos	Angra do Heroísmo	Terceira
LC-PA-06	137	**PA1**: 7.70	Posto Santo	Angra do Heroísmo	Terceira
LC-PA-07	137	**PA1**: 355.05	Posto Santo	Angra do Heroísmo	Terceira
LC-PA-08	143	**PA1**: 346.95	Posto Santo	Angra do Heroísmo	Terceira
IS-PA-01	1135	**PA1**: 23.77	São Bartolomeu de Regatos Terra Chã	Angra do Heroísmo	Terceira
IS-PA-02	1007	**PA1**: 5.77	Terra Chã Posto Santo	Angra do Heroísmo	Terceira
IS-PA-03	1036	**PA1**: 321.12	Porto Judeu Vila de São Sebastião	Angra do Heroísmo	Terceira
IS-PA-04	1026	**PA1**: 329.83	Feteira Ribeirinha	Angra do Heroísmo	Terceira
IS-PA-05	991	**PA1**: 296.55	Agualva	Praia da Vitória	Terceira

A. Preliminary selection of sites in the Azores Islands

A.5. Santa Bárbara volcano (Terceira Island)

A.5.1. Eruptive scenario SB1 (Map)

Eruptive scenario SB1, Santa Bárbara volcano. Volcanic and tectonic structures are from Madeira (2005), modified by CIVISA.

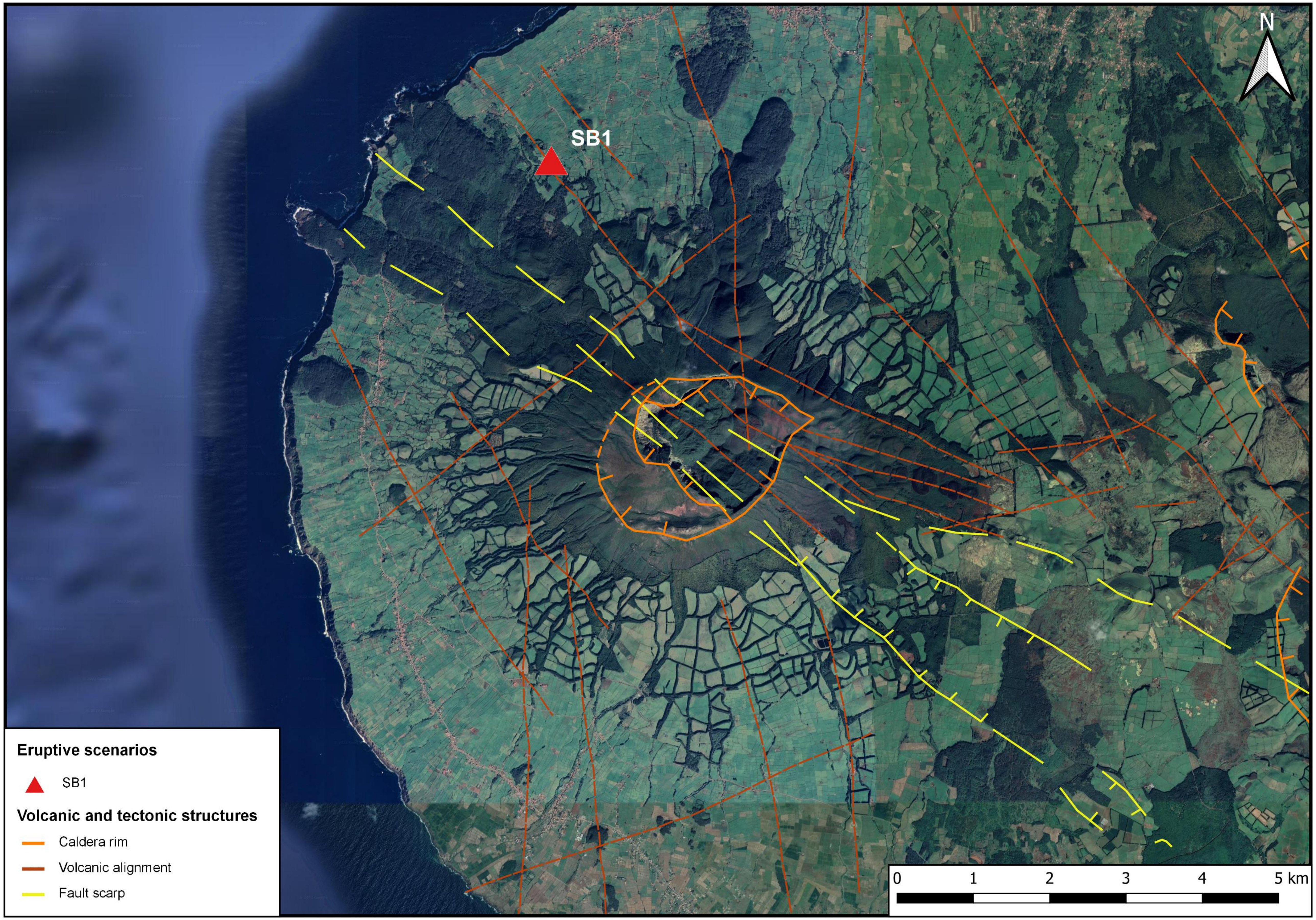
SB1
N
Eruptive scenarios
SB1
Volcanic and tectonic structures
Caldera rim
Volcanic alignment
Fault scarp
0
1
2
3
4
5 km

A. Preliminary selection of sites in the Azores Islands

A.5. Santa Bárbara volcano (Terceira Island)

A.5.2. LC and IS arrays (Map)

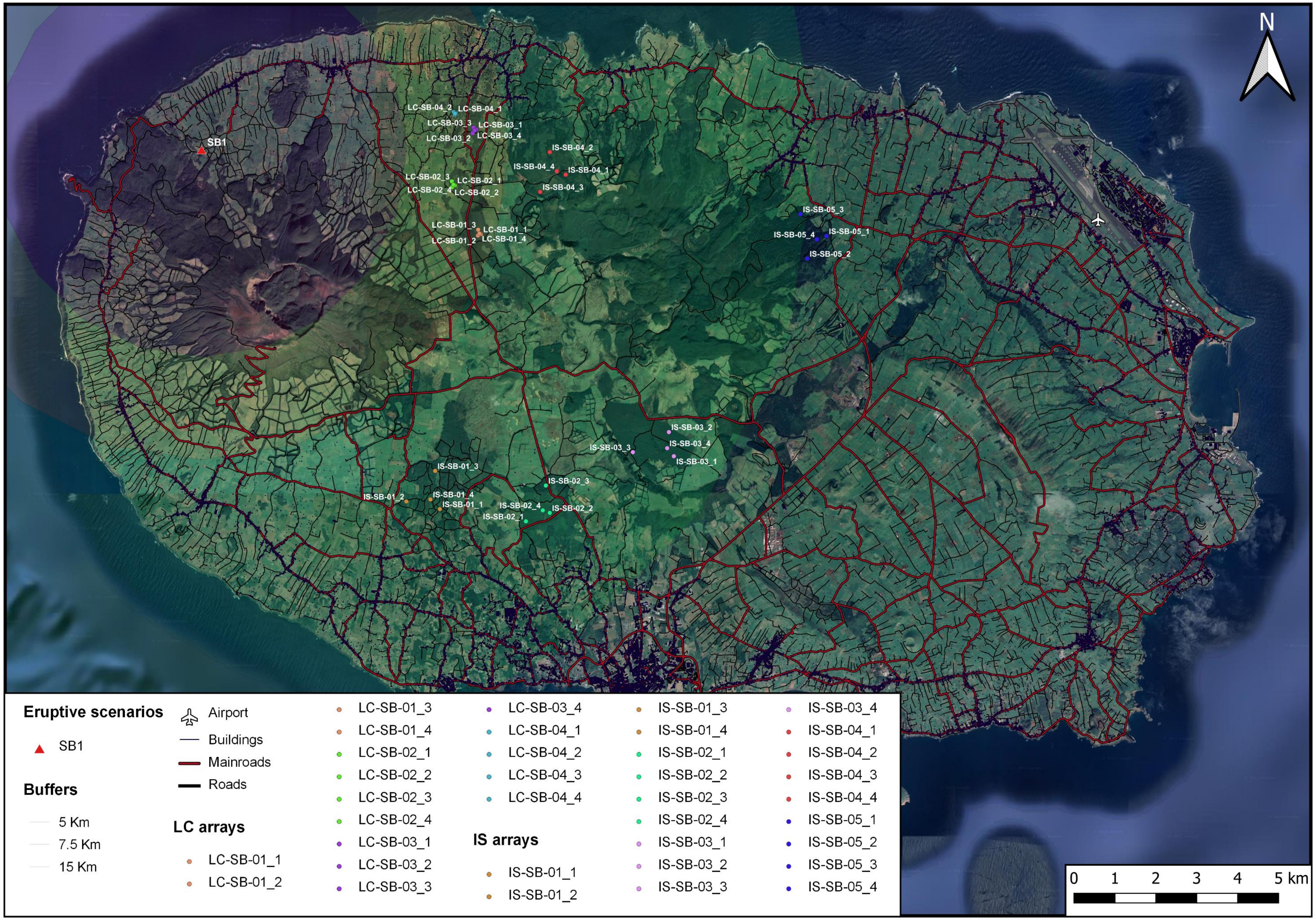
N
SB1
LC-SB-04_2
LC-SB-04_1
LC-SB-03_3
LC-SB-03_1
LC-SB-03_2
LC-SB-03_4
IS-SB-04_2
IS-SB-04_4
IS-SB-04_1
LC-SB-02_3
LC-SB-02_1
LC-SB-02_4
LC-SB-02_2
IS-SB-04_3
IS-SB-05_3
LC-SB-01_3
LC-SB-01_1
LC-SB-01_2
LC-SB-01_4
IS-SB-05_4
IS-SB-05_1
IS-SB-05_2
IS-SB-03_2
IS-SB-03_4
IS-SB-03_3
IS-SB-03_1
IS-SB-01_3
IS-SB-02_3
IS-SB-01_2
IS-SB-01_4
IS-SB-01_1
IS-SB-02_4
IS-SB-02_2
IS-SB-02_1
Eruptive scenarios
▲ SB1
Buffers
5 Km
7.5 Km
15 Km
Airport
Buildings
Mainroads
Roads
LC arrays
● LC-SB-01_1
● LC-SB-01_2
● LC-SB-01_3
● LC-SB-01_4
● LC-SB-02_1
● LC-SB-02_2
● LC-SB-02_3
● LC-SB-02_4
● LC-SB-03_1
● LC-SB-03_2
● LC-SB-03_3
● LC-SB-03_4
● LC-SB-04_1
● LC-SB-04_2
● LC-SB-04_3
● LC-SB-04_4
IS arrays
● IS-SB-01_1
● IS-SB-01_2
● IS-SB-01_3
● IS-SB-01_4
● IS-SB-02_1
● IS-SB-02_2
● IS-SB-02_3
● IS-SB-02_4
● IS-SB-03_1
● IS-SB-03_2
● IS-SB-03_3
● IS-SB-03_4
● IS-SB-04_1
● IS-SB-04_2
● IS-SB-04_3
● IS-SB-04_4
● IS-SB-05_1
● IS-SB-05_2
● IS-SB-05_3
● IS-SB-05_4
0 1 2 3 4 5 km

A. Preliminary selection of sites in the Azores Islands

A.5. Santa Bárbara volcano (Terceira Island)

A.5.3. Features of the LC and IS arrays (Table)

ID	Aperture (m)	Back azimuth to the source (°)	Parish	County	Island
LC-SB-01	144	**SB1**: 286.15	Biscoitos	Praia da Vitória	Terceira
LC-SB-02	146	**SB1**: 277.15	Biscoitos	Praia da Vitória	Terceira
LC-SB-03	140	**SB1**: 265.65	Biscoitos	Praia da Vitória	Terceira
LC-SB-04	62	**SB1**: 261.75	Biscoitos Altares	Praia da Vitória Angra do Heroísmo	Terceira
IS-SB-01	1041	**SB1**: 326.29	São Bartolomeu de Regatos	Angra do Heroísmo	Terceira
IS-SB-02	993	**SB1**: 316.16	Terra Chã Posto Santo	Angra do Heroísmo	Terceira
IS-SB-03	1011	**SB1**: 302.41	Posto Santo Porto Judeu	Angra do Heroísmo	Terceira
IS-SB-04	1001	**SB1**: 273.17	Biscoitos	Praia da Vitória	Terceira
IS-SB-05	1099	**SB1**: 278.19	Agualva	Praia da Vitória	Terceira

A. Preliminary selection of sites in the Azores Islands

A.6. Caldeira volcano (Faial Island)

A.6.1. Eruptive scenario CA1 (Map)

Eruptive scenario CA1, Caldeira volcano. Volcanic and tectonic structures are from Madeira (1998), modified by CIVISA.

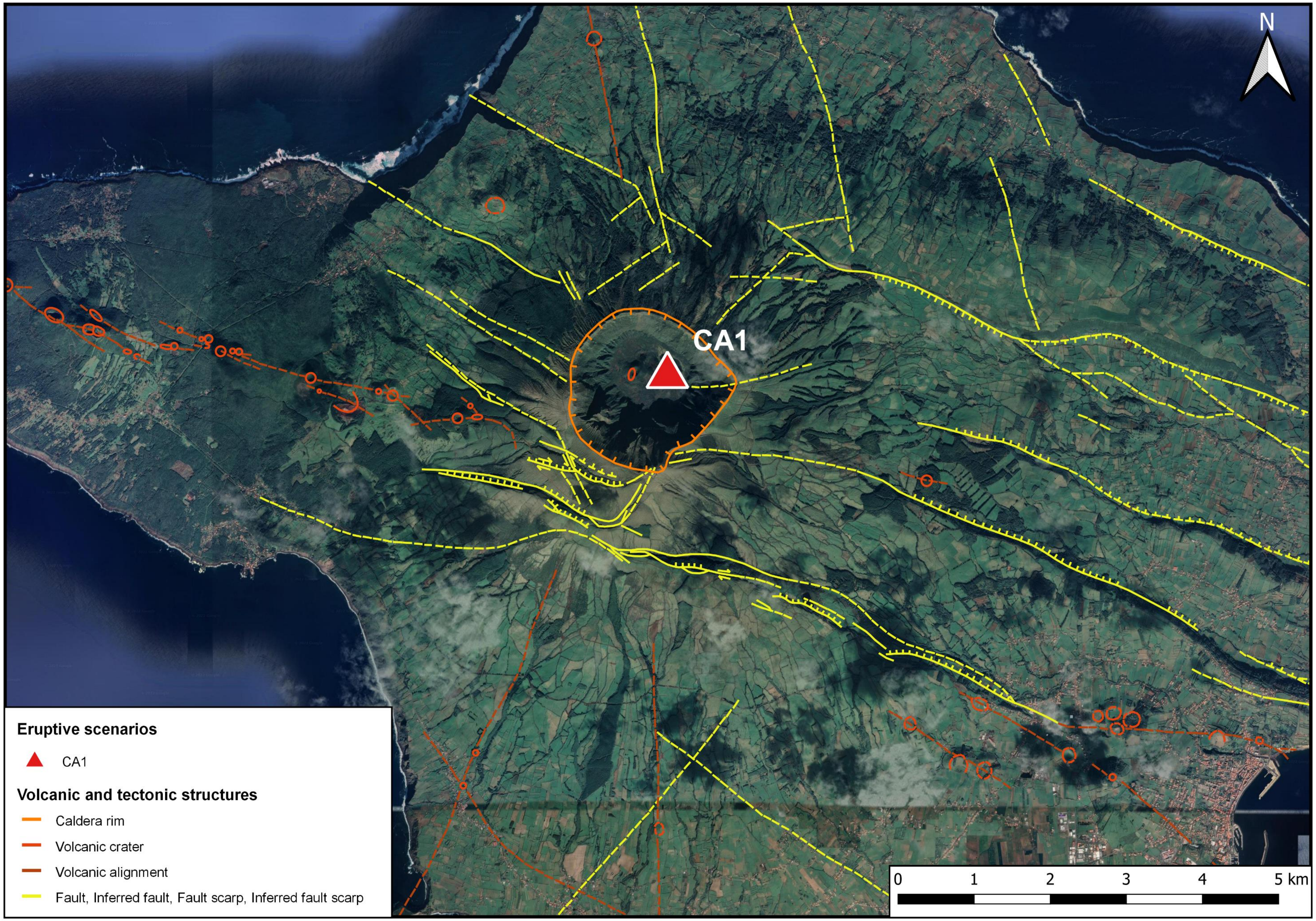
N
CA1
Eruptive scenarios
CA1
Volcanic and tectonic structures
Caldera rim
Volcanic crater
Volcanic alignment
Fault, Inferred fault, Fault scarp, Inferred fault scarp
0
1
2
3
4
5 km

A. Preliminary selection of sites in the Azores Islands

A.6. Caldeira volcano (Faial Island)

A.6.2. LC and IS arrays (Map)

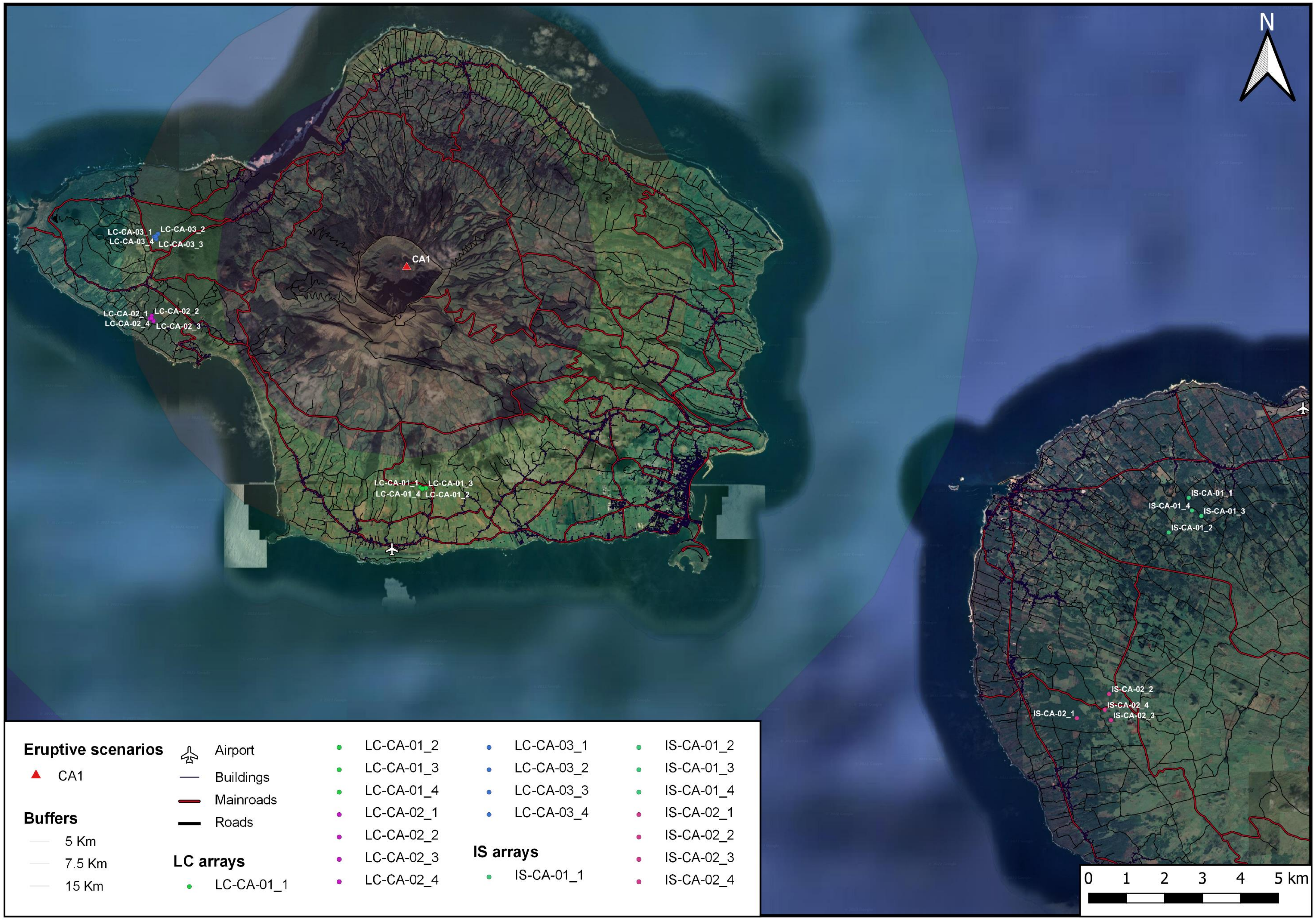
N
LC-CA-03_1
LC-CA-03_4
LC-CA-03_2
LC-CA-03_3
CA1
LC-CA-02_1
LC-CA-02_4
LC-CA-02_2
LC-CA-02_3
LC-CA-01_1
LC-CA-01_4
LC-CA-01_3
LC-CA-01_2
IS-CA-01_1
IS-CA-01_4
IS-CA-01_3
IS-CA-01_2
IS-CA-02_2
IS-CA-02_4
IS-CA-02_1
IS-CA-02_3
Eruptive scenarios
CA1
Buffers
5 Km
7.5 Km
15 Km
Airport
Buildings
Mainroads
Roads
LC arrays
LC-CA-01_1
LC-CA-01_2
LC-CA-01_3
LC-CA-01_4
LC-CA-02_1
LC-CA-02_2
LC-CA-02_3
LC-CA-02_4
LC-CA-03_1
LC-CA-03_2
LC-CA-03_3
LC-CA-03_4
IS arrays
IS-CA-01_1
IS-CA-01_2
IS-CA-01_3
IS-CA-01_4
IS-CA-02_1
IS-CA-02_2
IS-CA-02_3
IS-CA-02_4
0 1 2 3 4 5 km

A. Preliminary selection of sites in the Azores Islands

A.6. Caldeira volcano (Faial Island)

A.6.3. Features of the LC and IS arrays (Table)

ID	Aperture (m)	Back azimuth to the source (°)	Parish	County	Island
LC-CA-01	142	**CA1**: 355.60	Castelo Branco	Horta	Faial
LC-CA-02	143	**CA1**: 78.53	Capelo	Horta	Faial
LC-CA-03	140	**CA1**: 96.90	Capelo	Horta	Faial
IS-CA-01	1067	**CA1**: 287.69	Madalena	Madalena	Pico
IS-CA-02	1087	**CA1**: 302.72	Candelária Criação Velha	Madalena	Pico

A. Preliminary selection of sites in the Azores Islands

A.7. Montanha do Pico volcano (Pico Island)

A.7.1. Eruptive scenario MP1 (Map)

Eruptive scenario M1, Montanha do Pico volcano. Volcanic and tectonic structures are from Madeira (1998), modified by CIVISA.

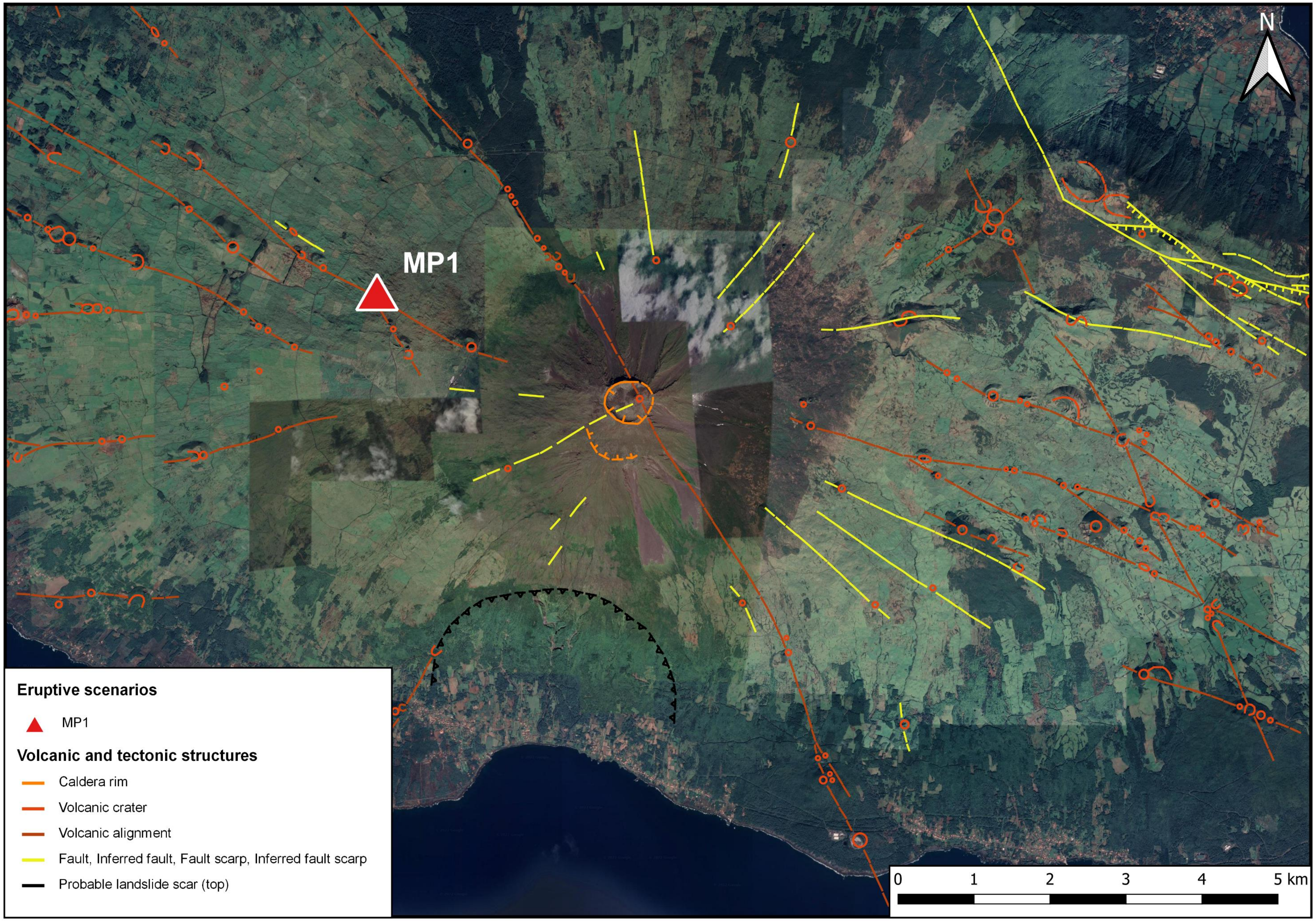
MP1
N
Eruptive scenarios
▲ MP1
Volcanic and tectonic structures
Caldera rim
Volcanic crater
Volcanic alignment
Fault, Inferred fault, Fault scarp, Inferred fault scarp
Probable landslide scar (top)
0
1
2
3
4
5 km

A. Preliminary selection of sites in the Azores Islands

A.7. Montanha do Pico volcano (Pico Island)

A.7.2. LC and IS arrays (Map)

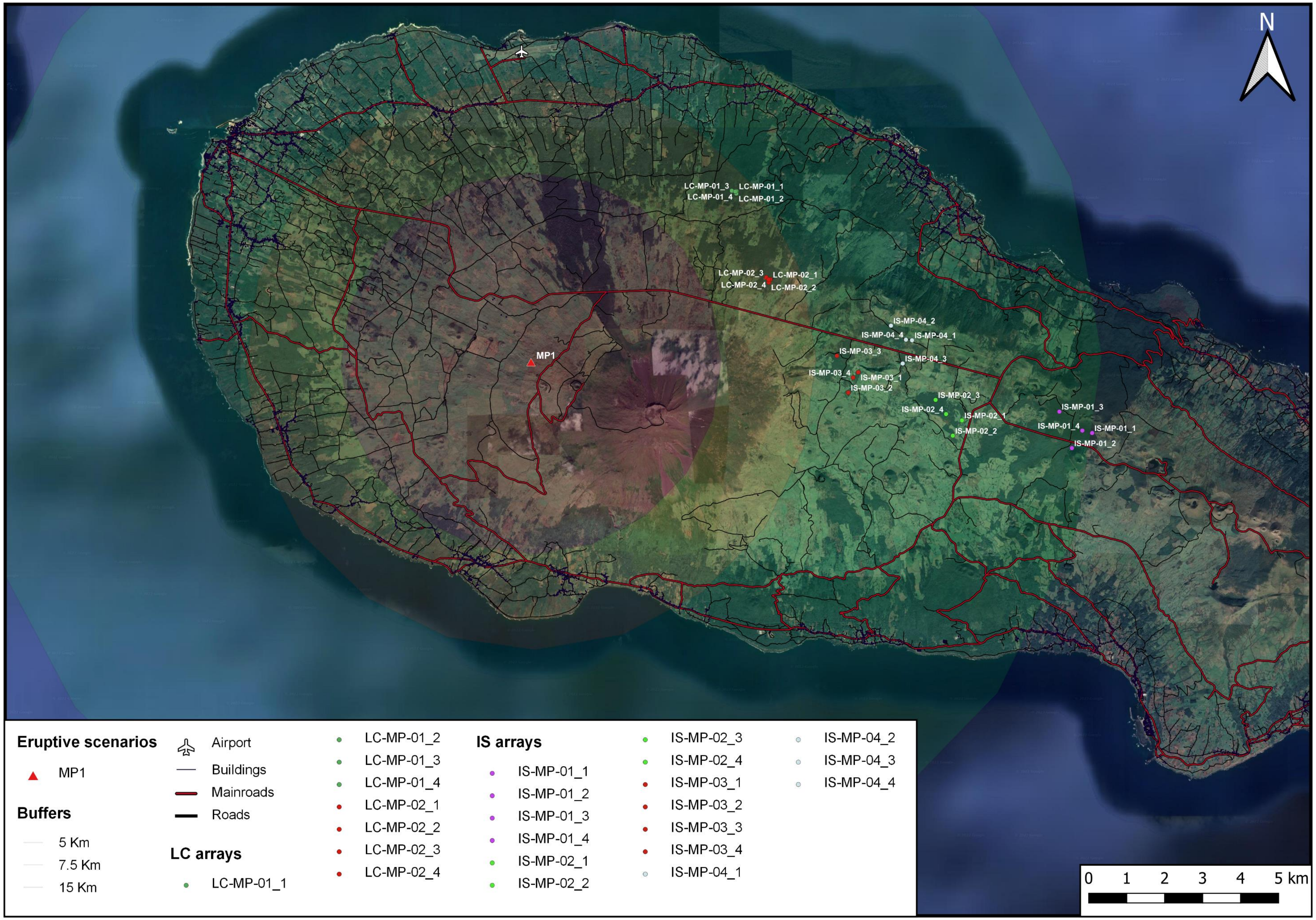
N
LC-MP-01_3
LC-MP-01_1
LC-MP-01_4
LC-MP-01_2
LC-MP-02_3
LC-MP-02_1
LC-MP-02_4
LC-MP-02_2
IS-MP-04_2
IS-MP-04_4
IS-MP-04_1
IS-MP-03_3
IS-MP-04_3
MP1
IS-MP-03_4
IS-MP-03_1
IS-MP-03_2
IS-MP-02_3
IS-MP-02_4
IS-MP-02_1
IS-MP-02_2
IS-MP-01_3
IS-MP-01_4
IS-MP-01_1
IS-MP-01_2
Eruptive scenarios
MP1
Buffers
5 Km
7.5 Km
15 Km
Airport
Buildings
Mainroads
Roads
LC arrays
LC-MP-01_1
LC-MP-01_2
LC-MP-01_3
LC-MP-01_4
LC-MP-02_1
LC-MP-02_2
LC-MP-02_3
LC-MP-02_4
IS arrays
IS-MP-01_1
IS-MP-01_2
IS-MP-01_3
IS-MP-01_4
IS-MP-02_1
IS-MP-02_2
IS-MP-02_3
IS-MP-02_4
IS-MP-03_1
IS-MP-03_2
IS-MP-03_3
IS-MP-03_4
IS-MP-04_1
IS-MP-04_2
IS-MP-04_3
IS-MP-04_4
0
1
2
3
4
5 km

A. Preliminary selection of sites in the Azores Islands

A.7. Montanha do Pico volcano (Pico Island)

A.7.3. Features of the LC and IS arrays (Table)

ID	Aperture (m)	Back azimuth to the source (°)	Parish	County	Island
LC-MP-01	143	**MP1**: 230.10	Santo António	São Roque do Pico	Pico
LC-MP-02	139	**MP1**: 250.80	Santo António	São Roque do Pico	Pico
IS-MP-01	1003	**MP1**: 277.05	São Roque do Pico Prainha Lajes do Pico	São Roque do Pico Lajes do Pico	Pico
IS-MP-02	1026	**MP1**: 277.73	São Roque do Pico Lajes do Pico	São Roque do Pico Lajes do Pico	Pico
IS-MP-03	1018	**MP1**: 271.28	São Roque do Pico	São Roque do Pico	Pico
IS-MP-04	1040	**MP1**: 266.59	São Roque do Pico	São Roque do Pico	Pico

B. Assessment in *situ* of the pre-selected sites - São Miguel Island

B.1. Sites to assess in *situ* (Map)

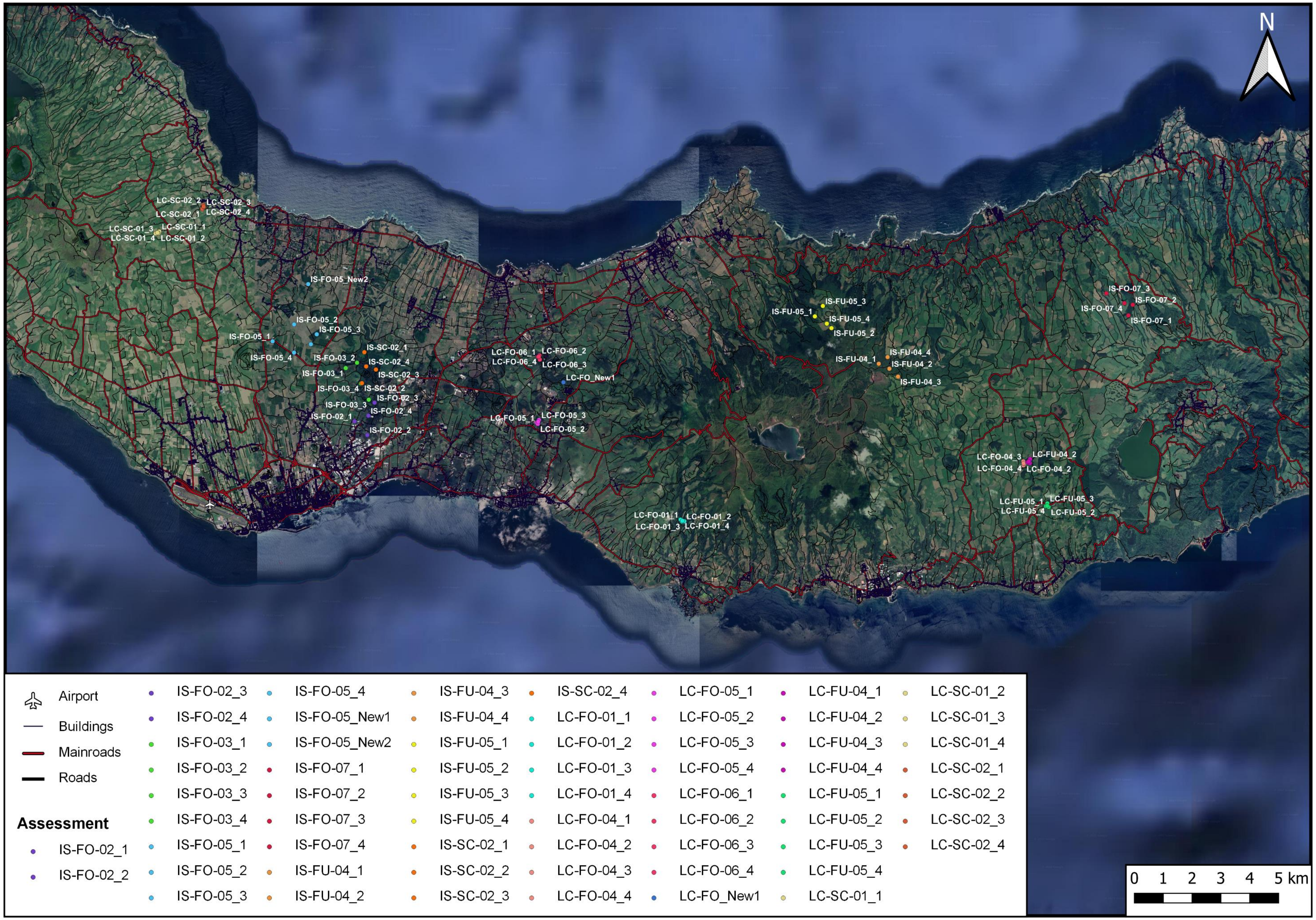
N
0 1 2 3 4 5 km
Airport
Buildings
Mainroads
Roads
Assessment
IS-FO-02_1
IS-FO-02_2
IS-FO-02_3
IS-FO-02_4
IS-FO-03_1
IS-FO-03_2
IS-FO-03_3
IS-FO-03_4
IS-FO-05_1
IS-FO-05_2
IS-FO-05_3
IS-FO-05_4
IS-FO-05_New1
IS-FO-05_New2
IS-FO-07_1
IS-FO-07_2
IS-FO-07_3
IS-FO-07_4
IS-FU-04_1
IS-FU-04_2
IS-FU-04_3
IS-FU-04_4
IS-FU-05_1
IS-FU-05_2
IS-FU-05_3
IS-FU-05_4
IS-SC-02_1
IS-SC-02_2
IS-SC-02_3
IS-SC-02_4
LC-FO-01_1
LC-FO-01_2
LC-FO-01_3
LC-FO-01_4
LC-FO-04_1
LC-FO-04_2
LC-FO-04_3
LC-FO-04_4
LC-FO-05_1
LC-FO-05_2
LC-FO-05_3
LC-FO-05_4
LC-FO-06_1
LC-FO-06_2
LC-FO-06_3
LC-FO-06_4
LC-FO_New1
LC-FU-04_1
LC-FU-04_2
LC-FU-04_3
LC-FU-04_4
LC-FU-05_1
LC-FU-05_2
LC-FU-05_3
LC-FU-05_4
LC-SC-01_1
LC-SC-01_2
LC-SC-01_3
LC-SC-01_4
LC-SC-02_1
LC-SC-02_2
LC-SC-02_3
LC-SC-02_4

B. Assessment in *situ* of the pre-selected sites - São Miguel Island

B.2. Characterization of the assessed sites (Tables and Photos)

ARRAY ID	LC-SC-01
Land cover	Irregular basaltic lava flow. Dense vegetation with incense trees and ginger lilies. Various side entrances.
Surrounding environment (background noise)	Silent. Paved road at 250 metres, with little traffic. Atlantic Ocean at 3 Km.
Gradient (slope) + GPS	High point (Solar panel): GPS: 37°49'36.23'', 25°43'9.47'', 455 m (app); 427 m (smartwatch). Midpoint: GPS: 37°49'39.20'', 25°43'6.79'', 442 m (app); 410 m (smartwatch). Low point: GPS: 37°49'39.46'', 25°43'3.47'', 438 m; 403 m (smartwatch). Slope ≈ 12 % (Google Earth Pro).
GSM	High point: Great (- 95 dB, 4 G). Midpoint (inside the forest): Bad (no GSM signal). Low point (outside the forest): Moderate (-113 dB).
Road accesses	Fair: 4 x 4 car. Difficult in winter.
Ownership	Private.
Security	High.
Observations	Site for signal testing.

Photo B.1 - View of the forest from the paved road.

Photo B.2 - Side entrance to the forest at the midpoint.

Photo B.3 - Vegetation inside the forest.

Photo B.4 - View from the high point to the extent of the forest (North-orientated).

Photo B.5 - South view.

Photo B.6 - Spot to install solar panel and GPS antenna.

Photo B.7 - Irregular basaltic lava flows of the same type that form the forest floor.

Photo B.8 - Low point of the forest.

ARRAY ID	LC-SC-02
Land cover	Irregular basaltic lava flow. Dense vegetation with tall and fruit trees (it is a closed farm).
Surrounding environment (background noise)	Several man-made sources of background noise: - Surrounding houses. - Regional road with heavy traffic at 640 metres. - Atlantic Ocean at 1 Km.
Gradient (slope) + GPS	Slope ≈ 18 % (Google Earth Pro).
GSM	Great (- 95 dB, 4 G).
Road accesses	Good.
Ownership	Private. Close property (Quinta do Maranhão, Capelas). Authorisation required.
Security	Very high.
Observations	Site excluded.

Photo B.9 - Entrance (farm gate).

Photo B.10 - Terrain high slope.

Photo B.11 - Surrounding environment (residential area and Atlantic Ocean).

ARRAY ID	IS-FO-05_2
Land cover	Basaltic lava flow; loose rock. Dense vegetation with tall trees of eucalyptus, incense, beech, and cryptomeria. Various side entrances.
Surrounding environment (background noise)	Mechanical milking at 375 metres (farming operation). High traffic main road at 960 metres. Atlantic Ocean at 4 Km.
Gradient (slope) + GPS	Solar panel: GPS: 37°47'55.06'', 25°39'53.12'', 244 m (app); 217 m (smartwatch). Flat terrain. Slope ≈ 1 % (Google Earth Pro).
GSM	Great (- 95 dB, 4 G).
Road accesses	Very good.
Ownership	Private. Fenced farming operation (Exploração Agrícola dos italianos - Exploração dos Beirais).
Security	High.
Observations	Site for signal testing.

Photo B.12 - Access 1 to the farm.

Photo B.13 - Identification of the owner and the farm.

Photo B.14 - Farm's entrance.

Photo B.15 - Access to the forest.

Photo B.16 - Forest length.

Photo B.17 - South view.

Photo B.18 - Solar panel spot.

Photo B.19 - Vegetation inside the forest.

ARRAY ID	IS-FO-05_1
Land cover	Pond with trees around.
Surrounding environment (background noise)	High traffic main road at 40 metres. Atlantic Ocean at 5 Km.
Gradient (slope) + GPS	
GSM	Great (- 94 dB, 4 G, at the main road).
Road accesses	Bad (barely accessible).
Ownership	Natural heritage (Lagoa do Charco da Madeira).
Security	Low.
Observations	Site excluded. Necessary to find another site to complete IS-FO-05 array.

Photo B.20 - Lagoa do Charco da Madeira viewed from the main road (Serra Gorda scoria cone behind).

ARRAY ID	IS-FO-05_4
Land cover	Dense bush.
Surrounding environment (background noise)	Beside a high traffic main road. Atlantic Ocean at 5 Km.
Gradient (slope) + GPS	
GSM	Great (- 94 dB, 4 G, at the main road).
Road accesses	Good.
Ownership	Private. Fenced property (Rádio Marconi).
Security	High.
Observations	Site excluded. Necessary to find another site to complete IS-FO-05 array.

Photo B.21 - Entrance.

Photo B.22 - View from the main road.

ARRAY ID	IS-FO-05_New1
Land cover	Irregular basaltic lava flow. Dense vegetation with tall trees of incense.
Surrounding environment (background noise)	Silent. Medium traffic main road at 500 metres. Atlantic Ocean at 4 Km.
Gradient (slope) + GPS	Solar panel: GPS: 37°47'33.51'', 25°39'29.72'', 238 m (app); 213 m (smartwatch). Flat terrain. Slope ≈ 0 % (Google Earth Pro).
GSM	Great (- 96 dB, 4 G).
Road accesses	Fair: 4 x 4 car. Difficult in winter.
Ownership	Private.
Security	High.
Observations	Site for signal testing.

Photo B.22 - Entrance.

Photo B.23 - Basaltic lava flow as ground base.

Photo B.24 - Scaled basaltic lava flow.

Photo B.25 - South view.

Photo B.26 - South-east view.

Photo B.27 - View to solar panel spot.

Photo B.28 - Vegetation inside the forest.

Photo B.29 - Vegetation inside the forest.

ARRAY ID	IS-FO-05_3
Land cover	Irregular basaltic lava flow. Dense vegetation with tall trees of incense, eucalyptus, and acacia as well as ginger lilies and ferns.
Surrounding environment (background noise)	Silent. Medium traffic main road at 530 metres. Atlantic Ocean at 4 Km.
Gradient (slope) + GPS	Solar panel: GPS: 37°47'38.15'', 25°39'31.29'', 199 m (app); 222 m (smartwatch). Flat terrain. Slope ≈ 1.6 % (Google Earth Pro).
GSM	Good (- 106 dB, 4 G).
Road accesses	Fair: 4 x 4 car. Difficult in winter.
Ownership	Private.
Security	High.
Observations	Site for signal testing. Find a more secure spot for solar panel. Extensive forested area: it can have two IS elements spaced by 500 metres.

Photo B.29 - View to the forest from the main road.

Photo B.30 - Road access.

Photo B.31 - South view.

Photo B.32 - Solar panel spot.

Photo B.33 - South facing extent of the forest (left)

Photo B.34 - South facing extent of the forest (right).

Photo B.35 - Vegetation inside the forest.

Photo B.36 - Other access.

ARRAY ID	IS-FO-05_New2
Land cover	Irregular basaltic lava flow. Dense vegetation with tall trees of incense and other trees.
Surrounding environment (background noise)	Several farming operations on the surroundings. Windy place. High traffic main road at 600 metres. Atlantic Ocean at 3 Km.
Gradient (slope) + GPS	Solar panel: GPS: 37°47'38.15'', 25°39'31.29'', 199 m (app); 222 m (smartwatch). Sloping terrain. Slope ≈ 10 % (Google Earth Pro).
GSM	Great (- 85 dB, 4 G).
Road accesses	Fair: 4 x 4 car. Difficult in winter.
Ownership	Private.
Security	High.
Observations	Site for signal testing. Maximum slope of the complete IS-FO-05 array (_2; _New1; _3; _New2) ≈ 3 % (Google Earth Pro).

Photo B.37 - Extent of the forest.

Photo B.38 - South view.

Photo B.39 - Spot for solar panel.

Photo B.40 - Possible entrance to the forest.

Photo B.41 - Vegetation inside the forest.

ARRAY ID	IS-FO-03_1
Land cover	Bush next to a scoria cone.
Surrounding environment (background noise)	Mechanical milking at High traffic main road at 190 metres. Atlantic Ocean at 4 Km.
Gradient (slope) + GPS	
GSM	
Road accesses	Good.
Ownership	Private.
Security	Low.
Observations	Site excluded. It is an area surrounded by several scoria cones which may interfere in the reception of direct infrasound waves. Therefore, other sites in this area were also exclude, namely: IS-FO-03_2 (military property); IS-FO-03_3/_4 and IS-SC-02_2 (beside a high traffic main road); IS-SC-02_1 (impossible access); IS-SC-02_3/_4 (inside the Recreational Forest Reserve of Pinhal da Paz, which is a governmental domain and highly frequented by the population).

Photo B.42 - Entrance.

Photo B.43 - Terrain viewed from the road, with a scoria cone behind.

ARRAY ID	IS-FO-02_3
Land cover	Irregular basaltic lava flow (clinker of an *aa* lava flow). Dense vegetation with tall trees of incense, beech, and other trees.
Surrounding environment (background noise)	Several farms around. Industry activity at 140 metres. High traffic main road at 190 metres. Atlantic Ocean at 3 Km.
Gradient (slope) + GPS	Solar panel: GPS: 37°47'38.15'', 25°39'31.29'', 199 m (app); 222 m (smartwatch). Sloping terrain. Slope ≈ 7 % (Google Earth Pro).
GSM	Great (- 96 dB, 4 G).
Road accesses	Good.
Ownership	Private. Walled terrain.
Security	High.
Observations	Site for signal testing. Due to a high level of background noise, it is a potential site only in case of belonging to an exclusive zone during a volcanic unrest.

Photo B.44 - Road access.

Photo B.45 - Entrance.

Photo B.46 - View to the forest (above the wall).

Photo B.47 - South view.

Photo B.48 - Spot for solar panel.

Photo B.49 - Vegetation inside the forest.

ARRAY ID	IS-FO-02_1 IS-FO-02_2 IS-FO-02_4
Land cover	Dense vegetation with tall and fruit trees, inside residential properties.
Surrounding environment (background noise)	Residential area. Ponta Delgada city at 1 Km. Atlantic Ocean at 2 Km.
Gradient (slope) + GPS	
GSM	
Road accesses	Fair: 4 x 4 car. Difficult in winter.
Ownership	Private. Huge properties with extent green areas in a VIP residential zone.
Security	Very high.
Observations	IS-FO-02_1*: Ask owner's permission to visit. IS-FO-02_2: Site excluded, due to its narrow and walled accessed (see photos below). IS-FO-02_4*: Ask owner's permission to visit (Quinta da Bela Vista). *Due to a high level of background noise, it is a potential site only in case of belonging to an exclusive zone during a volcanic unrest. It is necessary to find another spot to complete the array IS-FO-02.

Photo B.50 - Walled dirt road to access IS-FO-02_2.

Photo B.51 - Entrance to IS-FO-02_2 closed.

Photo B.52 - Dead-end dirt road (almost impossible to turn the car around).

ARRAY ID	LC-FO-06
Land cover	Irregular basaltic lava flow. Dense vegetation with tall trees of incense, beech as well as ginger lilies.
Surrounding environment (background noise)	Farming operations at 200 metres. Quarry activities at 1 Km. Highway at 40 metres. Atlantic Ocean at 3 Km.
Gradient (slope) + GPS	Solar panel: GPS: 37°47'9.87'', 25°34'10.50'', 180 m (app); 172 m (smartwatch). Flat terrain. Slope ≈ 1 % (Google Earth Pro).
GSM	Great (- 96 dB, 4 G).
Road accesses	Fair: 4 x 4 car. Difficult in winter.
Ownership	Private. Walled terrain.
Security	Moderate.
Observations	Site for signal testing. Due to a high level of background noise, it is a potential site only in case of belonging to an exclusive zone during a volcanic unrest.

Photo B.53 - View at the extension of the forest (at the back).

Photo B.54 - South view.

Photo B.55 - Spot for solar panel.

Photo B.56 - Possible entrance to inside the forest.

Photo B.57 - Vegetation inside the forest.

Photo B.58 - Access to the site (later discovered).

ARRAY ID	LC-FO-New1
Land cover	Irregular basaltic lava flow (clinker of an *aa* lava flow). Scattered vegetation between opening clearings.
Surrounding environment (background noise)	In the middle of an industrial and cattle zone. Atlantic Ocean at 3 Km.
Gradient (slope) + GPS	
GSM	Great (- 90 dB, 4 G).
Road accesses	Foot access next to Soluções M. Road access through a pig breeding (no permission granted). Other accesses are blocked with big rocks.
Ownership	Private.
Security	Low.
Observations	Site excluded.

Photo B.59 - Blocked accessed

Photo B.60 - Opening clearings inside the forest.

ARRAY ID	LC-FO-05
Land cover	Irregular basaltic lava flow. Dense vegetation with tall trees of incense, beech, acacia as well as ginger lilies.
Surrounding environment (background noise)	In the middle of Cabouco parish's urbanisation. Possible mechanical milking around. Quarry activities at 300 metres (Pico João Ramos quarry). High traffic road at 200 metres. Atlantic Ocean at 2 Km.
Gradient (slope) + GPS	Solar panel: GPS: 37°46'6.14'', 25°34'4.47'', 199 m (app); 207 m (smartwatch). Flat terrain. Slope ≈ 0 % (Google Earth Pro).
GSM	Great (- 95 dB, 4 G).
Road accesses	Fair: 4 x 4 car. Difficult in winter.
Ownership	Private. Owner: Ana Maria Faria e Maia. Tenants: Vítor Pacheco and Carlos Oliveira.
Security	Very high.
Observations	Site for signal testing. Due to a high level of background noise, it is a potential site only in case of belonging to an exclusive zone during a volcanic unrest.

Photo B.61 - Road access (Cabouco parish's main road).

Photo B.62 - Entrance.

Photo B.63 - South view.

Photo B.64 - Spot for solar panel.

Photo B.65 - Entrance to the forest.

Photo B.66 - Vegetation inside the forest.

ARRAY ID	LC-FO-01 LC-FO-04 LC-FU-05
Land cover	Tall trees on waterline.
Surrounding environment (background noise)	
Gradient (slope) + GPS	Embedded valley.
GSM	
Road accesses	
Ownership	
Security	
Observations	Sites excluded.

Photo B.67 - LC-FO-01 waterline.

Photo B.68 - LC-FO-04 waterline.

Photo B.69 - LC-FU-05 waterline.

ARRAY ID	LC-FU-05
Land cover	Ground based formed by pumice. Dense vegetation with tall trees of cryptomeria as well as ferns.
Surrounding environment (background noise)	Farming activities in the surroundings. Possible mechanical milking. Beside a waterline. Beside a low traffic road. Atlantic Ocean at 4 Km.
Gradient (slope) + GPS	Solar panel: GPS: 37°45'20.37'', 25°22'38.58'', 521 m (app); 508 m (smartwatch). Flat terrain. Slope ≈ 1 % (Google Earth Pro).
GSM	Moderate (- 92 dB, 2 G).
Road accesses	Good.
Ownership	Private.
Security	Moderate.
Observations	Site for signal testing. Several scoria cones around can act as topographic barriers for direct infrasound waves. Ideal site for an IS array element, not for a LC array. Therefore, it is necessary to find more 3 sites to complete a new IS array. It may show difficulties in recharging the solar panel in winter, as well as on GSM signal.

Photo B.70 - Road access to the site from the regional main road.

Photo B.71 - Aerial view of the site (drone).

Photo B.72 - Extension of the forest.

Photo B.73 - South view

Photo B.74 - Spot for solar panel.

Photo B.75 - Vegetation inside the forest.

ARRAY ID	IS-FU-05_1 IS-FU-05_2 IS-FU-05_3 IS-FU-05_4
Land cover	Bush vegetation and small trees on waterlines.
Surrounding environment (background noise)	Windy place. Farming activities. Regional main road at 1400 metres. Atlantic Ocean at 2 Km.
Gradient (slope) + GPS	Elevation: 517 m *a.s.l.* (app). Slope ≈ 6 % (Google Earth Pro).
GSM	Moderate (- 115 dB).
Road accesses	Fair: 4 x 4 car. Very difficult in winter.
Ownership	Private.
Security	High.
Observations	Sites excluded.

Photo B.76 - Areal view of the sites, with the waterlines well defined (drone).

Photo B.77 - South view, with Fogo volcano at the back.

Photo B.78 - IS-FU-05_1 waterline.

Photo B.79 - IS-FU-05_2 waterline.

Photo B.80 - IS-FU-05_4 waterline.

Photo B.81 - IS-FU-05_3 waterline.

Photo B.82 - Vegetation on the waterlines.

Photo B.83 - Taking notes on the elements.

ARRAY ID	IS-FU-04_4
Land cover	Ground based formed by pumice. Dense vegetation with tall trees of cryptomeria as well as ferns and moss.
Surrounding environment (background noise)	Very quiet inside the forest. Windy outside the forest. Possible mechanical milking. Beside a waterline. Low traffic road at 100 metres. Atlantic Ocean at 4 Km.
Gradient (slope) + GPS	Solar panel: GPS: 37.78935886°, -25.43172006°, 799 m (app). Flat terrain. Slope ≈ 2 % (Google Earth Pro).
GSM	Good (- 92 dB, 2 G).
Road accesses	Fair: 4 x 4 car. Difficult in winter.
Ownership	Private (Pastos da Margarida).
Security	Moderate.
Observations	Site for signal testing. It may show difficulties in recharging the solar panel in winter.

Photo B.84 - Aerial view of the site, with Monte Escuro scoria cone at the back (drone).

Photo B.85 - Road access by north side of the island.

Photo B.86 - Road access (forest at the back).

Photo B.87 - Dirt track entrance to the site.

Photo B.88 - South view and spot for solar panel facing south.

Photo B.89 - Vegetation inside the forest.

ARRAY ID	IS-FU-04_1
Land cover	Ground based formed by pumice. Dense vegetation with tall trees of cryptomeria as well as ferns and moss.
Surrounding environment (background noise)	Beside a waterline. Medium traffic road at 100 metres. Atlantic Ocean at 4 Km.
Gradient (slope) + GPS	Solar panel: GPS: 37.78671205°, -25.43476907°, 803 m (app). Flat terrain. Slope ≈ 1 % (Google Earth Pro).
GSM	Bad (- 103 dB, 2 G).
Road accesses	Fair: 4 x 4 car. Difficult in winter.
Ownership	Private (Pastos da Margarida).
Security	Moderate.
Observations	Site for signal testing. It may show difficulties in recharging the solar panel in winter once Monte Escuro scoria cone blocks the sunrays. Communications via telemetry (radios) should be a viable option since GSM signal is bad.

Photo B.90 - Aerial view of the site (drone).

Photo B.91 - Road access.

Photo B.92 - Entrance.

Photo B.93 - South view and spot for solar panel.

Photo B.94 - Vegetation inside the forest.

ARRAY ID	IS-FU-04_2
Land cover	Ground based formed by pumice. Dense vegetation with tall trees of cryptomeria as well as ferns and moss.
Surrounding environment (background noise)	Medium traffic road at 90 metres. Atlantic Ocean at 4 Km.
Gradient (slope) + GPS	Solar panel: GPS: 37.7854883°, -25.43149353°, 820 m (app). Flat terrain. Slope ≈ 3 % (Google Earth Pro).
GSM	Bad (- 108 dB, 2 G).
Road accesses	Fair: 4 x 4 car. Difficult in winter.
Ownership	Private (Pastos da Margarida).
Security	Moderate.
Observations	Site for signal testing. It may show difficulties in recharging the solar panel in winter once Monte Escuro scoria cone blocks the sunrays. Communications via telemetry (radios) should be a viable option since GSM signal is bad.

Photo B.95 - Aerial view of the site and the opening clearing (drone).

Photo B.96 - South view and the opening clearing to deploy solar panel.

Photo B.97 - Vegetation inside the forest.

ARRAY ID	IS-FU-04_3
Land cover	Ground based formed by pumice. Dense vegetation with tall trees of cryptomeria as well as ferns and moss.
Surrounding environment (background noise)	Beside a waterline. Medium traffic road at 130 metres. Atlantic Ocean at 4 Km.
Gradient (slope) + GPS	Solar panel: GPS: 37.782400°, -25.47832°, 799 m (app). Flat terrain. Slope ≈ 0 % (Google Earth Pro).
GSM	Good (- 92 dB).
Road accesses	Fair: 4 x 4 car. Difficult in winter.
Ownership	Private (Pastos da Margarida).
Security	Moderate.
Observations	Site for signal testing. Maximum slope of the complete IS-FU-04 array (_1; _2; _3; _4) ≈ 3 % (Google Earth Pro).

Photo B.98 - Waterline (left) and south side of the forest where a solar panel should be installed (right).

Photo B.99 - South view.

ARRAY ID	IS-F0-07_1 IS-F0-07_2 IS-F0-07_3 IS-F0-07_4
Land cover	Bush vegetation and tall trees on waterlines.
Surrounding environment (background noise)	
Gradient (slope) + GPS	
GSM	
Road accesses	Fair: 4 x 4 car. Very difficult in winter.
Ownership	Private.
Security	High.
Observations	Sites excluded.

Photo B.100 - IS-FO-07_1 waterline.

Photo B.101 - Vegetation on the IS-FO-07_1 waterline.

Photo B.102 - Road access and the result of 5 min lashing rain.

Photo B.103 - Access to IS-FO-07_2.

Photo B.104 - Impossible access to IS-FO-07_2 (on the right).

Photo B.105 - IS-FO-07_2 waterline.

B. Assessment in *situ* of the pre-selected sites - São Miguel Island

B.3. Sites selected for signal testing (Map)


N
LC-SC-01_3
LC-SC-01_1
LC-SC-01_4
LC-SC-01_2
IS-FO-05_New2
IS-FO-05_2
IS-FO-05_3
IS-FO-05_New1
LC-FO-06_1
LC-FO-06_2
LC-FO-06_4
LC-FO-06_3
IS-FO-02_3
IS-FO-02_1
IS-FO-02_4
LC-FO-05_1
LC-FO-05_3
LC-FO-05_4
IS-FU-04_1
IS-FU-04_4
IS-FU-04_2
IS-FU-04_3
LC-FU-04_4
LC-FU-04_2
LC-FU-04_1
LC-FU-04_3
Airport
Buildings
Mainroads
Roads
Signal testing
IS-FO-02_1
IS-FO-02_3
IS-FO-02_4
IS-FO-05_2
IS-FO-05_3
IS-FO-05_New1
IS-FO-05_New2
IS-FU-04_1
IS-FU-04_2
IS-FU-04_3
IS-FU-04_4
LC-FO-05_1
LC-FO-05_2
LC-FO-05_3
LC-FO-05_4
LC-FO-06_1
LC-FO-06_2
LC-FO-06_3
LC-FO-06_4
LC-FU-04_1
LC-FU-04_2
LC-FU-04_3
LC-FU-04_4
LC-SC-01_1
LC-SC-01_2
LC-SC-01_3
LC-SC-01_4
0 1 2 3 4 5 km

C. 2022 São Jorge Island seismovolcanic crisis - study case

C.1. Geological framework of São Jorge Island (Map)

Geological framework of São Jorge Island, illustrating its (1) volcanic complexes, (2) tectonics, as well (3) the vents of both historical eruptions at Manadas fissure volcanic system (modified by CIVISA from: (1) Madeira and Brum da Silveira, 2003, (2) Madeira, 1998, and (3) Zanon and Viveiros, 2019).


N
Rosais Volcanic Complex
Manadas Volcanic Complex
Topo Volcanic Complex
Tectonics
Volcanic crater
Volcanic alignment
Fault scarp, fault, inferred fault
Historical vents
1580 A.D.
1808 A.D.
Geological units
Modern (landslide and lava delta deposits, gravel beach, alluvial soil)
Historical eruptions
Manadas Volcanic Complex
Rosais Volcanic Complex
Topo Volcanic Complex
0 1 2 3 4 5 km

C. 2022 São Jorge Island seismovolcanic crisis - study case

C.2. Seismic activity on São Jorge Island: 19-03-2022 to 02-11-2022 (Map)

Seismic activity on São Jorge Island since 19 March 2022 until 2 November 2022 (data from CIVISA, 2022).

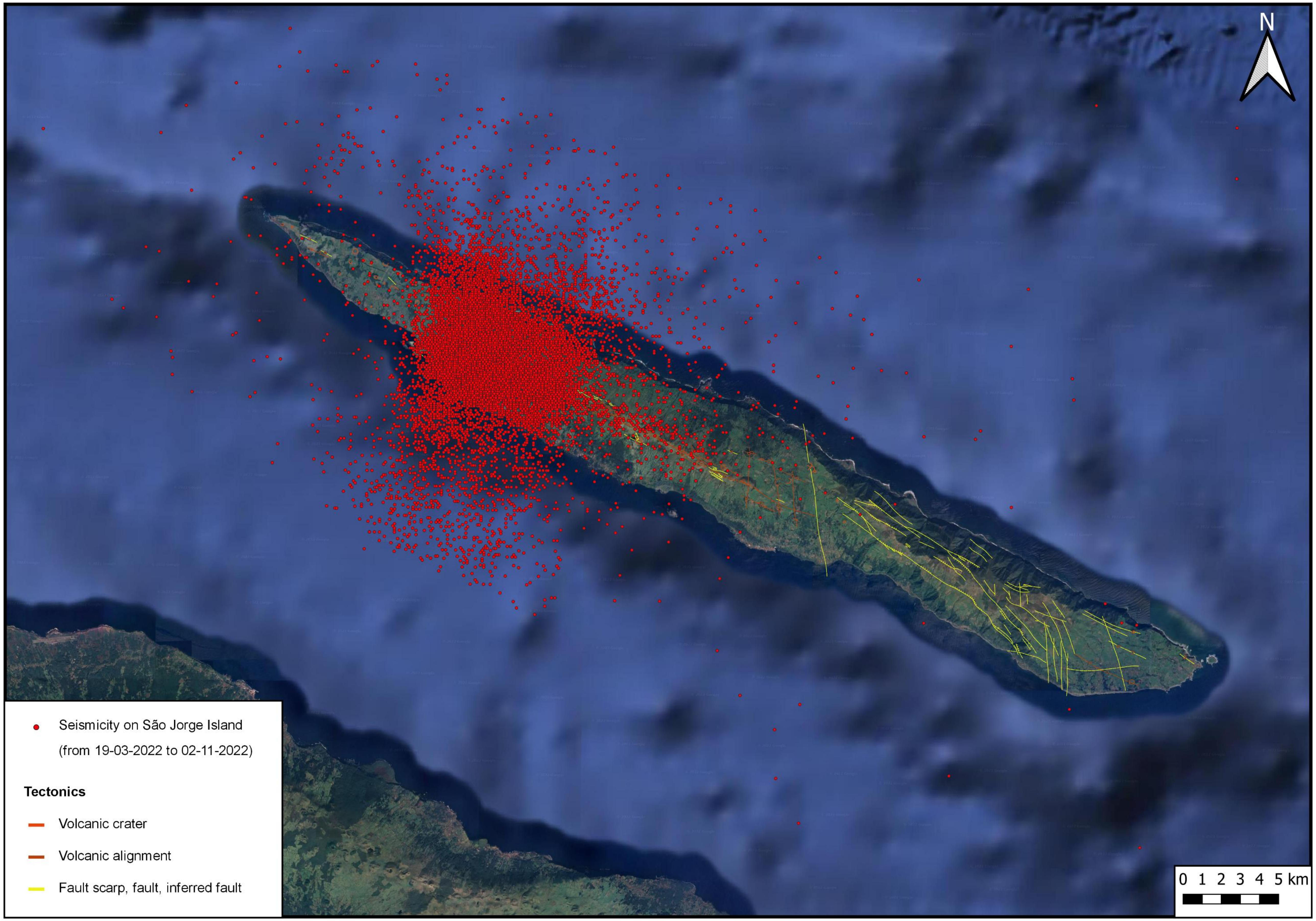
N
● Seismicity on São Jorge Island
(from 19-03-2022 to 02-11-2022)
Tectonics
Volcanic crater
Volcanic alignment
Fault scarp, fault, inferred fault
0 1 2 3 4 5 km

C. 2022 São Jorge Island seismovolcanic crisis - study case

C.3. Pre-selected sites for survey at São Jorge Island (Map)

Pre-selected sites for survey at São Jorge Island, with the back azimuths from the eruptive fissure considered to IS42 station. Historical vent's locations are from CIVISA with data from Zanon and Viveiros (2019) and probable eruptive fissure is from CIVISA with data from Madeira (1998).

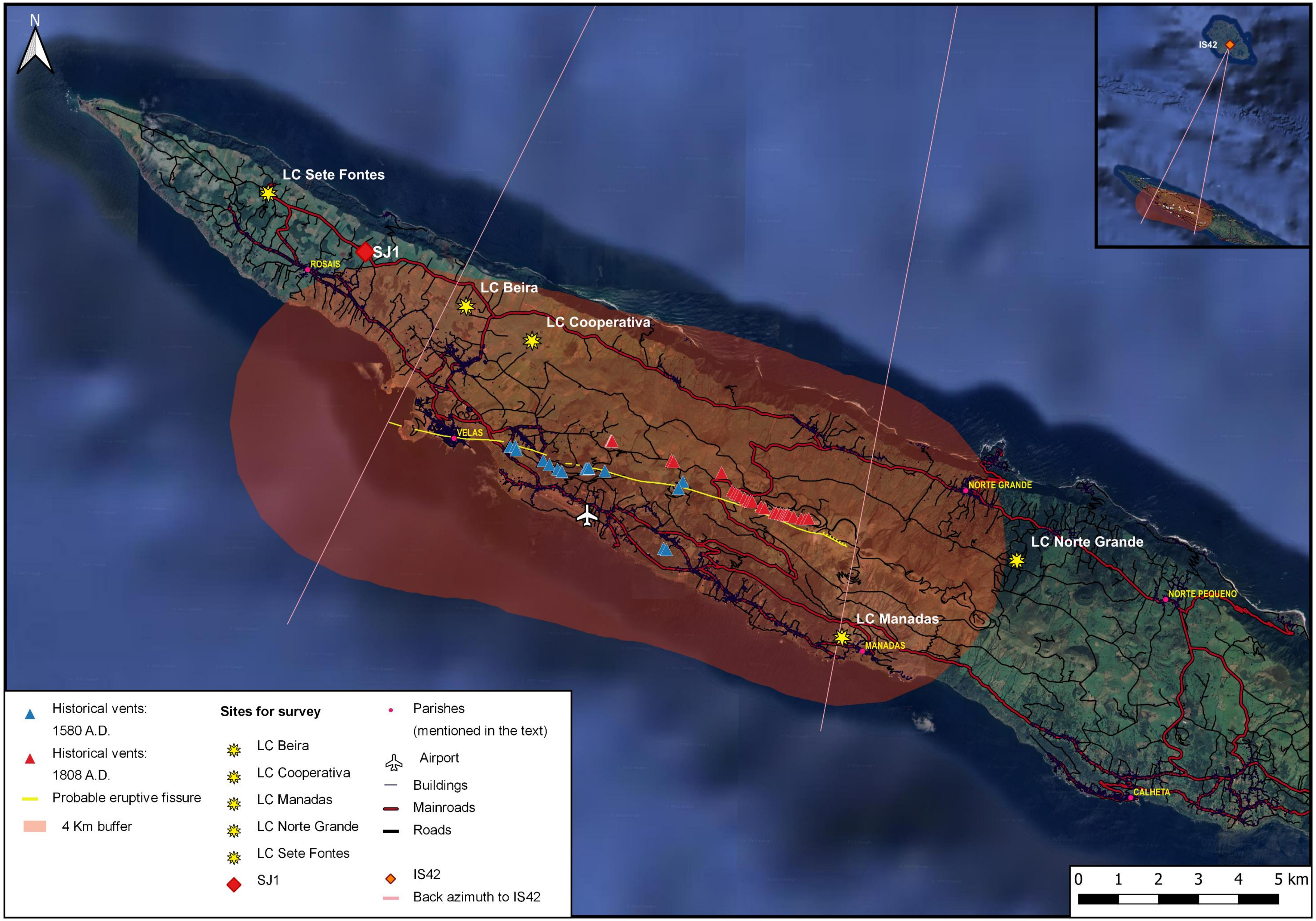
N
LC Sete Fontes
SJ1
ROSAIS
LC Beira
LC Cooperativa
VELAS
NORTE GRANDE
LC Norte Grande
NORTE PEQUENO
LC Manadas
MANADAS
CALHETA
IS42
Historical vents: 1580 A.D.
Historical vents: 1808 A.D.
Probable eruptive fissure
4 Km buffer
Sites for survey
LC Beira
LC Cooperativa
LC Manadas
LC Norte Grande
LC Sete Fontes
SJ1
Parishes (mentioned in the text)
Airport
Buildings
Mainroads
Roads
IS42
Back azimuth to IS42
0 1 2 3 4 5 km

C. 2022 São Jorge Island seismovolcanic crisis - study case

C.4. Array configurations (Maps)

a) Configuration of SJ1 from the 1st visit.

b) Configuration of SJ1 after the 2nd visit.

c) SJ1 arrays deployments compared geometries.

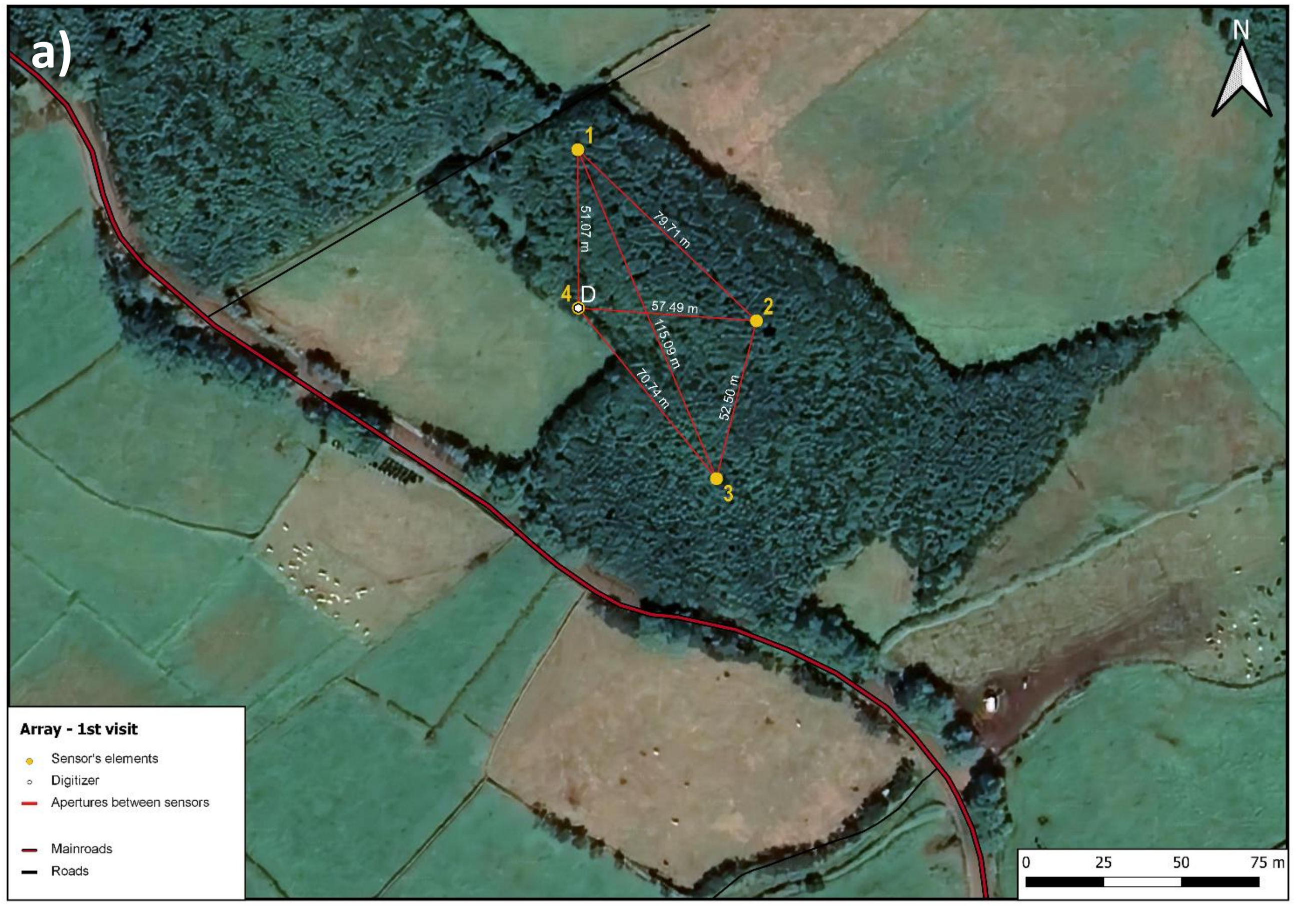
a)
N
1
51.07 m
79.71 m
4
D
57.49 m
2
115.09 m
70.74 m
52.50 m
3
Array - 1st visit
Sensor's elements
Digitizer
Apertures between sensors
Mainroads
Roads
0
25
50
75 m

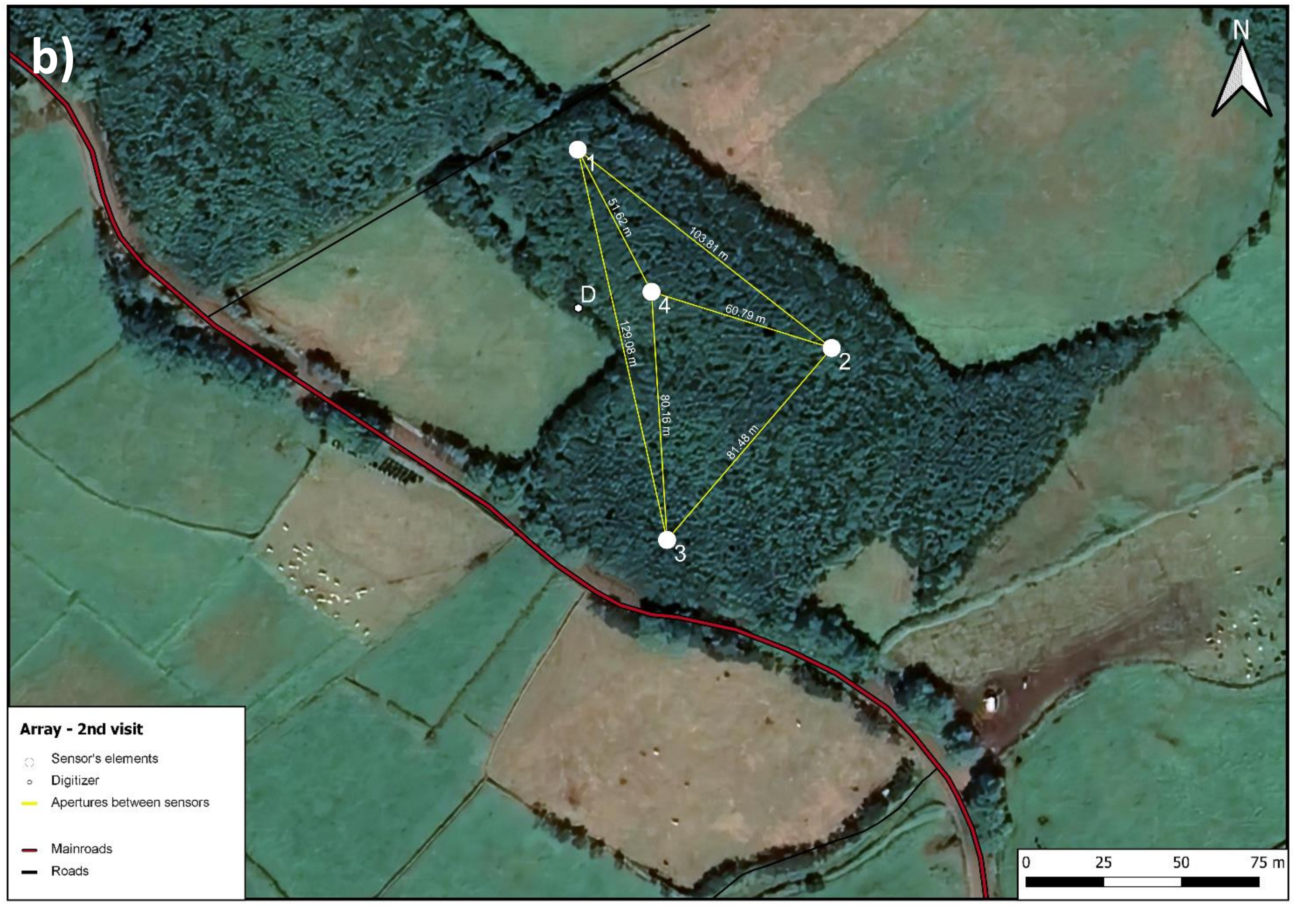
b)
N
1
51.62 m
103.81 m
D
4
60.79 m
2
129.08 m
80.16 m
81.48 m
3
Array - 2nd visit
Sensor's elements
Digitizer
Apertures between sensors
Mainroads
Roads
0
25
50
75 m

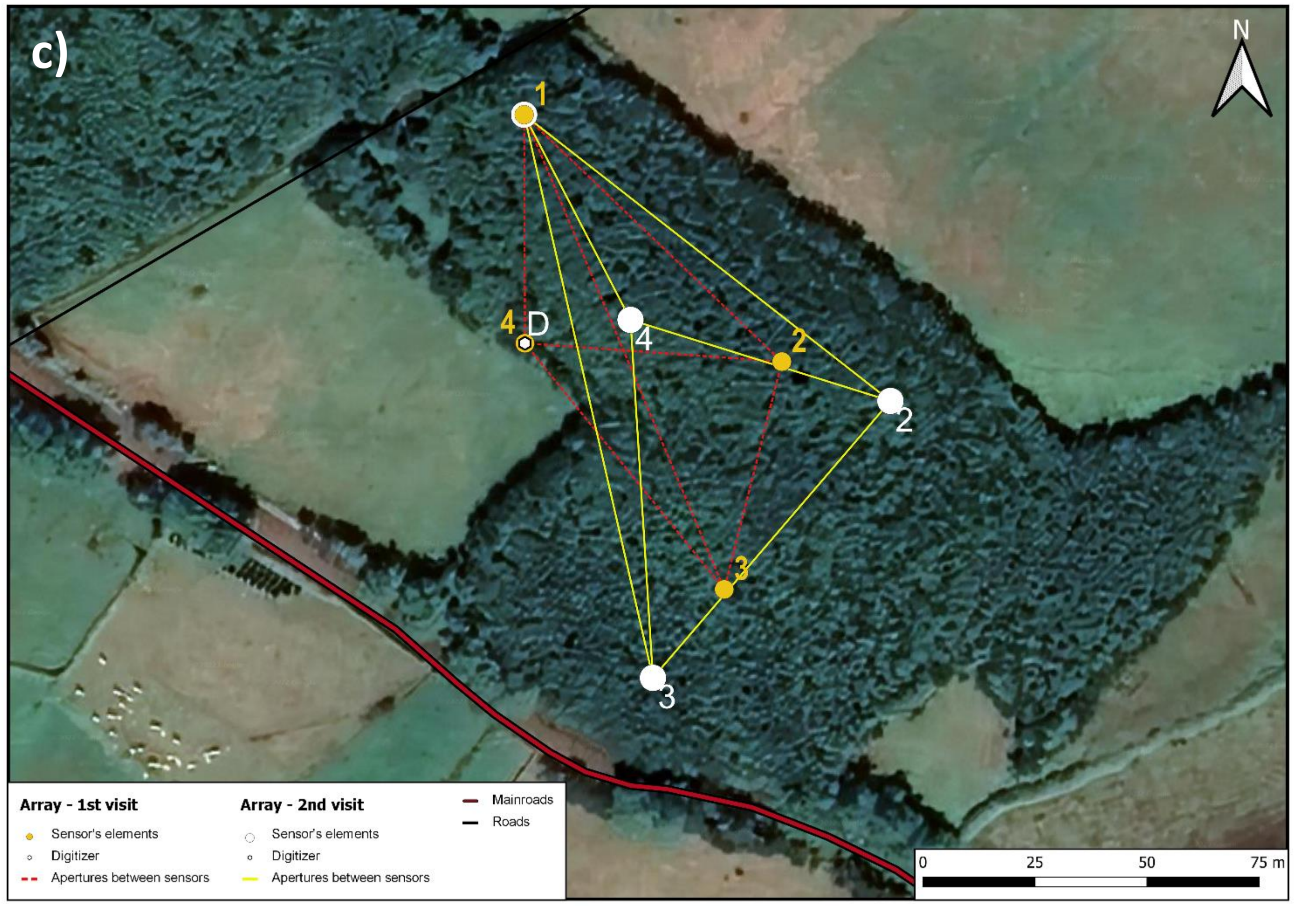
c)
N
1
4
D
4
2
2
3
3
Array - 1st visit
Sensor's elements
Digitizer
Apertures between sensors
Array - 2nd visit
Sensor's elements
Digitizer
Apertures between sensors
Mainroads
Roads
0
25
50
75 m

C. 2022 São Jorge Island seismovolcanic crisis - study case

C.5. Deployment of SJ1 (Photos from the 1st and 2nd visit)

Photo B.1 - Preparing the communications Pelicase® type box.

Photo B.2 - Preparing the communications Pelicase® type box.

Photo B.3 - Digitizer and sensor 4 inside the Pelicase® type box.

Photo B.4 - Preparing box with diverse tools.

Photo B.5 - Configurating digitizer and modem.

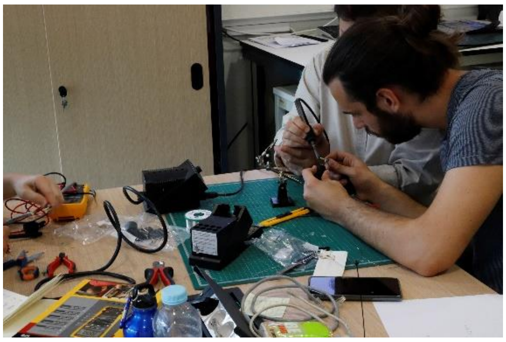

Photo B.6 - Welding cables and connectors.

Photo B.7 - Adding a cable entry on the barrel that keep one sensor.

Photo B.8 - Loading the van with all equipment to deploy SJ1.

Photo B.9 - Arriving at SJ1.

Photo B.10 - Access to SJ1.

Photo B.11 - South view.

Photo B.12 - Dividing material to start the array's deployment.

Photo B.13 - iTem differential pressure transducer (sensor).

Photo B.14 - Fixing a sensor.

Photo B.15 - Extended cables from the digitizer to the spot of the array element.

Photo B.16 - Preparing the spot to bury the barrel with the sensor.

Photo B.17 - Connecting sensor to the cable and adding a flexible hose for noise reduction.

Photo B.18 - Sensor inside the barrel.

Photo B.19 - Isolating the cable entry with silicone.

Photo B.20 - Final element, with a box covering the barrel, leaving a small space for the hose.

Photo B.21 - Layout of one array element inside the forest.

Photo B.22 - Electric cable insulated with protection tube.

Photo B.23 - Connecting cable from battery to solar panel.

Photo B.24 - Deploying solar panel.

Photo B.25 - Solar panel and mast with GPS and GSM antennas.

Photo B.26 - Preparing protection tubes to insulate electric cables.

Photo B.27 - Preparing protection tubes to insulate electric cables.

Photo B.28 - Extending electric cables already protected.

Photo B.29 - Welding connectors and cables.

Photo B.30 - Welding connectors and cables.

Photo B.31 - Welding connectors and cables.

Photo B.32 - GPS (bottom) and GSM (top) antennas.

Photo B.33 - Fence protecting solar panel and communications mast from the cattle.

Photo B.34 - Optimizing the recharge of batteries with a second solar panel.

Photo B.35 - Energy box with 1 battery.

Photo B.36 - A second battery was connected in parallel.

Photo B.37 - Setting up communications equipment inside Pelicase® type box.

Photo B.38 - Setting up communications equipment inside Pelicase® type box.

Photo B.39 - Setting up communications equipment inside Pelicase® type box.

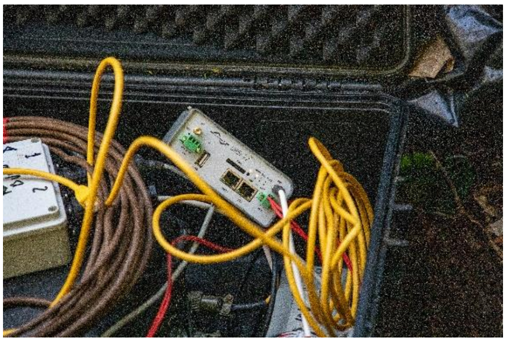

Photo B.40 - Connecting modem.

Photo B.41 - Configurating digitizer and modem .

Photo B.42 - Configurating digitizer and modem.

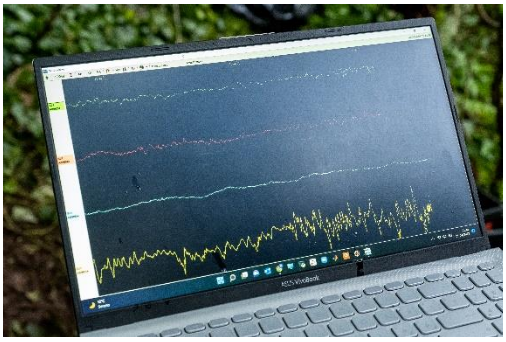

Photo B.43 - Checking signals from the 4 sensors.

Photo B.44 - Processing data on MATLAB®.

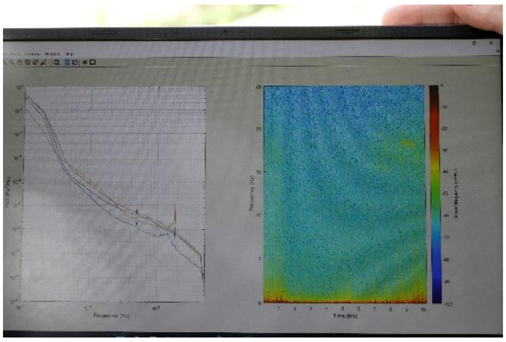

Photo B.45 - PSD and spectrogram (MATLAB®).

Photo B.46 - Data storage on a flash drive.

Photo B.47 - Communications (left) and energy equipment (right).

Photo B.48 - Protection with plastic bags.

Photo B.49 - Aerial view, with North on the left side (drone).

Photo B.50 - Waiting to collect 24-h data.

D. Field equipment

D.1. IS array equipment (SEISMOWAVE's SISTEM and MB3d datasheets)

SISTEM

READY-TO-USE PORTABLE INFRASOUND STATION

ALL-IN-ONE INFRASOUND STATION

SISTEM is an easy to deploy and transportable infrasound station which mainly includes an infrasound sensor MB3d or MB3a, a data transmission equipment, a power supply, an optional collocated weather station and a flexible wind noise reduction system.

EASY INSTALLATION

SISTEM is especially designed to facilitate its installation and uninstallation with minimum human and material resources, within the shortest time. SISTEM Infrasound station is ready to use after quick plug connections. Accessories are delivered in transportable and reusable cases.

MODULAR EQUIPMENT

SISTEM's standard electronic equipment (modem, battery or even sensor) can be modified according to your needs upon request.

REMOTE DATA RECOVERY

SISTEM is equipped with a GSM/3G/4G modem and a RS232 to ethernet converter allowing the remote transmission of your MB3d data.

MULTIPLE POWER CONNECTIONS SOLUTIONS

You can connect SISTEM to the mains, to external batteries or to solar panels, depending on your needs and on field constraints.

OPTIONAL WEATHER STATION AND WNRS

SISTEM is designed to be easily connected with a weather station and a flexible wind noise reduction SISTEM for more efficient measurements.

SEISMO WAVE

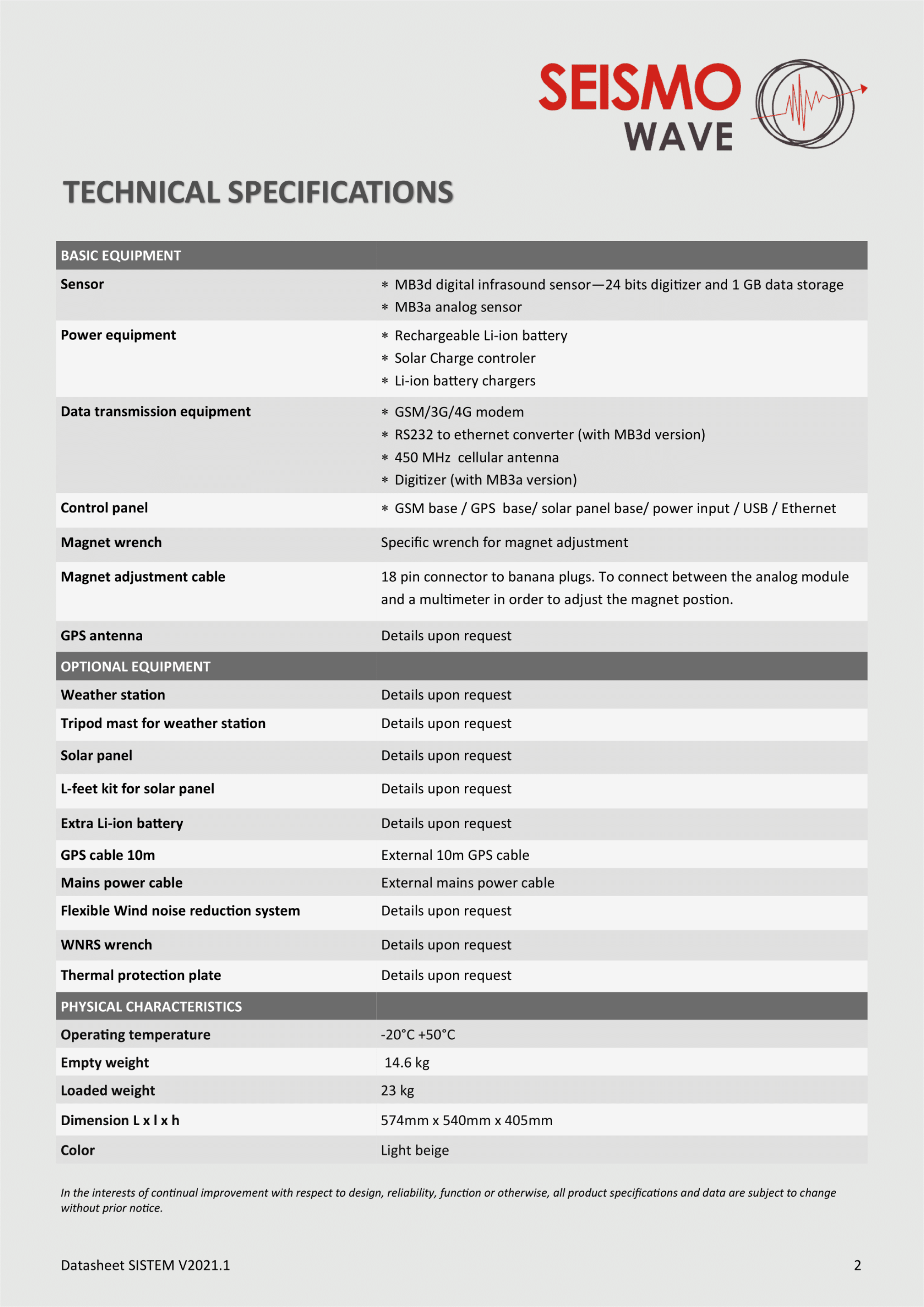

SEISMO WAVE

TECHNICAL SPECIFICATIONS

BASIC EQUIPMENT	
Sensor	∗ MB3d digital infrasound sensor—24 bits digitizer and 1 GB data storage ∗ MB3a analog sensor
Power equipment	∗ Rechargeable Li-ion battery ∗ Solar Charge controler ∗ Li-ion battery chargers
Data transmission equipment	∗ GSM/3G/4G modem ∗ RS232 to ethernet converter (with MB3d version) ∗ 450 MHz cellular antenna ∗ Digitizer (with MB3a version)
Control panel	∗ GSM base / GPS base/ solar panel base/ power input / USB / Ethernet
Magnet wrench	Specific wrench for magnet adjustment
Magnet adjustment cable	18 pin connector to banana plugs. To connect between the analog module and a multimeter in order to adjust the magnet postion.
GPS antenna	Details upon request
OPTIONAL EQUIPMENT	
Weather station	Details upon request
Tripod mast for weather station	Details upon request
Solar panel	Details upon request
L-feet kit for solar panel	Details upon request
Extra Li-ion battery	Details upon request
GPS cable 10m	External 10m GPS cable
Mains power cable	External mains power cable
Flexible Wind noise reduction system	Details upon request
WNRS wrench	Details upon request
Thermal protection plate	Details upon request
PHYSICAL CHARACTERISTICS	
Operating temperature	-20°C +50°C
Empty weight	14.6 kg
Loaded weight	23 kg
Dimension L x l x h	574mm x 540mm x 405mm
Color	Light beige

MB3d

DIGITAL INFRASOUND SENSOR

The MB3d sensor was developed by the CEA (Commissariat à l'Energie Atomique). This digital version of the well-known MB3a embedded a 24 bits digitizer. The transducer is an aneroid capsule coupled with a magnet & coil transducer.

Under licence of cea

RECORDING OF LOW-FREQUENCY ACOUSTIC SIGNALS FROM 0.01 TO 28HZ

The MB3d digital infrasound sensor allows the recording of very low-frequency acoustic signals over a broad frequency band, with an excellent resolution and a large dynamic range.

REMOTE CALIBRATION

Thanks to a secondary coil wrapped around the principal, the MB3d allows remote calibration of your sensor using MLS, pulse or sine waves.

LOW LEVEL OF INSTRUMENTAL NOISE

The MB3d is remarkable for an extremely low level of instrumental noise (<-80 dB.Pa / □ Hz @ 1 Hz) allowing the sensor to resolve more than 10 dB the Low Noise Model.

ONBOARD 24 BITS DIGITIZER

The Mb3d encapsulates a low-noise 24 bit digitizer (ADC), with a calibration board, a time card and a storage capacity of 1 Go.

DIONISOS SOFTWARE INCLUDED

Dionisos software has been specifically developed for the MB3d digital infrasound sensor:, it allows

- Graphic visualization of data , in real time as in deferred time.
- Calibration
- Configuration and visualization of the states of health of the sensor

VOLCANOLOGY

METEOROLOGY

CIVIL SECURITY

MILITARY SECURITY

SEISMO WAVE

KEY FEATURES

TRANSDUCER BLOCK	
Bandwitdth (f -3 db)	Pressure output: 0,01 - 28 Hz Pressure derived output: DC - 28 Hz
BLDR (Band Limited Dynamic Range) [0,02 ; 4 Hz]	111 dB @ f < 106 Hz 109 dB @ f = 4 Hz
Self-noise	0,13 mPa/□Hz @ 1 Hz < 10 dB under LNM (Low Noise Model)
Resolution [0,02 ; 4 Hz]	1,75 mPaRMS
Nominal sensitivity (adjustable gain)	• Pressure output: 20 mV/Pa • Pressure derived output: 2 mV/Pa.s-1 • Calibration output: 6 Pa/V
Auxiliary outputs Temperature sensor Atmospheric pressure Sensor	• [-40 ; +110]°C, 10 mV/°C, ±0,2°C • [150 ; 1150] hPa, 1 mV/Pa • Offset stability: 0,25% full scale / uncertainty: 1,5% full scale
DIGITAL HOOD	
Clipping level & output range	± min (12 000 [Pa/s] / 2.π.f[Hz] ; 1000 [Pa]) Pressure derived: ± 10 000 (Pa/s)
Sampling rate	20, 50, 100 Hz
Nominal sensitivity	1,178 10-4 Pa/lsb or 1,178 10-3 Pa/lsb @ gain = 1
Built-in gain	1, 2, 4, 8 (Digitizer gain)
Data storage / communication	1 GB / miniSEED
Power requirements	12 V DC (7-20 V) - 840 wW
ENVIRONMENTAL SPECIFICATIONS	
Operating temperature	-20°C to +50°C
Storage temperature	-30°C to +70°C
Seismic sensitivity	< 30 Pa/m.s-2
Sealing	CEI 60529-IP67 (with sealed acoustic inlets)
Shock / Drop	NF EN 60721-3-1, 2M1 (free fall, impact, shock)
Transport	NF EN 60721-3-2, 2M3 (vibration)
EMC	NF EN 55024 classes A & B (immunity) NF EN 55022 class B (emission)
PHYSICAL CHARACTERISTICS	
Weight	3.4 kg
Diameter	110 mm
Height	205 mm

SENSOR SENSITIVITY RESPONSE

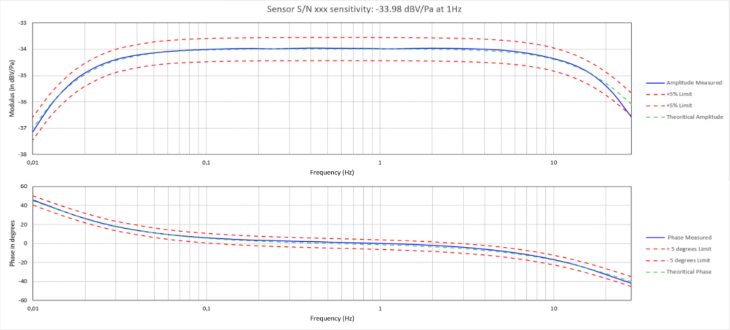

SENSOR SELF-NOISE

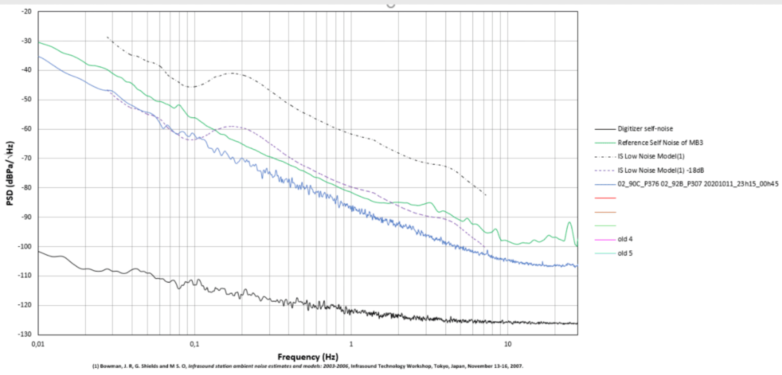

(1) Bowman, J. R, G. Shields and M S. O, *Infrasound station ambient noise estimates and models: 2003-2006*, Infrasound Technology Workshop, Tokyo, Japan, November 13-16, 2007.

RELATED PRODUCTS

SISTEM

READY-TO-USE
PORTABLE
INFRASOUND STATION

RS232 TO ETHERNET CONVERTER

D. Field equipment

D.2. LC array equipment (Table)

#	QTD.	SJ1 EQUIPMENT	SPECIFICATIONS
1	6	**Differential pressure transducer**	iTEM (UniFI)
		Sensivity:	400 mV/Pa
		Pressure range:	± 12.5 Pa (25 Pa peak to peak)
		Frequency response:	0.01-200 Hz
2	4	100-m eletric cable	
3	4	Flexible hose (WNRS)	
4	9	Connector	
5	8	50-m protection tube	
6	4	30 L barrel	
7	4	30 L box	
8	6	50-mm cable entry	
9	1	Pelicase® type box for digitizer and modem	
10	1	**Digitizer**	Guralp GCM-DM24
		Dynamic range:	24 bit
		Sampling rate:	100 Hz
11	1	GSM Modem	3G modem
12	1	GSM card	MEO services
13	1	Modem cable	
14	1	Modem antenna	
15	1	GPS cable	
16	1	GPS antenna	
17	1	Battery box	
18	4	**Battery**	12V 100Ah 830A B13 Lead Acid battery (BOSCH)
19	2	Crocodile claw	
20	2	Terminal	
21	1	Battery charger	
22	1	Solar panel 40 W	
23	1	Solar panel 115 W	
24	1	Charge controller	
25	1	Charge controller - solar panel cables	
26	1	Charge controller - digitizer cables	
27	1	Box with diverse material	
28	1	Power drill and accessories	
29	1	Tool case	
30	1	Solder iron and gas	
31	1	Shovel	
32	1	Hoe	
33	2	Machete	

E. Meteorological data

Plot of the raw meteorological data recorded at São Jorge Island from 02/04/2022 08:00 PM to 01/06/2022 06:00 PM (data from IPMA, 2022)

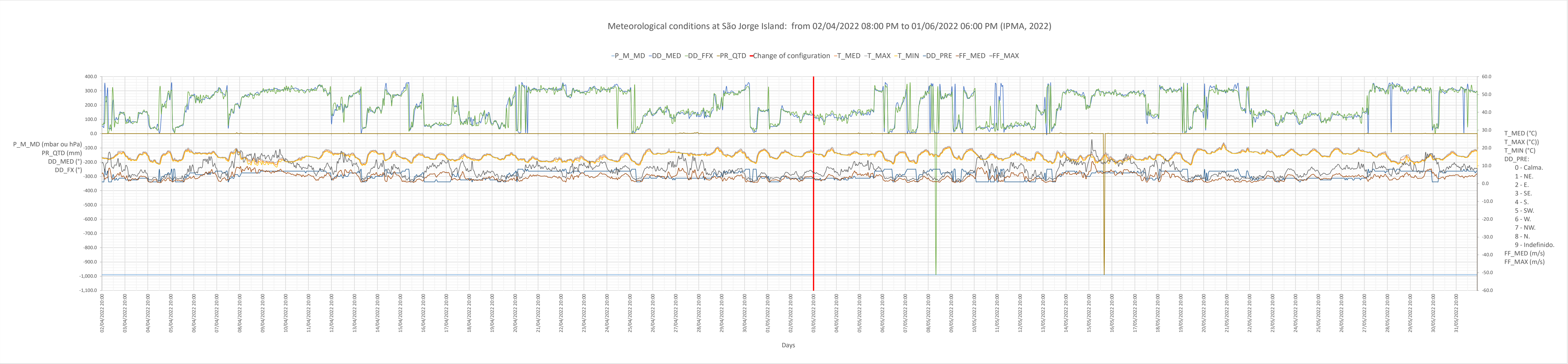

P_M_MD:	Average pressure at sea level (mbar or hPa)
T_MED:	Average air temperature (°C)
T_MAX:	Maximum air temperature (°C)
T_MIN:	Minimum air temperature (°C)
DD_MED:	Mean wind Direction (°)
DD_FX:	Maximum wind Direction (°)
DD_PRE:	Prevailing wind direction: 0 - Calm; 1 - NE; 2 - E; 3 - SE; 4 - S; 5 - SW; 6 - W; 7 - NW; 8 - N; 9 - Undefined.
FF_MED:	Average wind intensity (m/s)
FF_MAX:	Maximum instantaneous wind intensity (m/s)
PR_QTD:	Precipitation (mm)

UNIVERSIDADE DOS AÇORES
Faculdade de Ciências e Tecnologia

Rua da Mãe de Deus
9500-321 Ponta Delgada
Açores, Portugal

Site surveys to deploy infrasound mobile stations in the Azores Islands

Maria do Céu Neto de Jesus

DM

SICUT AURORA SCIENTIA LUCET
UNIVERSIDADE DOS AÇORES

2022